Experimental Investigation on Wire Arc Additive Manufacturing of Dissimilar Inconel and Stainless-Steel Alloys Using Cold Metal Transfer Welding

Thesis Submitted

in Partial Fulfilment of the Requirements for the

Degree of

DOCTOR OF PHILOSOPHY

in

MECHANICAL ENGINEERING

by

Rajendra Prasad Meena

(2K21/PhD ME/08)

Under the supervision of

Dr. N. Yuvaraj

(Department of Mechanical Engineering, DTU)

Prof. Vipin

(Department of Mechanical Engineering, DTU)

DEPARTMENT OF MECHANICAL ENGINEERING

DELHI TECHNOLOGICAL UNIVERSITY

(Formerly Delhi College of Engineering)

Main Bawana Road, Shahabad Daulatpur, Delhi-110042, India

August, 2024

ACKNOWLEDGEMENT

I want to express my sincere gratitude to the many people who have helped me during the tenure of my Ph.D. work. I take this opportunity to express my deep gratitude to all of them for their support and help during various phases of my doctoral research work. At this moment of accomplishment, first and foremost, I would like to give my utmost gratitude to my supervisors, **Dr. N. Yuvaraj** and **Prof. Vipin**. This work would not have been possible without their guidance, support, and encouragement. Under their guidance, I could overcome many difficulties and learned a lot. Despite being very busy, they reviewed my thesis progress, gave their valuable suggestions, and made corrections even during late hours. This persistent courage and opinion will always inspire me, and I can only thank them through my future work.

I am highly thankful to **Prof. Qasim Murtaza** for his advice at various stages of this work. This magnificent period would have been incomplete and tasteless without the company of my colleagues and friends.

I heartily admire the support provided by technical staff **Mr Tek Chand, Mr Girish Kumar, Mr Lalan Kumar Sinha**, and **Mr Netram**. **Mr. Rajesh Bohra**, thank you for your help and assistance in doing the wear test. Last but not the least, I would like to thank my father, **Mr Mahbub Singh Meena,** my mother, **Mrs Keshanti Meena** and my brother, **Mr Surendra Kumar Meena,** for always being there when I needed them most and for their moral support that kept my spirit up during the endeavour.

Rajendra Prasad Meena

MECHANICAL ENGINEERING DEPARTMENT

DELHI TECHNOLOGICAL UNIVERSITY

DELHI-110042, INDIA

DECLARATION

I certify that the work being presented in this thesis entitled "**Experimental Investigation on Wire Arc Additive Manufacturing of Dissimilar Inconel and Stainless-Steel Alloys Using Cold Metal Transfer Welding**", in the partial fulfilment of the requirement for the award of the degree of Doctorate in Philosophy submitted in the Department of Mechanical Engineering at Delhi Technological University, is an authentic record of my own work carried out during a period from August 2021 to August 2024, under the supervision of **DR. N. YUVARAJ** and **PROF. VIPIN**, Department of Mechanical Engineering, DelhiTechnological University, Delhi. The matter presented in this thesis has not been submitted to any other University/Institute for awarding any degree or diploma.

.

Date:

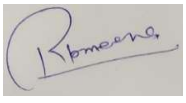

Rajendra Prasad Meena

(2K21/PhDME/08)

Mechanical Engineering Department

Delhi Technological University

MECHANICAL ENGINEERING DEPARTMENT

DELHI TECHNOLOGICAL UNIVERSITY

DELHI-110042, INDIA

CERTIFICATE

This is to certify that the thesis entitled "**Experimental Investigation on Wire Arc Additive Manufacturing of Dissimilar Inconel and Stainless-Steel Alloys Using Cold Metal Transfer Welding**", submitted to the Delhi Technological University, Delhi -110042, is a fulfilment of the requirements for the award of a degree of Doctorate in Philosophy in Mechanical Engineering embodies the original research work carried out by **Mr. Rajendra Prasad Meena,** Enrolment No: 2K21/PhD/ME/08 under my supervision. This work has not been submitted in part or full for any other degree or diploma from this or any other university.

Dr. N. Yuvaraj

Department of Mechanical Engineering

Delhi Technological University

Prof. Vipin

Department of Mechanical Engineering

Delhi Technological University

ABSTRACT

Wire Arc Additive Manufacturing (WAAM) has grown in popularity due to the many practical uses of additive manufacturing (AM), most notably in the fabrication of large metal structures. Cold Metal Transfer (CMT) is an advanced gas metal arc welding (GMAW) technology with minimal heat input, producing clean surfaces and little spatter. Inconel 718 and SDSS 2507 1.2 mm diameter filler wire were selected in this research. Stainless steel 304 was selected as substrate material with 200mm × 50mm × 5 mm dimensions. This research work outlines techniques for optimizing input parameters for the welding process, such as welding current, speed, and gas flow rate in relation to weld bead geometry and Dilution, using Response Surface Methodology (RSM). In the WAAM process, single-weld bead stability and quality play a prominent role in the final manufactured part's quality and shape. A single-bead geometry model was initially established using RSM, and experiments were carried out using a central composite design of experiments for depositing for Super Duplex Stainless Steel (SDSS) 2507 and Inconel (IN) 718 in WAAM. The design factors and responses were analysed using multiple regression equations, and the validity of the resulting regression equations was evaluated using ANOVA. The optimum values for weld bead width and bead height were 6.57 mm and 3.43 mm, respectively; the minimum dilution observed was 31.30 % for SDSS 2507. The predicted optimal input parameters were 190.46A current, 8.94 mm/s welding speed, and 15 l/min shielding gas flow rate for SDSS 2507. The results indicated that current was the most influential factor in determining the multiple responses, followed by welding speed and gas flow rate. The microstructures of SDSS 2507 were characterized by optical microscopy, and results indicated that the microstructure of the weld bead region consisted of ferrite and austenite. The WAAM wall is fabricated with optimal parameters. The optimum parameters for IN 718 are a welding current of 210 A, 6.91 mm/min speed, and a gas flow rate of 25 l/min. Microstructure characterization revealed small grains in the top layer, equiaxed in the middle

and side regions, and columnar in the lower region for IN 718. The microhardness of the CMT-based WAAM fabricated samples was also evaluated.

The current study involved manufacturing a dissimilar alloy wall using SDSS 2507 and IN718 through the CMT-based WAAM. The microstructural characteristics reveal a discontinuity in the dendritic structure and an abrupt transition at the Interface (IF). A confirmation of the fine disintegration of elements at the Interface (IF) was found by energy-dispersive X-ray spectroscopy (EDS), and no significant change in composition was noted. Microstructure investigation indicates build-direction epitaxial grain growth and deposited layer non-equilibrium microstructures. SDSS 2507's SEM microscopy displays austenite and ferrite in the lower part, and IN 718's shows columnar and cellular crystals with white laves phases, which form when Nb and Mo elements segregate. The interface (IF) samples at a 90° angle in the SDSS 2507L region experienced failure due to a lower Ultimate Tensile Strength (UTS) than IN718. The fracture mode observed was ductile. The microhardness measurements illustrate the progressive variation in building direction hardness.

Ultrasonic vibration has been used in melting material solidification procedures to enhance part performance. This research proposes using ultrasonic vibration (UV) assisted CMT-based WAAM deposition to potentially manufacture dissimilar SDSS 2507-IN718 parts to decrease fabrication defects. Experimental studies are carried out to examine the impact of ultrasonic vibration on the microstructures and mechanical properties of parts manufactured using CMT. The findings demonstrated that the application of ultrasonic vibration improved the microstructure, leading to an average grain size of 4.59 um. In addition, it effectively fragmented the harmful Laves precipitated phase into small particles that were evenly distributed. Consequently, the yield strength, UTS, and microhardness of the fabricated dissimilar SDSS 2507-IN718 parts were improved.

This research presents the wear summary on the dissimilar alloy wall manufactured using the WAAM technique, subjected to dry sliding under extreme loading conditions. Wear testing was conducted in a dry, unlubricated environment using a standard high-load ball-on-disc tribometer. Wear rate and coefficient of friction are minimum at low loading conditions for SDSS 2507. Worn surfaces reveal grooving, delamination, delamination cracks, ploughing grooves, parallel grooves, and particle adherence, confirming adhesion and abrasive wear mechanism.

TABLE OF CONTENTS

ACKNOWLEDGEMENT i

DECLARATION ii

CERTIFICATE iii

ABSTRACT iv

TABLE OF CONTENTS vii

LIST OF TABLES xii

LIST OF FIGURES xiv

ABBREVIATIONS xix

CHAPTER 1: INTRODUCTION

1.1 Introduction 1

1.2 WAAM classification 4

1.3 Cold Metal Transfer operation principle 7

1.4 Overview of thesis 10

1.5 Summary 11

CHAPTER 2: LITERATURE REVIEW

2.1 Introduction 12

2.2 Wire Arc Additive Manufacturing of alloys 12

2.2.1 Role of Deposition Strategy in WAAM 38

2.3 Materials employed in the WAAM process 38

2.3.1 Nickel-based superalloys 39

2.3.2 Titanium alloys 44

2.3.3 Aluminium alloys 46

2.3.4 Magnesium alloys 50

2.3.5 Steels 50

2.3.6 Other alloys 52

2.4 Recent challenges in WAAM 53

2.4.1 Residual stress and deformations 54

2.4.2 Porosity 55

2.4.3 Cracks and delamination 56

2.4.4 Automation and integrated machining 57

2.5 Recent advances for quality improvement in WAAM 58

2.5.1 Interlayer rolling 58

2.5.2 Post-process heat treatment 59

2.5.3 Double wire WAAM (DWAAM) 60

2.5.4 Near-immersion active cooling (NIAC) 61

2.6 Numerical Simulation 62

2.7 Research gaps 64

2.8 Research objectives 64

2.9 Flow chart for work 65

2.10 Summary 65

CHAPTER 3: MATERIALS AND METHODS

3.1 Materials 67

3.1.1 Substrate metal/ Base material 67

3.1.2 Filler Material 68

3.2 Sample preparation 69

3.2.1 Macrostructure Characterization 69

3.2.2 Microstructure Characterization 70

3.2.3 Microhardness 71

3.2.4 Tensile Testing 72

3.2.5 Tribological properties 73

3.3 Experimental Machines 73

3.3.1 CMT Machine 73

3.3.2 Microhardness Machine 76

3.3.3 Tensile testing machine 78

3.3.4 Optical Microscope 80

3.3.5 Field Emission Scanning Electron Microscope 83

3.3.6 X-Ray Diffraction 85

3.3.7 Linear Reciprocating Tribometer 88

3.4 Optimisation of CMT process parameters 90

3.4.1 Response Surface Methodology 90

3.4.2 Process parameters 92

3.4.3 The limits of the process parameter and design matrix 94

3.5 Experimental procedure 95

3.5.1 Bead on plate 95

3.5.2 CMT WAAM wall 99

3.5.3 Ultrasonic vibration-assisted CMT WAAM wall 100

3.6 Summary 102

CHAPTER 4: RESULTS AND DISCUSSIONS ON OPTIMIZATION OF PROCESS PARAMETERS

4.1 Optimisation of process parameters of SDSS 2507 103

4.2 Mathematical modelling 103

4.2.1 Bead Geometry Mathematical Modelling 104

4.2.2 Effect of input parameters on response variables 109

4.2.3 Conformity test 112

4.2.4 Process parameter optimization 113

4.3 Microstructure characterization of SDSS 2507 WAAM samples at optimum parameters 115

4.4 Mechanical properties of SDSS 2507 WAAM samples 117

4.5 Optimisation of process parameters of IN 718 119

4.5.1 Developing the predictive mathematical models 121

4.6 Process Parameters Effect on Responses 124

4.6.1 Parameter Effect on Bead Width 125

4.6.2 Parameter Effect on Bead Height 125

4.6.3 Parameter Effect on Dilution 125

4.7 Study of predicted v/s actual data 127

4.8 Process parameter optimization 127

4.9 Microstructure analysis of IN 718 WAAM samples at optimum parameters 130

4.10 Mechanical properties of Inconel 718 Wall 132

4.11 Summary 133

CHAPTER 5: RESULTS AND DISCUSSIONS ON DISSIMILAR SDSS 2507-IN 718 WAAM WALL

5.1 Microstructure and Mechanical Characterisation of Dissimilar Super Duplex Stainless Steel 2507 -Inconel 718 alloy structure 134

5.1.1 Introduction 134

5.1.2 X-Ray Diffraction Analysis of Phase Structure 135

5.1.3 Microstructure Analysis 136

5.1.4 Microhardness 144

5.1.5 Tensile Properties 145

5.1.6 Fractography of tensile specimens 147

5.2 Ultrasonic Vibration Assisted Microstructure and Mechanical Characterisation of Dissimilar Super Duplex Stainless Steel 2507 -Inconel 718 alloy structure 149

5.2.1 Introduction 149

5.2.2 Microstructure 150

5.2.3 Phase composition analysis 152

5.2.4 Microhardness analysis 155

5.2.5 Tensile Properties 156

5.3 Wear characteristics of Dissimilar SDSS 2507- IN 718 alloy WAAM wall 159

5.3.1 Introduction 159

5.3.2 Tribological behaviour 161

5.3.4 Wear mechanism 164

5.4 Summary 167

CHAPTER 6: CONCLUSIONS AND SCOPE FOR FUTURE WORK

6.1 Conclusions 169

6.1.1 Optimization of process parameters of CMT WAAM for fabrication of SDSS 2507 wall 169

6.1.2 Optimization of process parameters of CMT WAAM for fabrication of IN 718 wall 170

6.1.3 Dissimilar SDSS 2507-IN 718 Alloy CMT WAAM 170

6.1.4 Ultrasonic Assisted Dissimilar SDSS 2507-IN 718 Alloy CMT WAAM 171

6.1.5 Wear Characterization of Dissimilar SDSS 2507-IN 718 Alloy CMT WAAM 171

6.2 Scope for Future Work 172

REFERENCES 173

LIST OF PUBLICATIONS 202

CURRICULUM VITAE 204

LIST OF TABLES

Table 1.1 Different WAAM processes 5

Table 2.1 CMT-based WAAM process effects on microstructure and mechanical properties 15

Table 2.2 GMAW-based WAAM process effects on microstructure and mechanical properties 26

Table 2.3 GTAW-based WAAM process effects on microstructure and mechanical properties 31

Table 2.4 Plasma-based WAAM process effects on microstructure and mechanical properties 35

Table 2.5 FCAW-based WAAM process effects on microstructure and mechanical properties 37

Table 2.6 Ni-based superalloy mechanical characteristics of different WAAM techniques 43

Table 2.7 Ti-based superalloy mechanical characteristics of GTAW WAAM techniques 45

Table 2.8 Al-based alloy mechanical characteristics of different WAAM techniques 49

Table 3.1 Chemical compositions (wt%) obtained by chemical spectroscopy of substrate materials as per ASTM standards 67

Table 3.2 Mechanical properties of substrate material 67

Table 3.3 Chemical composition (Wt %) of the filler wire 69

Table 3.4 Specification of CMT machine 76

Table 3.5 Specification of Microhardness Tester (Struers Duramin-40) 77

Table 3.6 Specification of Tensile Testing Machine 79

Table 3.7 Specifications of Optical Microscope 82

Table 3.8 Specification of FESEM machine 85

Table 3.9 Specification of XRD machine 87

Table 3.10 Specification of linear reciprocating tribometer 89

Table 3.11 Input parameters and their levels for SDSS 2507 95

Table 3.12 Input parameters and their levels for IN 718 95

Table 3.13 Design Matrix and Responses for SDSS 2507 97

Table 3.14 Design Matrix and Responses for IN 718 98

Table 3.15 CMT WAAM deposition parameters used in this experiment 100

Table 3.16 Ultrasonic-assisted CMT WAAM deposition parameters used in this experiment 101

Table 4.1 ANOVA test result for weld bead width (BW) 106

Table 4.2 ANOVA test result for Weld bead height (BH) 107

Table 4.3 ANOVA test result for Dilution 108

Table 4.4 Coefficient of determination values 109

Table 4.5 Validity of regression model test results 113

Table 4.6 ANOVA for Bead Width 122

Table 4.7 ANOVA for Bead Height 122

Table 4.8 ANOVA for Dilution 123

Table 4.9 Coefficients of determination values 123

Table 4.10 Confirmation results 129

Table 5.1 Tensile testing results of as-deposited dissimilar alloy wall 146

Table 5.2 Wear properties of samples 162

LIST OF FIGURES

Fig. 1.1 Industry 4.0 Technologies 1

Fig. 1.2 Classification of Additive Manufacturing 2

Fig. 1.3 Classification of WAAM 4

Fig. 1.4 WAAM input and output parameters 6

Fig. 1.5 Principle of CMT welding operation 8

Fig. 1.6 Waveform of current and voltage of CMT process 9

Fig. 2.1 CMT-based WAAM papers (a) Publication's year variation (b) Article type variation 13

Fig. 2.2 CMT-WAAM Country-wise research publication variation plot 13

Fig. 2.3 WAAM nozzle path direction during operation (a) Unidirectional (b) Bi-directional 38

Fig. 2.4. As-fabricated (A.F.) and homogenized-annealed (H.A.) WAAM IN718 samples' cross-sectional optical micrographs: plane sections parallel to B.D. for (a) A.F. and (c) H.A. and perpendicular for (b) A.F. and (d) H.A. 40

Fig. 2.5 The microscopic appearance of the distinct IN 625 deposition layers 41

Fig. 2.6 Mechanical properties variation of Inconel (a) Tensile strength, yield strength and % elongation of IN625 (b) Microhardness of IN 718 42

Fig. 2.7 (a) Macrograph of the deposited wall in cross-section (b) Optical micrographs of the following regions: a, b, c, d, e, and f 46

Fig. 2.8 CMT fabricated wall longitudinal cross-section and corresponding optical micrograph (a, b, c, d) 47

Fig. 2.9 UTS variation plot of different Al alloys fabricated by CMT WAAM 48

Fig. 2.10 Optical micrographs of the as-deposited SDSS wall at several positions along the building direction: IGA intragranular austenite, WA Widmanstatten austenite, GBA grain boundary austenite, and c2-secondary austenite 52

Fig. 2.11 WAAM major defects with certain materials 54

Fig. 2.12 Schematic diagram of Hybrid WAAM rolling and deposition system setup for experimentation 59

Fig. 2.13 Schematic DWAAM experimental apparatus set up 61

Fig. 2.14 Schematic NIAC experimental setup 62

Fig. 2.15 Flow chart of research work 65

Fig. 3.1 Cross-section macrostructure specimen of the weld bead 70

Fig. 3.2 Steps of sample preparation for microstructure characterization 71

Fig. 3.3 Microhardness indentation on SDSS 2507 sample 72

Fig. 3.4 Tensile Specimen as per ASTM E8 72

Fig. 3.5 TPS400i CMT machine 75

Fig. 3.6 Microhardness tester (Struers Duramin-40) 77

Fig. 3.7 Tensile machine (Model: Tinius Olsen H50KS) 80

Fig. 3.8 Olympus GX41 compact inverted metallurgical microscope 81

Fig. 3.9 Field Emission Gun Scanning Electron Microscope (Model-Nova Nano FE-SEM 450) 84

Fig. 3.10 XRD (Model: BRUKER D8 ADVANCED) 86

Fig. 3.11 Linear Reciprocating Tribometer (Model-Ducom) 89

Fig. 3.12 Weld on bead CMT experimental set-up 96

Fig 3.13. CMT WAAM experimental setup 99

Fig 3.14. Schematic Ultrasonic Assisted CMT WAAM experimental setup 101

Fig. 3.15 Schematic diagram of (a) Extracted samples (b) Tensile test specimen 102

Fig. 4.1 Macro-images of weld bead 104

Fig. 4.2 Effect of input parameters on output responses (a) Weld bead width (b) Weld bead height (c) Dilution (%) 111

Fig. 4.3 Exhibits the predicted v/s actual data values for (a) Bead width, (b) Bead height, (c) Dilution (%) 112

Fig. 4.4 Numerical optimization ramps of the input parameter and response variable 114

Fig. 4.5 CMT WAAM wall of SDSS 2507 side view and front view 114

Fig. 4.6 Microstructure of SDSS 2507 samples (a) Optical microscope image (b) SEM image of the middle section 116

Fig. 4.7 Microhardness variations of SDSS 2507 along the deposition direction of the lower, middle, and upper region of the deposited wall 117

Fig. 4.8 (a) Single weld bead (b) Schematic diagram of weld bead geometry (c) Cross-section image of all single weld bead 120

Fig. 4.9 Contour plot for (a-c) Weld bead width (d-f) Weld bead height (g-i) Dilution 124

Fig. 4.10 Surface plot of the responses (a–c) Bead width (d–f) Height of the beads (g-i) Dilution for various combinations of the input parameters 126

Fig. 4.11. Predicted versus actual values for the (a) weld bead width (b) weld bead height (c) Dilution. 127

Fig. 4.12 Optimized values of input and output parameters curve of IN 718 128

Fig. 4.13 Three weld bead images constructed on the optimum process parameters of IN 718 128

Fig. 4.14 The CMT WAAM Inconel 718 wall front view and top view with the optimized process parameters 129

Fig. 4.15 Microstructure of Inconel 718 samples (a) Optical microscope image at 100x (b) Optical microscope image at 500x (c) SEM image of Inconel 718 131

Fig. 4.16 Microhardness variation of the deposited wall at the lower region, middle region, and upper region via (a) Line diagram variation (b) Bar diagram variation 132

Fig. 5.1 X-ray diffraction pattern of dissimilar SDSS 2507-IN718 alloy WAAM samples as in-built direction 136

Fig. 5.2 Optical microscope image of dissimilar alloy wall (a) Macrograph (b) IN 718 region (c) Interface of SDSS2507- In718 (d) SDSS 2507 region 138

Fig. 5.3 Section morphology and SEM Micrograph of Dissimilar SDSS 2507-IN 718 (a) section morphology (b) Upper part (c) Middle part (d) Lower part (e) In 718 (f) Interface region with EDS mapping (g) SDSS 2507 microstructure close to interface zone 141

Fig. 5.4 SEM micrograph and EDS analysis at various scan areas (1) IN 718 (2) IN 718-SDSS 2507 interface (3) SDSS 2507 143

Fig. 5.5 Microhardness curve of dissimilar alloy WAAM 145

Fig. 5.6 Tensile test result for five samples (a) Stress-strain curve of the dissimilar wall (b) Fractured samples 147

Fig. 5.7 Fracture morphology of Tensile specimens (a) IN718 (b) SDSS 2507-IN718 interface (c) SDSS 2507 (d, e, f) Magnified view of locations 1,2 and 3 148

Fig. 5.8 (a) Microstructural characteristics without and with UV (b) Grain size variation under different processing conditions 151

Fig. 5.9 Energy dispersive X-ray spectroscope analysis results of dissimilar SDSS2507-IN718 parts fabricated by CMT WAAM (a) Without ultrasonic vibrations (b) With ultrasonic vibrations 154

Fig. 5.10 Microhardness variation of Dissimilar SDSS 2507- IN 718 parts with or without UV 155

Fig. 5.11 Tensile test results of dissimilar SDSS 2507-IN 718 fabricated samples with or without UV (a) Stress-strain curve (b) UTS (c) Yield strength and (d) Ductility 157

Fig. 5.12 SEM morphology of fractured surfaces (a, b, c) Without UV (d, e, f) With UV of Tensile specimens 158

Fig. 5.13 (a) Linear Reciprocating ball on disk wear set up (b) wear chamber with sample holder and specimen (c) ball surface contacting the disk with load (d) sliding marks on disk surface (e) Worn out samples 161

Fig. 5.14 Wear rate of different specimens at different loading conditions 162

Fig. 5.15 (a) Coefficient of friction variation with time (b) Average COF of samples 163

Fig. 5.16 FESEM image and EDS analysis of worn-out surface of specimens (Left column SDSS 2507-IN 718 interface, Right column IN 718) 166

ABBREVIATIONS

AA	Aluminium Association
AF	As Fabricated
ALS	Arc Length Correction
AM	Additive Manufacturing
ANOVA	Analysis of Variance
ASTM	American Society for Testing and Materials
BD	Build-up Direction
BH	Bead Height
BJ	Binder jetting
BM	Base Metal
BMS	Bi-metallic Structure
BW	Bead Width
CAD	Computer-Aided Design
CCD	Central Composite Design
CCFCD	Central Composite Face-Centred Design
CMT	Cold Metal Transfer
CMT-ADV	Cold Metal Transfer Advanced
CMT-P	Cold Metal Transfer Pulse
CMT-PADV	Cold Metal Transfer Pulse Advanced
COF	Coefficient of Friction
CTWD	Contact Tip to Work Distance
DCEP	Direct Current Electrode Positive
DED	Direct Energy Deposition

DOE	Design of Experiment
DPC	Digital Processing Control
DSS	Duplex Stainless Steel
DWAAM	Double Wire Arc Additive Manufacturing
EDM	Electric Discharge Machining
EDS	Energy Dispersive X-Ray Spectroscope
EL	Elongation
FCAW	Flux Core Arc Welding
FCD	Face Centred Design
FESEM	Field Emission Scanning Electron Microscope
FGM	Functionally Graded Materials
FSOA	Fish Swarm Optimization Algorithm
GBA	Grain Boundary Austenite
GMAW	Gas Metal Arc Welding
GTAW	Gas Tungsten Arc Welding
IGA	Intragranular Austenite
IMC	Intermetallic Compounds
IML	Intermetallic Layer
IMP	Intermetallic Phases
IN	Inconel
NIAC	Near Immersion Active Cooling
PAW	Plasma Arc Welding
PBF	Powder Bed Fusion
PDAS	Prime Dendrite Arm Spacing
PDC	Pulse Dynamic Correction

PREN	Pitting Resistance Equivalency Number
RSM	Response Surface Methodology
SDSS	Super Duplex Stainless Steel
SS	Stainless Steel
TD	Travel Direction
THI	Thermal Heat Input
TS	Travel Speed
U-CMT	Ultrasonic Cold Metal Transfer
UC-WAAM	Ultra-cold Wire Arc Additive Manufacturing
UTM	Universal Testing Machine
UTS	Ultimate Tensile Strength
UV-WAAM	Ultrasonic Vibration Wire Arc Additive Manufacturing
WA	Widmanstädter Austenite
WAAM	Wire Arc Additive Manufacturing
XRD	X-Ray Diffraction
YS	Yield Strength

CHAPTER 1

INTRODUCTION

1.1 Introduction

Amidst the fast-paced industrial revolution, there is a growing demand for better engineering materials, resulting in the development of new, more efficient, and more rapid manufacturing techniques. Industry 4.0 is founded upon nine pillars, as shown in Fig.1.1 (Dilberoglu et al., 2017; Kumar et al., 2022). AM is part of Industry 4.0. AM is a process that produces three-dimensional components by incrementally adding materials layer by layer, utilizing computer-aided design (CAD) models (Al Noman et al., 2023). This technique offers the advantage of constructing components with intricate geometries and compositions that cannot be achieved through subtractive manufacturing processes (Guo and Leu, 2013; Piedra-Cascón et al., 2021).

Fig. 1.1 Industry 4.0 Technologies

The categorization of additive manufacturing comprises four distinct types: Binder Jetting (B.J.), Powder-Bed Fusion (PBF), Sheet Lamination, and Direct Energy Deposition (DED). The DED and PBF technologies exhibit considerable potential for AM of metal structural components (Rosli et al., 2021; Thomas-Seale et al., 2018). Metal additive manufacturing employs laser beams, electron beams, and arcs as heat sources, and feedstock material is in the form of filament and powder. Fig 1.2 depicts the classification of the AM process (Carroll et al., 2015; Popovich et al., 2017).

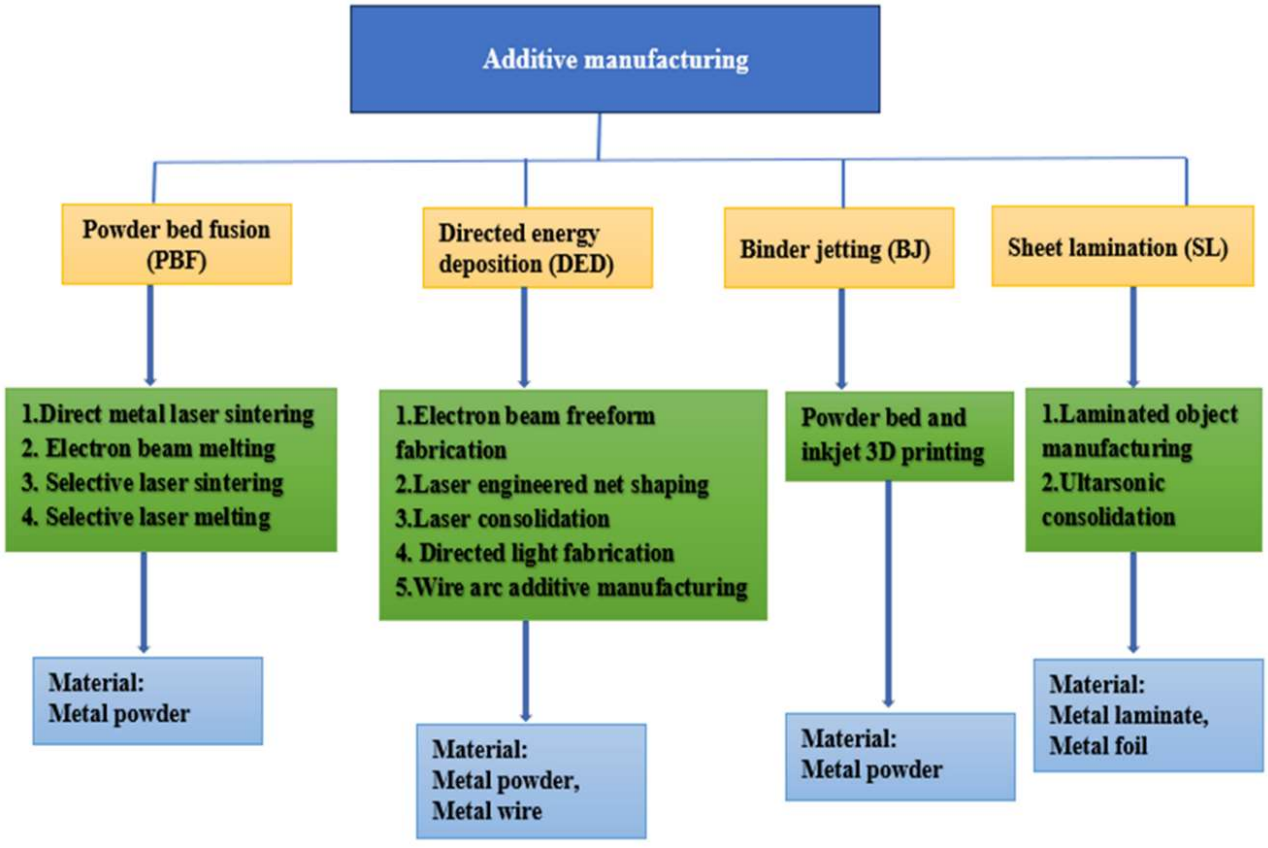

Fig. 1.2 Classification of Additive Manufacturing

The inception of the WAAM technique can be attributed to Baker, who, in the 1920s, suggested the utilization of an electric arc as the primary source of heat and filler wires as raw materials to deposit metallic embellishments (Williams et al., 2016). After that time, this technology has been a persistent advancement, notably within the previous decade. WAAM falls under the AM's directed energy deposition processes, which utilize an electric arc to serve as the heat source and feed it through the nozzle (Chandra et al., 2024). The benefits of WAAM, which make it one of the most potent and vital DED processes, include high deposition, quick production lead time, and high material utilization (Wu et al., 2018b, 2018e).

WAAM presents several advantages over laser-assisted and plasma-assisted additive manufacturing processes, including lower machine capital costs, increased material flexibility, and more. A primary welding station for WAAM comprises an energy source, welding torch, wire feedstock, a robotic system for controlling the deposition bed, and a unit for supplying inert gas. Notably, WAAM demonstrates superior deposition rates compared to powder-based additive manufacturing systems (Pattanayak et al., 2023; Sarathchandra et al., 2020a). The wire form is subjected to thermal energy generated by an arc, melting the feed metal. Using the provided 3D CAD model data, molten metal is deposited layer-by-layer onto a designated substrate (Hamrani et al., 2023). A comprehensive 3D metal structure is manufactured using a robotic arm or a gantry system machine, enabling a seamless layer-by-layer deposition process (Cunningham et al., 2018a). The user's intended use primarily determines the choice of an appropriate welding source for a specific WAAM application. Classification of the WAAM process is depicted in Fig. 1.3.

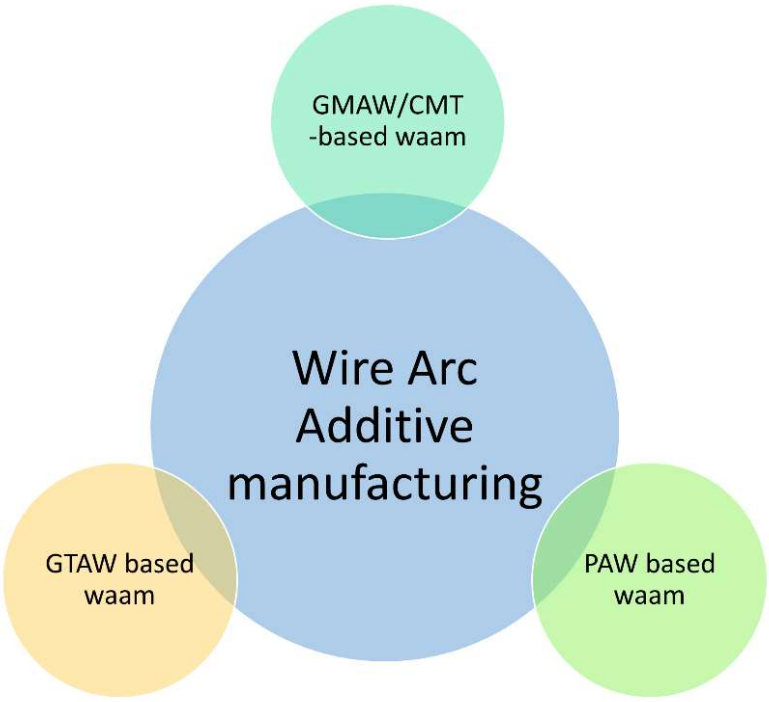

Fig. 1.3 Classification of WAAM

1.2 WAAM classification

WAAM processes can be categorised into three types based on the heat source: GMAW (Pattanayak and Sahoo, 2021), GTAW (Wang et al., 2011a), and PAW (Artaza et al., 2020; Cunningham et al., 2018b; Ding et al., 2015a; Oliveira et al., 2019; Shi et al., 2019). Table 1.1 exhibits the characteristics shared by each group of WAAM methods. The GMAW-based WAAM technique reveals a deposition rate 2-3 times greater than that of the GTAW or PAW-based methods. The WAAM based on the GMAW process exhibits reduced stability and increased fume and spatter production attributed to the direct action of electric current on the feedstock (Le et al., 2021; Li et al., 2022; P. Wang et al., 2021a). WAAM technology affects target component processing conditions and production rate. The WAAM process parameters are shown in Fig.1.4.

Table 1.1 Different WAAM processes

WAAM Process	Method	Prominent features
PAW based (Suárez et al., 2021; Y. Zheng et al., 2022)	Plasma	• Capital cost high • Minimum distortion • Deposition rate 2-4 kg/hr • The wire feed process is performed separately. • Non-consumable type electrode
GTAW based (Ding et al., 2015b; Wang et al., 2011b)	GTAW	• Non-consumable types of electrodes • Independent wire feed mechanism involving torch and wire rotation. • Lesser rates of deposition between 1 and 2 kg/h
GMAW based (Farabi et al., 2023; Hu et al., 2023; Suryakumar et al., 2011; Y.	GMAW	• Wire electrode consumable and 3-4 kg/hr deposition rate • Spatter and poor arc stability • The process requires less time • Lower process stability and weld quality

Wang et al., 2021a)	CMT	• Low heat input and zero spatter • High process stability • Typical deposition rate 2-3 kg/hr • A retractable and consumable wire electrode is fed

.

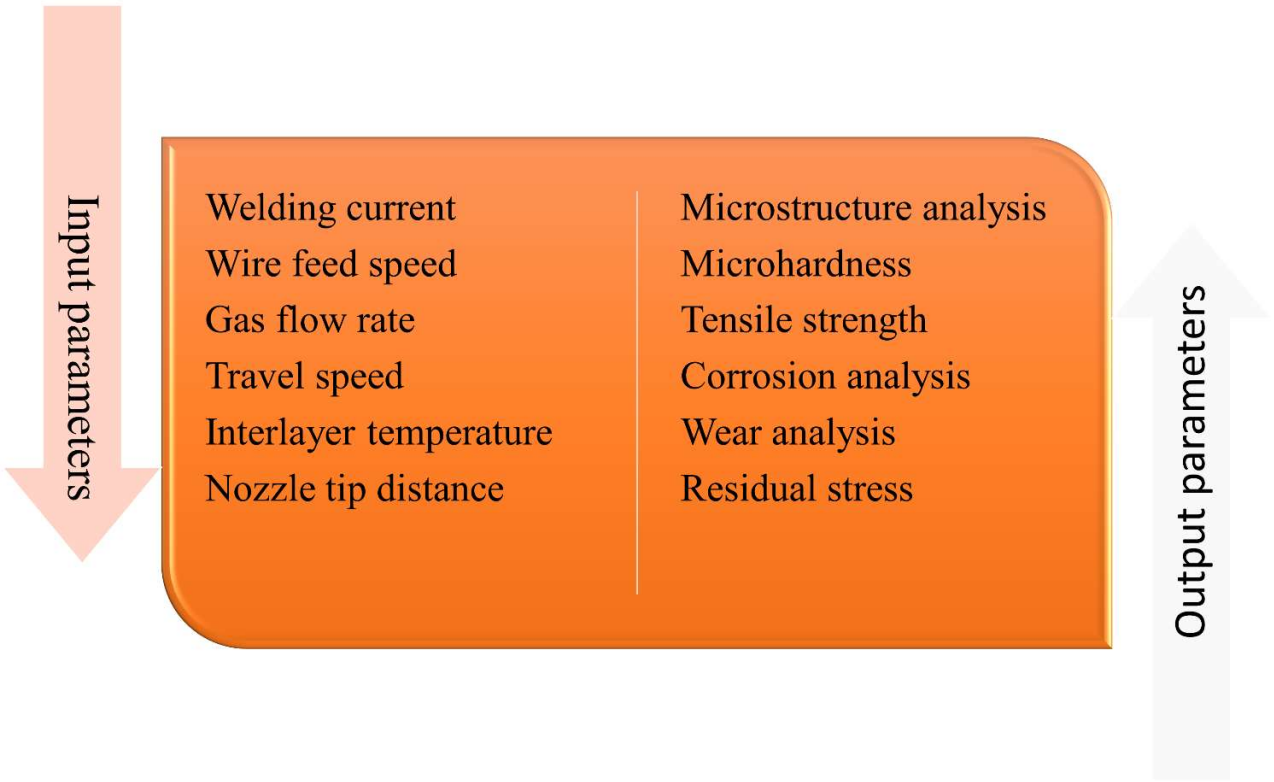

Fig. 1.4 WAAM input and output parameters

1.3 Cold Metal Transfer operation principle

Cold Metal Transfer was invented in 2004 by an Austrian company called Fronius as an improved variant of the GMAW method. The procedure relies on the short-circuiting transfer mechanism and differs from the GMAW technique in the droplet detachment approach from the feedstock wire (Chakkravarthy and Jerome, 2020; Yang et al., 2013). The wire retracting facilitates droplet separation during short circuits, allowing the metal to enter the welding pool without electromagnetic force (Zhang et al., 2009). Compared to conventional welding procedures like arc welding, CMT is performed at a very low current where the short circuit occurs (Selvamani et al., 2022). As a result, CMT requires less heat input and produces no spatter (Bless, 1974; Wu et al., 2022). CMT's low melting point makes it a promising material for the additive manufacture of aluminium and magnesium alloys (Derekar, 2018; Yang et al., 2020a). Regarding the aforementioned benefits, CMT has identified potential applications for WAAM of dissimilar materials (Tian et al., 2019). The CMT welding technique is considered more suitable for joining thin sheets, plates, and materials due to the advantageous characteristic of lower heat volume (Srinivasan et al., 2022).

The oscillating feed mechanism of CMT welding is adapted for use in CMT-WAAM in combination with a high-speed digitally controlled system (Pickin and Young, 2006). Upon contact of the feed wire tip with the molten pool, a digitally controlled process initiates the reversal of the servomotor that is affixed to the welding torch (Sarathchandra et al., 2020b; Wu et al., 2022b). The method includes pulling out the feedstock wire and making it easier to move molten metal droplets without electromagnetic force (Farabi et al., 2023b; Selvi et al., 2018a). CMT uses less current than GMAW needs to accomplish the same amount of material transfer. Due to the retraction force, there is no need for a greater current to transfer the same amount of metal (Feng et al., 2009). The oscillation of the wire is especially important as it imparts the

liquid wire more kinetic energy and makes it easier to move to the melt pool with less heat (Rajeev et al., 2019).

By reducing the current to nearly zero during the molten metal transfer, spatter production is also minimized in CMT (Cornacchia et al., 2018; Kannan et al., 2019). CMT welding principles are depicted in Fig. 1.5. Fig. 1.5(a) illustrates the motion of the molten wire with filler material toward the joint pool. We can see that the arc is turned off by dipping the filler wire into the joint pool in Fig. 1.5(b). As illustrated in Fig. 1.5(c), the wire turned during this time, which aided in separating the droplet. At this juncture, the current associated with the short circuit was sustained at low magnitudes. Subsequently, as shown in Fig. 1.5(d), the filler's wire moves forward, and the process starts again (Girinath et al., 2020).

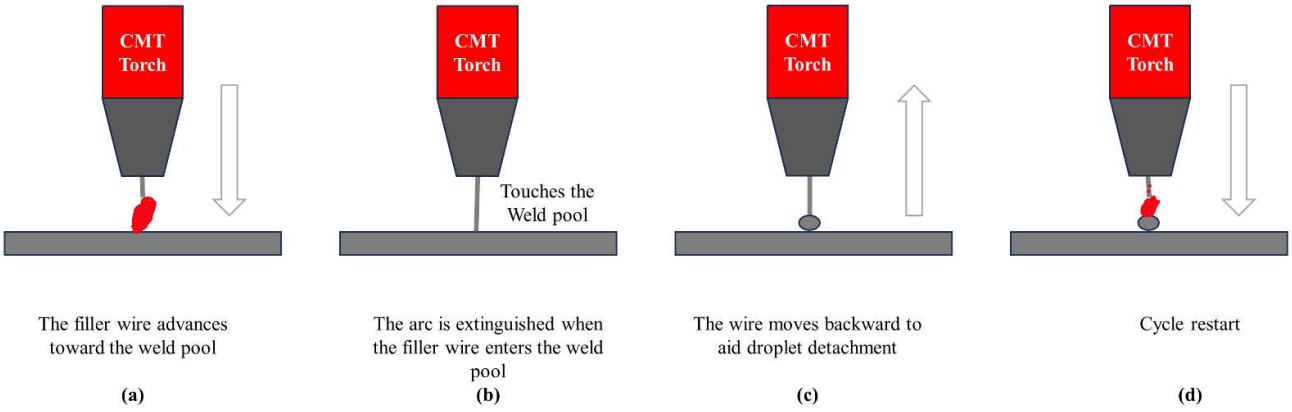

Fig. 1.5 Principle of CMT welding operation

In a typical CMT procedure, the electrical cycle concludes when drops of molten feedstock wire are deposited into the melt pool. The welding cycle of CMT is divided into three phases (as shown in Fig. 1.6) as follows:

a. **The Peak current phase:** During this stage, the welding arc is easily initiated due to a consistent arc voltage accompanied by a high current. The arc generated during the

process causes the feedstock wire to undergo heating and melting, forming liquid droplets.

b. **The background current phase:** The pre-short-circuit stage is characterized by a consistent voltage and a comparatively lower current. A decrease in current hinders the globular liquid transfer to the melt pool.

c. **The short-circuit phase:** Arc voltage is not present in this phase. The wire-feeding servomotor receives reverse signals, prompting the extraction of the wire from the melt pool. This movement assists in removing droplets from the wire tip and transporting them into the melt pool (Feng et al., 2009; Mezrag et al., 2015).

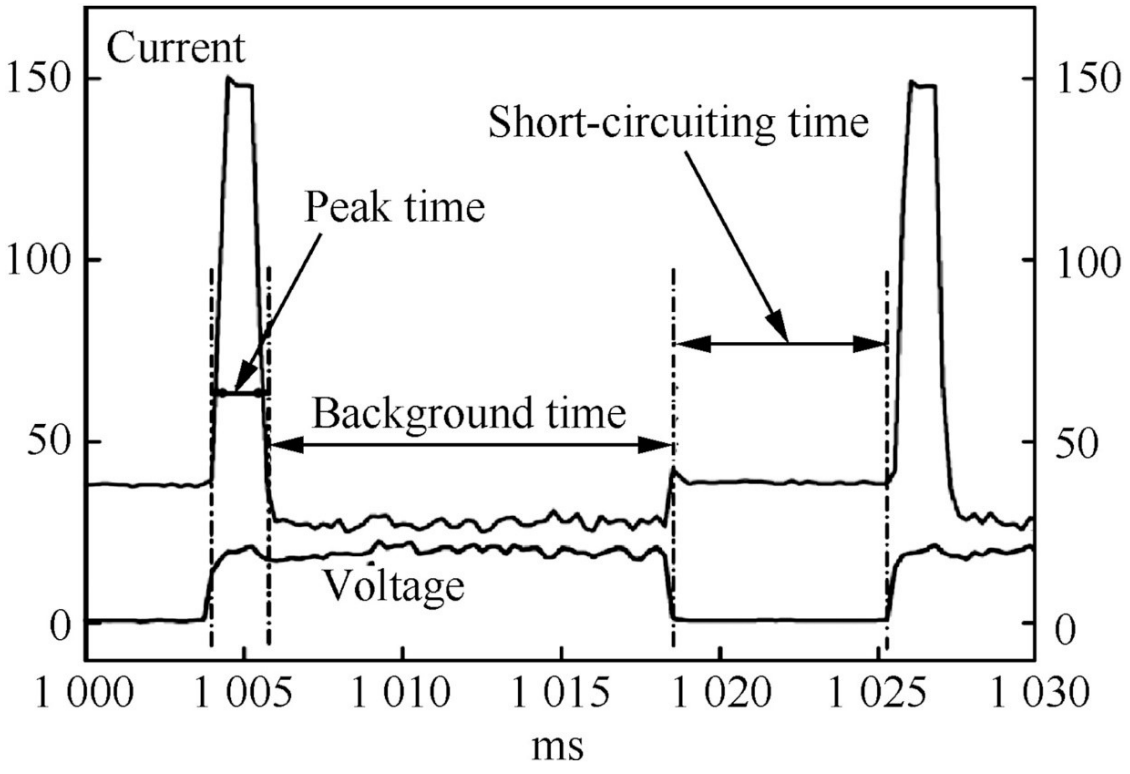

Fig. 1.6 Waveform of current and voltage of CMT process [60]

1.4 Overview of the thesis

Chapter 1 includes an introduction to additive manufacturing and wire arc additive manufacturing, a classification of the WAAM process, and an introduction to the CMT process and the principle of the CMT Process.

Chapter 2 encompasses a literature review focused on CMT, examining the diverse outcomes achieved by researchers in the field of various forms of material by the WAAM process. It also highlights the existing research gaps in this area. This chapter also discussed the research aims and presented a flow diagram of the experimentation.

Chapter 3 covers the mechanism, methodology, and experiments of CMT, as well as details the experimental setup that was built for bead-on-plate for SDSS 2507 & IN 718 and WAAM of dissimilar SDSS 2507-IN 718 alloys utilizing CMT and U-CMT. This section also discussed the detailed working principle of CMT welding and the advancements made in employing ultrasonic vibrations during WAAM. This section elaborates on the experimental process's parameters and technique. This chapter includes the micro-hardness, microstructure, wear, and tensile tests.

Chapter 4 presents the procedure of the WAAM fabricated samples and analysis of the optimization of process parameters for SDSS 2507 and IN 718. This chapter analyses the impact of different process factors on bead width, bead height, and dilution. The optimization of process parameters utilized in the weld-on bead is achieved by the implementation of RSM, which is also discussed. The optimal parameters are determined, and a confirmation test is conducted to validate them.

Chapter 5 includes results and discussion on the Microstructure and Mechanical Characterisation of Dissimilar SDSS 2507 -IN 718 alloy structure built by CMT-based WAAM

and with UV-CMT, Wear characteristics of Dissimilar SDSS 2507- IN 718 parts fabricated by CMT based WAAM.

Chapter 6 encompasses the findings from this research work, notable contributions, and prospective areas for further investigation.

1.5 Summary

This chapter highlights the importance of advanced manufacturing techniques in the context of the ongoing industrial revolution inspired by the principles of Industry 4.0. One technique that stands out is AM, which allows the production of intricate three-dimensional parts by depositing materials layer by layer according to CAD models. The WAAM is well-known for its efficiency in creating metal structures. It offers numerous benefits, including high deposition rates, fast production times, and optimal material utilization. An advanced variant of GMAW called CMT, developed by Fronius in 2004, is also mentioned. The CMT process utilizes a low-current short-circuiting transfer mechanism, reducing heat input and spatter. This makes it an ideal choice for additive manufacturing of materials with low melting points, like aluminium and magnesium alloys. The CMT process is known for its three-phase welding cycle, which reduces spatter and improves material transfer efficiency. This makes it a highly promising method for the WAAM of dissimilar materials. It also summarises the organisation of the thesis.

CHAPTER 2

LITERATURE REVIEW

2.1 Introduction

This chapter focused on a literature review on WAAM of different alloys. It gives an overview of the microstructure and mechanical properties of WAAM using various techniques: CMT-based WAAM, GMAW-based WAAM, GTAW-based WAAM, Plasma-based WAAM, and FCAW-based WAAM. It delves into the mechanical characteristics and microstructure of different metals and alloys made using this process. This chapter describes common difficulties encountered in the WAAM, including high residual stresses, porosity, delamination, and fracture. The methods used to reduce defects and the latest developments in WAAM. This chapter presents a future vision for improving WAAM technology to fulfil the demands of the industrial sector and argues that WAAM can be an excellent alternative technique for high-quality production. By thoroughly examining the existing literature, the study has successfully identified the research gaps and established clear objectives for the work. At last, a plan of work is presented for fabricating the samples.

2.2 Wire Arc Additive Manufacturing of alloys

The chapter presents a brief description of WAAM using the CMT process. Different materials' microstructure and mechanical attributes, including titanium and its alloys, aluminium and its alloys, magnesium-based alloys, nickel-based alloys, and steels, have been recorded using CMT-WAAM. It is noteworthy that there is a shortage of research on WAAM utilizing cold metal transfer, as shown in Fig.2.1.

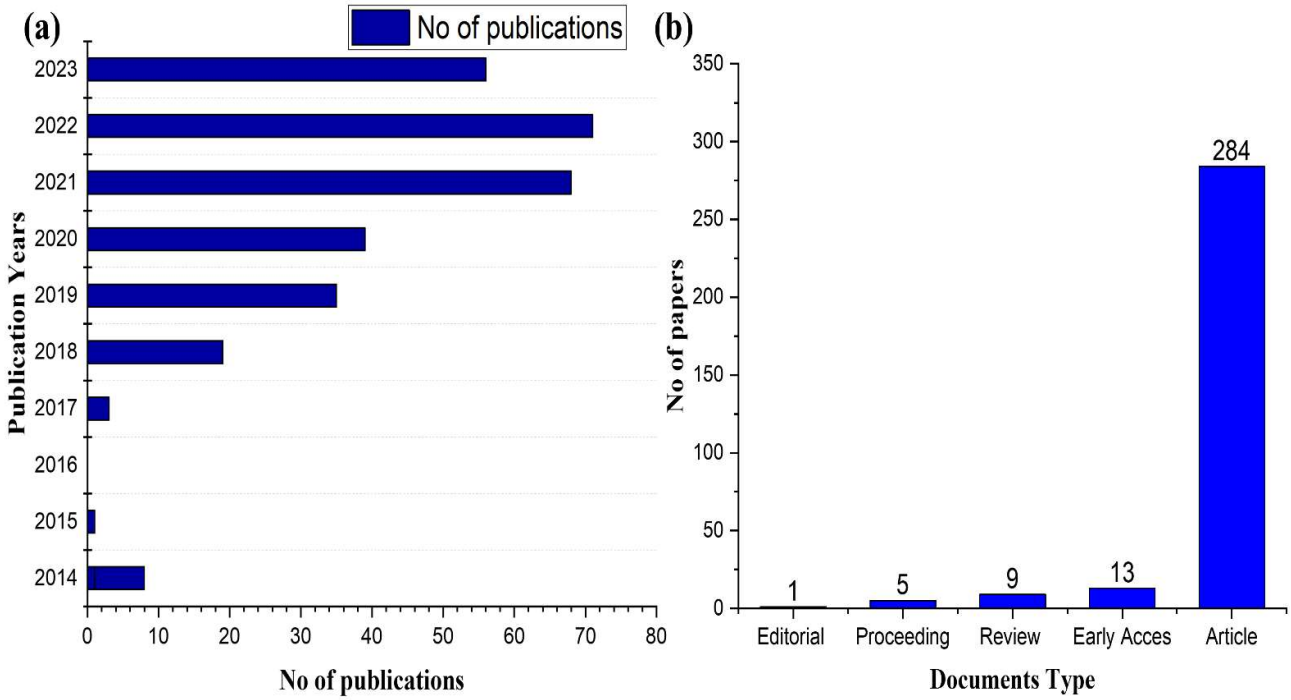

Fig. 2.1 CMT-based WAAM papers (a) Publication's year variation (b) Article type variation

The present study thoroughly evaluates the literature on WAAM that employs the CMT technique. A comprehensive discussion is presented, encompassing recent developments and prospective avenues of investigation for CMT-WAAM. Fig. 2.2 demonstrates County or region-wise variation of research on CMT-WAAM.

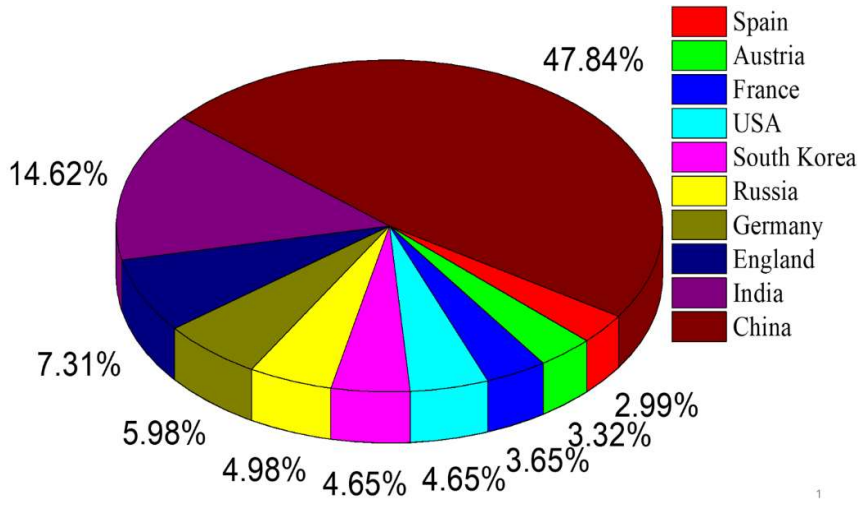

Fig. 2.2 CMT-WAAM Country-wise research publication variation plot

CMT WAAM built a Bimetallic SS316LSi-IN625 thin wall. It is noted that build-direction epitaxial grain development with non-equilibrium microstructures in deposited layers. During tensile tests, bimetallic specimens of the weaker SS316LSi showed enough plastic deformation and fracture (Motwani et al., 2023a). CMT-based WAAM produced AZ31 Mg alloy Wall. It is found that increasing secondary-phase particle volume per cent increased microhardness from substrate to single track top. Equiaxed grain formation has equivalent ultimate tensile strength (UTS), yield strength (Y.S.), and % elongation (E.L.) in the build and travel directions of the multilayer thin wall (Manjhi et al., 2023). CMT-WAAM-deposited TiC-inoculated SS316LSi Thin Wall. It is observed that TiC-nanoparticles in the molten pool sped up heterogeneous nucleation, which led to more refined grains in samples with TiC added. The finer grain structure of the TiC-inoculated specimen improved tensile strength, hardness, and anisotropy (Manjhi et al., 2023). SS316L wall fabricated by CMT WAAM method. It is detected that the micrograph shows fine equiaxed dendrites at the bottom, columnar grains with residual ferrite in the middle, and columnar dendritic structure at the top. It was found that as the structure's height increased, the hardness value fell (Koppu et al., 2023). Tables 2.1 to 2.5 present the microstructural and mechanical characteristics of various materials utilizing different welding processes, including CMT-based WAAM, GMAW-based WAAM, GTAW-based WAAM, Plasma-based WAAM, and Flux Cored Arc Welding (FCAW) based WAAM, respectively.

Table 2.1 CMT-based WAAM process effects on microstructure and mechanical properties

Material and method	Process parameters	Prominent results	References
Aluminium ER2319 and ER5087, CMT	• Wire feed speed: 6m/min, • Travel speed: 0.6 m /min, • Interlayer cooling time: 2 min,	• Due to their varied microstructures and solidification modes, 2319 and 5087 pores have diverse inner morphologies. • Vacant sites left by eutectic phase particles that melted could be the origin of the newly emerged pores in 2319. • Inter-layer rolling progressively creates oblate spheroids from the pores of both alloys. • The dissociated hydrogen consists primarily of confined locations and vacancies caused by rolling.	(Gu et al., 2016)
ER4043 aluminium CMT and CMT mix drive	**CMT** • Current: 32 A, • Voltage: 11.1 V,	• Due to the reduced heat input and tinner wall size of CMT technology, the microstructure size in the CMT arc zone is finer	(Campatelli et al., 2020a)

	• Wire-speed: 1.8 m/min, • Torch speed: 300 mm/min **CMT mixed drive** • Current: 133A, • Voltage: 18.5V, • Wire-speed: 6 m/min, • Torch speed: 300 mm/min	than CMT mix drive, but CMT sample is less uniform. • CMT technology's less uniform structure with columnar grains yields large differences in mechanical characteristics. • CMT saves 61% more energy than CMT mix drive because CMT mix shifts continuously between pure pulsed and CMT modes (higher efficiency).	
Dissimilar 2319 and 5306 aluminium alloys, CMT	**In case 2319** • Speed: 0.5 m/min, • wire feed speed: 6.5 m/min, • Gas flow rate:20 L/min **In case 5306** • Travel speed: 0.42 m/min,	• Cracks originate from residual tensile tension from solidification shrinkage, thermal contraction, and liquation cracks in the partially molten zone. • Depositing the 5306 alloy on top of the 2319 alloy prevents cracks from joining along grain boundaries, resulting in better tensile characteristics.	(Chang et al., 2022)

	• Wire feed speed: 6 m/min, • Gas flowing rate: 20 L/min		
ER4043, CMT based	CMT ARC • Arc current: 66A • Arc voltage: 11.8V, • Welding speed: 450mm/min, CMT Pulse • Arc current: 58A, • Arc voltage: 15.8 V, • Speed: 500mm/min	• Columnar grain development in 4043 Al deposits along construction direction. CMT pulse mode showed fine and coarse dendrites. • ER4043 was filling material repaired AA5052 in saltwater.	(Vishnukumar et al., 2021)
ER5356 Al-Mg alloy, CMT based	• Arc current: 158-178A, • voltage: 16.8-17.0 V,	• The effective wall width varies with WFS and T.S., with an increasing trend as WFS increases and T.S. decreases.	(Su et al., 2019a)

	• Wire feed speed (WFS): 7-8m/min, • Travel speed (TS): 0.6-0.9 m/min, • Arc flow rate:20 l/min	• By adjusting WFS and T.S. values, huge columnar grains in the inner and interlayer become refined equiaxed.	
Al–Mg–Si alloy, CMT	• Mean wire feed rate: 3.5 m/min, • Deposition rate: 0.64 kg/h, • Current $\bar{I}/I_{max}$: 82/102 A, • Travel speed: 12 mm/s	• Analysing cross-sections and deposit topography optimized porosity, fractures, and surface quality. • Ti-rich phases, such as TiB2, maintain grain refinement efficiency under arc and heat exposure, unlike Wire and WAAM deposit microstructures. • The β-Mg2Si-phase causes heat treatment-induced age hardening.	(Klein et al., 2022)
AZ91 Mg alloy, CMT based	• Wire feed speed: 12m/min	• The sample contains mostly matrix α-Mg and a minor quantity of precipitated β-	(Bi et al., 2020a)

	• Travel speed: 0.6m/min • Shielding gas (pure argon): 15l/min	Mg17Al12 and Al8Mn5, a typical microstructure. • The transverse and longitudinal specimens had stable microhardness distributions of 75.1 ± 2.5 HV0.1 and 77.2 ± 2.5 HV0.1, respectively. • Equiaxed grains increase ultimate tensile strength and minimize anisotropy.	
High nitrogen Cr-Mn steel, CMT	• Wire feed speed: 6 m/min, • Arc travel speed: 30 cm/min, • Interface temperature: less than 100 °C	• The tensile properties with the maximum values were 679.8±12.9 MPa for Y.S., 931.6±1.7 MPa for UTS, and 39.5±3.7 for elongation. • Dendrites of columnar austenite and delta ferrite dominated the as-built microstructure. • Due to the migration of Delta-Gamma boundaries, high temperature and short-time treatment significantly increased the Y.S. and UTS levels.	(X. Zhang et al., 2019)

Stainless steel 316L, CMT	• Arc current: 150A, • Arc voltage: 14.1V, • Wire feeding rate: 11m/min, • Scanning speed: 0.7m/min	• The 316L microstructure had many layers in both the building and transverse directions. • Microstructures had alternating re-melting area (R.A.) and overlapping area (O.A.) in the transverse direction. • In contrast to O.A., R.A. exhibited greater yield and tensile strength in the transverse orientation. R.A. demonstrated greater elongation than O.A., and both exhibited higher transverse elongation than longitudinal. • The multilayered structure had a stronger impact on tensile property in the transverse direction than in the building direction.	(Wang et al., 2020)
ER2594 super-duplex stainless-steel, CMT based	• Deposition Current (I):120A	• Multiple reheating cycles altered austenitic ferrite balance and increased toughness.	(Nikam et al., 2020)

	• Deposition Voltage (V): 15.6V • Shielding gas: – Argon Shielding • Gas flow rate: 15 L/min • Inter-pass temperature: 100–110 ◦C • Wire Speed: 55	• Dislocation density increased due to -phase boundaries/nitrides/carbides restricting dislocation motion. • Tensile strength increases horizontally. • Slip mechanisms in -FCC austenite increases vertical elongation.	
ER70S-6, CMT, GMAW	CMT • Current: 200A, • Voltage: 16V, • Wire feed speed 7000 mm/min GMAW • Current: 229A, • Voltage: 18.3V,	• GMAW WAAM exhibited lower single-layer height than CMTAM due to greater penetration over the previously deposited layer. • CMTAW surface is more exact and consistent due to equal thermal stress and lower heat input.	(Nagasai et al., 2022)

	• Wire feed speed: 6700 mm/min		
Mild steel ER70S-6 and ER100S-1, CMT	• Gas flow rate: 15 l/min, • Wire feed speed: 7.5 m/min, • Robot travelling speed: 7.33 mm/sec, • Dwell time: 120 sec	• ER70S-6 is more ductile than ER100S-1 due to its lower strain at failure and yield stress. • Due to the martensite/bainite structure, ER1002-1 has substantially higher hardness than ER70S-6, which exhibits a heat cycle-induced fluctuation in hardness between the middle and bottom. • Lower resistance curves and fracture durability at the bottom are caused by a greater number of thermal cycles at the bottom.	(Ermakova et al., 2020)
300M flux cored steel, CMT	• Deposition current: 189 A, • Deposition voltage: 18.1 V, • Wire feed speed: 6 m/min,	• The average width of a straight wall plate (SWP) continuously increases with layer temperature, whereas surface waviness first reduces and then increases due to increased kinetic energy,	(Xiong et al., 2022)

	• Deposition: 0.42 m/min,	improving metal liquid wettability and spreadability. • Solid solution strengthening increases top region microhardness. Interlayer microhardness reduces due to NLB and FLB appearance as the temperature.	
Co25.4Cr15Fe37.9Mn 3.5Ni16.8Si1.4 High entropy alloy, CMT WAAM	• Welding voltage: 22V, • Welding speed: 0.1mm/min, • Wire feed speed: 13m/min	• Due to heat propagation, the sample stratum consists of vertical dendrites that solidify vertically. • Compressive and tensile experiments revealed comparable UTS and Y.S. values but greater UCS (1689 MPa) and elongation than earlier studies.	(Osintsev et al., 2022)
Inconel 625, CMT	• Deposition current: 105 A, • Deposition voltage: 12.5 V,	• Magnetic fields align dendrites along the deposition direction, creating tiny crystals. • Magnetic force in melts helps solute metal components like Nb	(Y. Wang et al., 2021b)

	• Travel speed: 4 mm/sec, • Distance b/w torch and workpiece 15 mm	and Mo diffuse into residual liquid, reducing Cr, Nb, and Mo levels in alloy samples. • Due to dendritic refinement, homogeneous dendrite orientation, and alloying element segregation suppression, UTS increased by 6% from 695 MPa to 740 MPa, while yield strength increased by 14%.	
Inconel-718 alloy, CMT	• Wire feed speed: 7m/min, • Contact tip to work distance: 14 mm, • Torch travel speed: 6 mm/s, • Interpass cooling time: 3 min, • Shielding gas flow rate: 15 L/min	• The shift from columnar to fine equiaxed grains reduces average grain sizes and more uniform distribution than cold-rolled material. • Due to greater deformation, warm samples have a slightly lower hardness than cool samples.	(T. Zhang et al., 2022a)

Titanium alloys, CMT	• Wire feed rate: 5.8 m/min, • Mean current: 96 A, • Mean voltage: 14.8V, • Torch speed: 140 mm/min, • Arc energy: 444 KJ/m	• Conventional wire use causes arc wandering and instability in both polarities, leading to uneven weld bead deposition due to abrupt voltage variation during arc burning. • Surface-treated wire has a consistent arc behaviour and low wandering and debris accumulation due to its oxidized surface.	(Choudhury et al., 2021)

Table 2.2 GMAW-based WAAM process effects on microstructure and mechanical properties

Material and method	Process parameters	Prominent results	References
Al-Mg-Mn alloy, GMAW based	• Arc current: 104-300A, • Wire feed rate: 3.8m/min	• With a process (Deposition rate) of 2.2 kg/hr and a maximum porosity of 2%, the developed process applies to both thin and dense structures. • The ultimate tensile strength of manufactured structure metal (295MPA) is 2.8% less than that specified by GOST R 56371-2015 (315MPA). • Due to the coarse structure and microporous closure, the ductility is 2 to 3 times that of GOST.	(Panchenko et al., 2020)
ERNiCrFe-7A alloy, GMAW	• Current: 280 A, • Voltage: 12 V, • welding speed: 109 mm/min, • Feed speed: 1000 mm/min, • Gas flow rate: 23 L/min	• Columnar grains were produced due to quick cooling rates in the initial layers due to substrate contact. As the cooling rate drops, the top layer microstructure changes from columnar to eqi-axial. • Due to carbon content reduction and residual stress, hardness drops	(J. Zheng et al., 2022)

		dramatically in the superficial layer from 0-30 mm from the fusion line. • Carbide blocks dislocation movement and strengthens WAAM metal; hence, carbon inclusion improves WAAM product mechanical characteristics.	
ER70S-6, Ultrasonic GMAW	• Deposition voltage: 22.2V, • Deposition current: 198 A, • Deposition speed: 6 mm/s, • Wire feed speed: 5 m/min, • Shielding gas flow rate: 15 L/min	• Increased wettability and molten pool spreading led to a broader deposition layer but decreased height and depth. • Columnar grains growing in a decreasing temperature gradient become equiaxed with arbitrary orientation in a molten pool due to cavitation and shock waves.	(Ji et al., 2022)
Cu-coated steel wire H08Mn2Si, GMAW	• Welding current: 163-167 A, • Voltage: 19.6-23.3 V, • Wire feed rate: 4.07-4.27 m/min,	• Bead geometry deviation causes most deposited part defects. • Material shortages should be rectified at the edges of sloped multilayer	(Li et al., 2018)

		multi-bed sections by depositing more material. • Bead deposition order affects negative slope shape more than positive slope shape.	
316LSi stainless steel, GMAW	• Voltage: 20.5 V, • Current: 160 A, • Wire feed speed: 8.5 m/min,	• Due to unregulated competitive growth, coarse, strongly oriented grains and a prominent <100> texture along the building directions are found in the overlapping fusion zone. • The microstructure is austenite, ferrite, and tiny oxides. At the fusion interface, the ferrite shape is generally cellular and globular, whereas, in the middle, it is vermicular and lathy.	(Palmeira Belotti et al., 2022a)
ER70S-6 low carbon steel, GMAW	• Arc voltage: 20 V, • Wire feeding rate: 10m/min, • Arc current: 120A, • Shielding gas flow rate: 10 L/min	• The upper layer has fine grain refinement because of high heat buildup and low thermal gradient, whereas the lower layer has a bigger grain size and lesser hardness. • The warmed base plate has a smoother surface due to less	(Warsi et al., 2022)

		fluctuation in average bead height due to humping.	
316L stainless steel, GMAW	• Voltage: 15.6 V, • Current: 120A, • Welding speed: 40 cm/min, • Gas flow rate: 15 L/min, • Interlayer waiting time: 40 sec	• The SEM pictures show that the surfaces have a lot of pores, which is what biomedical applications need. • Macro tests show that the WAAM plate has no other defects. • Rough surfaces get worn down faster than smooth ones.	(Vinoth et al., 2022)
P.H. 13-8MO martensitic steel, GMAW	• Average arc current: 135 A, • Arc voltage: 28 V, • Wire feed speed: 67 mm/s, • Travel speed: 4 mm/s	• WAAM microstructure consists of residual δ-ferrite, vermicular due to proximity of primary ferrite planes to austenite, and lathy due to cooling and Creq/Nieq. • The top area has higher hardness and UTS than the bottom layer because of the lower volume percentage of preserved austenite and δ-ferrite.	(Ghaffari et al., 2022)
NiTi and S.S.	• Wire feed speed: 5.5 m/min,	• Higher hardness at the interface, 400 HV, is obtained predominantly due to the formation of intermetallic phases.	(Kannan et al., 2022a)

Bimetallic, GMAW	• Argon gas flow rate: 15 L/min • Voltage: 16.5 V • Stand-off distance: 15 mm	• The fusion zone is the most fragile zone on the NiTi alloy side, as joint fractures occur here. • Surface brittleness is caused by the presence of brittle intermetallic phases at the joint.	

Table 2.3 GTAW-based WAAM process effects on microstructure and mechanical properties

Material and method	Process parameters	Prominent results	References
ER 304 Stainless steel, TIG based	• Current: 80 A, • Height of the nozzle: 10mm, • Travel speed: 104 mm/min, • Wire feed speed: 1130 mm/min, • Gas flow rate (pure argon): 6 l/min	• Stable burning arc continuously melted metallic wire, producing oriented droplet transfer and low heat input. • When gas flow surpasses 1 CBN, ceramic nozzles provide outstanding high-temperature stability at 2800 degrees Celsius, containing the arc. • From 3mm to 5mm nozzle diameter, the temperature rises from 780 C to 1300 C. • Microstructure analysis showed fine granularity and uniform distribution.	(J. Zhou et al., 2021)
High strength low alloy steel (HSLA) ER110S-G, GTAW	• Wire feed speed: 3-4m/min, • Travel speed: 150-200mm/min • Voltage: 17 V	• Ultra-Cold (U.C.)-WAAM offers superior arc stability, wall appearance, and spatter prevention, but narrower and higher layers result from faster solidification and less diluting of previous layers.	(Rodrigues et al., 2021)

		• UC-WAAM achieves 11°C/s cooling speeds and 400°C peak temperature variations with the same heat input. • Developed fine particle architectures in UC-WAAM and GMAW-based WAAM, resulting in exceptional mechanical strength and ductility.	
Low carbon steel, TIG	• Wire material melting point: 1500 ̊c, • Melting point of wire material: 1535 ̊c, • Substrate melting point: 1510 ̊c, • Power of TIG source: 800 W	• The shape at the turning point is deformed by temperatures between 1600 and 1800 degrees Celsius, which exceeds the melting point. • At the intermediate stage, the temperature is close to the melting point, so the shape remains uniform without degradation.	(Gokhale and Kala, 2021)
Low carbon steel ER70S-6, GTAW	• Current: 95A, • Travel speed: 80mm/min, • Gas flow rate: 10 l/min, • Wire speed: 80 mm/min	• The last build surface features acicular and polygonal ferrite with minimal secondary pearlite, while middle-build surfaces have fine polygonal ferrite and minimal lamellar phase from many passes and	(Tripathi et al., 2022)

		post-heating. The last pass cools faster. • The heat cycle and coarse ferrite particle size make the last layer hard. • Charpy test failure is ductile due to homogeneous ferritic microstructure.	
Functionally graded stainless steel from TC4 to 316L, GTAW	• Welding current, • Voltage • Welding speed	• Due to differences in thermophysical characteristics, stainless steel and Ti alloy deform differently during heating and cooling, causing internal stress and cracks. • Due to an increase in the Fe2Ti and FeTi phases, the maximum microhardness is about 945 HV0.2 in the area where Fe is 60%.	(Chen et al., 2021)
TA1 titanium alloy, GTAW	• Pulse frequency: 0.1,0.2,0.5 Hz, • Peak current: 120,140,160,180,200 • Wire feed speed:10-50 cm/min, • Hotwire current: 100A,	• Due to unidirectional droplet accumulation, heat input increases rod diameter. Heated droplets grow. • Due to an increase in arc length as thickness increases, heat input decreases, and due to a decrease in arc	(Xu et al., 2021)

	length as thickness decreases, heat input increases. • The molten pool collapses due to temperature differences between the front and back and the movement of its centre of gravity.

Table 2.4 Plasma-based WAAM process effects on microstructure and mechanical properties

Material and method	Process parameters	Prominent results	References
ERNiCu7, Ni-Cu alloy, Dual wire plasma arc welding	• Welding current: 120A • Arc voltage: 21.50 V • Welding speed: 300 mm/min • Wire feed speed: 4.24 m/min	• Columnar dendrites arise in the middle and top areas due to several hot layers underneath the newly deposited molten layer, with upward expansion. • Columnar and equiaxed dendrites form in the bottom region due to higher cooling rates (Higher heat dissipated to the substrate). • Passive file creation in metallic surfaces reduces marine structure corrosion and pitting. • The uniform spread of Ti and Al components in top specimens reduces corrosion resistance compared to bottom samples.	(Kannan et al., 2022b)
Ti–45Al titanium aluminide, Twin-wire plasma arc	• Deposition current: 90A,	• The microstructure is predominantly lamellar due to β → α phase change and heat treatments from subsequent layers.	(L. Wang et al., 2021)

	• Interpass temperature: 500℃, • Travel speed: 120 mm/min	• Non-equilibrium lamellar colony microstructure and rapid cooling caused increased residual stresses and intergranular cracks.

Table 2.5 FCAW-based WAAM process effects on microstructure and mechanical properties

Material and method	Process parameters	Prominent results	References
E2209T0-4/1 Duplex stainless-steel wire, Flux-cored arc welding	• Current: 145 A, • Voltage: 30 V, • Deposition speed: 5.4 mm/s • Shielding gas: 80%Ar+20%Co2	• Flux-cored arc welding (FCAW)-AM noticed high Creq and PREN due to sluggish cooling and repeated reheating. • PREN and fine intra-granular austenite (IGA) increase FCAW-AM DSS corrosion resistance. • FCAW-AM DSS's Y.S. and UTS exceeded WAAM DSS's welding wires and rolled and cast DSS's strength requirements.	(Y. Zhang et al., 2022)
E2209 Duplex stainless-steel wire, FCAW	• Deposition current: 187 A, • Voltage: 25V, • Deposition speed: 4.7 mm/s, • Interpass temperature: < 150 °C	• Heat treatment at 1250,1300,1350 °C can reduce the austenite content of WAAM DSS and remove gamma2 because of the transition of the gamma phase into ferrite. • Due to chromium nitrate precipitation, duplex stainless steel's resistance to pitting corrosion and ductility deteriorates.	(Y. Zhang et al., 2021a)

2.2.1 Role of Deposition Strategy in WAAM

Fig. 2.3 illustrates the direction of the nozzle path in the WAAM process. In Fig. 2.3(a), the nozzle direction is unidirectional, resulting in lower dimensional accuracy due to defects for the WAAM product. On the other hand, Fig. 2.3(b) demonstrates a bidirectional nozzle direction, where metal deposition occurs in both the forward and reverse directions of the nozzle. This bidirectional approach enhances the deposition rate, reduces processing time, and minimizes defects in the WAAM process (Haribaskar et al., 2023; Koli et al., 2022).

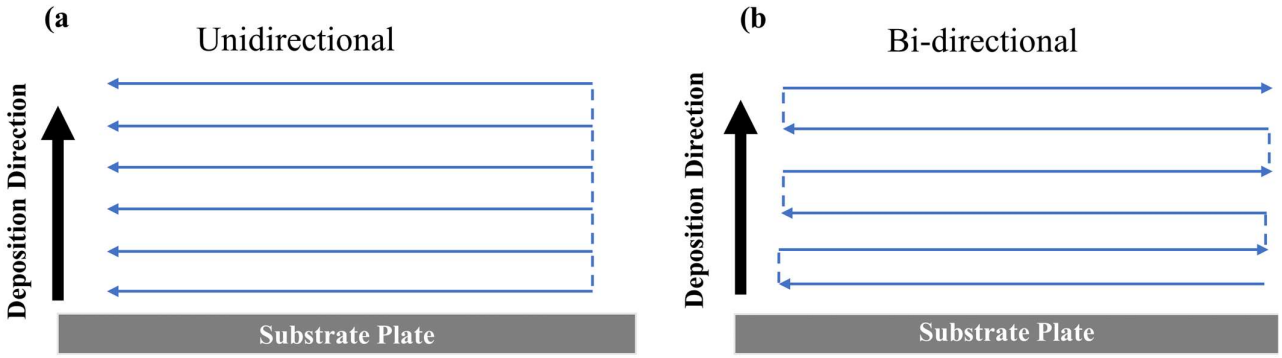

Fig. 2.3 WAAM nozzle path direction during operation (a) Unidirectional (b) Bi-directional

2.3 Materials employed in the WAAM process

Wires manufactured for the welding industry are used as feedstock materials in WAAM processes. These wires can be procured commercially in spool form and come in a wide variety of alloys. Understanding the process options, physical processes, feedstock materials, process control methods, common defects, and solutions is essential to creating a structurally sound and defect-free component. This section gives a general outline of the metals that are commonly used in WAAM, with an emphasis on the mechanical and microstructural properties of the alloys that are additively manufactured.

2.3.1 Nickel-based superalloys

Superalloys are advanced alloys with exceptional mechanical properties, including high strength and toughness, particularly at elevated temperatures. Additionally, they demonstrate a remarkable resistance to corrosion in harsh environments (Pollock and Tin, 2006). These alloys are utilized in the aero engine's combustor and turbine section (Mukherjee, 2023). Nickel-based superalloys are a subject of extensive research among the AM community owing to their exceptional mechanical stability when exposed to elevated temperatures exceeding 550◦C (M. Xu et al., 2023). Nickel-based superalloys produced through AM techniques are frequently utilized in the aerospace, aeronautical, and petroleum sectors (James et al., 2023). WAAM has been used to investigate nickel-based superalloys, i.e., Inconel (IN) 718 and 625.

The microstructural characteristics of IN 718 produced through the WAAM process typically consist of sizable columnar grains accompanied by irregularly shaped island-like precipitates, referred to as the Laves phase and a few carbides that are spherical or square in shape (Baufeld, 2012; Sujan et al., 2023). Yangfan et al. (Yangfan et al., 2019a) reported that in the as-fabricated (A.F.) state, coarse austenite (γ)-matrix grains with a columnar-dendritic form developed epitaxially parallel to the built-up direction (B.D.) (plane section BD-WD), having the maximum heat loss rate (Fig. 2.4a). However, it was discovered that the grains in a plane piece of welding direction (TD-WD) were of an equiaxed shape, as shown in (Fig. (2.4b)). The grains in the plane section BD-WD exhibited a conserved columnar-dendritic morphology (Fig. (2.4c))., whereas the grains in the TD-WD section displayed an equiaxed shape (Fig. (2.4d)). Heat treatments applied after processing can reduce dendritic arm spacing, reduce niobium segregation, and eliminate discontinuous Laves phase within interdendritic regions. This, in turn, improves the material's mechanical properties.

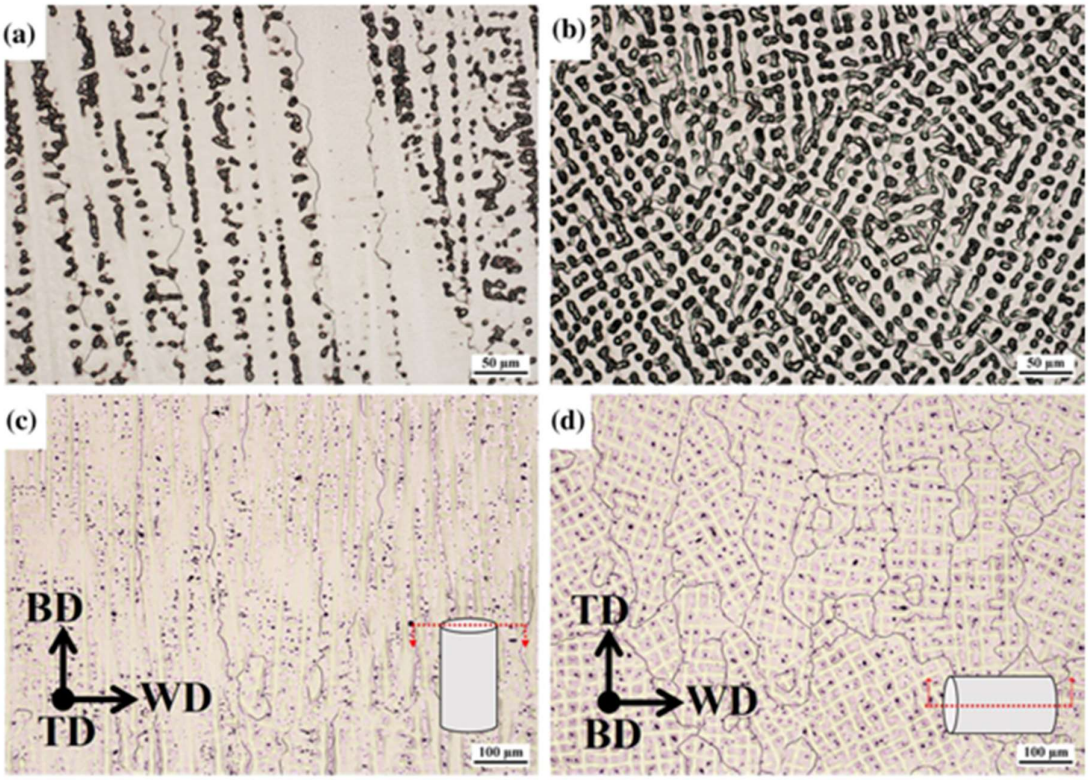

Fig. 2.4 As-fabricated (A.F.) and homogenized-annealed (H.A.) WAAM IN718 samples' cross-sectional optical micrographs: plane sections parallel to B.D. for (a) A.F. and (c) H.A. and perpendicular for (b) A.F. and (d) H.A. (Sujan et al., 2023)

Xu et al. (Xu et al., 2013) examined WAAM methods' potential for IN 625 alloy production. The IN 625 alloy was cast utilising a WAAM technique based on CMT, and torch travel speed greatly affected its mechanical properties. It was because precipitates formed in the alloy. At different levels, the sample had different microstructures (as shown in Fig.2.5), with fine primary cellular structures making up most of the bottom layers. The structural transformation to a columnar dendritic morphology with secondary dendritic arms occurred owing to the increased deposition of layers and heat input. The final layers exhibited an equiaxed microstructure.

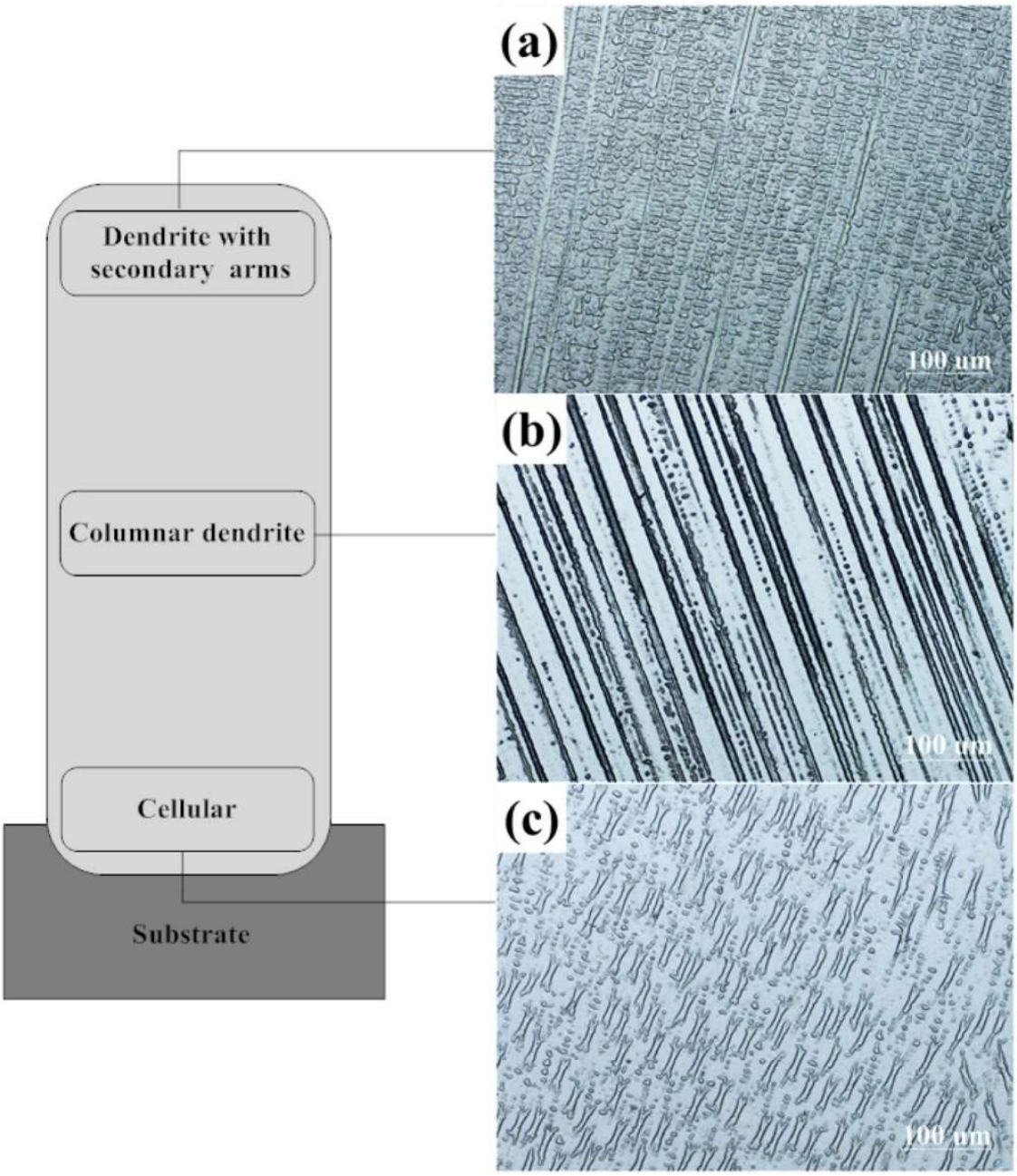

Fig. 2.5 The microscopic appearance of the distinct IN 625 deposition layers (Yangfan et al., 2019a)

The as-deposited specimen UTS was about 660 MPa, the Y.S. was about 390 MPa, and the elongation was about 44%, similar to the as-cast metal (Xu et al., 2013). The dendritic

microstructure was eliminated, and the Laves and phases dissolved during the solution heat treatment of the IN 625 alloy manufactured by WAAM at 1100 °C (SAFARZADE et al., 2020).

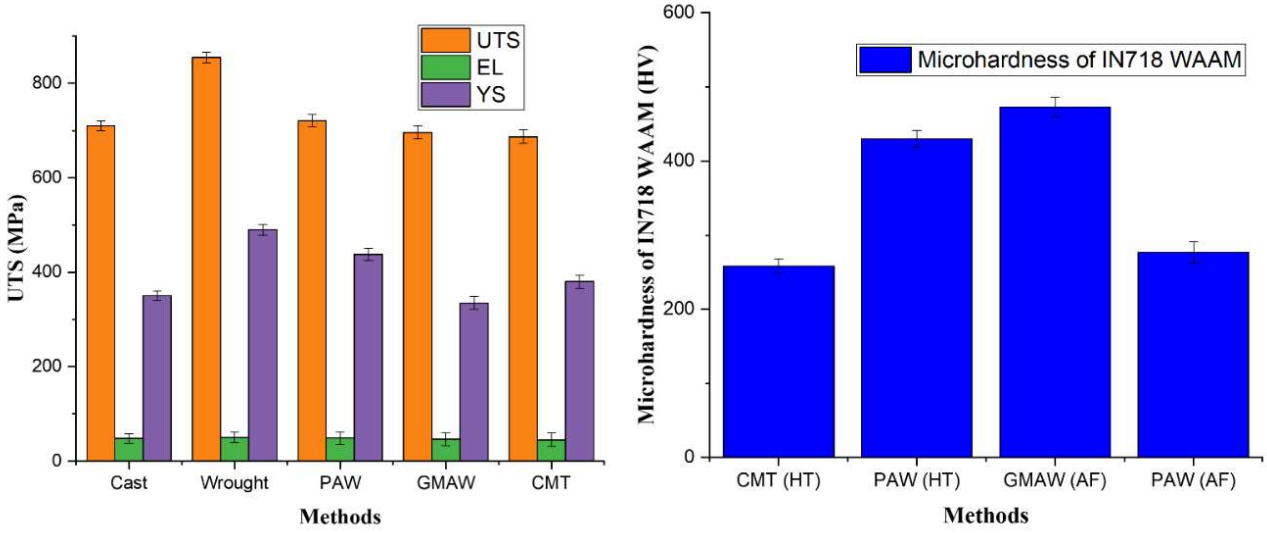

Fig. 2.6 Mechanical properties variation of Inconel (a) Tensile strength, yield strength and % elongation of IN625 (b) Microhardness of IN 718

Fig. 2.6 displays the general tendency of Inconel's mechanical characteristics as measured by several WAAM techniques. CMT, GMAW, and PAW-fabricated IN 625 WAAM products have ultimate tensile strengths and yield strengths that are very close to those of cast alloys of IN 625 (see Fig. 2.6 (a)). Compared to GMAW and CMT WAAM, PAW WAAM has a higher UTS. The micro-hardness of IN 718 WAAM products formed with the CMT, PAW, and GMAW WAAM methods in a fabricated and heat-treated state is shown in Fig. 2.6 (b). The graph demonstrates that in a heat-treated state, PAW WAAM products have a greater hardness than CMT WAAM products, and in the case of fabricated conditions, GMAW WAAM products have more hardness than PAW WAAM. Table 2.6 shows the mechanical properties of Inconel with different WAAM techniques.

Table 2.6 Ni-based superalloy mechanical characteristics of different WAAM techniques

Materials	Process	Condition	Microstructure	YS (MPa)	UTS (MPa)	E.L. (%)	Other properties	References
Inconel 625	CMT	As fabricated (AF)	Cellular dendritic structure + coarser dendritic crystal	376.9–400.8	647.9–687.7	43–46.5	246– 259.9 HV	(Yangfan et al., 2019b)
Inconel 625	MIG	As fabricated (AF)	Laves + NbC + MC + γ— matrix	335	696.5	46.6	270–285 HV	(Ravi et al., 2020)
Inconel 718	CMT	Heat treated (HT)	NbC carbides + TiN inclusions + acicular δ phase	949	1194	19.9	258 ± 9 HV	(Xu et al., 2019)
Inconel 718	GMAW	As fabricated (AF)	Nb precipitates + dendritic structure	473 ± 6	828 ± 8	28 ± 2	473 ± 6 HV	(Baufeld, 2012)
Inconel 718	PAAW	As fabricated (AF)	Laves + γ phases	563 ± 14	872 ± 31	34 ± 3	249–277 HV	(K. Wang et al., 2020)
Inconel 718	PAAW	Heat treated (HT)	Lamellar + γ + δ phases	864 ± 21	1152 ± 28	23 ± 2	377–436 HV	

2.3.2 Titanium alloys

The remarkable strength-to-weight ratio of titanium alloys has rendered them highly sought-after materials in different sectors, such as aviation and aerospace, military and armaments, marine and shipbuilding, automotive, and biomedical engineering (Xiong et al., 2024). Due to their high cost and low machinability, titanium alloys require an economical replacement for subtractive production. Traditional manufacturing methods offer a poor ratio of fly-to-buy for aerospace component designs (Froes and Whittaker, 2022). WAAM has developed as a promising new manufacturing method for industry useecause it can generate nearly net-shaped components (Wu et al., 2018c; S. Zhou et al., 2022a). Amidst titanium alloys, the Ti–6Al–4V alloy is the subject of the most research (Ding et al., 2020a). It is widely known that the structures of the phases in Ti6Al4V alloy, such as primary α, lathlike α, colony α and hcp martensite α (α'), grain boundary α, acicular α, and preceding phases, are determined by the thermal history of the material (Wu et al., 2018a). Huang et al.(Huang et al., 2022) studied the influence of heat accumulation on the microstructure of the Ti6Al4V alloy wall (as shown in Fig. 2.7) produced by GMAW WAAM. The microstructure of the as-deposited metal can be roughly split into two different regions. Higher cooling rates and less heat build-up in the area close to the base lead to a martensitic matrix with lath-like lamellae (Fig. 2.7(a)) and a completely lamellar α morphology with basketweave structures (Fig. 2.7(b)). In the top zone, increased heat production slows down the rate at which the process cools. It causes a big α colony to form between the previous β grains and the grain boundary of the β phase (Fig. 2.7(d-f)). Good mechanical properties were shown by the as-built WAAM samples, which were equivalent to the wrought material in terms of yield strength (884 ± 27 MPa), tensile strength (995 ± 29 MPa), and estimated elongation (18.6%). Table 2.7 shows the mechanical properties of Ti alloy with GTAW WAAM techniques.

Table 2.7 Ti-based superalloy mechanical characteristics of GTAW WAAM techniques

Materials	Process	Condition	Microstructure	YS (MPa)	UTS (MPa)	E.L. (%)	Other properties	References
Ti6A14V	GTAW	As fabricated	equiaxed primary α phase + acicular secondary α-lath or β-lath phase	-	661.9	7.37	Hardness 322HV	(Huang et al., 2022)
Ti - 6.5Al– 2Zr– 1Mo–1V	GTAW	Heat treated	lamellar basketweave structure with some α colonies and grain boundary (G.B.) α	739 ± 17	832 ± 28	17.0 ± 3.3		(Lu et al., 2020)

Metastable β-Ti alloys have better strength, toughness, and wear resistance than α and α +β Ti alloys, which makes them a good candidate for use in structural applications (Lu et al., 2020). The infrequent exploration of these alloys may be attributed to the concurrent existence of unfavourable secondary α, ω, and α" phases with the initially deposited metastable β-Ti, resulting in inferior mechanical properties . C.H. Ng et al. (Ng et al., 2021) explored that a metastable β-Ti alloy may be produced with a unique β-phase microstructure by adjusting the alloy composition and processing parameters during deposition.

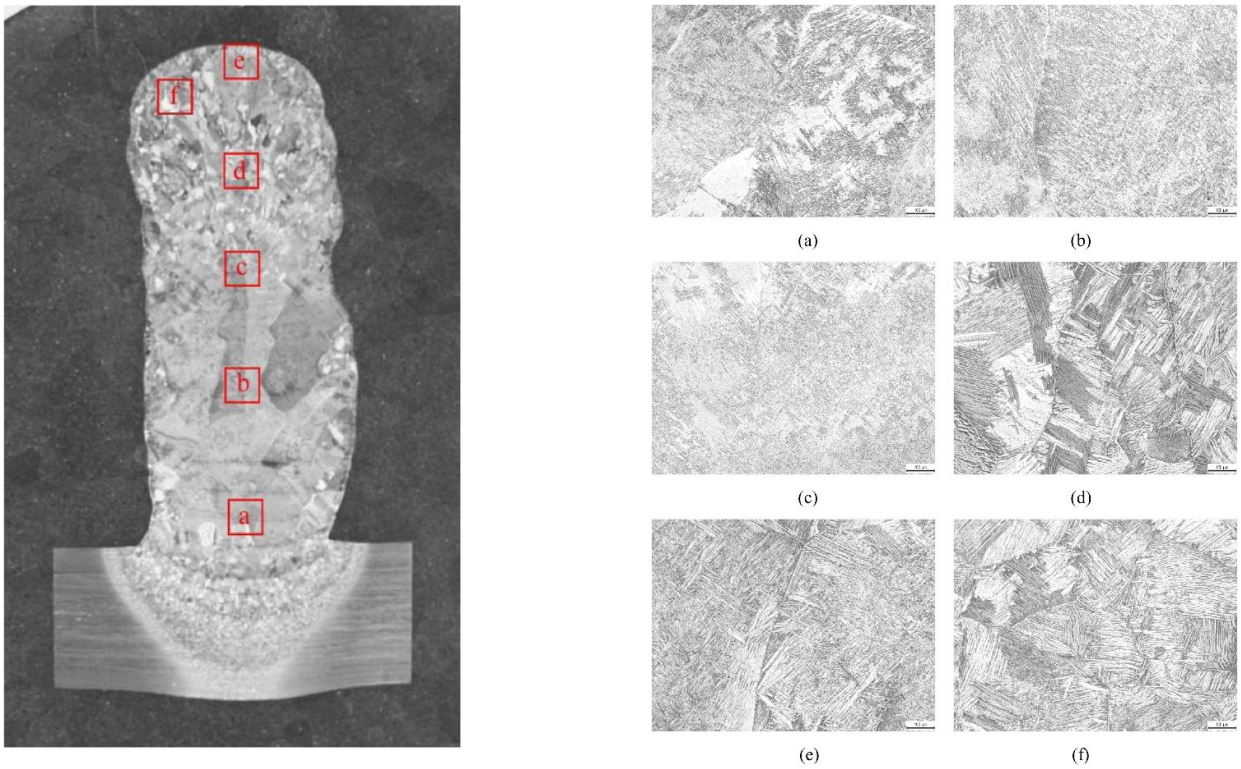

Fig. 2.7 (a) Macrograph of the deposited wall in cross-section (b) Optical micrographs of the following regions: a, b, c, d, e, and f (Huang et al., 2022)

The material characterisation results did not indicate any presence of β-Ti decomposition when the thermal processing and processing parameters were optimized. A moderate tensile strength of 739 ± 17 MPa and a 20% elongation were achieved. This figure was marginally lower than the wrought alloy, which had a UTS of 794 MPa and 25% elongation (Schmidt et al., 2011).

2.3.3 Aluminium alloys

Aluminium is the third most abundant element in the Earth's crust and readily available. A diverse range of alloys containing aluminium exhibits a favourable strength-to-weight ratio, exceptional resistance to corrosion, and commendable thermal conductivity, rendering them well-suited for utilization in numerous industrial applications (Langelandsvik et al., 2021). WAAM is most economically viable for big, intricate, thin-walled structures, even though Al-

Cu (2xxx), Al-Si (4xxx), and Al-Mg (5xxx) have been successfully fabricated. This is due to as it doesn't cost much to make small, simple aluminium alloy parts with standard machining methods (Brice et al., 2015). Welding Al 7xxx and Al 6xxx aluminium alloys is challenging because of the metals' turbulent melt pools and weld defects (Wu et al., 2018d). GMAW-based CMT is the most energy-efficient WAAM technology for fabricating Al-based alloys, which is attributed to less heat generation in the CMT process (Wei et al., 2023a; Xizhang Chen et al., 2018). Campatelli et al.(Campatelli et al., 2020b) fabricated an ER-4043 Al defect-free wall using CMT WAAM. They found that due to reduced heat input and tinner wall size of CMT technology, microstructure size in the CMT arc zone is finer than the CMT mix drive (as shown in Fig. 2.8). CMT saves 61% more energy than the CMT mix drive because CMT mix changes between pure pulsed and CMT modes (higher heat input). The average longitudinal UTS of manufactured samples were 125 MPa, and the transverse UTS was 112 MPa, identical to cold-

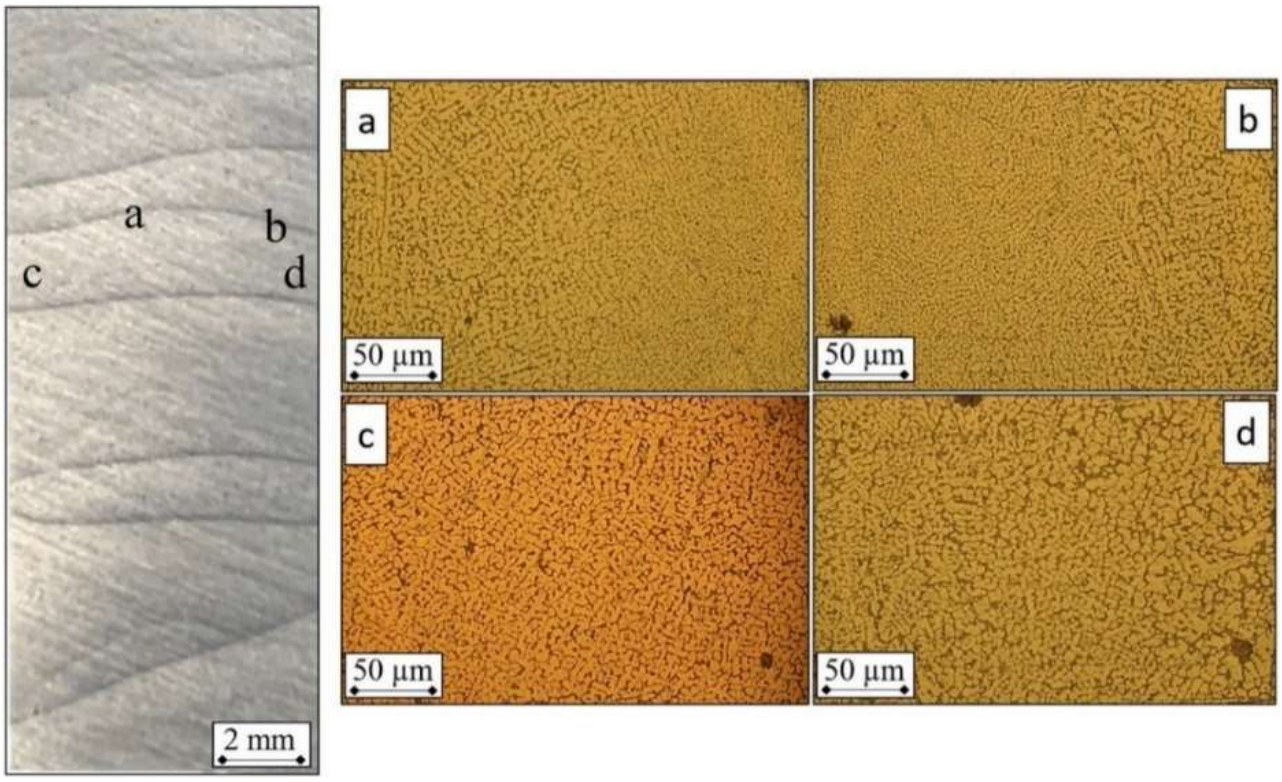

Fig. 2.8 CMT fabricated wall longitudinal cross-section and corresponding optical micrograph (a, b, c, d) (Campatelli et al., 2020b)

drawn samples. The ultimate tensile strength of several Al alloys manufactured by CMT WAAM is shown graphically in Fig. 2.9.

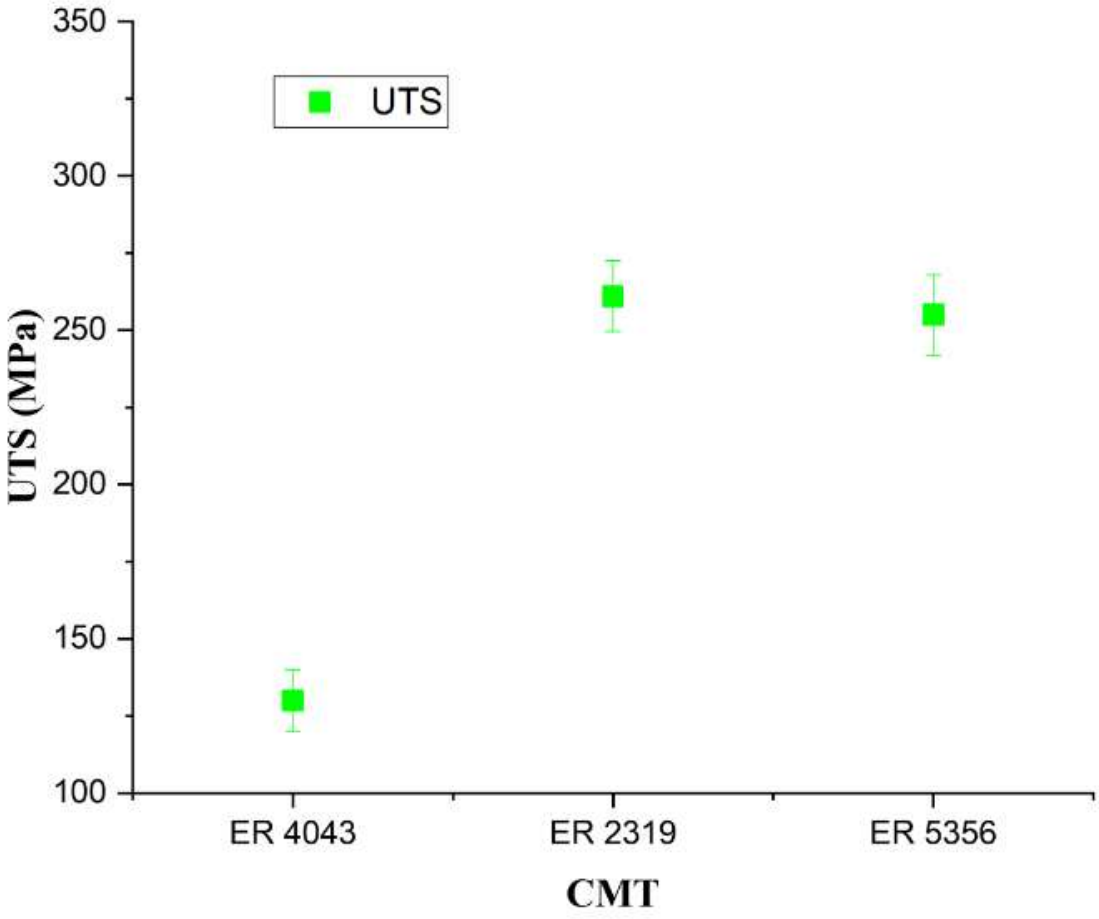

Fig. 2.9 UTS variation plot of different Al alloys fabricated by CMT WAAM

The present study reveals that the ER 4043 aluminium alloy exhibits a lower UTS in comparison to the ER 5356 and ER 2319 aluminium alloys attributed to the presence of columnar grains in the microstructure of the ER 4043 alloy. Table 2.8 shows the mechanical characteristics of Al alloy with different WAAM techniques.

Table 2.8 Al-based alloy mechanical characteristics of different WAAM techniques

Materials	Process	Condition	Microstructure	YS(MPa)	UTS (MPa)	E.L. (%)	Other properties	References
ER5356	CMT	As fabricated	Multilayer with α & β phase	128 ± 3	255 ± 9	23 ± 1.8	70-77Hv	(Su et al., 2019b)
ER2219	GTAW	As fabricated	equiaxed and columnar grain zones	(182.9 MPa)	(273.5 MPa)	12.8	83.6-102.6HV	(Zhou et al., 2020)
ER4043	CMT	As fabricated	Equiaxed grains + columnar dendrites		130 ± 4			(Campatelli et al., 2020b)
ER4043	CMT-P	As fabricated	Uniform grains + equiaxed dendrites		125 ± 4			
ER2319	CMT	As fabricated	Equiaxed grains + continuous second phase	113	261	13.1		(Dong et al., 2021)
ER2319	CMT	Heat treated	Dendritic + discontinuous second phase	296	371	4.5		

2.3.4 Magnesium alloys

Magnesium alloy offers several notable advantages, including its low density, high specific modulus, high specific strength, and specific rigidity. Additionally, magnesium alloy exhibits commendable casting performance, thermal conductivity, and shock resistance. The utilization of this material is prevalent across various industries, such as automotive, electronics, aviation, and others, wherein it serves as a substitute for steel and aluminium components (Wang et al., 2023). Potential magnesium alloy monolithic components are usually vast and complex in shape since manufacturers currently pay considerable emphasis on developing lightweight components. Immediate research must be conducted on the WAAM technology for magnesium alloy (P. Wang et al., 2021b).

Limited work has been done on the WAAM fabrication of magnesium alloys. The AZ91 sample produced through WAAM displays equiaxed grains with an average size of 13.9 μm above and 33.2 μm below the fusion line, significantly smaller than the as-cast size of the substrate (44.4 μm) (Bi et al., 2020b). The thin-walled AZ31 deposit is made up of columnar dendrite arrays with an α-Mg matrix and α-Mg and β-Mg17Al12 interdendritic eutectics as well as dispersed η-Al8Mn5 phases (Yang et al., 2020b). The ultra-frequency pulsed-WAAM deposit has good forming quality, with no flaws and fewer micropores. It features an entire equiaxed-grain microstructure and mechanical isotropic ultimate tensile strength in both directions (UTS = 203 MPa: building, 211 MPa: journey) (Cao et al., 2022). The WAAM technique has the potential to be a viable manufacturing method for magnesium alloys.

2.3.5 Steels

Steels can have a variety of qualities depending on their composition, but in general, they have a high tensile strength and are inexpensive. Steel has extensive applications across various

industries such as construction, naval, gas and oil, wind energy, and automotive (Wang et al., 2019). Thus, numerous studies are being conducted on the CMT-WAAM route for the fabrication of stainless steels (J. Chen et al., 2021), tool steels (Ali et al., 2019a), high-strength steels (Wang and Beese, 2017), and high-strength low-alloyed steel.

The microstructure, including the austenite-to-ferrite ratio, is mainly determined by the thermal history during WAAM procedures. Therefore, the microstructure can be regulated by changing the process parameters (Jin et al., 2020). Belloti et al. (Palmeira Belotti et al., 2022b) reported that CMT WAAM of hot work tool steel 1.2343 (37CrMoV 5-1) and found that the microstructure is formed up of austenite, ferrite, and fine oxide inclusions. At the fusion boundary, the ferrite shape is mostly cellular and globular, whereas, at the centre, it is vermicular and lathy. Super duplex stainless steel 2594 microstructural analysis revealed the existence of various constituents, including ferrite, intragranular austenite, Widmanstätten austenite, grain-boundary austenite, and secondary austenite (As shown in Fig. 2.10). The study revealed that the proportion of austenite and ferrite varied throughout the wall as a consequence of the intricate cyclic thermal history experienced during the deposition process. The micro-hardness gradually increased from 281 to 310HV0.2 in the fabrication direction, which was consistent with the changing proportions of ferrite and austenite. Tensile samples in horizontal and vertical directions revealed anisotropy from directed columnar ferrite propagation and grain boundary hardening from the varied austenite-ferrite ratio along the built direction (Kannan et al., 2021a).

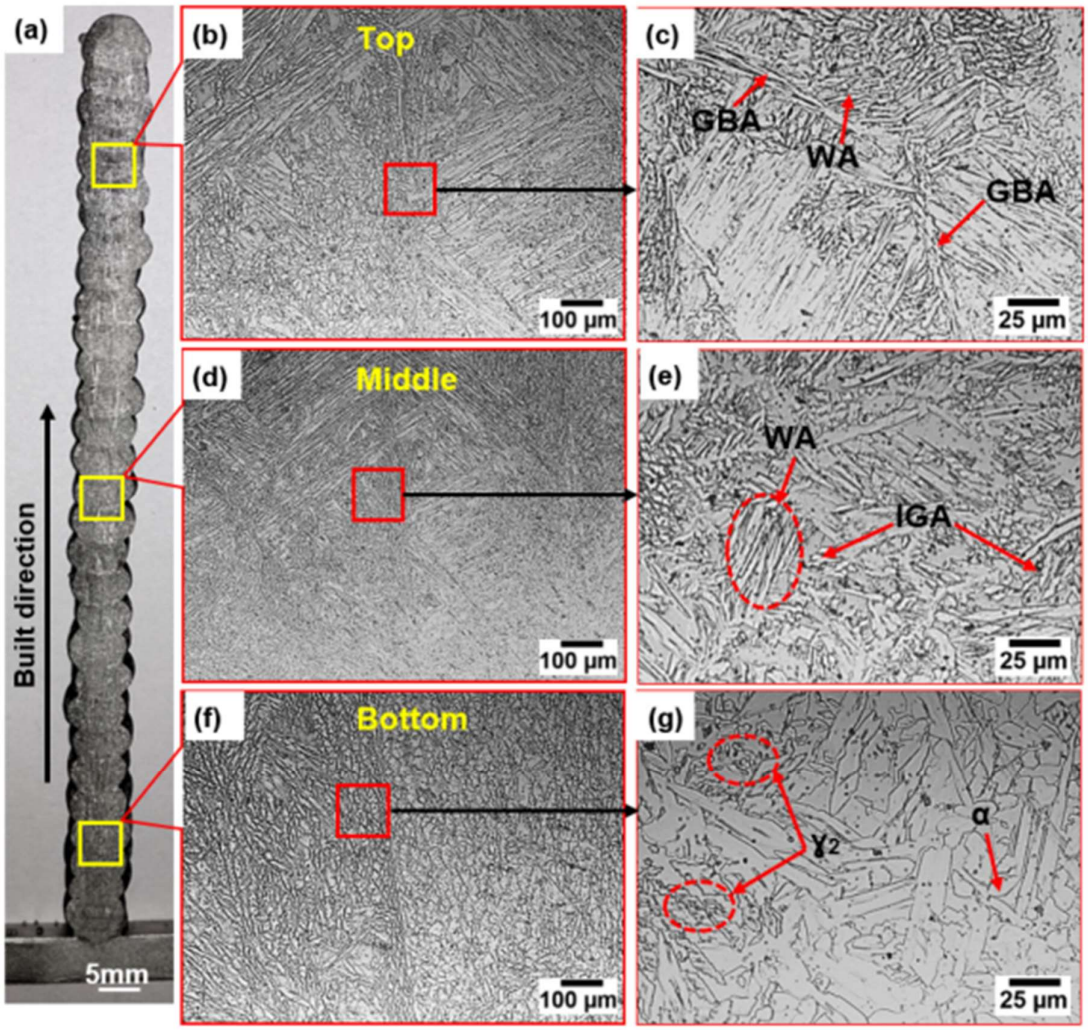

Fig. 2.10 Optical micrographs of the as-deposited SDSS wall at several positions along the building direction: IGA intragranular austenite, WA Widmanstatten austenite, GBA grain boundary austenite, and c2-secondary austenite (Kannan et al., 2021a).

2.3.6 Other alloys

Additional metals have also been examined for their potential suitability in the process of CMT WAAM, such as Al-Mg alloys (Su et al., 2019c), Bimetallic Ni-Fe alloys (Motwani et al., 2023b), Ni-Al intermetallic compounds (Meng et al., 2023), Functionally graded materials (Ayan and Kahraman, 2022; Rodrigues et al., 2022) for application in aerospace, automobile, and marine sector applications. Most existing research has primarily concentrated on the

characterization of microstructural and mechanical properties of specimens extracted from uncomplicated structures with straight walls rather than on advancing a methodology for producing functional components. The process of WAAM still presents significant challenges in achieving precise pre-determined composition when manufacturing intermetallic parts, Dissimilar alloys, and Bimetallic structures.

2.4 Recent challenges in WAAM

The potential advantages of WAAM processes are increasingly evident, including improved material utilization and the ability to produce sizable structural components with moderate intricacy. To maintain the integrity of parts exposed to severe environments and mitigate failure modes such as high-temperature fatigue, it is imperative to minimize porosity, excessive residual stress levels, and cracking (Madhuri et al., 2021). Inadequate programming techniques, unstable weld pool dynamics caused by incorrect parameter configuration, thermal deformation from heat accumulation, environmental impacts including gas contamination, and machinery malfunction are some of the reasons that might lead to WAAM deficiencies (Dhinakaran et al., 2020; Wu et al., 2017). This section of the chapter provides an overview of prevalent defects and their correlation with specific materials. Fig. 2.11 shows that certain materials are susceptible to particular defects.

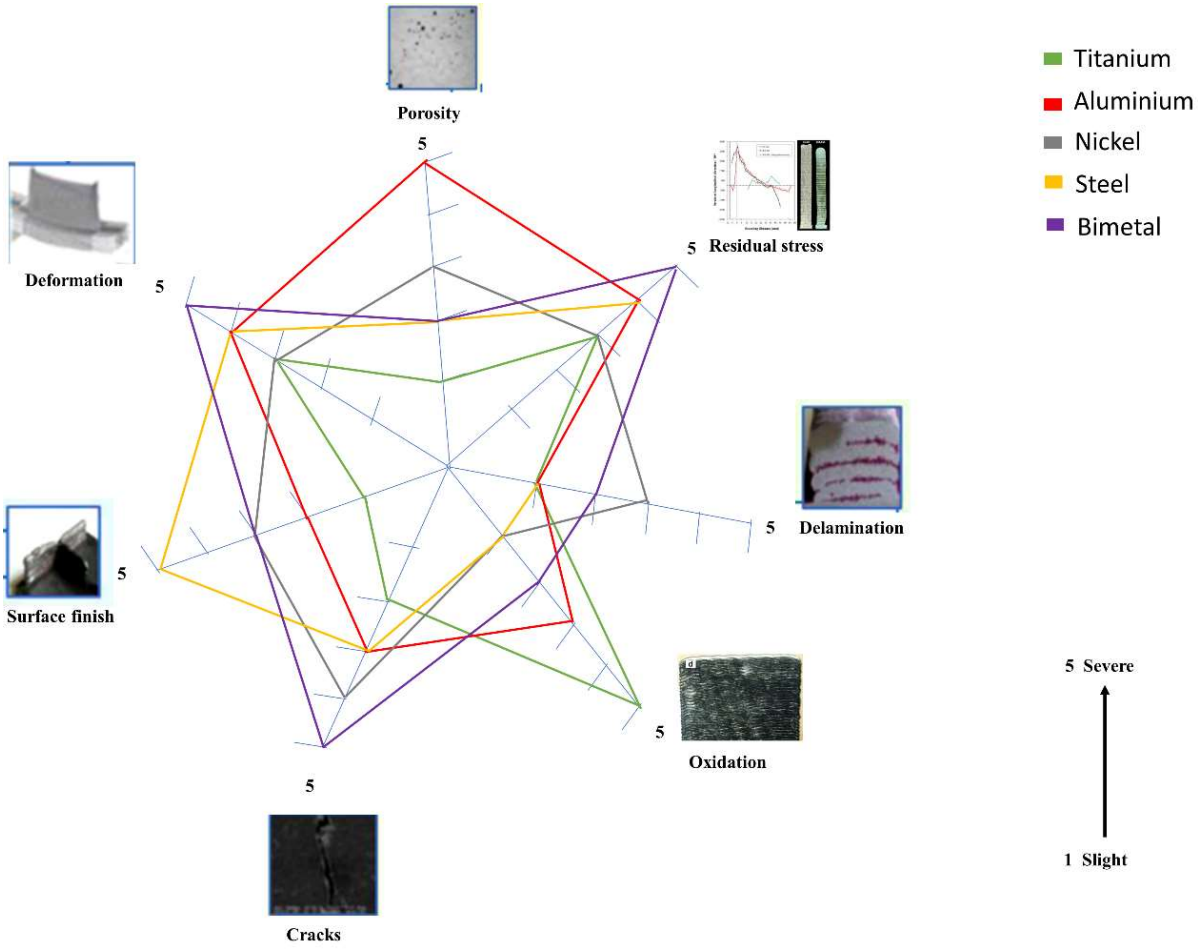

Fig. 2.11 WAAM major defects with certain materials (Wu et al., 2018d)

2.4.1 Residual stress and deformations

The residual stress characteristics are influenced by various factors such as process parameters, micro-segregation, microstructure, and material properties. Residual stresses in AM components give rise to different undesirable effects, including deformation, inaccuracies in shape and size such as distortion and twisting, material fractures occurring within the layers during the fabrication process, and compromised fatigue performance within the deposited layers (Barath Kumar and Manikandan, 2022).

Residual stresses are internal stresses that remain within a structure even after completely removing all external loads and clamping. If the volume of the component is constrained from

expanding or contracting due to temperature changes, it can lead to the generation of thermal stress in the part (Ding et al., 2011; Srivastava et al., 2021). In WAAM, residual stress is caused by multiple factors, namely layer thickness, temperature distribution, substrate thickness, deposition direction, and pattern. Distortions caused by the part's thermal expansion and contraction during repeated melting and cooling procedures are more likely to occur in large, thin-walled constructions. If the component's residual stress is higher than the yield strength of the material, plastic deformation will occur, leading to inaccurate dimensions and tighter tolerances (Gullipalli et al., 2023b; Yuan et al., 2023). In addition, if it raises the material's ultimate tensile strength, cracking is to be anticipated (KA and MJ, 2022). Bimetal components, within the realm of WAAM engineering materials, are known to display notable levels of residual stress and deformation due to disparities in thermal expansion between the constituent materials. Therefore, it is imperative to maintain precise control over the inter-pass temperature when utilizing bimetal materials (Mukherjee et al., 2017). Mughal et al.(Mughal et al., 2006) studied deformation on the base plate and substrate in weld-based additive manufacturing and substrate deflection in bolted and unbolted circumstances. Bolting dominates at deposition edges and centres. Several mitigation methods can be employed, such as subtracting preheating, clamping, implementing a deposition strategy, and utilizing inter-pass rolling (Costello et al., 2023; Wei et al., 2023b; Zahidin et al., 2023a), as shown in section 2.5.

2.4.2 Porosity

Additive manufactured aluminium alloy is the material most susceptible to porosity defects. Hydrogen and vapour generated at high temperatures by evaporating hydrogen atoms or low melting point elements like magnesium in the molten pool make up the majority of the pores in aluminium alloy. The rapid decrease in temperature makes it difficult for moisture to leave the body (Wei et al., 2023c). First, the mechanical strength of the component drops because of

gas porosity-related microcrack development (Costello et al., 2023b). Next, the geographical distribution of the varying form and size patterns often causes the deposited layer to exhibit inferior fatigue properties (Zahidin et al., 2023b). Moisture, impurities, and grease are all examples of surface contaminants in the raw material that might lead to the development of porosity in the layered structure. The porosity changes with the amount of heat applied. Researchers have shown that more porosity happens when more heat is added (Bai et al., 2017). Wang et al. (Wang et al., 2022) found that as-deposited Al alloys had hydrogen micropores and micro-voids that were caused by the solidification process. To control porosity, a few things should be taken care of, like air leaks, turbulence in the weld pool, and a high gas flow rate. By cleaning and removing grease from the workpiece, any hydrogen pollution can be kept to a minimum. Cong et al.(Cong et al., 2015) examined Conventional CMT, CMT pulse (CMT-P), CMT advanced (CMT-ADV), and CMT pulse advanced (CMT-PADV) for their impact on porosity in AA2219 aluminium alloy WAAM. Based on the data, CMT-PADV has proven to be the most effective method for minimizing porosity, while traditional CMT has the opposite effect. In CMT-based WAAM, the inter-layer rolling process can reduce the pores of the aluminium alloy, remove the source of dangerous gases, and choose the proper pulsed arc.

2.4.3 Cracks and delamination

Thermal and material parameters determine residual stress, deformation, cracking, and delamination during the process. Two types of WAAM-deposited component cracks occur in solidification grain boundary cracks (Sames et al., 2016). Solidification cracks primarily occur due to the solidification pattern exhibited by the material employed. A solidification crack forms when the molten pool experiences a large strain or when an impediment blocks the flow of the formed grain (Srivastava et al., 2023a; Zhong et al., 2021). Grain boundary cracks arise

from variations in boundary morphology and the processes of precipitate formation and dissolution (Davis, 2004).

The phenomenon of delamination, or the detachment of neighbouring layers, can be ascribed to the incomplete fusion or insufficient re-fusion of the solid substance situated amidst these layers. This shortcoming is usually apparent and cannot be fixed by adding further processing steps. To mitigate this defect, it is necessary to consider pre-processing measures, such as applying heating to the substrate (Srivastava et al., 2023b). Ni-based alloys and bimetallic material combinations exhibit increased vulnerability to delamination during fabrication using the WAAM process. Differences in the total solubility of the metals cause the production of intermetallic compounds. The issue of delamination poses a significant challenge in the AM process of FGM (C. Zhang et al., 2019).

2.4.4 Automation and integrated machining

The primary obstacle to expanding the use of WAAM in production is the need for full automation and in-house machining to improve precision, confidence, and productivity. Till now, WAAM requires significant human interaction to alter the tool path and build procedures. WAAM's industrial use requires integrated sensing and machining. WAAM's optical sensors may identify defects in the surface and geometrical abnormalities (Tomar et al., 2022b). Using acoustic and thermal sensors can offer advantages in identifying online defects during the structure deposition (Xia et al., 2020). The utilization of in-process machining techniques, identified defects have the potential to be effectively rectified and eradicated, resulting in a reduction of waste and debris to a minimum (Ramalho et al., 2022). Integrating various sensing devices and the complete automation of real-time applications is a significant problem that must be overcome. To hybridize the manufacturing process to maximise efficiency and minimise the need for post-processing, it is necessary to create a fully automated WAAM

system that incorporates machining skills (Singh and Khanna, 2021). The integrated optical sensors can detect surface defects and geometrical aberrations, while the in-built acoustics and temperature sensors can detect online issues with the deposition process.

2.5 Recent advances for quality improvement in WAAM

Parts produced utilizing the WAAM technology frequently require further treatment after production. To enhance material properties, reduce surface porosity and roughness, and remove residual stress and distortions, this post-processing is essential. Most problems influencing the deposition quality can be reduced or even eliminated using effective post-processing procedures. Improving WAAM part quality is an objective of multiple reported post-process treatment solutions.

2.5.1 Interlayer rolling

Porosity is the major problem in the case of Al alloy for WAAM, as shown in section 5. During the WAAM process, the temperature difference and repeated heating and cooling cycles between deposition layers cause the finished part to have an uneven microstructure and different mechanical properties. Plastic deformation of the deposited material during the cold rolling process effectively decreases microstructural anisotropy (Gu et al., 2018). Weld bead interpass rolling is a very effective method for reducing deformation and residual stresses (Colegrove et al., 2017). Zhang et al.(T. Zhang et al., 2022b) reported the impact of cold rolling on CMT WAAM fabricated Inconel 718 alloy, as shown in Fig 2.12. They observed that Warm rolling the alloy results in grain refinement, which leads to the as-deposited columnar dendrites in the sample changing into smaller, 16.4 m equiaxed grains. Due to its finer grains and evenly dispersed strengthening phases, warm-rolled alloys can achieve isotropic mechanical characteristics.

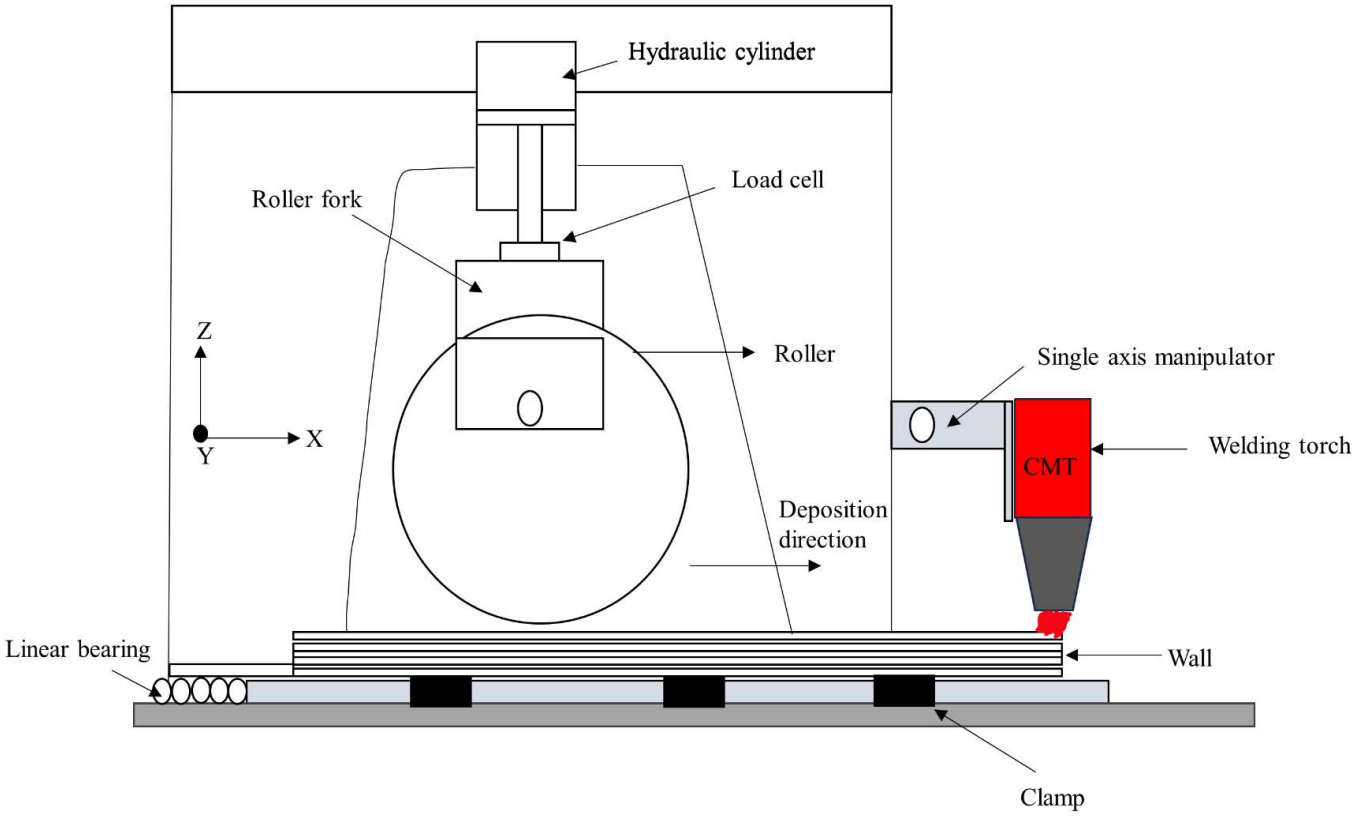

Fig. 2.12 Schematic diagram of Hybrid WAAM rolling and deposition system setup for experimentation (T. Zhang et al., 2022b).

Hu et al. (Hu et al., 2021) used the WAAM technique to confirm the effectiveness of interpass rolling in manufacturing Ti6Al4V alloys. They outperformed the as-fabricated WAAM samples in mechanical characteristics, with UTS of 876 MPa, YS of 789 MPa, and elongation of 11%. These improvements were attributed to void reduction and higher dislocation density due to the deposited material being rolled in situ.

2.5.2 Post-process heat treatment

Post-processing heat treatments are of considerable importance in the WAAM process as they enhance the material's strength, alleviate residual stress, and control the hardness of the manufactured structure. To mitigate the risk of cracking resulting from an improper heat-

treatment process, an appropriate heat-treatment approach is chosen, considering factors such as the deposited material, the additive manufacturing method used, and the available conditions for subsequent processing (Tanvir et al., 2019).

Increases in mechanical strength of 4% for titanium alloy, 78% for aluminium alloy, 5% for Nickel-based alloys, and 17% for intermetallic Ti/Al alloy were observed after heat treatment for WAAM-fabricated parts (Baufeld et al., 2011). The role of post-process heat treatments significant grain refinement, particularly in the case of aluminium and Inconel alloy fabricated using WAAM (Bhuvanesh Kumar et al., 2023; Y. Zhou et al., 2021). Li et al.(Li et al., 2021) examined the impact of heat treatment on Al-Zn-Mg aluminium produced by WAAM. They depict that T6 heat treatment resulted in a more uniform distribution of Zn and Mg throughout the matrix. The microhardness and strength of WAAM Al-6.2Zn-2.2 Mg aluminium alloy enhanced considerably after T6 heat treatment.

2.5.3 Double wire WAAM (DWAAM)

In the CMT-WAAM, the deposit rate, the amount of heat input, and the quality of the deposits are all directly controlled by the number of feedstock wires supplied (Wu et al., 2020; T. Xu et al., 2023a). The utilization of Double-wire arc additive manufacturing (DWAAM) exhibits significant potential in the fabrication of components due to its superior deposition efficiency compared to WAAM (T. Xu et al., 2023b). Zhou et al.(W. Zhou et al., 2022) examined the microstructure evolution and tensile properties of the DWAAM TiAl-4822 alloy. The prepared sample exhibited exceptional mechanical properties at a temperature of 650 °C, which can be attributed to a uniformly distributed anisotropic microstructure. In a recent study by Klein et al. (Klein et al., 2020), researchers used a twin-wire CMT-WAAM system to investigate in situ alloying of aluminium-based alloys. This method ensured chemical and microstructural homogeneity for two distinct compositional wires. The dual-wire CMT improves welding

feedstock deposition rate and in situ alloying. Multi-wire CMT-WAAM can be expanded from dual-wire. The double-wire arc additive manufacturing setup is shown in Fig. 2.13.

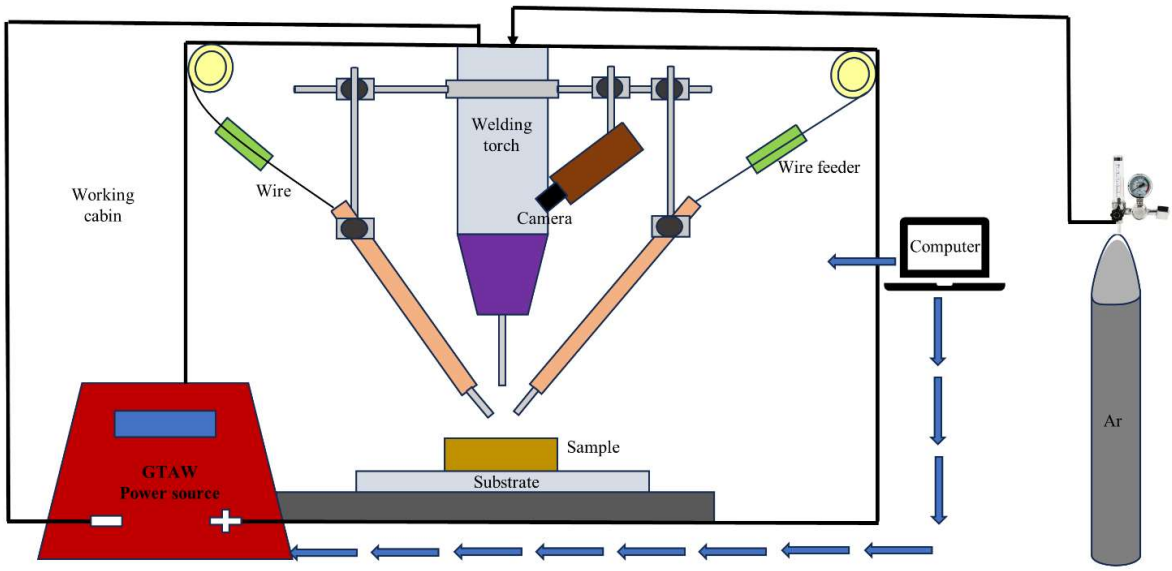

Fig. 2.13 Schematic DWAAM experimental apparatus set up

2.5.4 Near-immersion active cooling (NIAC)

Thermal management is identified as a primary difficulty in the WAAM procedures in Section 2.4 of the report. The thermal cycle history and interpass temperature experienced during the deposition process significantly impact the microstructure and mechanical qualities of a structure formed by WAAM (Kozamernik et al., 2020). The concept of near-immersion active cooling (NIAC) has emerged as a novel approach in the field of thermal management for WAAM. Its primary objective is to mitigate the adverse effects of heat accumulation resulting from the substantial heat input involved in the process. The concept of NIAC was formulated by Selva et al. (da Silva et al., 2020), and this process deposits the preform in a water-filled work tank, which rises as the metal layers are formed. The utilisation of NIAC to reduce heat accumulation during WAAM manufacturing of ER5356 alloy was confirmed by Silva et al. (Silva, 2019). The result indicated that the NIAC technique facilitated substantial and

immediate cooling of the preforms. The interpass temperature is maintained at a low level and remains consistent regardless of the height of the preform. There was no noticeable rise in porosity due to water cooling. Fig. 2.14 depicts the experimental setup for the NIAC idea. Therefore, the NIAC method proved effective in reducing the impact of heat build-up in WAAM.

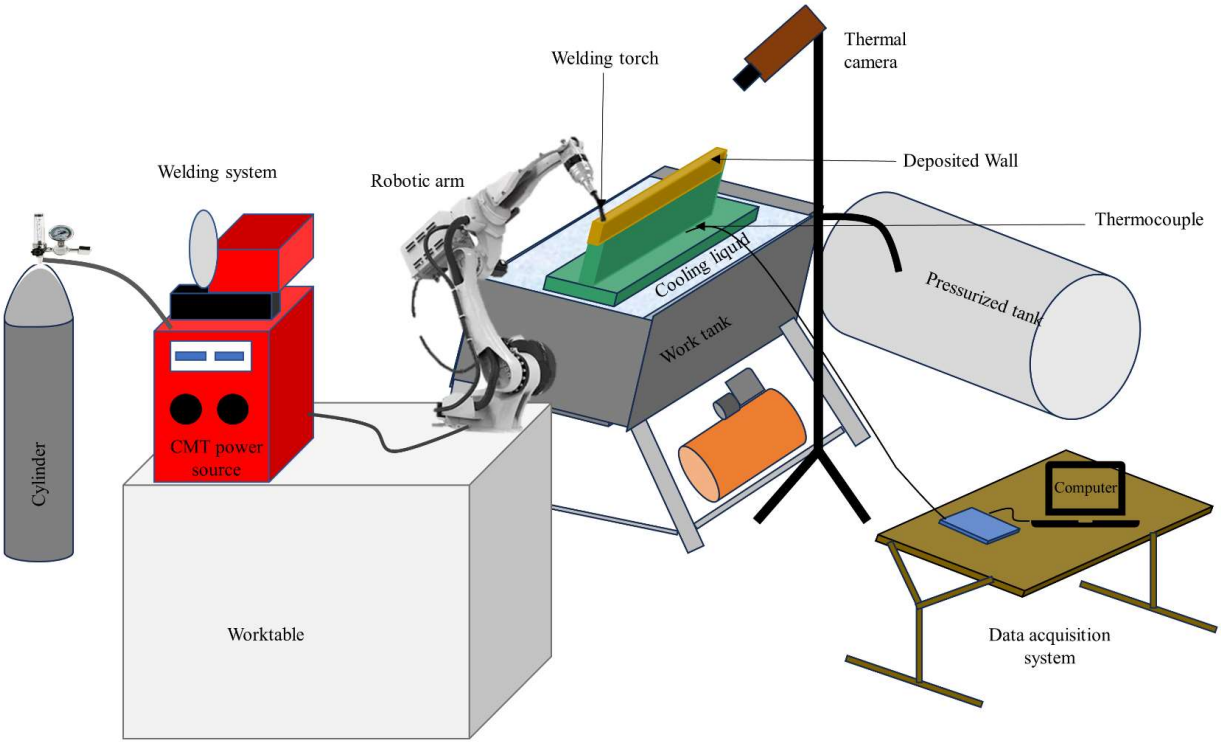

Fig. 2.14 Schematic NIAC experimental setup

2. 6 Numerical Simulation

The properties of the weld joint, such as weld penetration, bead shape, and weld quality, are primarily influenced by the wire feed rate, arc voltage, polarity of the power source, and travel speed of the welding torch. These factors are crucial in ensuring the absence of defects such as porosity, materials cracking, deformations, and high residual stress (Caruso and Umbrello, 2022; Jurić et al., 2019). Since empirical evaluations are expensive and time-consuming due

to the number of variables, numerous authors have turned to numerical simulation to evaluate welding processes in recent years. The spread of Industry 4.0 is driving manufacturing process digitization and virtualization, focusing on numerical simulation. The existing numerical models have been developed to mimic several components of the GMAW process, such as the generation of the welding arc and plasma arc, as well as the distribution of heat and temperature fields during welding. The creation of metal droplets and the solidification and thermal stress fields during metal transfer can be analysed and understood by simulation. Rubino et al. (Rubino et al., 2023) Sequentially, it models GMAW filler deposition, heat transmission, and distortions. It uses field variables for phase transitions and numerical models for Multiphysics analysis. Welding two AISI 441 steel blanks with AISI 307 filler material for the automotive industry is studied in various joint configurations. Prior experimental testing is needed for input parameters before Sysweld simulates the stress-strain field. A simplified Abaqus numerical model without fluid dynamics or birth/death elements predicts these parameters. Experimentally creating GMAW joints and comparing distortions numerically/experimentally validate the proposed approach. Deng et al. (Deng and Murakawa, 2006) analyses welding transient temperature and residual stress fields using finite element models. A 3-D model is first created to simulate these fields, followed by a 2-D axisymmetric model using temperature and tension. The results show that the 2-D axisymmetric model accurately simulates temperature cycles and welding residual stresses for SUS304 stainless steel pipes, reducing computing time. Experimental validation shows that 3-D and 2-D models match measured data, proving the numerical approach's reliability.

2.7 Research gaps

After the literature review, it is observed that the following scope can be

- Limited research work is carried out in dissimilar nickel-duplex steel alloy, and nickel-super duplex steel alloy for the manufacturing of WAAM components.
- No research work in the field of fabrication of WAAM of dissimilar super DSS 2507 and nickel-based filler wire and the effect of microstructural and mechanical properties of the WAAM process.
- Limited research work in the field of tribological studies and corrosion resistance of dissimilar WAAM samples of Nickel alloys, Super DSS 2507 and DSS 2209 based on CMT WAAM.
- Very less work for optimization of process parameters in the area of CMT-WAAM technology.

2.8 Research objectives

After having a literature review, we have found the following objective for the research.

- To study the weld-bead geometry of dissimilar super duplex stainless-steel and Inconel alloys using the CMT process.
- Fabrication of WAAM of the dissimilar alloy of super duplex stainless steel and Inconel alloys.
- To study microstructure and mechanical properties of fabricated WAAM samples.
- To study the wear characteristics of fabricated samples.
- To study the effect of Ultrasonic vibration on microstructure and mechanical properties.

2.9 Flow chart for work

A flow chart provides a concise representation of the intricate tasks. Fig. 2.15 depicts the flow chart of the current study, illustrating the sequential approach and methodology employed in this work.

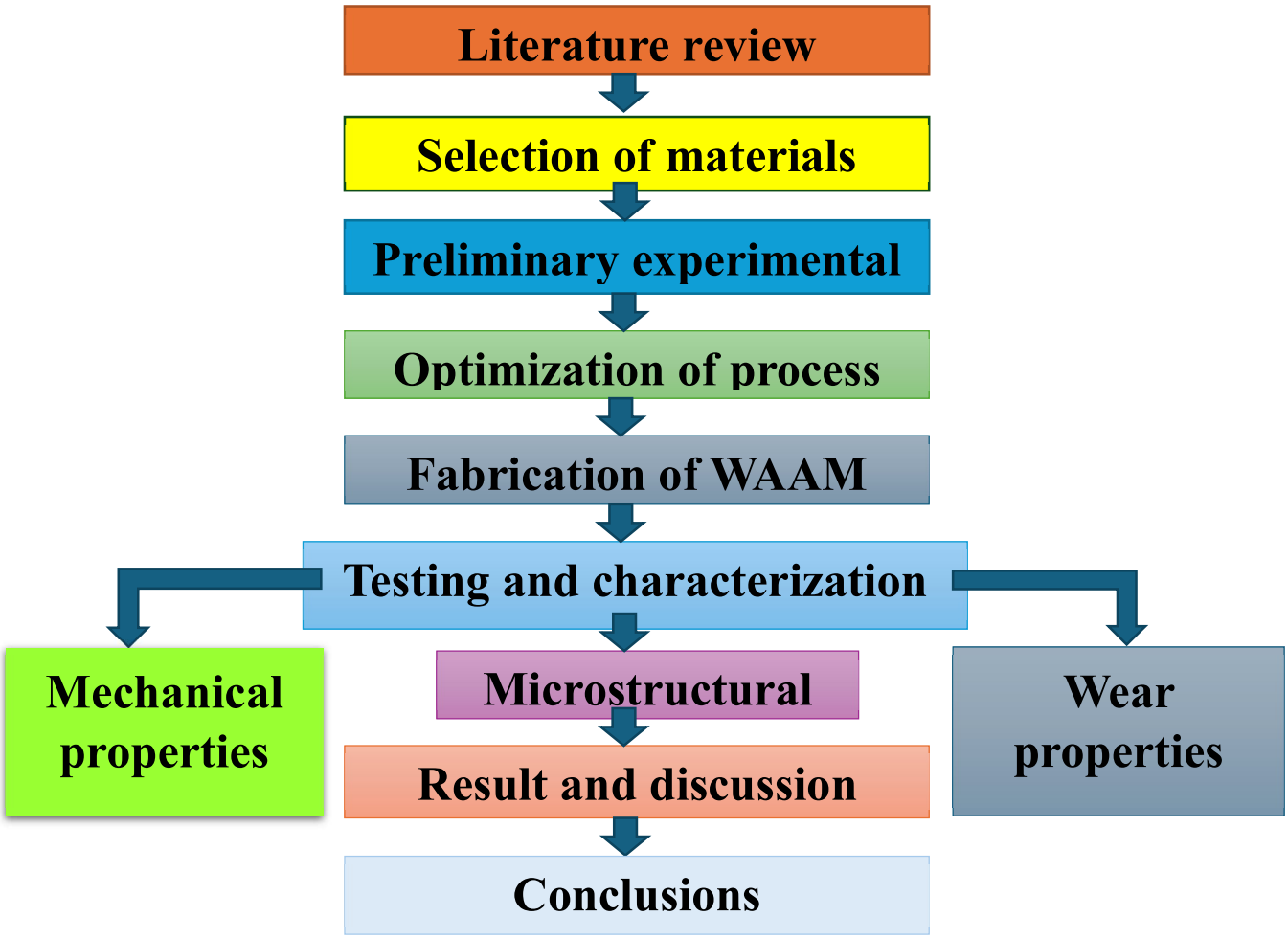

Fig. 2.15 Flow chart of research work

2.10 Summary

The literature review chapter offers a thorough analysis of WAAM applied to different alloys, focusing on techniques like CMT, GMAW, GTAW, Plasma, and FCAW-based WAAM. The review focuses on the microstructural and mechanical properties of materials such as titanium,

nickel, steel, aluminium, and magnesium alloys produced through WAAM. The chapter highlights the challenges of WAAM, such as residual stresses, porosity, delamination, and fracture. It also explores different approaches to address these issues and minimize these defects. The review also highlights a lack of research on CMT-based WAAM despite its potential for creating precise microstructures and improved mechanical properties.

CHAPTER 3

MATERIALS AND METHODS

3.1 Materials

3.1.1 Substrate metal/ Base material

The substrate for the WAAM process was selected to be stainless steel alloys of grade 304, with dimensions of 200mm × 50mm × 5mm. This experiment used a substrate plate to develop an additive wall. The chemical composition of stainless steel 304 is shown in Table 3.1. It is robust and attractive, with 18-20% chromium and 8-10.5% nickel, king it perfect for kitchen equipment, food processing, and architecture (Agrawal et al., 2017).

Table 3.1 Chemical compositions (wt%) obtained by chemical spectroscopy of substrate materials as per ASTM standards

Chemical Composition %	**C**	**Si**	**Mn**	**P**	**S**	**Ni**	**Cr**	**Fe**
Stainless steel (304)	0.07	1.03	2.05	0.045	0.030	8.04	17.95	70.78

The substrate material's mechanical properties are evaluated according to ASTM standards and displayed in Table 3.2.

Table 3.2 Mechanical properties of substrate material

Property	**Value**
Tensile strength	515 MPa
Yield strength	205 MPa
Elongation (in 50mm)	40%

Hardness	140-200 HV
Modulus of elasticity	193 MPa
Density	8 g/cm^3
Melting range	1400-1450 °C

3.1.2 Filler Material

In this study, Inconel 718 and SDSS 2507 diameter of 1.2 mm filler wire was selected, provided by Advanced PMI Solutions. According to the literature survey and comprehensive trial tests, this filler wire is compatible with stainless steel 304 alloy. Inconel 718 is a superior-performance nickel-ferrous-chromium-based superalloy that has excellent mechanical properties. Due to high-temperature alloys, it is widely used in aerospace, nuclear energy, and gas turbines (Sonar et al., 2021). The strength of Inconel 718 superalloy is primarily ascribed to γ' (Ni_3(Al, Ti)) phase with cubic L12 crystal structure and γ" (Ni_3Nb) phase with a tetragonal DO22 crystal structure, where γ" is the main strengthening phase (Huan et al., 2022). SDSS have excellent mechanical properties and wear properties due to their Cr & Ni contents and unique ferritic-austenitic microstructures, making them highly effective in challenging environments (Kumar and Maji, 2023; Leif, 2012). SDSSs are found in various applications in the nuclear, petroleum, automotive, shipbuilding, marine, and chemical industries (Sales et al., 2021). Table 3.3 displays the weight percentages of the filler material's chemical compositions, determined by chemical spectroscopy according to the ASTM E 1251:2011 standard.

Table 3.3 Chemical composition (Wt %) of the filler wire

Chemical Composition %	**C**	**Si**	**Mn**	**P**	**Ni**	**Cr**	**Mo**	**Fe**	**Nb**
Inconel 718	0.08	0.35	0.45	0.015	51.05	17.55	2.9	22.14	4.89
Super Duplex 2507	0.030	0.80	1.20	0.035	7	25	4	57.82	-

3.2 Sample preparation

3.2.1 Macrostructure Characterization

Macrostructure describes the overall shape and size of the weld bead. It is crucial to quantify these dimensions to gain a comprehensive understanding of the bead geometry, which affects the entire cost of welding. The specimens were made by extracting the size of 15 x 15 mm from the weld bead. Next, the cross-sectional surface of the weld bead was polished using emery paper of various grades, including 100, 320, 400, 600, 800, 1000, 1200, 1500, 1800, 2000, and 2500. Exploring the macrostructure of the weld bead requires dry polishing. The macrostructure of the material displays the bead geometry, as depicted in Fig. 3.1. This comprises measurements of the bead height (BH), bead penetration (BP), and bead width (BW).

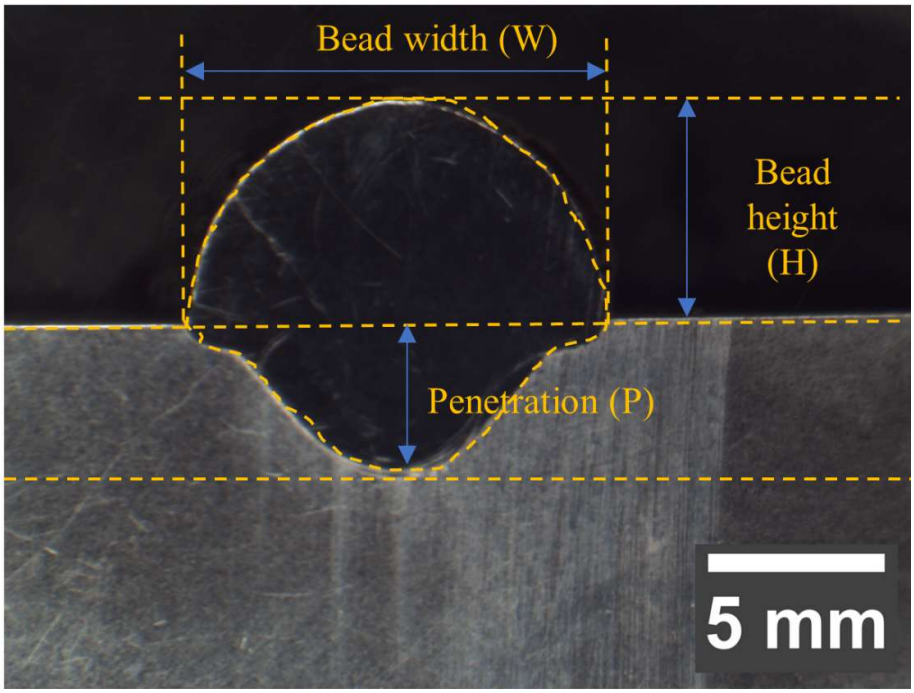

Fig. 3.1 Cross-section macrostructure specimen of the weld bead

3.2.2 Microstructure Characterization

Microstructure characterisation provides detailed information about the arrangement of grains, the boundaries between them, and the size of individual grains. The optical microscope is employed as the primary tool for analysing the interior grain structure of the metal. The samples were obtained by extracting the size of a 15 x 15 mm square piece from the weld bead. The cross-sectional phase was embedded in a bakelite powder using a hot mounting press at a temperature of 135ºC for 20 minutes. Subsequently, the aforementioned samples were let to cool within the mounting press for 15 to 20 minutes. The cross-sectional surface of the weld bead is polished using emery paper of various grades, including 100, 320, 400, 600, 800, 1000, 1200, 1500, 1800, 2000, and 2500. Subsequently, wet polishing was performed using velvet emery paper and alumina powder. They were then etched in a chemical solution containing a 50:50 mixture of oxalic acid and hydrochloric acid for IN 718 (Kattimani et al., 2023) and chemical 80 ml deionized water, 20 ml hydrochloric acid, 0.3 g sodium metabisulfite for SDSS

2507 (Zhu et al., 2021) followed by polishing with alumina powder on a felt pad. The samples were examined under a microscope after being dried using a hot air blower after etching. The procedure for preparing samples for microstructure characterization is illustrated in Fig. 3.2.

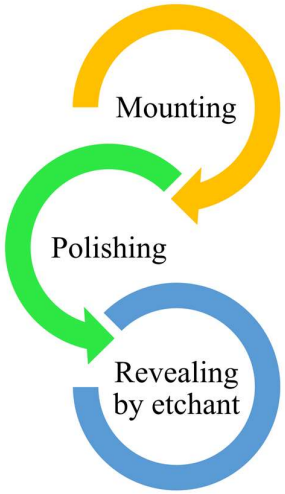

Fig. 3.2 Steps of sample preparation for microstructure characterization

3.2.3 Microhardness

Microhardness is a mechanical property that provides insight into the material's hardness at a microscopic level. It exhibits excellent resistance to indentation. The surface underwent preparation for microhardness testing through a series of steps:

- First, dry polishing the specimen using emery papers of several grades (180-2500) was performed.
- The second stage involves wet polishing with various grades (I, II, and III) of alumina powder applied with a velvet cloth.

In order to ensure precise measurements, the surface was polished to make the indenter's diagonal visible, as seen in Fig. 3.3.

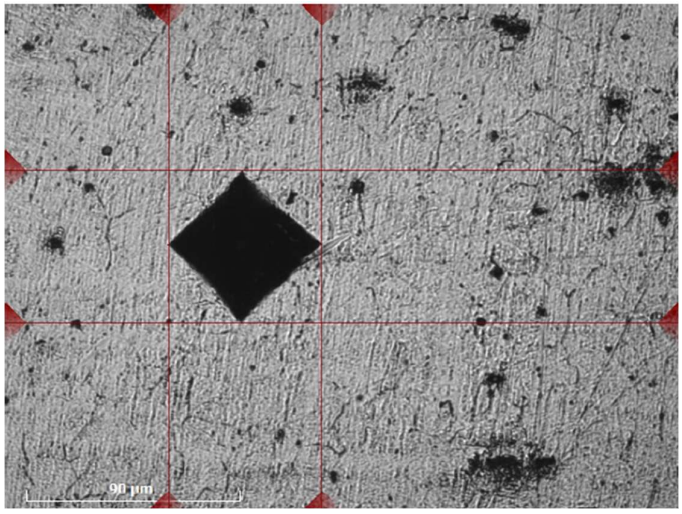

Fig. 3.3 Microhardness indentation on SDSS 2507 sample

3.2.4 Tensile Testing

Tensile testing measures the strength of a material undergoing a basic lengthening procedure. The primary purpose of the testing machine is to generate the stress-strain curve and the load vs displacement curve. The tensile test is employed to ascertain the material's mechanical characteristics. The results of tensile testing can be utilized in engineering applications to aid the material selection process. Tensile characteristics are frequently included in material specifications to ensure quality. Performing standard tensile testing, the samples with a shorter grip length were prepared according to ASTM-E8 standards. The tensile samples are extracted from the WAAM samples, as shown in Fig. 3.4.

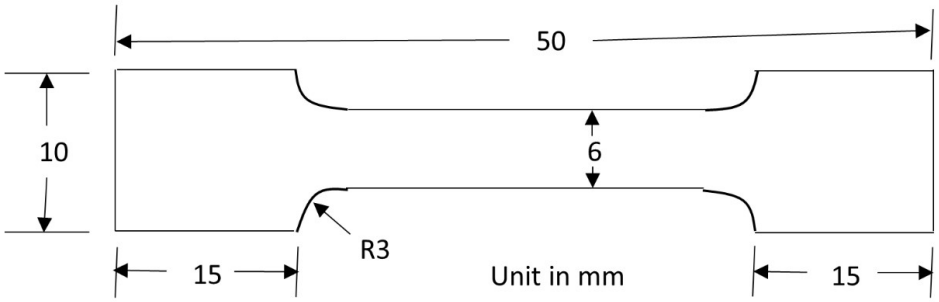

Fig. 3.4 Tensile Specimen as per ASTM E8

3.2.5 Tribological properties

The study of friction, wear, and lubrication of contacting surfaces in relative motion, known as tribological characteristics, is crucial for mechanical components' long-term performance and durability. These characteristics govern the behaviour of materials while in touch, directly influencing aspects such as energy efficiency, material deterioration, and maintenance needs in different applications. Friction undermines the effectiveness of moving components since greater friction results in amplified energy dissipation and possible overheating. At the same time, wear affects material degradation and surface integrity, posing a risk of component failure. By creating a protective film between contact surfaces, lubrication significantly reduces both friction and wear, extending the components' operational life. The tribological performance of materials is affected by several parameters, including material composition, surface roughness, hardness, ambient conditions, and lubricant presence. A comprehensive grasp and effective enhancement of these characteristics are crucial for enhancing the dependability and efficiency of components in various sectors, including automotive, aerospace, manufacturing, and biomedical electronics. The specimens for wear measurement were obtained by cutting them using a wire EDM machine with dimensions of 10 mm x 10 mm square cross-section as per ASTM G133-05. Next, the cross-sectional surface is meticulously polished using waterproof emery paper of varying grades.

3.3 Experimental Machines

3.3.1 CMT Machine

The CMT machine is a more sophisticated iteration of the GMAW machine. The TPS400i CMT machine (Fig. 3.5) is utilized in this research study, and its technical specifications are exhibited in Table 3.4. The total duration of CMT welding is reduced to one-fourth during the

short-circuit phase when the maximum current approaches zero (Selvi et al., 2018b). It significantly decreases the expenses associated with welding and reduces energy usage by 30% to 40%. The combination of high-speed digital process control (DPC) and wire buffer is responsible for achieving this (Pickin et al., 2011). During the short-circuiting phase, if a short-circuit occurs, the DPC promptly signals the wire buffer to retract the filler wire using the synergic power source. This action automatically decreases the current level in this phase. This decrease in electrical current contributes to a decrease in thermal heat input (THI), minimum splatter, minimal distortion, low dilution, and other benefits (Cao et al., 2014, 2013; Lin et al., 2013; Lorenzin and Rutili, 2009; Wang et al., 2008). The CMT machine utilizes direct current electrode positive (DCEP), also known as direct current reverse polarity (DCRP). Due to the shorter distance between the electrode and the base metal, known as the CTWD (Contact Tip to Work Distance), a greater quantity of metal ions is incorporated into the plasma arc column. DCEN produces thicker welds with an unstable arc, leading to frequent interruptions in the arc. In CMT welding of synergic lines, the variables of voltage (V), current (I), and wire feed speed (WFS) are interconnected. Altering any of these parameters will result in corresponding changes to the other two. Arc length correction (ALC) is a factor that adjusts the arc length, enabling more exact regulation of heat input. The range varies from a decrease of 10% to an increase of 10%. The negative range achieves a shorter arc length, resulting in a narrower weld bead and more penetration by reducing the voltage. The positive range achieves a longer arc length, resulting in a broader weld bead and less penetration by increasing the voltage. The zero setting corresponds to a neutral arc length, meaning there is no adjustment to the correction factor.

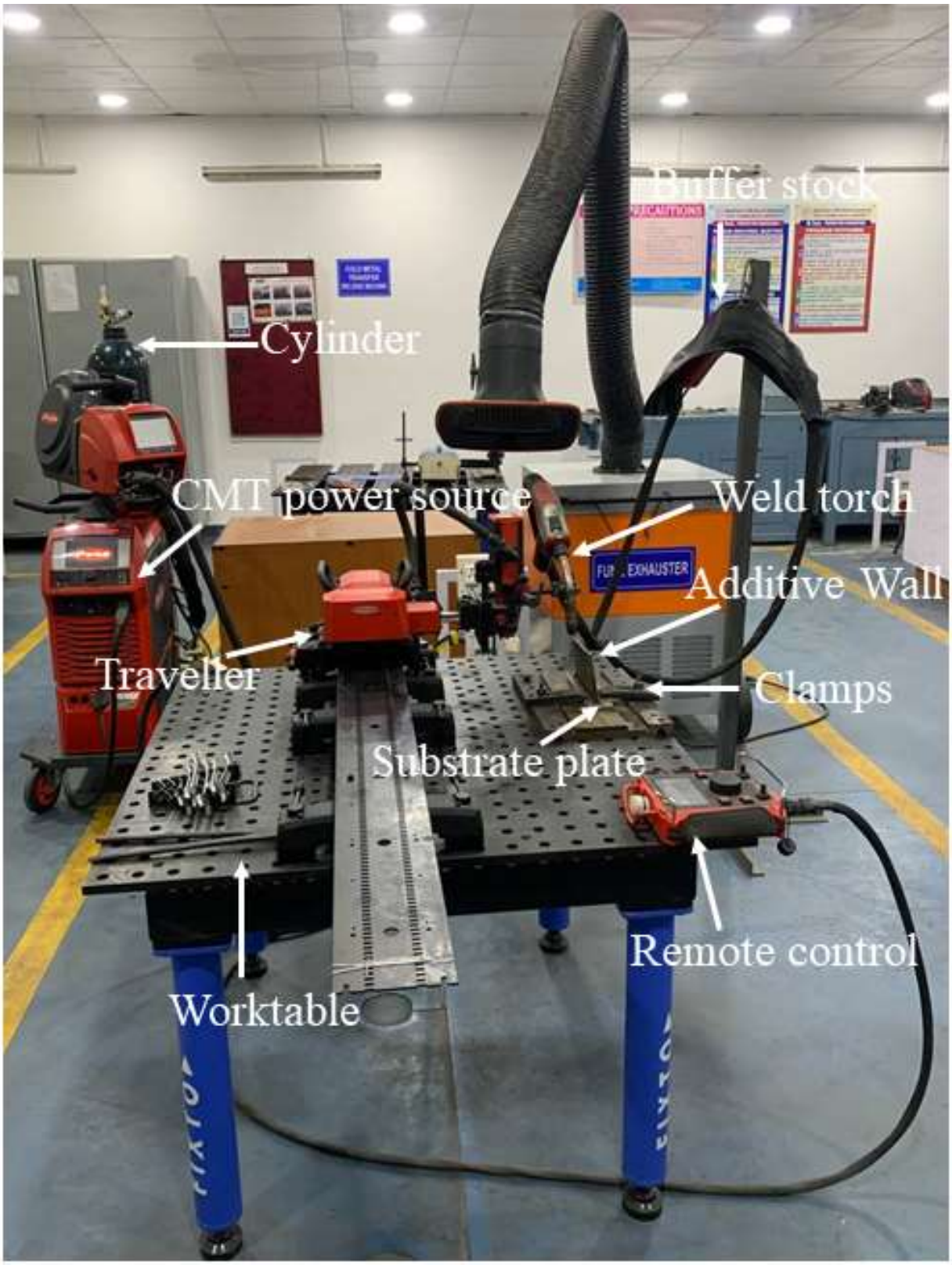

Fig. 3.5 TPS400i CMT machine

Table 3.4 Specification of CMT machine

Specifications	Units	Range
Maximum/minimum welding current	A / A	400 / 3
Welding current / Duty cycle [10 min/40°C]	A / %	400 / 40
Welding current / Duty cycle [10 min/40°C]	A / %	360 / 60
Welding current / Duty cycle [10 min/40°C]	A / %	320 / 100
Operating voltage	V	14, 2-34, 0
Open circuit voltage (OCV)	V	73
Mains frequency	Hz	50-60
Mains voltage	V	3 x 400
Mains fuse	A	35
Dimension / b	mm	300
Dimension / l	mm	706
Weight	kg	36, 45
Degree of protection	-	IP23

3.3.2 Microhardness Machine

The microhardness analysis is conducted using a Struers Duramin-40, as depicted in Fig. 3.6. The technical specifications of the Struers Duramin-40 can be found in Table 3.5. During the microhardness test, a Vickers diamond indenter is applied to the material's surface using a penetrator and a weight of 500 grams. When a force is exerted on a material, it creates an indentation that results in permanent deformation on the material's surface in the shape of the indenter.

Fig. 3.6 Microhardness tester (Struers Duramin-40)

The test is conducted in a controlled environment by monitoring the pressure for a specific duration (10 seconds of dwell time) using a square-shaped diamond indenter. The diagonal resulting from the indentation on the material surface is measured, and the Vickers hardness value is calculated.

Table 3.5 Specification of Microhardness Tester (Struers Duramin-40)

Model	Duramin-40 M1
Loads and Applications	
Load Range (Main Loads)	10 gf – 10 kgf
Vickers Capability	Yes
Knoop Capabiblity	Yes
Brinell Capability	Yes
Stages and Turrets	
XY-stage	Manual

XY-stage or anvil size (mm)	90 x 90
XY-stage stroke, max (mm)	25 x 25
Vertical capacity	172
Throat depth (mm)	170
Motorized Z-axis	Yes
Motorized turret	Yes
Turret positions	6
Anti-collision protection	Yes
Machine weight	101 kg
Camera and Optics	
Evaluation camera resolution	18 MP
Auto illumination	Yes
Stage illumination	Yes
Laser or LED guider	Yes
Interfaces and Connectivity	
Operation	Embedded Windows 10 PC with 15 inch touch screen.
Communication Ports	HDMI, VGA, RJ45, WLAN, USB, RS232
Wifi	Yes
Bluetooth	Optional

3.3.3 Tensile testing machine

Materials for engineering purposes are selected based on their mechanical qualities, including tensile strength and percentage elongation. The technical specifications of the UTM are provided in Table 3.6.

Table 3.6 Specification of Tensile Testing Machine

Capacity	KN/Kg	50/5000
Clearance between columns	mm	405
Load cells	-	Rapid change, low profile Z type load cells with digital encoding for automatic recognition.
Maximum crosshead travel	mm	1100
Testing speed range	mm/min	0.001-500
Capacity at maximum speed	KN	25
Maximum speed at capacity	mm/min	250
Jog speed	mm/min	0.001-500
Return speed	mm/min	0.001-500
Dimensions (H x W x D)	mm	1613 x 720 x 500
Weight	Kg	140

The material undergoes tensile testing using a Universal Testing Machine (UTM) called Tinius Olsen H50KS, as depicted in Fig. 3.7. The specimens are made as per the ASTM-E8 standard, as shown in Fig. 3.4. The tensile tests on the treated samples are conducted at room temperature using a constant cross-head speed of 1 mm/min.

Fig. 3.7 Tensile machine (Model: Tinius Olsen H50KS)

3.3.4 Optical Microscope

The Olympus GX41 compact inverted metallurgical microscope, depicted in Fig. 3.8, is utilized for optical microscopy. The technical specifications of this microscope can be found in Table 3.7. The GX41 inverted metallographic microscope is ideal for quickly and accurately analysing specimens and assessing whether their metallurgical qualities meet production

standards. The tiny and lightweight form of the device enables easy portability. Three notable features of this product are its mobility and ergonomics, ergonomic eyepoint adjustment, and exceptional image quality and resolution with brightfield and polarized illumination. A small and efficient body allows for easy movement and optimal comfort. A compact body may be easily installed in a limited area and is also portable, making it suitable for both laboratory and on-site inspection needs in production settings.

Fig. 3.8 Olympus GX41 compact inverted metallurgical microscope

The GX41 is equipped with a Tilting Binocular Observation Tube that allows for ergonomic Eyepoint Adjustment. This feature enables users to comfortably utilize the GX41 when either standing or seated, creating a pleasant working environment. Superior image quality and excellent resolution in both brightfield and polarized illumination enable clear and bright observation at any level of magnification. The high-clarity observation and superb image quality filling the complete field of view (F.N.22) are made possible by using infinity-corrected UIS2 optics. The objective magnifications for bright-field and clear polarizing observations vary from 5x to 100x.

Table 3.7 Specifications of Optical Microscope

Optical System		UIS2 Optical System (Infinity-corrected)	
Microscope Frame	Observation Method	BF/KPO*	
Reflected/Transmitted		Reflected	
Illuminator		-	
Illumination System	Reflected light	30W Halogen or Fiber Light Guide (Light source:100 W)	
Transmitted light		-	
Focus	Motorized/Manual	Manual Revolving Nosepiece Up/Down Movement (Stage Stationary Type)	
Stroke		9 mm	
Resolution/Fine adjustment sensitivity		Fine Stroke per Rotation 0.2 mm	
Revolving Nosepiece	Motorized type	-	
Manual type		Quadruple for BF	
Stage	Stroke	120(X)x78(Y) mm	
Observation Tube	Standard Field (Field number 18)	Inverted Image	Tilting Binocular Observation Tube

Standard Field (Field number 20)	Inverted Image	Binocular/Trinocular/Tilting Binocular Observation Tube
Wide Field (Field number 22)	Inverted Image	Binocular/Trinocular/Tilting Binocular Observation Tube
Erect Image	-	
Dimensions	236(W) x 624(D) x 407(H) mm	
Weight	10 kg (in Standard Combination)	

3.3.5 Field Emission Scanning Electron Microscope

Field emission refers to the phenomenon when electrons are emitted from a material's surface due to a strong electric field. FESEM utilizes an electron-optical column, as depicted in Fig. 3.9. The technical specifications of FESEM can be found in Table 3.8. The electron beam, also known as the electron probe, used to capture the image should be minimized to a size of approximately 10 nm. The size of the electron probe directly affects the resolution of the picture obtained through the FESEM procedure. Raster scanning is the technique in which the electron probe uniformly covers the specimen. High-energy electrons are sent towards the object and collide during the scanning process, causing scattering. The scattering events are detected as elastic and inelastic manifestations of electron interaction.

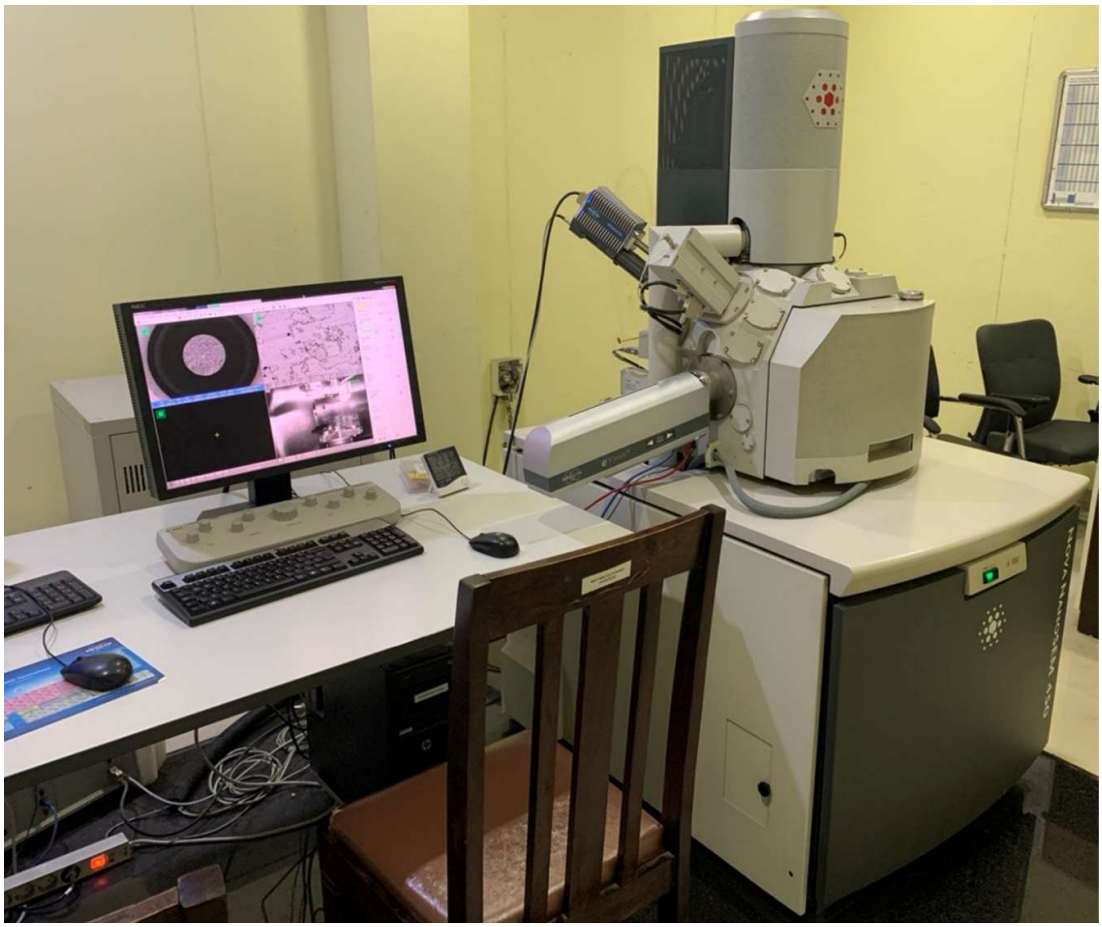

Fig. 3.9 Field Emission Gun Scanning Electron Microscope (Model-Nova Nano FE-SEM 450)

The resulting image from the scanning process may exhibit varying brightness levels due to the impact of electron bombardment. The varying brightness can be attributed to the presence of secondary and backscattered electrons, which can be distinguished based on their kinetic energy, with the latter possessing more energy. The images produced by the secondary electron display solely the surface structure, providing no information about the underlying structure. Only topographical contrast is observed. On the contrary, backscattered electron pictures possess depth and offer insights into the underlying structure of the material. This is owing to the information derived from signals originating from half of the penetration depth. They exhibit contrasting pictures based on the chemical composition of the item.

Table 3.8 Specification of FESEM machine

Electron optics	High-resolution FESEM column optimized for high brightness/high current
Ion optics	Magnum ion column with Ga liquid metal ion source with a lifetime of 1500 hours
Electron beam resolution	- 1.2 nm @ 30 kV @ high vacuum mode - 1.5 nm @ 30 kV @ ESEM mode - 1.5 nm @ 3 kV @ low vacuum mode
Ion beam resolution	10 nm @ 30 kV @ 1pA
Accelerating voltage	200V to 30 kV for electron beam imaging and 5 to 30kV for ion beam imaging
Detectors	Everhardt-Thornley SED, Low-vacuum SED, Gaseous SED, IR-CCD, EDS detector and Gaseous BSED
Specimen stage	4-axis motorized eucentric goniometer stage X = 50 mm, Y = 50 mm, T = -15 +75°(manual), Z = 50 mm (25 mm motorized), rotation = 360° continuous

3.3.6 X-Ray Diffraction

Diffraction patterns occur when light is scattered by a regularly arranged structure with a high degree of organization, resulting in constructive interference. Constructive interference is only noticed at certain angles. The XRD data analysis aims to identify trends corresponding to the crystal structure's orientation. This is further examined by analysing the Miller indices of the peaks in the diffraction pattern. The wavelength utilized for X-ray imaging is nearly identical to the spacing between the atoms. When X-rays encounter atoms, they scatter and create a diffraction pattern. This pattern provides valuable information about the arrangement of atoms in the crystal. The Bruker D8 advanced equipment is utilized for XRD spectrum analysis, as depicted in Fig. 3.10. Its technical specifications are provided in Table 3.9.

Fig. 3.10 XRD (Model: BRUKER D8 ADVANCED)

The diffraction peaks recorded on the XRD correspond to the atomic planes. The diffraction peaks that are created are directly linked to the atomic planes, aiding in the analysis of both the atomic structure and microstructure. The position of the diffraction peaks is determined using Bragg's law ($n\lambda=2\ dhkl Sin\theta$). The term "dhkl" refers to the distance between parallel planes of atoms in a crystal. θ represents the angle formed between the incident beam and the normal to the lattice where the reflection occurred. The symbol λ represents the wavelength, whereas n represents the order of reflection, an integer. Bragg's law facilitates the determination of the angle at which diffraction peaks occur due to the constructive interference produced by X-rays

scattered from the crystal lattice planes of atoms. The intensity and position of the diffraction peaks are contingent upon the crystal structure, namely the spatial organization of atoms in a periodic array throughout the entire crystal.

Table 3.9 Specification of XRD machine

X-ray	
Source	2.2 kW Cu anode long fine focus ceramic X-ray tube
Running Condition	40 kV and 40 mA
X-ray Beam Shaping Optics	
Beam [Cu-Ka1]	Collimated, compressed and frequency filtered by a Göbel mirror and V-Groove
Collimated beam dimensions	0.3 mm by 11 mm
Göbel mirror	60 mm multilayer X-ray mirror on a high precision parabolic surface
Goniometer	
Maximum and minimum measurement circle diameter	250 mm & 100 mm
Smallest angular step size	0.0001o
Reproducibility	+/- 0.0001o
Maximum rotational speed	1500 o/min
Angular range (Theta)	-5o to 40o
Angular range (2Theta)	-10o to 60o
Reflectometry Sample Stage	
Samples size	200 mm in diameter and 50 mm thick
Detector	

Maximum count rate	2 x 106 s-1 (although it should not be exposed to in excess of 5 x 10 5s-1 for periods longer than about 1 second)
Detector electronics count rate	3 x 107 s-1

3.3.7 Linear Reciprocating Tribometer

A linear reciprocating tribometer is a specialized device used to quantify materials' tribological characteristics, including friction, wear, and lubrication efficiency, in simulated sliding contact scenarios. This device facilitates the regulated contact between a sample, commonly referred to as the "pin" or "counter face," and another sample, known as the "disc" or "flat surface," while applying a particular load. The tribometer replicates the reciprocating movements commonly observed in various mechanical systems by moving one sample linearly back and forth against the other. The DUCOM advanced linear reciprocating tribometer was used to analyse wear properties, as shown in Fig. 3.11. The Technical Specification of the tribometer is exhibited in Table 3.10.

The controlled environment enables accurate quantification of frictional forces and rates of wear. Furthermore, several models can replicate diverse environmental factors, including temperature, humidity, and lubrication. This makes the tribometer highly adaptable for conducting material testing, evaluating lubricant effectiveness, and studying surface engineering. The ability of this material to provide essential data on its resistance to wear and its frictional qualities makes it vital in materials science and engineering. It is precious for creating mechanical systems that are more durable and efficient.

Fig. 3.11 Linear Reciprocating Tribometer (Model-Ducom)

Table 3.10 Specification of linear reciprocating tribometer

Top specimen	Spherical ball	Dia. 4,6,8,10 & 12 mm
	Cylindrical Pin	Dia. 4,6,8,10 & 12 mm × 15mm long
Bottom specimen	Flat	50 × 50 × 5 mm
Normal Load	5-50 N dead weight in step of 5N	
Frequency	Up to 50 Hz	
Stroke length	1-20mm	

Frequency	Stroke Length
1-8 Hz	20mm
8-10 Hz	16mm

10-20 Hz	15mm
20-30 Hz	5mm
30- 40 Hz	2mm
40-50 Hz	1mm
Friction Force	0-50 N
Temperature	Ambient to 550 ºC
Data Acquisition card	Ni-6321
Equipment size	600 × 520 × 900mm

3.4 Optimization of CMT process parameters

The design of experiments (DOE), computational techniques, and optimization techniques are predominantly employed to establish mathematical relationships to identify the optimal parameters and validate the findings through simulation software. Design of Experiments (DOE) is a systematic approach used to examine the correlation between elements that influence a process and to ascertain the resulting impact on that process.

3.4.1 Response Surface Methodology

Response surface methodology (RSM) is primarily employed to model and analyse the impact of multiple independent variables on a dependent variable to optimise the response (Montgomery DC., n.d.). The Central Composite Design (CCD) is employed to determine the statistical significance of the model for the Design of Experiments (DOE). CCD under RSM is achieved through the utilization of a Design Expert. In response surface design analysis, the independent variables (x1, x2, ... xn) influence a dependent variable Y or response. The objective is to maximize the response. The bead shape and mechanical characteristics of bead-on-plate are influenced by several factors, including travel speed (mm/sec), current (A), shielding gas flow rate (L/min), CTWD, stick-out distance, filler wire material, welding torch

angle, type of shielding gases, and diameter of filler wire. The weld geometry response function is represented in equation 3.1, with only two chosen independent variables.

$$Y = \varphi (A, B) \quad (3.1)$$

The variable Y represents the replies, φ is the response function, and A and B are the input variables, such as current and welding speed, respectively. The relationship between answers and independent variables is established by integrating them into the quadratic equation, as depicted in equation 3.2.

$$Y = b_0 + b_1 x_1 + b_2 x_2 + b_{12} x_1 x_2 + b_{11} x_1^2 + b_{22} x_2^2 \quad (3.2)$$

The variable Y represents the responses; bo is the intercept, b1 and b2 represent the coefficients for linear effects, b12 represents the coefficients for interaction effects, and b11 and b22 are the coefficients for quadratic effects. $x1$ and $x2$ represent the coded levels for independent variables such as current (A) and welding speed (B).

Three independent factors, including welding speed, shielding gas flow rate, and current, are selected in CMT WAAM. Alright, equation 3.3 shows the response function that represents the CMT butt joints.

$$Y = \varphi (A, B, C) \quad (3.3)$$

Y stands for the responses, φ is the function that expresses them, and A, B, and C are input variables, such as current, welding speed, and shielding gas flow rate, respectively. The relationship between answers and independent variables is established by integrating them into the quadratic equation, as depicted in equation 3.4.

$$Y = bo + b_1 x_1 + b_2 x_2 + b_3 x_3 + b_{12} x_1 x_2 + b_{23} x_2 x_3 + b_{31} x_3 x_1 + b_{11} x_1^2 + b_{22} x_2^2 + b_{33} x_3^2 \quad (3.4)$$

Y represents the answers, bo is the intercept, and b1, b2, and b3 are the coefficient values for linear effects. The values b12, b23, and b31 reflect the coefficients for the interaction effects. The coefficients b11, b22, and b33 are the values for quadratic effects. The variables $x1$, $x2$,

and $x3$ are the coded levels for independent variables such as current (A), welding speed (B), and shielding gas flow rate (C).

3.4.2 Process parameters

Current (I): Current can be further categorized into peak current and base current, which is also referred to as background current.

- Peak current: It has a significant impact on various metal transfer modes (such as globular, spray, pulse, etc.), penetration, detachment of molten metal droplets, and tapering of an electrode.
- Base current: These factors have a considerable impact on the detachment of molten metal droplets, the temperature of the transferred metal, its fluidity, the width of the weld pool, the wetting of the weld bead, and the size of the droplets.

The current effects are both on the weld bead and the penetration. As the electric current increases, the diameter of the weld bead expands, and the depth of penetration becomes greater. If the current falls, the width of the weld bead grows narrower, and the penetration becomes shallower.

Voltage (V): The utilization of a constant arc voltage power supply is extensive. As the arc length (voltage) decreases slightly, there is a significant rise in the welding current, which automatically raises the pace at which the electrode burns off. The operator manipulates the arc voltage to the appropriate level, and after that, the machine sustains the level across a broad spectrum of amperage configurations.

Welding speed/ Travel speed (S): The nozzle's velocity across the welding plate. It significantly impacts the depth of penetration and the mechanism of metal transfer.

Wire Size: The wire diameter commonly utilized in CMT is 1.2 mm diameter, as indicated by the literature survey. It aids in modulating the extent or amount of deposition. Augmenting the

wire size results in reduced depth of penetration and accelerated deposition rate, whilst reducing the wire size leads to increased depth of penetration and decelerated deposition rate.

Filler wire type: This factor significantly affects the mechanical and metallurgical properties, resulting in a reduction in the thickness of the intermetallic layer (IML) and a minimal presence of intermetallic phases/compounds.

Wire feed rate: The velocity at which the wire is extruded from the wire spool and propelled into the nozzle. It has an impact on the deposit rate and the form of the weld bead. An increase in wire feed rate results in a larger bead and a faster deposit rate, whereas a decrease in wire feed rate leads to a smaller bead and a slower deposit rate (Little, 1973).

Shielding gas flow rate: Insufficient weld shielding occurs when the flow rate is too low, whereas excessively high flow rates might disrupt the stability of the arc. Each of the four metal transfer modes in GMAW has distinct requirements for shielding gas flow. The short-circuiting and pulsed spray modes necessitate a flow rate of around 10 L/min (20 ft3/hr), which is usually appropriate. However, for globular transfer, a flow rate of 15 L/min (30 ft3/hr) is preferred (Liang et al., 2017). The flow rate in the spray transfer variation is approximately 20-25 L/min (40-50 ft3/hr), which is higher than other variations. This is due to the higher heat input, which results in a larger weld pool (Cary, 2004).

Based on the literature survey and early trials, the crucial parameters that significantly affect the weld bead are the current, shielding gas flow rate, and welding speed. In addition to these factors, the selection of filler wire, filler wire size, shielding gas, joint type, and pre-weld cleaning process are also crucial to wettability, spreadability, and joint strength.

3.4.3 The limits of the process parameter and design matrix

A substantial number of preliminary trial runs were conducted to establish the top and lower bounds of CMT process parameters by altering one parameter at a time while keeping the others constant. Prevalent defects such as inadequate penetration, fractures, insufficient fusion, and undercuts were discovered during the trial periods. Each factor's feasible upper and lower limits were selected to ensure that the processed composite was completely devoid of any visible faults. This study utilizes the central composite face-centered design (CCFCD) to assess the importance of the model for the design of experiment (DOE). Central Composite Design (CCD) under Response Surface Methodology (RSM) is implemented utilizing the Design Expert program. This software aids in obtaining optimal outcomes with a high level of accuracy while minimizing the number of trials required. An alpha value of 1 is preferable since it guarantees that the axial point is located within the factorial portion region. The concept is referred to as face-centered design (FCD), and it offers three clearly defined levels for the variables that will be included in the experimental design matrix. The total number of experiments devised by CCD is determined using equation 3.11.

$$N = k^2 + 2k + n \quad (3.11)$$

The variable "N" represents the total number of experiments, "k" represents the number of factors evaluated, and "n" represents the number of replicates. In the bead-on-plate experiment, there are three process parameters that need to be considered. According to the CCFCD method, in the case of CMT weld bead investigations, three criteria require a minimum of 20 experiments according to CCFCD guidelines, which include five replicates. The highest value and lowest value of each factor were encoded as +1 and -1 accordingly.

This study endeavour involved conducting sufficient sample trials to establish the parameter ranges in which successful and error-free welding takes place. The process parameters and their corresponding levels for bead-on-plate for SDSS 2507 and IN 718 are exhibited in Table 3.11

and 3.12, respectively. The design matrices for the bead-on-plate for SDSS 2507 and IN 718 are displayed in Table 3.13 and Table 3.14, respectively.

Table 3.11 Input parameters and their levels for SDSS 2507

Sr. No.	Input parameters (unit)	Notations	Levels		
			-1	0	+1
1.	Current, Ampere	I	160	180	200
2.	Welding speed, mm/s	S	6	7.5	9
3.	Gas flow rate, l/min	G	15	20	25

Table 3.12 Input parameters and their levels for IN 718

Sr. No.	Input parameters (unit)	Symbols	Levels		
			-1	0	+1
1.	Current, Ampere	I	170	190	210
2.	Welding speed, mm/min	V	6	7.5	9
3.	Gas flow rate, l/min	G	15	20	25

3.5 Experimental procedure

3.5.1 Bead on plate

The Fronius CMT-based WAAM setup, consisting of a Remote (FRC-45 Pro) controlled table unit and TPS 400i power source (Fig. 3.12), was used to fabricate the samples. The current, voltage and wire feed rate are interrelated process factors in the CMT welding process due to synergic lines and the optimal design of the CMT machine for a particular filler wire. Based on the trial test and literature study indicate that welding speed is the most significant process parameter, among others. Changes in the gas flow rate affect the cooling rate, thereby

modifying the solidification rate of the sample. This study selected current, welding speed, and shielding gas flow rate as key welding parameters due to their substantial impact on the mechanical properties of the samples seen during experimental trials. Pure argon (99.99%) was utilized as a shielding gas to prevent contamination and oxidation of deposited material. The nozzle was fixed with the movable traveller, which has automatically remote-controlled linear rectilinear motion. As argon gas flow increases the droplet transfer rate, the arc temperature rises and melts additional wire electrodes. Therefore, it is one of this study's variables, and other researchers have reported on similar studies (Dinovitzer et al., 2019). Substrate material was cleaned with acetone, and bead layer deposition occurred by the CMT-based WAAM setup. The nozzle-workpiece gap was set at 15mm.

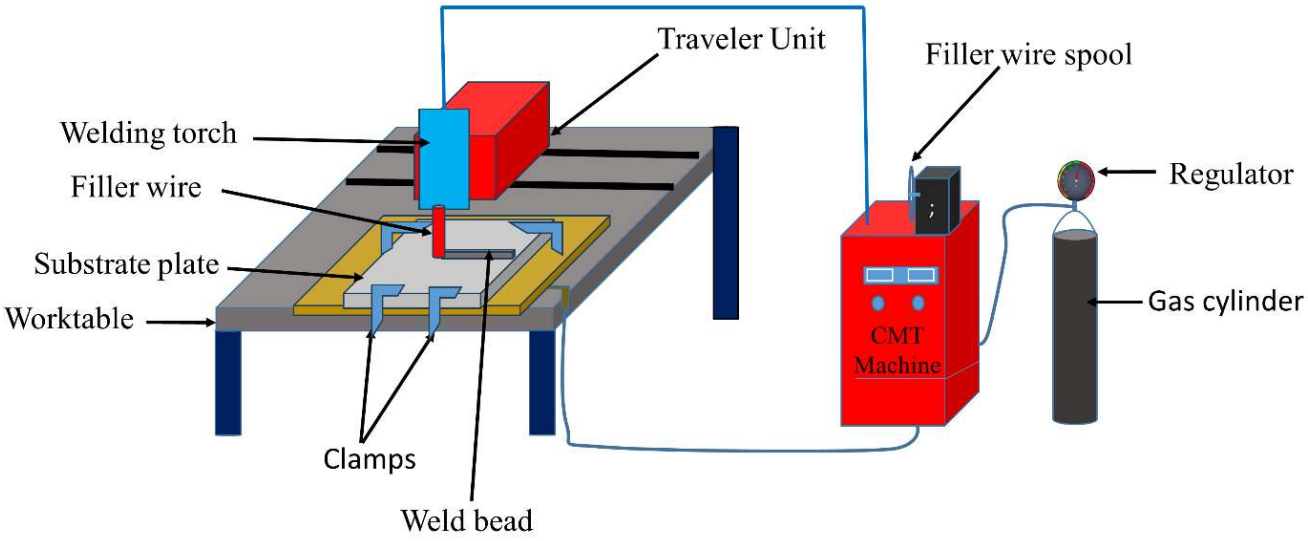

Fig. 3.12 Weld on bead CMT experimental set-up

Table 3.13 Design Matrix and Responses for SDSS 2507

Std	Run	Current	Welding Speed	Gas flow rate	Bead width (BW)	Bead height (BH)	Dilution
		A	mm/s	l/min	mm	mm	%
9	1	170	7.5	20	8.48	2.65	24.04
18	2	190	7.5	20	9.48	2.64	28.03
2	3	210	6	15	11.33	2.64	27.81
8	4	210	9	25	9	2.57	24.67
7	5	170	9	25	7.27	2.51	27.24
6	6	210	6	25	11.67	3.03	26.31
3	7	170	9	15	7.71	2.22	29.72
5	8	170	6	25	7.59	3.09	21.67
19	9	190	7.5	20	9.53	2.64	27.64
4	10	210	9	15	8.4	2.19	28.14
17	11	190	7.5	20	9.43	2.65	27.64
15	12	190	7.5	20	9.52	2.64	27.7
11	13	190	6	20	8.94	2.9	27.08
16	14	190	7.5	20	9.46	2.63	27.66
10	15	210	7.5	20	10.82	2.65	25.66
12	16	190	9	20	7.41	2.38	29.96
20	17	190	7.5	20	9.52	2.64	27.64
13	18	190	7.5	15	10.23	2.47	29.52
1	19	170	6	15	8.51	2.76	22.12
14	20	190	7.5	25	10.13	2.8	26.68

Table 3.14 Design Matrix and Responses for IN 718

Std	Run	Current	Welding speed	Gas flow rate	Bead width (BW)	Bead height (BH)	Dilution
		A	mm/s	l/min	mm	mm	%
13	1	180	7.5	15	6.28	3.05	29.48
1	2	160	6	15	5.85	2.93	32.71
2	3	200	6	15	6.34	2.9	30.57
8	4	200	9	25	5.74	2.87	34.57
6	5	200	6	25	6.21	3.02	35.4
11	6	180	6	20	6.24	2.99	32.2
14	7	180	7.5	25	6.1	2.9	30.87
7	8	160	9	25	6.05	2.62	32.55
5	9	160	6	25	6.42	3.12	34
9	10	160	7.5	20	6.15	2.96	34.22
19	11	180	7.5	20	6.2	3.02	31.67
10	12	200	7.5	20	6.2	3.07	34.11
16	13	180	7.5	20	6.19	3.02	31.72
20	14	180	7.5	20	6.22	3.02	31.59
4	15	200	9	15	6.68	3.57	32.8
15	16	180	7.5	20	6.19	3.02	31.62
3	17	160	9	15	6.27	3.18	34.45
17	18	180	7.5	20	6.19	3.02	31.67
12	19	180	9	20	6.18	3.04	32.59
18	20	180	7.5	20	6.19	2.98	31.51

3.5.2 CMT WAAM wall

The WAAM system was installed on a Remote (FRC-45 Pro) controlled table unit and a TPS 400i power source to fabricate the samples, as shown in Fig. 3.13. The material SDSS 2507 and IN 718 wire is fed into the middle of an electric arc during printing. The continuous line-by-line and layer-by-layer deposition produced a 60-layer dissimilar alloy block of 150mm length and 100 mm height that is crack-free. Table 3.15 summarises the specific optimum process parameters. A shielding gas composed of 99.99% pure argon was employed for welding SDSS 2507 and IN 718, as it is compatible with these materials. A nozzle-to-workpiece spacing of 15mm was selected. The CMT-based WAAM system deposited bead layers after acetone cleaning. The interpass dwell period was 120 seconds between layers.

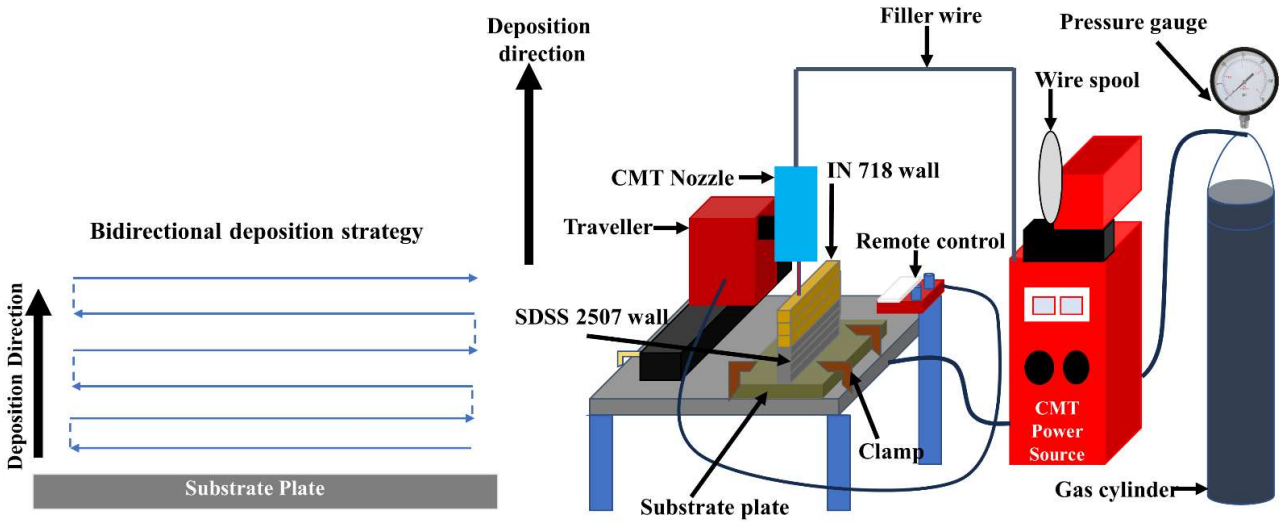

Fig 3.13 CMT WAAM experimental setup

Table 3.15 CMT WAAM deposition parameters used in this experiment

WAAM Parameters	Value for SDSS 2507	Value for IN 718
Current (I)	210	190
Travel speed (mm/s)	6.91	8.94
Gas flow rate (l/min)	25	15
Nozzle tip distance (mm)	15	15

3.5.3 Ultrasonic vibration-assisted CMT WAAM wall

The WAAM system was set up on a Remote (FRC-45 Pro) operated table unit with an ultrasonic vibration unit and a TPS 400i power source to create the samples, as depicted in Fig. 3.14. The ultrasonic vibration unit generates vibrations during the WAAM process. High-energy ultrasound control systems typically include a transducer, power supply, and ultrasonic horn. Extremely powerful ultrasonic waves are produced by the transducer. Its frequency is 30 kHz. The power supply controls the input energy and electrical signals. The ultrasonic horn amplifies high-power ultrasound and insulates heat carried through the substrate, preventing transducer damage.

The material SDSS 2507 and IN 718 wire is introduced into the central area of an electric arc during the printing process. The meticulous process of depositing the material, line by line and layer by layer, resulted in a flawless dissimilar alloy block with or without ultrasonic vibration. This block measures 150mm in length and 100mm in height, consisting of an impressive 60 layers. Table 3.16 lists optimal process parameters. Due to its compatibility with SDSS 2507 and IN 718, 99.99% pure argon was used for welding. We chose 15mm nozzle-to-workpiece spacing. The CMT-based WAAM technology applied layers of beads following a cleaning process using acetone. The time interval between layers, known as the interpass dwell duration,

was set to 120 seconds. Fig. 3.15 shows a schematic diagram of samples and extracted samples for characterisation.

Table 3.16 Ultrasonic-assisted CMT WAAM deposition parameters used in this experiment

WAAM Parameters	Value for SDSS 2507	Value for IN 718
Current (I)	210	190
Travel speed (mm/s)	6.91	8.94
Gas flow rate (l/min)	25	15
Nozzle tip distance (mm)	15	15

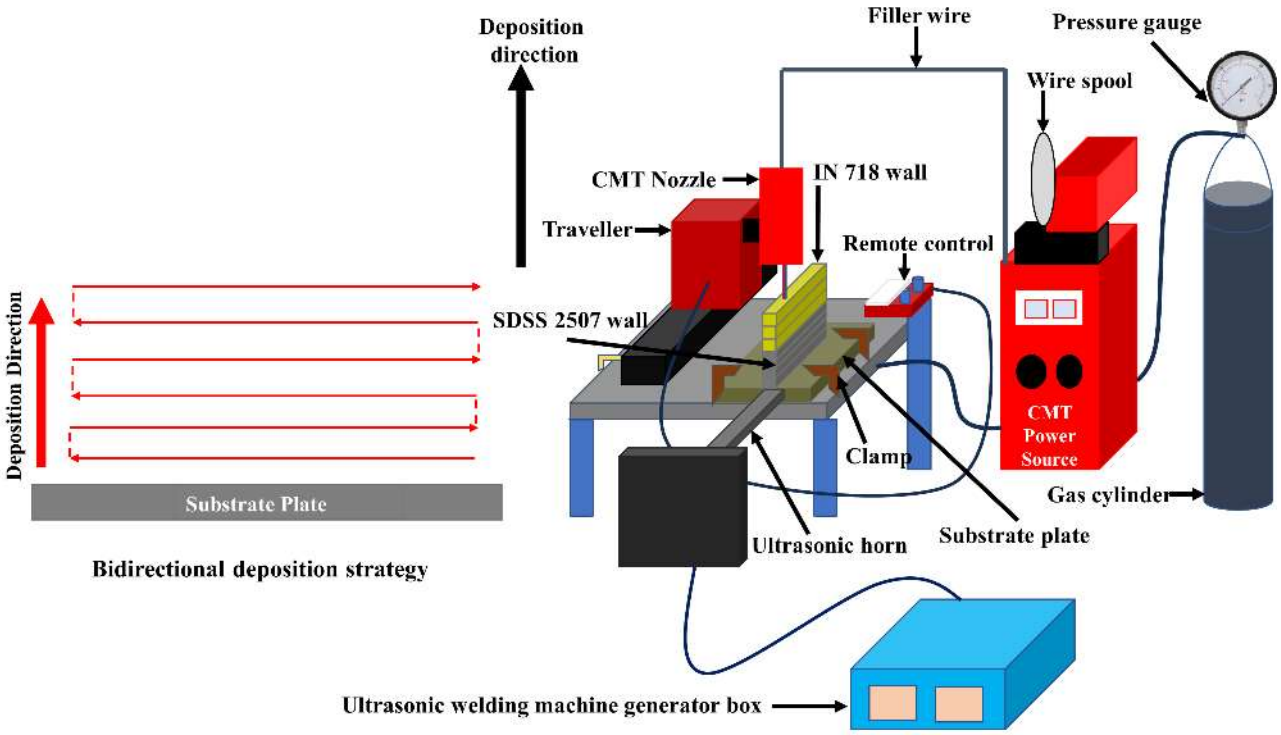

Fig 3.14 Schematic Ultrasonic Assisted CMT WAAM experimental setup

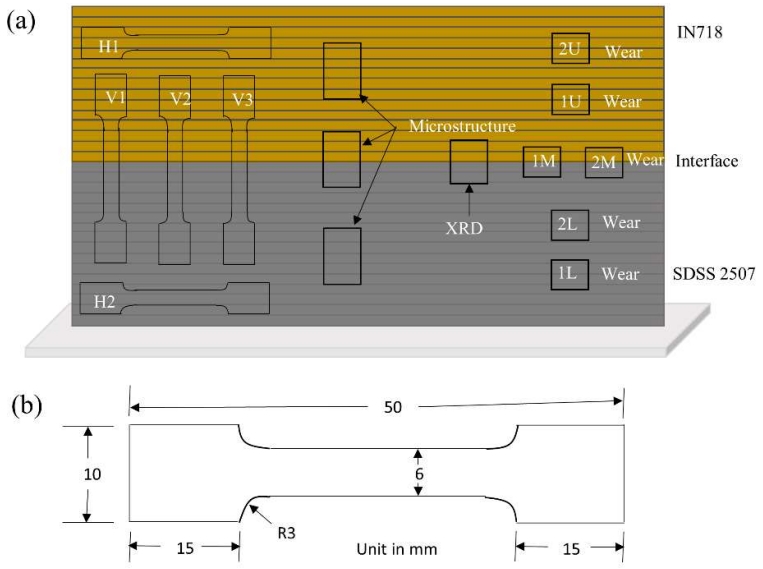

Fig. 3.15 Schematic diagram of (a) Extracted samples (b) Tensile test specimen

3.6 Summary

This chapter offers a thorough overview of the materials and methodology employed in the study. The process starts by carefully choosing the materials, such as stainless steel 304 as the base and IN 718 and SDSS 2507 as the fillers. Their chemical compositions and mechanical properties are emphasized. The chapter provides a comprehensive overview of the sample preparation process for analysing macrostructure, microstructure, microhardness, tensile strength, and tribological properties. The experimental machines' technical specifications, such as the CMT machine, microhardness tester, tensile testing machine, optical microscope, and FESEM, are also provided. In this section, we explore the optimization of the CMT process parameters for welding SDSS 2507 and IN 718 using the DOE and RSM. The study investigates the impact of various welding parameters, including current, welding speed, and shielding gas flow rate, on the shape of the bead and its mechanical properties. A statistical model was developed using CCD to optimize these parameters. The study also covers the implementation of UV-assisted CMT WAAM, emphasizing its setup and process parameters.

CHAPTER 4

RESULTS AND DISCUSSIONS ON OPTIMIZATION OF PROCESS PARAMETERS

4.1 Optimisation of process parameters of SDSS 2507

The process parameters in WAAM are crucial for improving the quality, mechanical properties, and efficiency of the components being produced. It is vital to maintain precise control and make careful adjustments to key parameters like wire feed rate, arc current, travel speed, and layer thickness. Various optimization techniques, such as Design of Experiments (DoE), response surface methodology (RSM), and machine learning algorithms, are utilized to identify the most optimal settings. Optimizing parameters can result in a better surface finish, lower residual stresses, and fewer defects like porosity and cracking. In this study, the RSM technique is adopted to find the optimum process parameters of the weld bead.

4.2 Mathematical modelling

A cross-sectional sample was taken from a stable site of each weld bead, and the macro images were taken with a stereo-zoom microscope. The graphic diagram of weld-on bead geometry is given in Fig. 4.1. The input process parameters and their responses are shown in Table 3.13. The evaluation of dilution (%) is given in Equation 4.1 (Koli et al., 2020).

$$\text{Dilution (\%)} = \frac{A_P}{A_P + A_R} \quad \text{.....(4.1)}$$

Where A_P and A_R demonstrate an area of penetration and reinforcement, respectively. Image J software measured the width (BW), height (BH), and dilution of the deposited beads. For every experimental result, an average of three samples are taken.

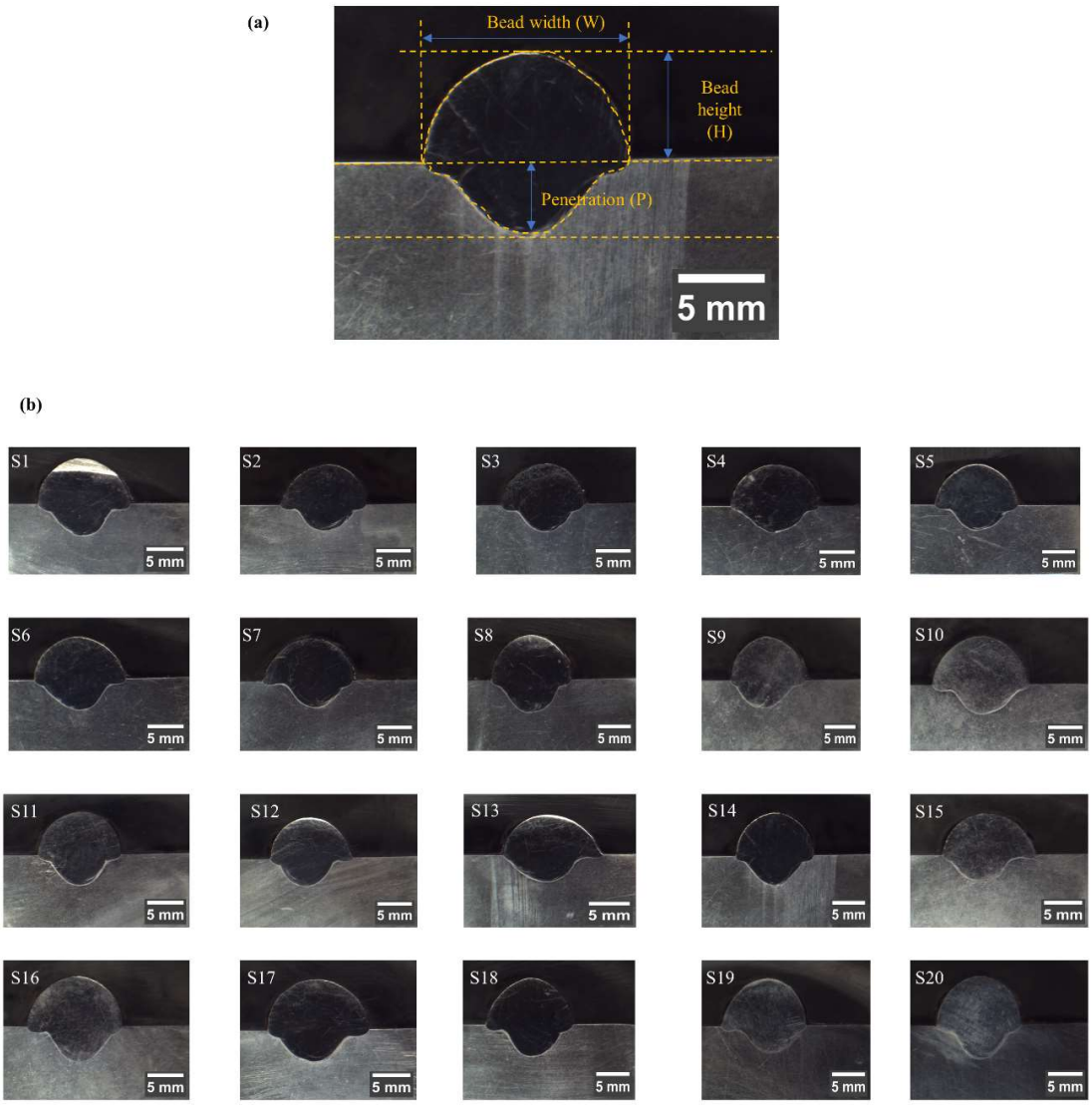

Fig. 4.1 Macro-images of weld bead

4.2.1 Bead Geometry Mathematical Modelling

The predictive mathematical models for BW, BH, and Dilution were developed in this study using a second-order regression equation (Shah et al., 2022). Equations 4.2, 4.3, and 4.4 illustrate the developed RSM models. The Design Expert 13 software was deployed to generate these models, which are dependent on the process factors of current (I), welding speed (S), and gas flow rate (G).

BW = 2.48901 + 0.00842619 * I - 0.00303398 * S - 0.0180091 * G - 0.00509323 * IS - 0.0356826 * IG - 0.040276 * SG - 0.00360003 * I^2 + 0.00343022 * S^2 - 0.000644357 (4.2)

BH = 1.73408 + 0.0176008 * I + 0.00810168 * S - 0.0313933 * G + 0.0273723 * IS - 0.00630934 * IG - 0.0561819 * SG + 0.00494747 * I^2 + 0.00500478 * S^2 - 0.00667405 * G^2 (4.3)

Dilution = 5.6248 - 0.00487416 * I + 0.0186666 * S + 0.0647337 * G + 0.0129368 * IS + 0.0782173 * IG - 0.0680145 * SG + 0.219168 * I^2 + 0.0657211 * S^2 - 0.1331 * G^2 (4.4)

ANOVA was used to evaluate the adequacy of the developed model with 95% confidence and 5% significance (Kumar et al., 2023). The ANOVA results for the BW, BH, and Dilution regression models are depicted in Table 4.1, Table 4.2, and Table 4.3, respectively. In the developed models, p-values below 0.05 indicate significant terms and above 0.05 indicate insignificant ones (Montgomery and Wiley, 2017; Surani et al., 2023). ANOVA shows that for BW and BH, terms A, B, C, AB, AC, and BC are significant, A^2, B^2, and C^2 are insignificant, and Dilution has all terms significant.

Table 4.1 ANOVA test result for weld bead width (BW)

Source	Sum of Squares	df	Mean Square	F-value	p-value	
Model	0.0275	9	0.0031	363.32	< 0.0001	significant
A-Current	0.0007	1	0.0007	84.52	< 0.0001	
B-Welding speed	0.0001	1	0.0001	10.96	0.0079	
C-Gas flow rate	0.0032	1	0.0032	386.09	< 0.0001	
AB	0.0002	1	0.0002	24.70	0.0006	
AC	0.0102	1	0.0102	1212.57	< 0.0001	
BC	0.0130	1	0.0130	1544.85	< 0.0001	
A^2	0.0000	1	0.0000	4.24	0.0664	
B^2	0.0000	1	0.0000	3.85	0.0781	
C^2	1.142E-06	1	1.142E-06	0.1359	0.7201	
Residual	0.0001	10	8.400E-06			
Lack of Fit	0.0001	5	0.0000	1.84	0.2592	not significant
Pure Error	0.0000	5	5.910E-06			
Cor Total	0.0276	19				

Table 4.2 ANOVA test result for Weld bead height (BH)

Source	Sum of Squares	df	Mean Square	F-value	p-value	
Model	0.0454	9	0.0050	115.52	< 0.0001	significant
A-Current	0.0031	1	0.0031	70.95	< 0.0001	
B-Welding speed	0.0007	1	0.0007	15.03	0.0031	
C-Gas flow rate	0.0099	1	0.0099	225.72	< 0.0001	
AB	0.0060	1	0.0060	137.28	< 0.0001	
AC	0.0003	1	0.0003	7.29	0.0223	
BC	0.0253	1	0.0253	578.32	< 0.0001	
A^2	0.0001	1	0.0001	1.54	0.2427	
B^2	0.0001	1	0.0001	1.58	0.2377	
C^2	0.0001	1	0.0001	2.81	0.1249	
Residual	0.0004	10	0.0000			
Lack of Fit	0.0003	5	0.0001	2.93	0.1316	not significant
Pure Error	0.0001	5	0.0000			
Cor Total	0.0458	19				

Table 4.3 ANOVA test result for Dilution

Source	Sum of Squares	df	Mean Square	F-value	p-value	
Model	0.3422	9	0.0380	1541.56	< 0.0001	significant
A-Current	0.0002	1	0.0002	9.63	0.0112	
B-Welding speed	0.0035	1	0.0035	141.28	< 0.0001	
C-Gas flow rate	0.0419	1	0.0419	1699.09	< 0.0001	
AB	0.0013	1	0.0013	54.29	< 0.0001	
AC	0.0489	1	0.0489	1984.50	< 0.0001	
BC	0.0370	1	0.0370	1500.54	< 0.0001	
A^2	0.1321	1	0.1321	5356.01	< 0.0001	
B^2	0.0119	1	0.0119	481.61	< 0.0001	
C^2	0.0487	1	0.0487	1975.36	< 0.0001	
Residual	0.0002	10	0.0000			
Lack of Fit	0.0000	5	5.989E-06	0.1382	0.9756	not significant
Pure Error	0.0002	5	0.0000			
Cor Total	0.3424	19				

Table 4.4 Coefficient of determination values

Responses	R^2	Adjusted R^2	Predicted R^2
BW	0.9970	0.9942	0.9827
BH	0.9905	0.9819	0.9419
Dilution	0.9993	0.9986	0.9983

The accuracy of BH, BW, and Dilution was analysed by using the determination coefficients, namely "R^2," "Adj. R^2," and "pred. R^2. The coefficients of determination (R^2) for BW, BH, and Dilution in the developed model were calculated as 0.9970, 0.9905, and 0.9993, respectively. These values, close to the ideal value of 1, indicate a strong correlation between the predicted and experimental values and show a good model fit, as exhibited in Table 4.4 (Oza et al., 2019). The ANOVA models for BW, BW, and Dilution have "Pred. R^2" values of 0.9827, 0.9419, and 0.9983, respectively. These values align consistently with the corresponding "Adj. R^2" values. Based on the results attained, it can be concluded that the BW, BH, and Dilution models have been thoroughly verified throughout the entire design space. As a result, these models are deemed suitable for accurately predicting the optimized processing parameters (Kumar et al., 2020; Oza et al., 2020).

4.2.2 Effect of input parameters on response variables

Fig. 4.2 (a) and (b) show that welding current and gas flow rate significantly affect weld bead size. An increase in current results in an increase in the weld bead size, as it leads to higher heat input. Consequently, the deposition rate rises alongside the heat input when the current increases (Ali et al., 2019b; Le et al., 2022a). Fig. 4.2 (c) exhibits the impact of input parameters on dilution. It depicts that current and welding speed are the most influencing factors. It

indicated that dilution increases with the welding current. As the welding current rises, it leads to an escalation in the heat flow rate, resulting in an augmentation of both the depth and area of penetration (Jindal et al., 2014a; Le et al., 2022a). Fig. 4.3 illustrates a scatter plot demonstrating the three experimental versus predicted value responses. The diagonal line in the plot represents the point where the observed and predicted values align perfectly. Fig. 4.3 (a-c) demonstrates that the predicted values perfectly match the diagonal line. It indicates the significance and good fit of the created model. Furthermore, this showcases the robustness of the constructed model in accurately predicting the data.

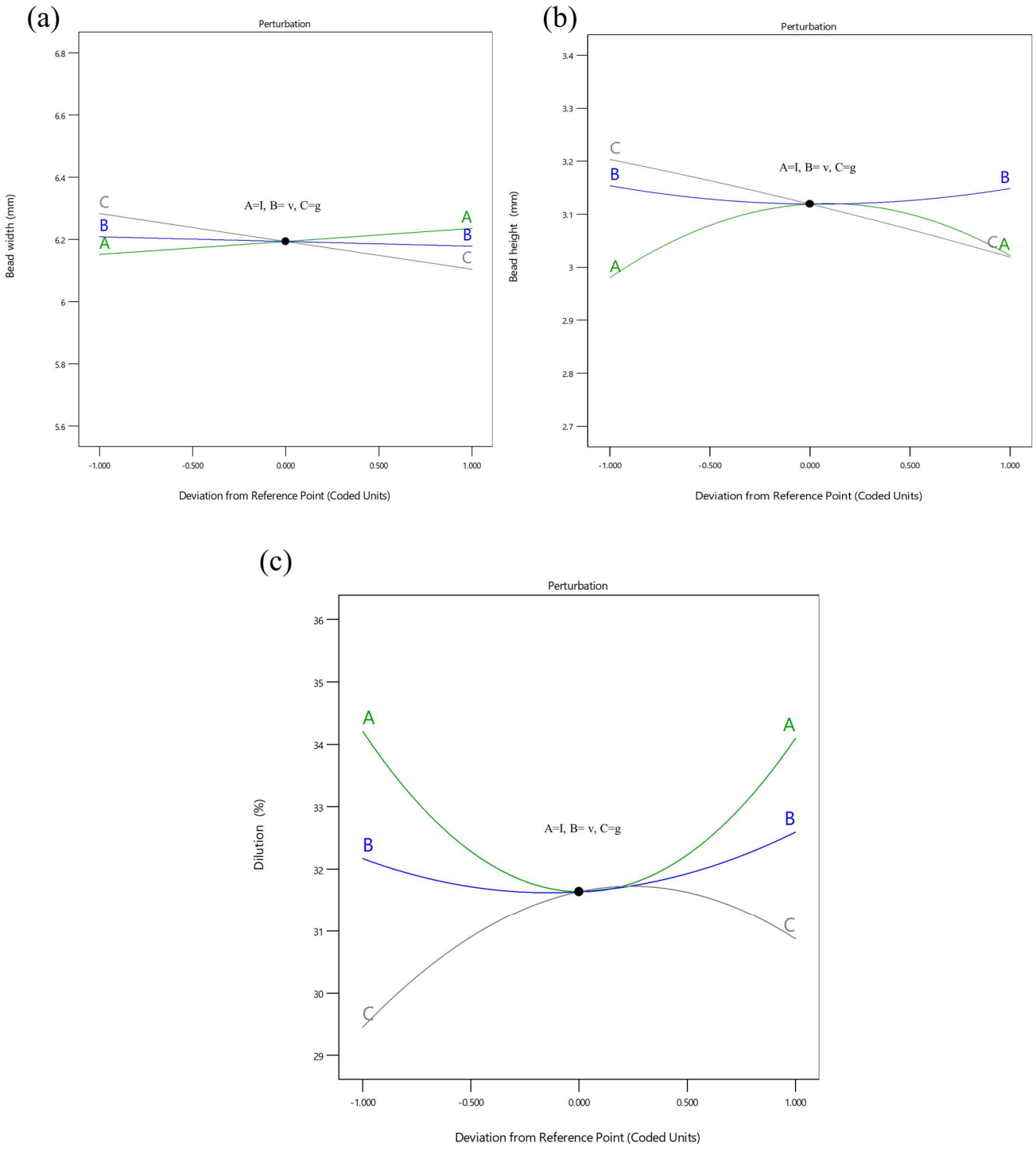

Fig. 4.2 Effect of input parameters on output responses (a) Weld bead width (b) Weld bead height (c) Dilution (%)

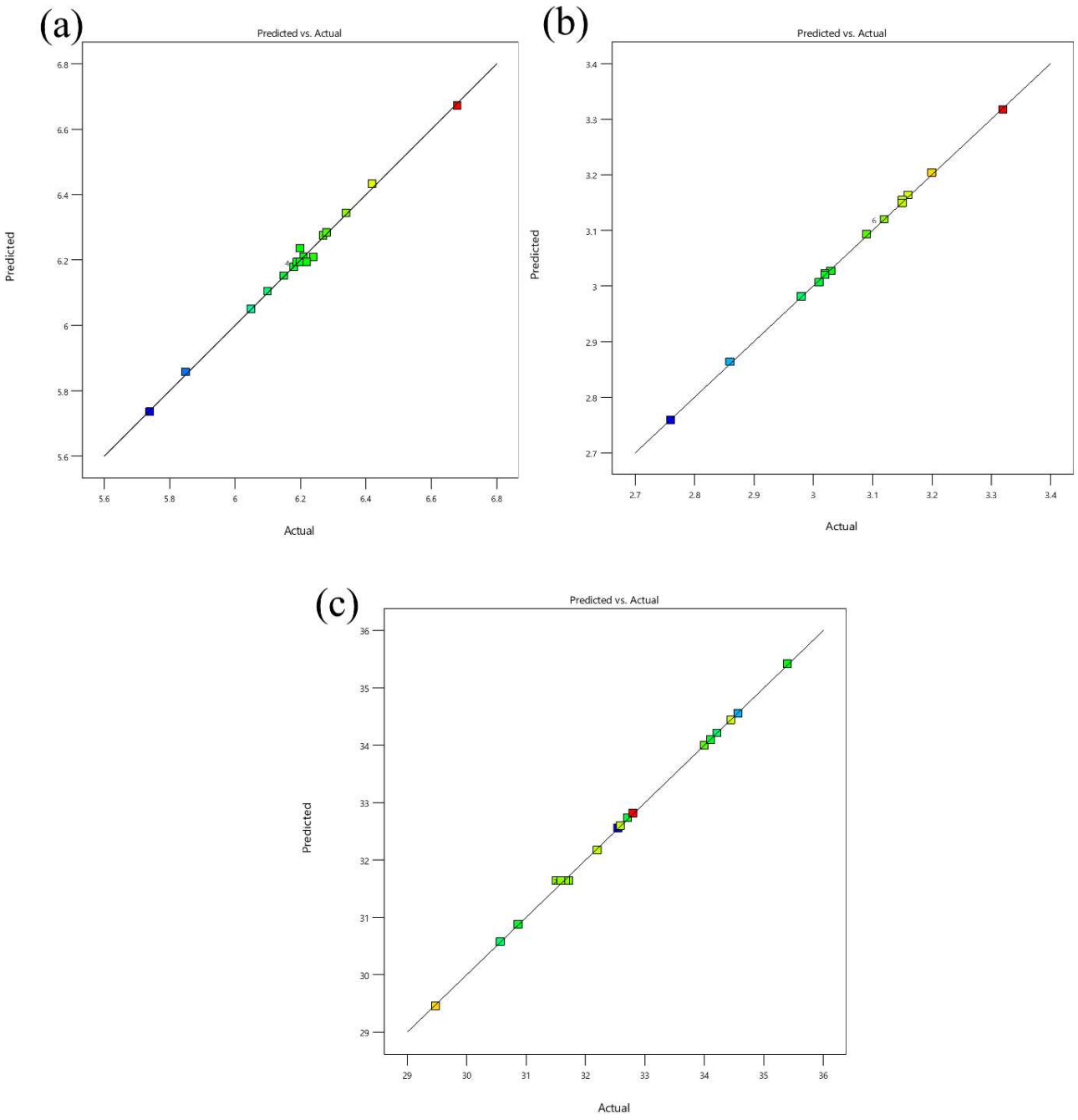

Fig. 4.3 Exhibits the predicted v/s actual data values for (a) Bead width, (b) Bead height, (c) Dilution (%)

4.2.3 Conformity test

Experiments are undertaken to validate the empirical correlation between bead width, bead height, and dilution, as expressed by equations 4.2,4.3 and 4.4. Three experiments of weld on

bead were conducted using the same experimental setup, with the process parameters set at their optimal process values, to validate the model. The validity test results are exhibited in Table 4.5 The results closely match the predicted values, revealing that the designed model is accurate.

Table 4.5 Validity of regression model test results

S.no.	CMT process parameters			Bead width (BW)		Error (%)	Bead height (BH)		Error (%)	Dilution (%)		Error (%)
	I (A)	S (mm/s)	G (l/min)	Actual value	Predicted value		Actual value	Predicted value		Actual value	Predicted value	
1.	190.46	8.94	15	6.67	6.57	1.534	3.4	3.43	-0.91	31.70	31.30	1.30
2.	190.46	8.94	15	6.39	6.57	-2.73	3.45	3.43	0.60	30.59	31.30	-2.32
3.	190.46	8.94	15	6.74	6.50	2.61	3.52	3.43	2.71	31.39	31.30	0.29

* Error, % =[Actual value-predicated value)/predicated value]*100

4.2.4 Process parameter optimization

Accurately predicting the first layer is critical to ensure the manufacturability of the entire 3D metal parts. To achieve optimal conditions for WAAM, it is desirable to minimize Dilution while maximizing BW and BH (Sarathchandra et al., 2020b). To ensure manufacturing stability, it is important to achieve a high deposition efficiency and produce taller walls with fewer layers (Corradi et al., 2020). The optimum welding current, speed, and gas flow rate parameters are 190.46 A, 8.94 mm/min, and 15 l/min, respectively. The optimum response values for BW, BH, and Dilution parameters are 6.57 mm, 3.43 mm, and 31.3 %, respectively, as shown in Fig. 4.4. The desirability of the predicted response is 0.809.

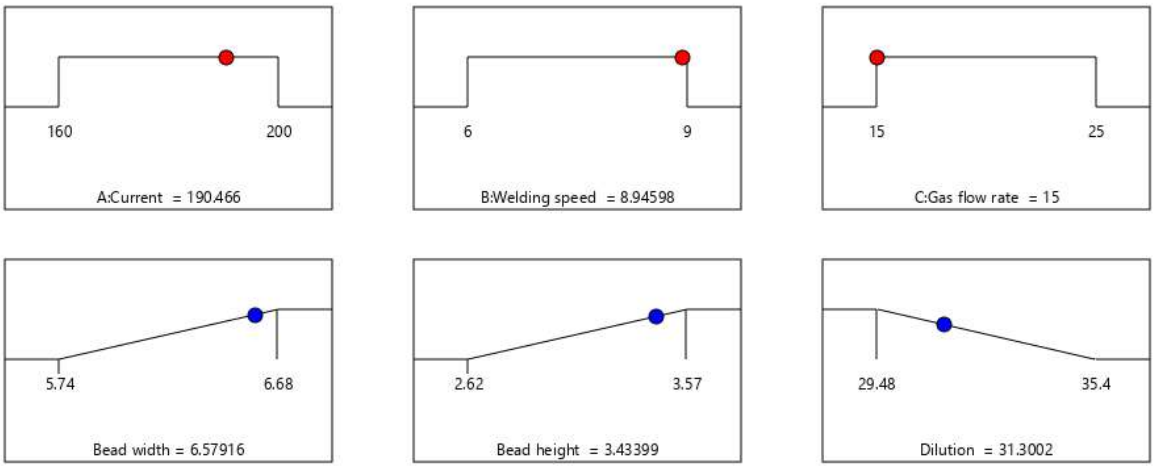

Fig. 4.4 Numerical optimization ramps of the input parameter and response variable

This multi-objective optimization problem was solved using the Design-expert 13 optimization module software. The three nearly identical single-weld beads were produced using optimized process parameters. All the weld beads exhibit a continuous, smooth appearance without notable defects. Using the optimal process parameters, single-bead multi-layered SDSS 2507 walled samples were produced (Fig. 4.5). The Analysis shows that the multi-layered wall exhibits a favourable shape, along with consistent height and width.

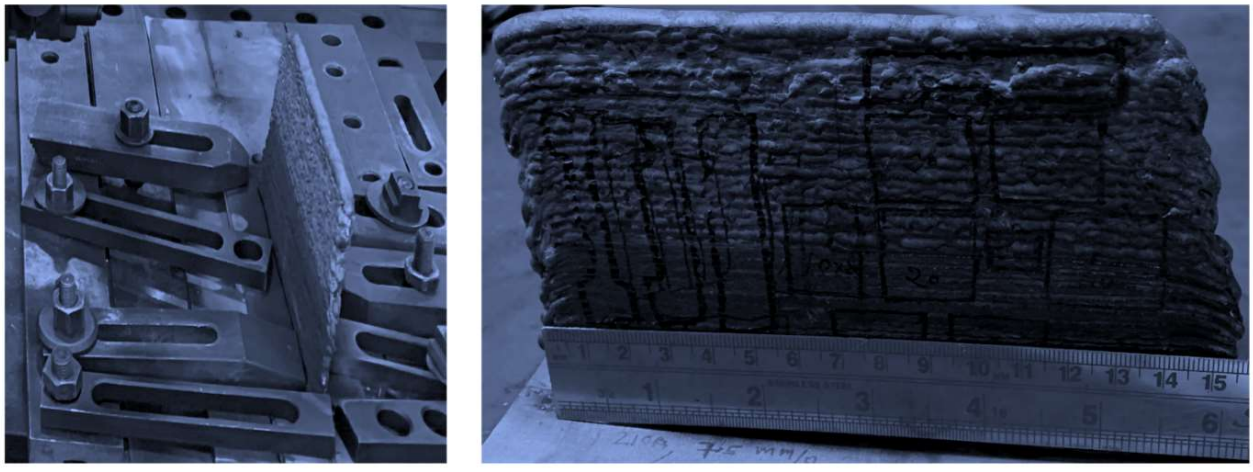

Fig. 4.5 CMT WAAM wall of SDSS 2507 side view and front view

4.3 Microstructure characterization of SDSS 2507 WAAM samples at optimum parameters

The cross-section of the middle WAAM sample is extracted for microstructural studies. The optical and SEM images of the WAAM sample are shown in Fig. 4.6. The grain size becomes fine grains from coarse grains due to complex cyclic thermal history during remelting of the adjacent layers along the building direction, as seen in Fig. 4.6 (a) (Y. Zhang et al., 2021b). The cooling rate affects the formation of γ-austenite in super duplex steel (Zhang et al., 2020). In Fig. 4.6 (b), the dark region demonstrates the ferrite, and the white region is shown by austenite. Further, austenite morphologies are classified into three types in as-deposited walls, namely Widmanstädter austenite (WA), Intragranular austenite (IGA), and grain boundary austenite (GBA). GBA predominantly existed along ferrite grain boundaries and exhibited a straight orientation in the Z direction. WA displayed a side-plate morphology and occupied a significant portion of the columnar ferrite. IGA was smaller than GBA and WA and dispersed within the ferrite grains (A Hosseini et al., 2019; Lervåg et al., 2020). Materials with smaller grain sizes exhibit better resistance to intergranular fracture due to the compactness of grain boundaries. Consequently, an extremely fine-grained structure provides exceptional strength and notable microhardness characteristics.

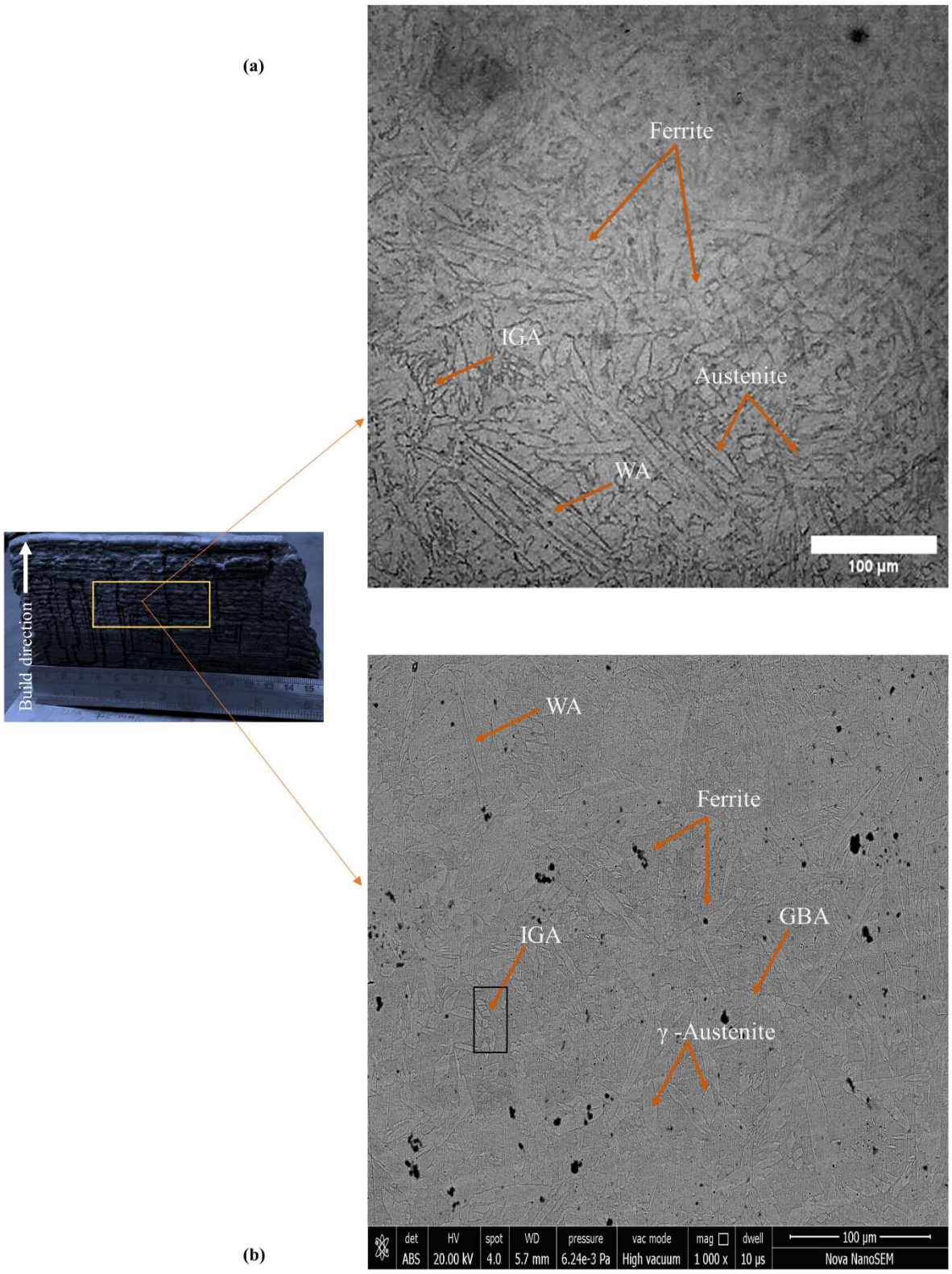

Fig. 4.6 Microstructure of SDSS 2507 samples (a) Optical microscope image (b) SEM image of the middle section

4.4 Mechanical properties of SDSS 2507 WAAM samples

The microhardness of the deposited wall was measured using a Vickers microhardness tester (DRAMIN-40 STRUERS) as per ASTM E34 standard with a load of 500gf and dwell time of 10 seconds. The microhardness variations of the WAAM sample taken at different regions are shown in Fig. 4.7 The average of five locations within each zone is taken for microhardness value.

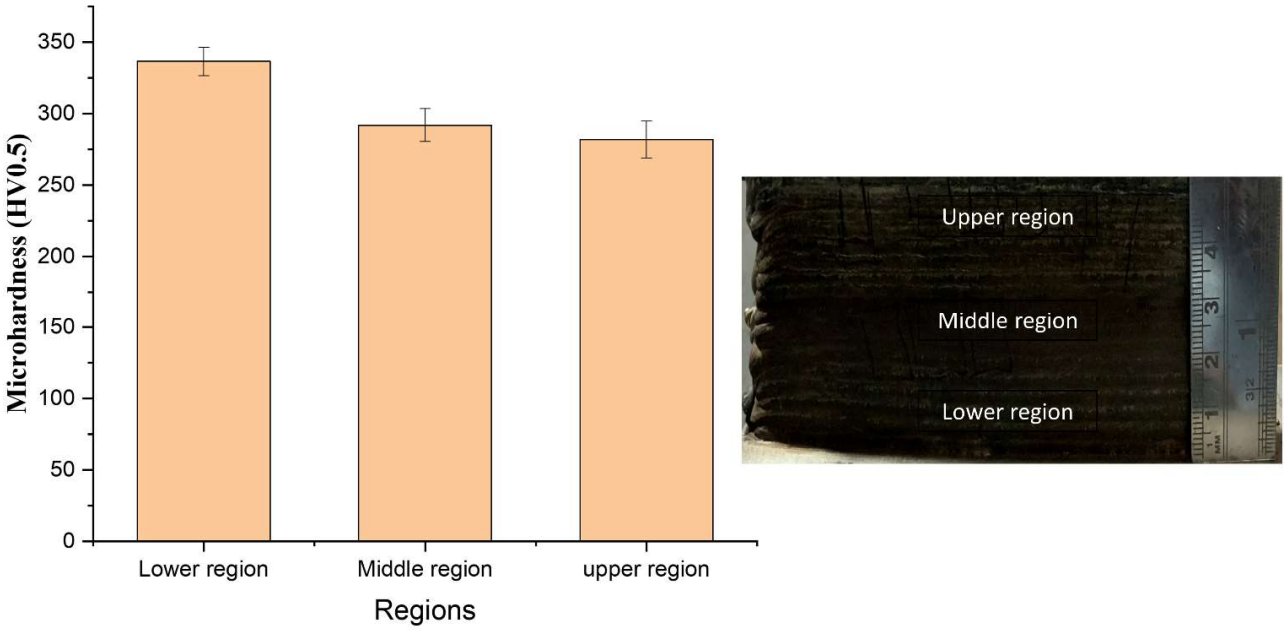

Fig. 4.7 Microhardness variations of SDSS 2507 along the deposition direction of the lower, middle, and upper region of the deposited wall

The mean microhardness measurements for the upper, middle, and lower regions are 289 ± 5.20, 303 ± 2.36, and 332 ± 2.67 HV0.5. However, the uppermost layer had an average hardness of 325.5 HV. Compared to the lower zone, the intermediate and upper zones of the SDSS 2507 deposited wall had a lower hardness. The variations in hardness can be attributed to differences in microstructural characteristics and the complex cyclic thermal history. During solidification and cooling at room temperature, the bottoms of samples near the substrate could dissipate heat through the substrate. The zones exhibiting finer grains in the microstructure of materials are

expected to demonstrate higher hardness (Fuse et al., 2022; Gao et al., 2019a; Sharma et al., 2023). The presence of larger grain sizes inside the microstructure impedes the movement of material dislocations, decreasing hardness within the central zone (Prado-Cerqueira et al., 2018). Therefore, the lower region of the wall demonstrates the highest average microhardness. The middle zone has a coarser microstructure than the lower zone, making it softer. This trend in microhardness variation is also comparable to that observed in previously published studies (Wu et al., 2019).In addition to this, due to the uneven distribution of ferrite and austenite phases, the microhardness value decreases slightly from the bottom region to the intermediate region of the deposited wall.

4.5 Optimisation of process parameters of IN 718

A cross-sectional sample of each weld bead was obtained from a stable site (Fig. 4.8a), prepared by grinding and polishing, and then measured to determine its width, height, and Dilution. From the cross-sectional pictures (Fig. 4.8c), the deposited beads' width (BW) and height (BH) were measured by an inverted metallurgical optical microscope. Dilution was calculated using Equation 4.5 (Le et al., 2022b).

$$\text{Dilution (\%)} = \frac{A_P}{A_P + A_R} \quad \ldots\ldots\ldots\ldots\ldots\ldots\ldots\ldots\ldots\ldots \quad (4.5)$$

Where A_R and A_P represent an area of reinforcement and penetration, respectively. The A_R and A_P for each weld bead were calculated using the ImageJ software.

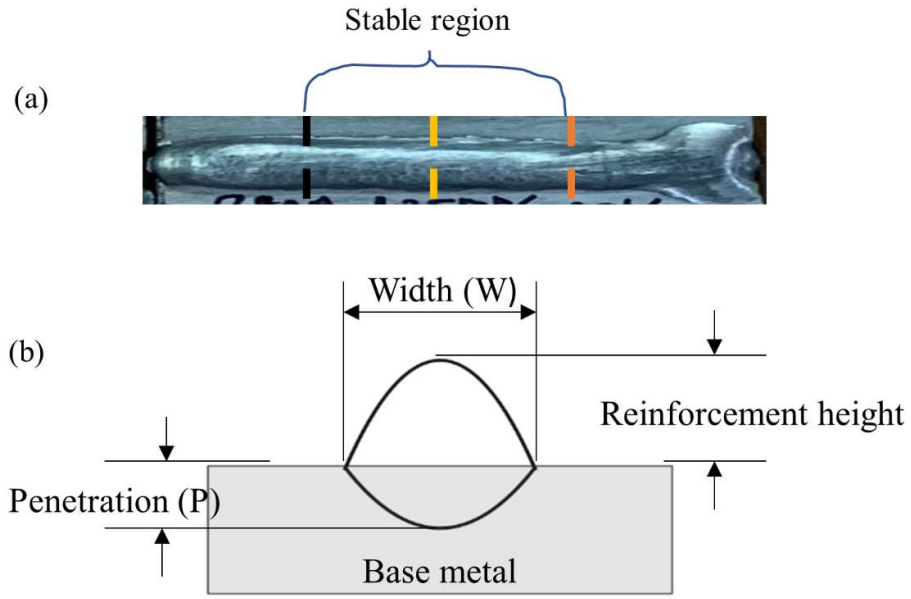

(c) Cross-section

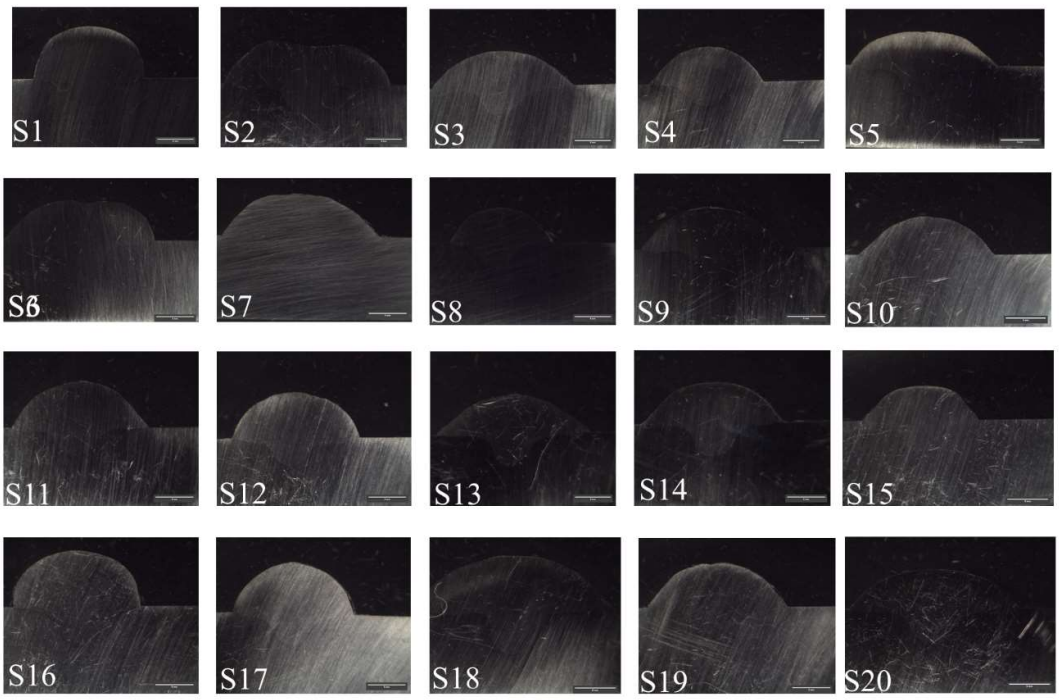

Fig. 4.8 (a) Single weld bead (b) Schematic diagram of weld bead geometry (c) Cross-section image of all single weld bead

4.5.1 Developing the predictive mathematical models

The second-order mathematical regression equation created BW, BH, and Dilution predictive models. Experimental data from weld beads was used to build a mathematical model of BW, BH, and dilution RSM in Design Expert 13. The bead geometry parameters, BW, BH, and Dilution, are represented by equations 4.6, 4.7, and 4.8 as the second-degree.

$$BW = 3.08174 + 0.191258 * I - 0.135092 * V - 0.0106405 * G - 0.0855832 * IV + 0.0493058 * IG + 0.0166741 * VG + 0.0172177 * I^2 - 0.227435 * V^2 + 0.107109 * G^2 \quad (4.6)$$

$$BH = 1.62566 - 0.00449447 * I - 0.0787624 * V + 0.0531682 * G + 0.0077987 * IV + 0.00603658 * IG + 0.000648995 * VG + 0.000954258 * I^2 - 0.00409605 * V^2 - 0.00445609 * G^2 \quad (4.7)$$

$$Dilution = 5.26549 + 0.0807865 * I + 0.145099 * V - 0.103047 * G - 0.180468 * IV - 0.02519 * IG - 0.0472447 * VG - 0.282206 * I^2 + 0.0721877 * V^2 + 0.0327288 * G^2 \quad (4.8)$$

ANOVA was used to assess adequacy at 95% confidence and 5% significance level. Tables 4.6, 4.7 and 4.8 show the ANOVA results of the BW, BH, and Dilution regression models, respectively. Degree of freedom adjusted sum of squares and adjusted mean square are abbreviated DF, Adj SS, and Adj MS. P-values below 0.05 indicated significant terms in constructed models, whereas those above 0.05 indicated insignificant terms. The accuracy of BH, BW, and Dilution was measured by the determination coefficients, i.e., "R^2", "Adj. R^2", and "pred. R^2" (Montgomery and Wiley, 2017).

Table 4.6 ANOVA for Bead Width

Source	Sum of Squares	df	Mean Square	F-value	p-value	
Model	0.7886	9	0.0876	2230.25	< 0.0001	significant
I-Current	0.3658	1	0.3658	9310.86	< 0.0001	
V-Welding Speed	0.1825	1	0.1825	4645.27	< 0.0001	
G-Gas flow rate	0.0011	1	0.0011	28.82	0.0003	
IV	0.0586	1	0.0586	1491.47	< 0.0001	
IG	0.0194	1	0.0194	495.03	< 0.0001	
VG	0.0022	1	0.0022	56.61	< 0.0001	
I²	0.0008	1	0.0008	20.75	0.0010	
V²	0.1422	1	0.1422	3620.73	< 0.0001	
G²	0.0315	1	0.0315	803.03	< 0.0001	
Residual	0.0004	10	0.0000			
Lack of Fit	0.0002	5	0.0000	0.8626	0.5624	not significant
Pure Error	0.0002	5	0.0000			
Cor Total	0.7890	19				

Table 4.7 ANOVA for Bead Height

Source	Sum of Squares	df	Mean Square	F-value	p-value	
Model	0.0915	9	0.0102	894.66	< 0.0001	significant
I-Current	0.0002	1	0.0002	17.77	0.0018	
V-Welding Speed	0.0620	1	0.0620	5456.95	< 0.0001	
G-Gas flow rate	0.0283	1	0.0283	2486.66	< 0.0001	
IV	0.0005	1	0.0005	42.80	< 0.0001	
IG	0.0003	1	0.0003	25.64	0.0005	
VG	3.370E-06	1	3.370E-06	0.2964	0.5981	
I²	2.504E-06	1	2.504E-06	0.2203	0.6489	
V²	0.0000	1	0.0000	4.06	0.0716	
G²	0.0001	1	0.0001	4.80	0.0532	
Residual	0.0001	10	0.0000			
Lack of Fit	0.0001	5	0.0000	5.00	0.0509	not significant
Pure Error	0.0000	5	3.788E-06			
Cor Total	0.0916	19				

Table 4.8 ANOVA for Dilution

Source	Sum of Squares	df	Mean Square	F-value	p-value	
Model	0.9316	9	0.1035	276.29	< 0.0001	significant
I-Current	0.0653	1	0.0653	174.20	< 0.0001	
V-Welding Speed	0.2105	1	0.2105	561.96	< 0.0001	
G-Gas flow rate	0.1062	1	0.1062	283.43	< 0.0001	
IV	0.2606	1	0.2606	695.45	< 0.0001	
IG	0.0051	1	0.0051	13.55	0.0042	
VG	0.0179	1	0.0179	47.66	< 0.0001	
I^2	0.2190	1	0.2190	584.57	< 0.0001	
V^2	0.0143	1	0.0143	38.25	0.0001	
G^2	0.0029	1	0.0029	7.86	0.0187	
Residual	0.0037	10	0.0004			
Lack of Fit	0.0027	5	0.0005	2.50	0.1690	not significant
Pure Error	0.0011	5	0.0002			
Cor Total	0.9354	19				

The created model's coefficients of determination (R^2) for BW, BH, and Dilution were determined to be 0.9995, 0.9988, and 0.9960 (Close to ideal value 1), showing a good correlation between the predicted and experimental values, as shown in Table 4.9. Consequently, the BW, BH, and dilution models have been validated across the entire design space. Therefore, these models are suitable for accurately predicting the optimized processing parameters.

Table 4.9 Coefficients of determination values

Responses	R^2	Adjusted R^2	Predicted R^2
BW	0.9995	0.9991	0.9957
BH	0.9988	0.9976	0.9903
Dilution	0.9960	0.9924	0.9762

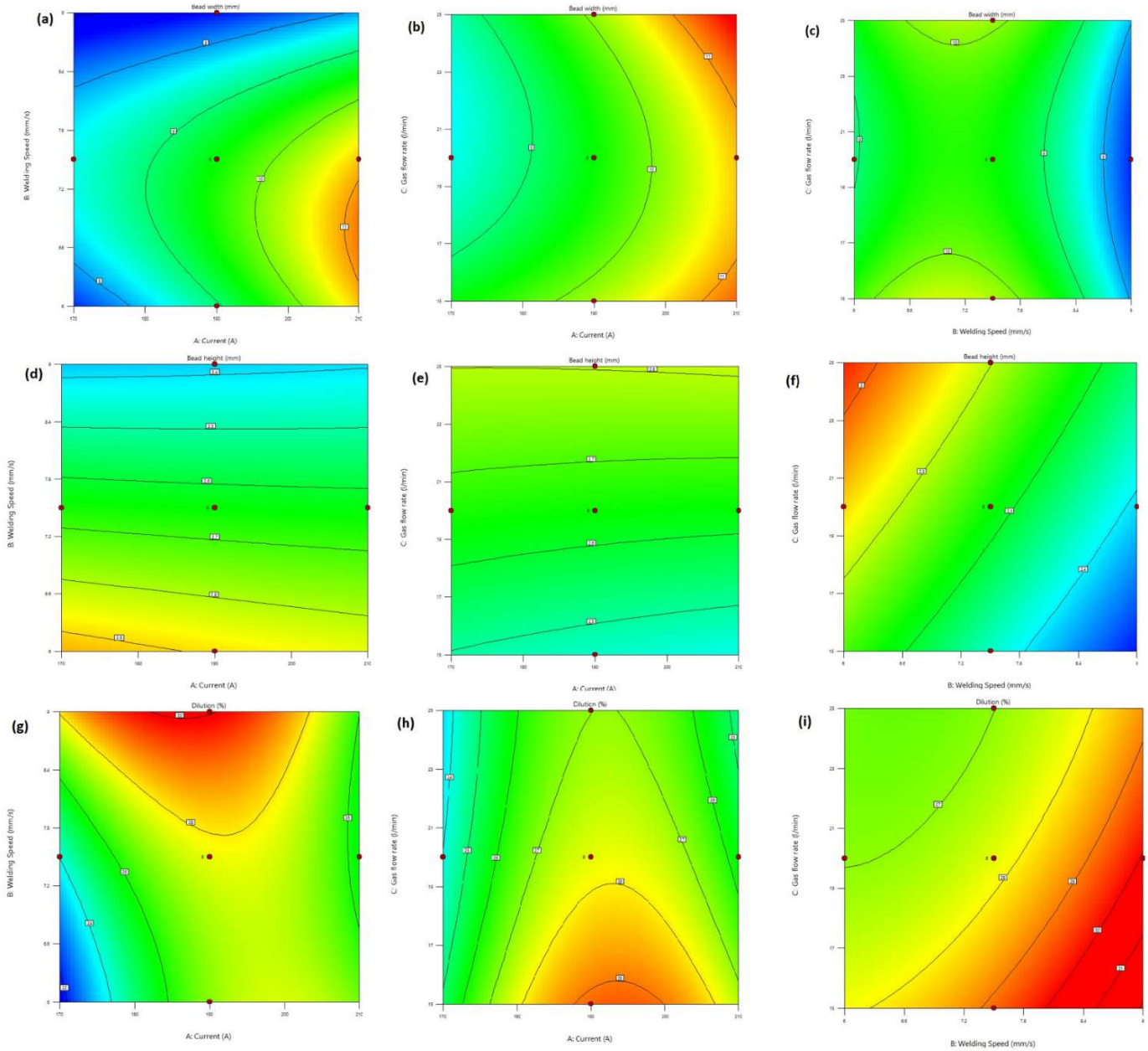

Fig. 4.9 Contour plot for (a-c) Weld bead width (d-f) Weld bead height (g-i) Dilution

4.6 Process Parameters Effect on Responses

Fig. 4.9 and 4.10 indicate contour and surface plots of BW, BH, and Dilution as a function of process parameters. Variations in colour in counter graphs show variations in BW, BH, and Dilution. (Butola et al., 2023).

4.6.1 Parameter Effect on Bead Width

From all the graphs in Fig. 4.9 and 4.10, when the welding current is increased weld bead width increases due to wire feed rate and material deposition. As a result, this leads to a larger weld pool size and ultimately augments the weld bead width. As welding speed and gas flow rate increase, weld bead width reduces due to reduced heat input, lowering wire metal deposition rate per unit length (Kannan and Yoganandh, 2010; Sarathchandra et al., 2020c). As a result, the bead width gets smaller as the travel speed and gas flow rate go up.

4.6.2 Parameter Effect on Bead Height

Fig. 4.10 (d, e, f) illustrates process factors' effect on weld bead height. It showed that weld bead height increases with current due to high heat input per unit length and a larger deposition rate per unit length (Rao et al., 2009). As the welding speed increases, less material is deposited per length unit. Thus, weld bead height decreases (Sarathchandra et al., 2020c). In contrast, when the gas flow rate increases, weld bead height increases due to the greater force exerted on the bead's walls, resulting in an inward force that generates a greater height (Nagesh and Datta, 2002).

4.6.3 Parameter Effect on Dilution

Fig. 4.10 (g, h, i) depicts the effect of process parameters on the dilution of the weld bead. It indicated that dilution increases with welding speed. Dilution also increases with welding current up to 190A. However, dilution decreases with the increase of welding current from 190 to 210A. Conversely, dilution shows a decreasing trend when the gas flow rate increases. The reason for the above is that as the welding speed increases, there is less material deposition rate per unit length, increasing reinforcement height. When the current increases, high heat input results in deeper penetration and an increase in penetration area. As the gas flow rate increases,

reinforcement height and an increase in penetration area. Similar type of results reported by various researchers (Jindal et al., 2014b; Nagesh and Datta, 2002; Palani and Murugan, 2006).

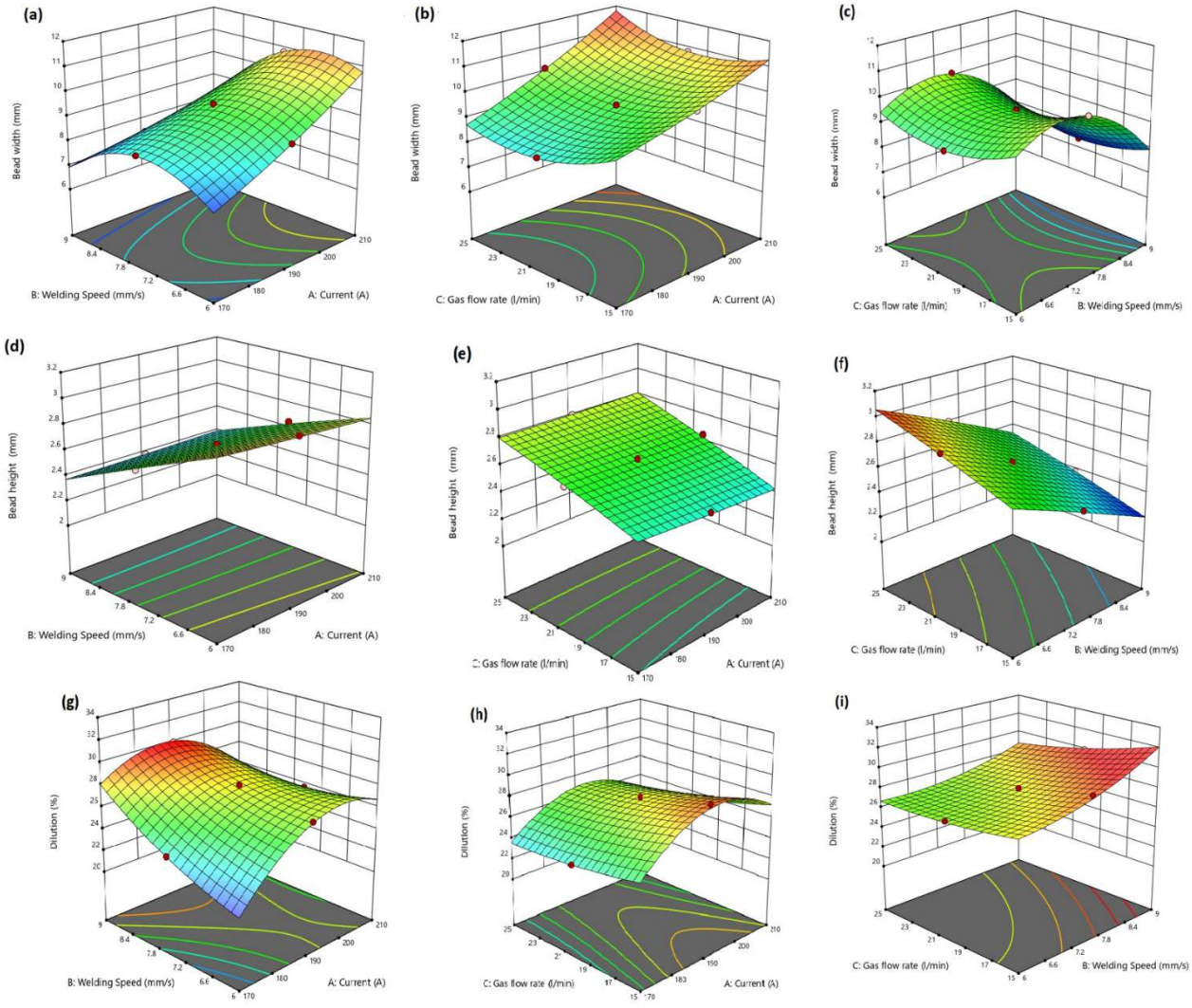

Fig. 4.10 Surface plot of the responses (a–c) Bead width (d–f) Height of the beads (g-i) Dilution for various combinations of the input parameters

4.7 Study of predicted v/s actual data

Fig. 4.11 depicts a scatter plot between actual data and model-predicted values. The fact that the line is about 45 degrees and will pass through the origin if extended shows how closely predicted data resembles recorded data. It demonstrates the significance and great fit of the created model. It also indicates that the constructed model is strong enough to forecast the data accurately.

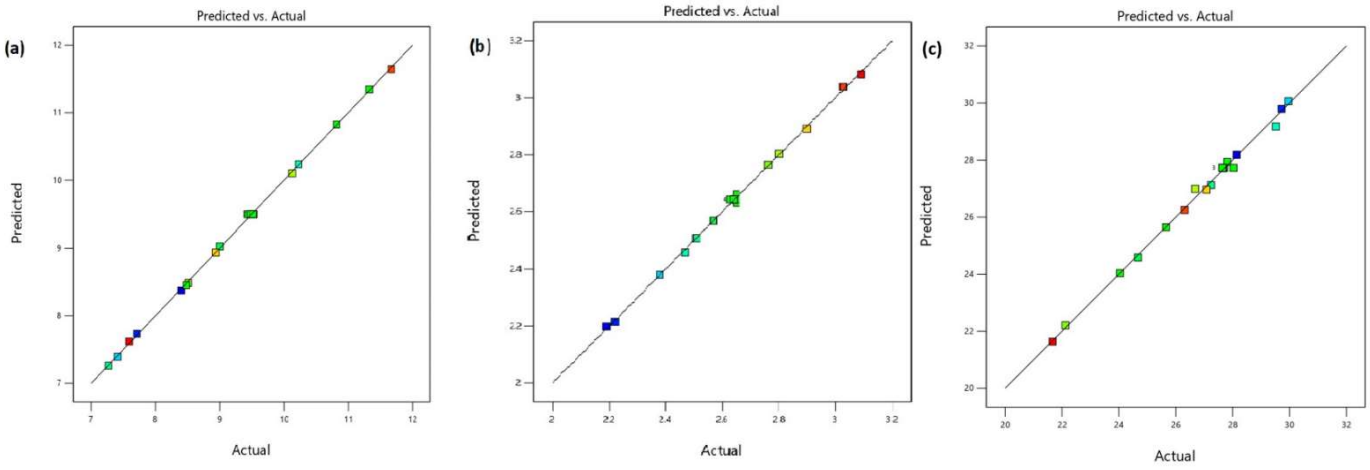

Fig. 4.11 Predicted versus actual values for the (a) weld bead width (b) weld bead height (c) Dilution.

4.8 Process parameter optimization

In the CMT WAAM process, weld bead stability and quality are important. The multi-objective optimization was done using RSM in Design-expert 13. In the WAAM process, BW and BH are expected to be at the maximum, while dilution for the CMT process should be at the minimum. Due to this, deposition stability is ensured and reduces residual stress and distortion (Kumar and Maji, 2023b; Le et al., 2022c; Youheng et al., 2017).The process parameter optimization problem is expressed as follows:

Find [I, V, G] to maximize BW, maximize BH, and minimize Dilution.

Subject to $190 \leq I \leq 210$ (A); $6 \leq V \leq 9$ (mm/s); $15 \leq G \leq 25$ (l/min).

Optimal process parameters were I = 210 (A), V = 6.9191 (mm/s), and G = 25 (l/min). The optimal output responses for BW, BH, and dilution were 12.1166 mm, 2.9018 mm, and 25.1143 mm, respectively, as shown in Fig. 4.12. The desirability of the predicted response is calculated to be 0.769.

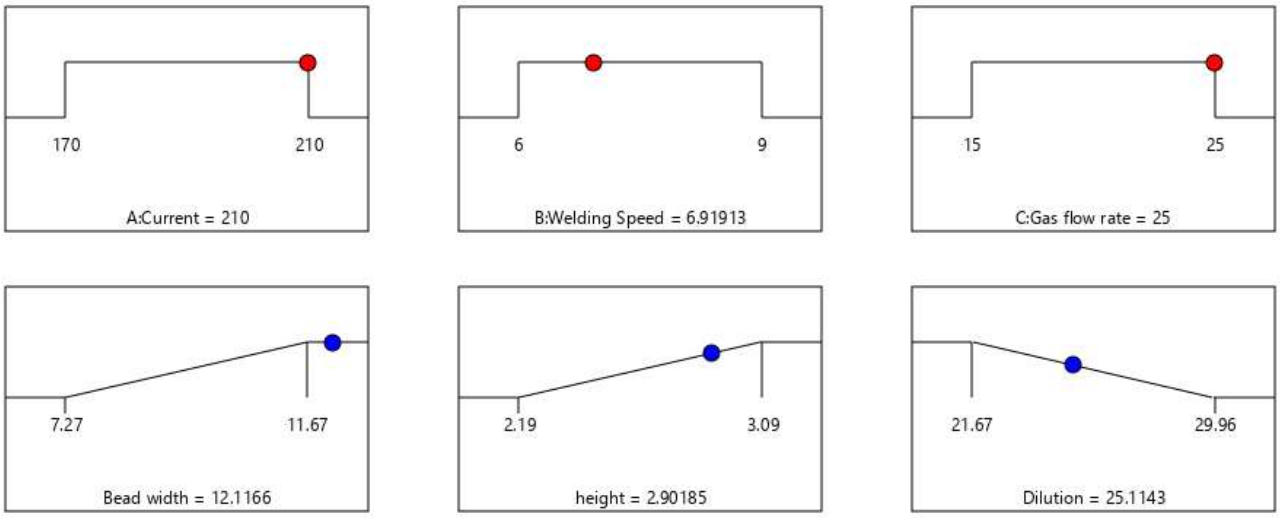

Fig. 4.12 Optimized values of input and output parameters curve of IN 718

Three practically similar single-weld beads produced utilizing optimized process parameters are illustrated in Fig. 4.13 All weld beads are smooth, continuous, and defect-free.

Fig. 4.13 Three weld bead images constructed on the optimum process parameters of IN 718

In the stable area of these weld beads, the values of BW, BH, and Dilution were computed (Table 4.10). It shows that the CMT technology may produce good weld bead shapes with

optimized process parameters. The optimal process parameters were utilized to build single-bead multi-layered Inconel 718 Walled samples (Fig. 4.14). It revealed that the Multi-layered wall has a good shape and regular height and width.

Table 4.10 Confirmation results

S.no.	Bead width (BW)		Error (%)	Bead height (BH)		Error (%)	Dilution (%)		Error (%)
	Actual value	Predicted value		Actual value	Predicted value		Actual value	Predicted value	
1.	11.92	12.11	-1.56	2.95	2.90	1.72	25.19	25.11	0.31
2.	12.55	12.11	3.63	2.81	2.90	-3.10	24.23	25.11	-3.50
3.	12.35	12.11	1.98	2.99	2.90	3.10	26.14	25.11	4.10

* Error, % =[Actual value-predicated value)/predicated value]*100

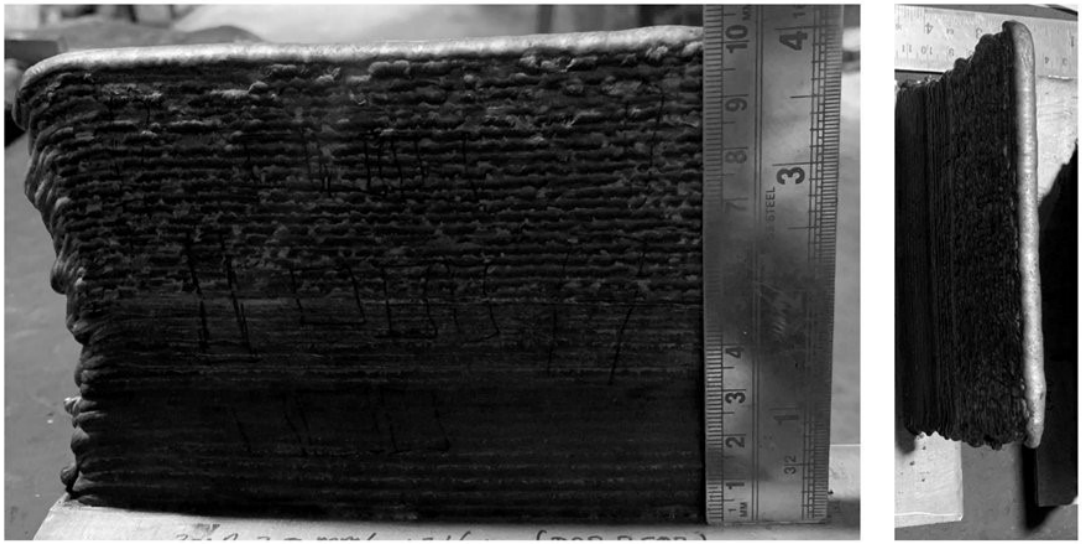

Fig. 4.14 The CMT WAAM Inconel 718 wall front view and top view with the optimized process parameters

4.9 Microstructure analysis of IN 718 WAAM samples at optimum parameters

The microstructure study of WAAM samples created using the optimum input parameters, 210 A current, 6.91 mm/s welding speed, and 25 l/min gas flow, is displayed in Fig. 4.15. The cross-section of the sample was cut through the middle to examine the microstructure of IN 718. The optical microscope images and SEM images are shown in Fig. 4.15 (a-b) and 4.15 (c), respectively. In accordance with heat transfer, the microstructure consists of fine dendrites grains in the top layer region, equiaxed dendrites in the middle and side regions, and columnar dendrites in the lower region. Due to the last layer encountering an accelerated cooling rate brought on by an air-surrounding sample and a lack of remelting that occurs during the WAAM process, the top region, as illustrated in Fig. 4.15 (a), exhibits a transitional microstructure from elongated dendrites to fine dendrites (Rodrigues et al., 2020). Similar fine top layer microstructures are seen in materials made via AM, including the nickel-based alloy Inconel 625 (J. F. Wang et al., 2016) and NiTi intermetallic (Zeng et al., 2020). Lower deposited layers Fig. 4.15 (b-c) have columnar grains due to repeated thermal cycles from the subsequent depositions; the grain size is often bigger in the lower layer than the top layer, and growth follows the highest thermal gradient. During the WAAM process, the dendrites formed in the preceding layers undergo partial remelting due to heat cycling. These dendrites then act as nucleation sites for the subsequent layer (Fang et al., 2018). The optimum process parameters were also responsible for the defect-free WAAM deposited wall. Due to the dense nature of grain boundaries, materials with finer grain sizes withstand intergranular fracture better. Hence, a fine grain structure gives extraordinary strength and great microhardness qualities.

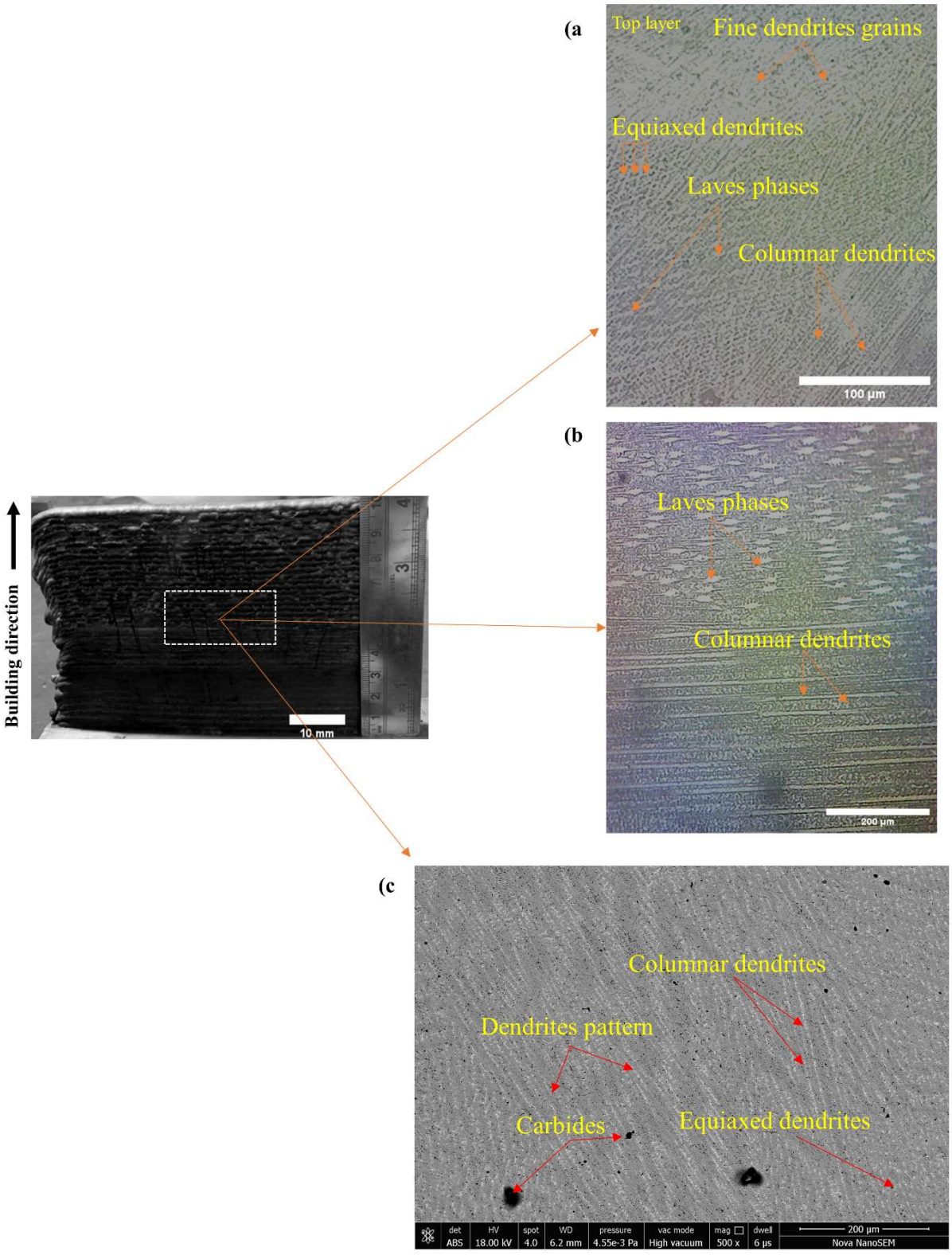

Fig. 4.15 Microstructure of Inconel 718 samples (a) Optical microscope image at 100x (b) Optical microscope image at 500x (c) SEM image of IN 718

4.10 Mechanical properties of IN 718 Wall

Measurements of hardness were used to assess the mechanical characteristics of the CMT WAAM-deposited wall. A Vickers microhardness machine (DRAMIN-40 STRUERS) was used to measure the hardness of the Inconel 718-deposited wall. According to the ASTM E34 Standard, the hardness was measured by putting a 500-gf load on the material and keeping the dwell time at 10 seconds. The average hardness value was found by measuring microhardness at five different spots in each zone, as shown in Fig. 4.16.

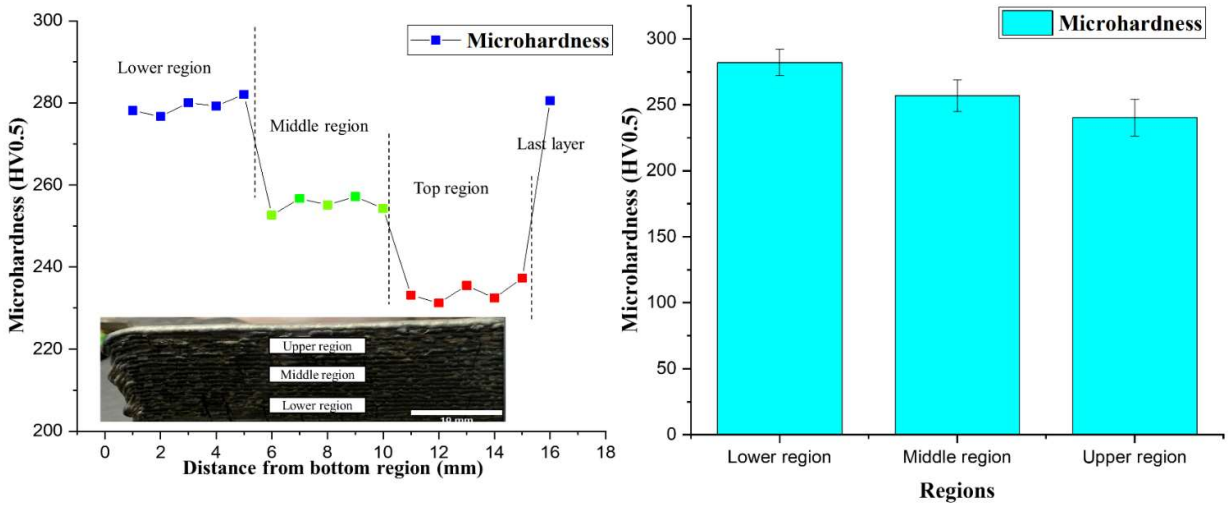

Fig. 4.16 Microhardness variation of the IN 718 wall at the lower region, middle region, and upper region via (a) Line diagram variation (b) Bar diagram variation

The average microhardness measurements for the upper, middle, and lower regions are 235 ± 1.50, 245 ± 2.36, and 280 ± 2.67 HV0.5, respectively. However, the final layer had an average hardness of 275.5 HV. Correspondingly, the lowest and last layers have fine crystals and strong micro-hardness. Similarly, crystals are coarser at the top, and micro-hardness is lower (Yangfan et al., 2019b).The observed inequalities in hardness can be ascribed to variances in microstructural characteristics that arise due to the cyclical fluctuations in temperature, as shown in section 4.9. It is projected that regions displaying smaller grain sizes in the

microstructure of materials will exhibit elevated levels of hardness (Gao et al., 2019b). Consequently, the lower portion of the wall indicates the most elevated mean value of hardness.

4.11 Summary

In this chapter, a comprehensive investigation was conducted to optimise the process parameters for the CMT WAAM of SDSS 2507 and IN 718. This involved the development of mathematical models to predict the weld bead width (BW), bead height (BH), and dilution. The impact of welding current, speed, and gas flow rate on these parameters was found to be significant, as indicated by regression equations and analysis of variance (ANOVA). The high coefficients of determination (R^2) further validate the accuracy of the models. The optimization focused on maximizing BW and BH while minimizing dilution, leading to the identification of optimal parameters. The process resulted in seamless welds without defects, and the predicted error margin was calculated for BW, BH, and dilution. The optimised samples' analysis showed fine dendritic grains in the top layer and columnar grains in the lower layers. These grain structures were found to align with the expected thermal gradients during the deposition process. The hardness measurements in the lower region of the deposited wall indicated a superior strength and quality of the welds, likely attributed to the finer grain structure.

CHAPTER 5

RESULTS AND DISCUSSIONS ON DISSIMILAR SDSS 2507-IN 718 WAAM WALL

5.1 Microstructure and Mechanical Characterisation of Dissimilar Super Duplex Stainless Steel 2507 -Inconel 718 alloy structure

5.1.1 Introduction

Joining dissimilar metal components is a common need in various industrial sectors, such as aviation, aerospace, shipbuilding, and automobile manufacturing. These components can include alloys of copper, steel, magnesium, titanium, and superalloys based on nickel (Sridar et al., 2022). Achieving high-quality combinations of different metals through standard techniques for joining or welding can be difficult because of the significant risk of forming significant amounts of brittle intermetallic compounds (IMCs) during solidification (Soysal et al., 2016). Solid-state bonding must limit fusion heat input to overcome this primary obstacle to sound contact between dissimilar materials. Steel-nickel alloys have the potential to be used as structural materials in nuclear energy, chemical plants and, in particular, within gas turbine engines due to their performance in severe combustion (Gazella et al., 2024), chemical environments with remarkable mechanical qualities, exceptional corrosion resistance, strong creep strength at elevated temperatures, and outstanding resistance to radiation damage (Abe and Sasahara, 2016a). Inconel 718 is a remarkable nickel-ferrous-chromium superalloy that possesses exceptional properties such as high-temperature strength, corrosion resistance, tensile and fatigue strength, and ideal creep behaviour. SDSS 2507 excels in demanding conditions due to its strong corrosion resistance and mechanical qualities, owing to its Cr and Ni concentration and ferritic-austenitic microstructures (Meena et al., 2024b). However, the SDSS 2507 is significantly cheaper than the IN 718superalloy. Consequently, to keep material

costs down, it is more economical to use SDSS 2507 for the components that operate at lower temperatures and IN718 superalloys for the sections that operate at higher temperatures.

. Researchers experimented with dissimilar alloys to study the microstructure and mechanical properties of WAAM-manufactured products. Abe demonstrated that the WAAM technique may be used to process Bi-metallic structures (BMS) made of stainless steel and Ni-based superalloy. The resulting materials exhibit outstanding mechanical properties, and the interface between the two metals is free from any flaws, indicating a robust metallurgical link (Abe and Sasahara, 2016b). Twin-WAAM with direct interface (FGM 100–100) and smooth interface (FGM 5) deposition procedures produced 316 L stainless steel/Inconel 625 functionally graded material (FGM) by Rodrigues et al.(Rodrigues et al., 2022b). Secondary phases were absent in the direct interface technique, resulting in better mechanical characteristics and decreased residual stress.

Presently, although several investigations on wire-based additive manufacturing have predominantly utilized GTAW and GMAW-based WAAM systems for dissimilar alloys like steel, aluminium, and Nickel, there is no single study in the literature on the dissimilar alloy SDSS2507 and IN 718 wire arc additive manufacturing using CMT WAAM. This work incorporated successful CMT-based WAAM of dissimilar SDSS 2507 and IN 718 alloy walls. The microstructure and mechanical evaluation of the interface zone have been conducted in this study.

5.1.2 X-Ray Diffraction Analysis of Phase Structure

Fig. 5.1 illustrates XRD results for dissimilar SDSS2507-IN718 alloy WAAM samples. The peaks identified at 10-11 degrees (deg) on the (103) plane, 43-44 deg on the (111) plane, 50-51 deg on the (200) plane, and 75-76 deg on the (220) plane represent the Aluminium-silicon, iron-nickel and chromium-nickel (γ phase) matrix microstructural composition (Sui et al., 2020). Intermetallic compounds, particularly the phases that result from mixing dissimilar

types of materials (Tanrikulu et al., 2024), such as Cr_2Ni_3 and Fe_3Ni_2, were also observed in dissimilar SDSS2507-IN718 additive walls. It is widely acknowledged that the creation of IMCs, which are the most fragile phases that weaken mechanical characteristics, is identified as the primary obstacle (Niu et al., 2021).

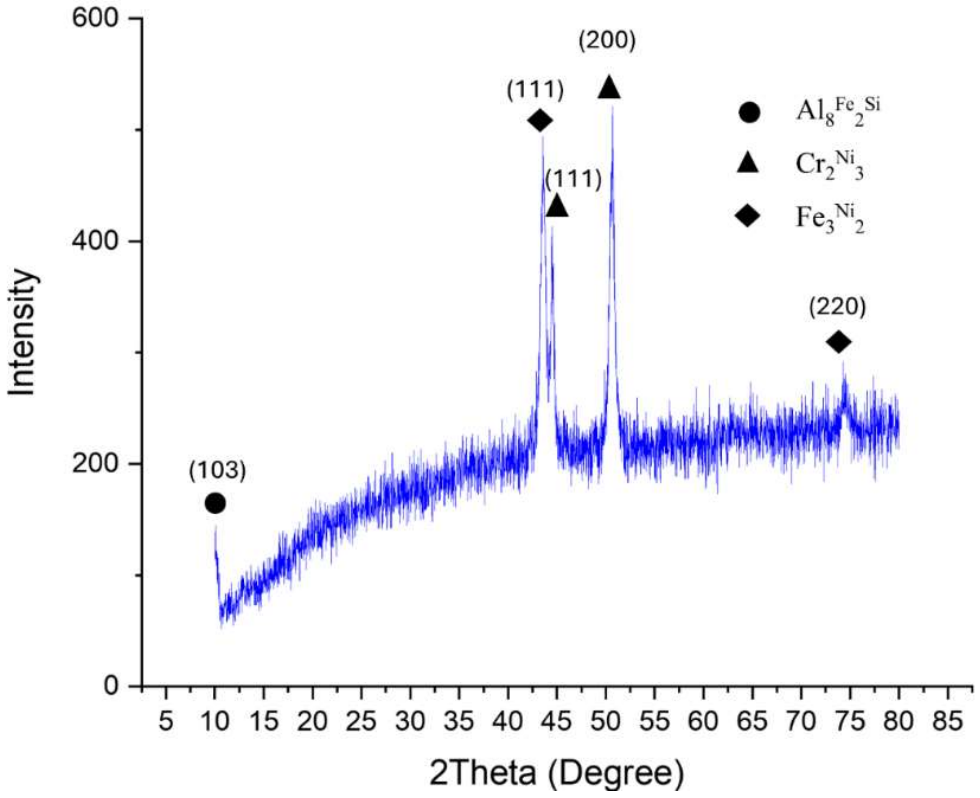

Fig. 5.1 X-ray diffraction pattern of dissimilar SDSS 2507 -IN718 alloy WAAM samples as in-built direction

5.1.3 Microstructure Analysis

Fig. 5.2 displays the optical micrographs of the as-deposited dissimilar alloy in several areas, while Fig. 5.2(a) shows the overall cross-section. Fig. 5.2(b) displays the IN718 layers' microstructural properties at the top. The IN718 layers exhibited interdendritic grains with a mixture of dendrites, emphasizing their directionality (Ganesh et al., 2010). As shown in Fig

5.2(b), IN 718 microstructure consists of columnar dendrites and laves phases. Varied microstructure of IN718 was observed from the interface to the upwards. The distance between dendritic arms grew as one progressed from the intermediate to the upper layers. The area near SDSS2507 displayed a growth pattern of columnar dendrites with fine dendrites. The complex cyclic heat history supports the microstructural feature change during deposition (Meena et al., 2024c). During the WAAM process, convection and radiation from the surrounding atmosphere are the principal causes of heat dissipation at the IN718 layers. The accelerated crystallization rate and heat energy accumulation facilitated the development of elongated dendritic formations. The prime dendrite arm spacing (PDAS) is directly proportional to the decrease in temperature gradient along the building direction. Fig. 5.2(d) displays the microstructure of SDSS 2507, which consists predominantly of columnar and equiaxed grains. Columnar grains formed due to the partial melting of earlier layers; these grains then acted as nucleation sites for the subsequent layer's solidification (Haldar et al., 2024).

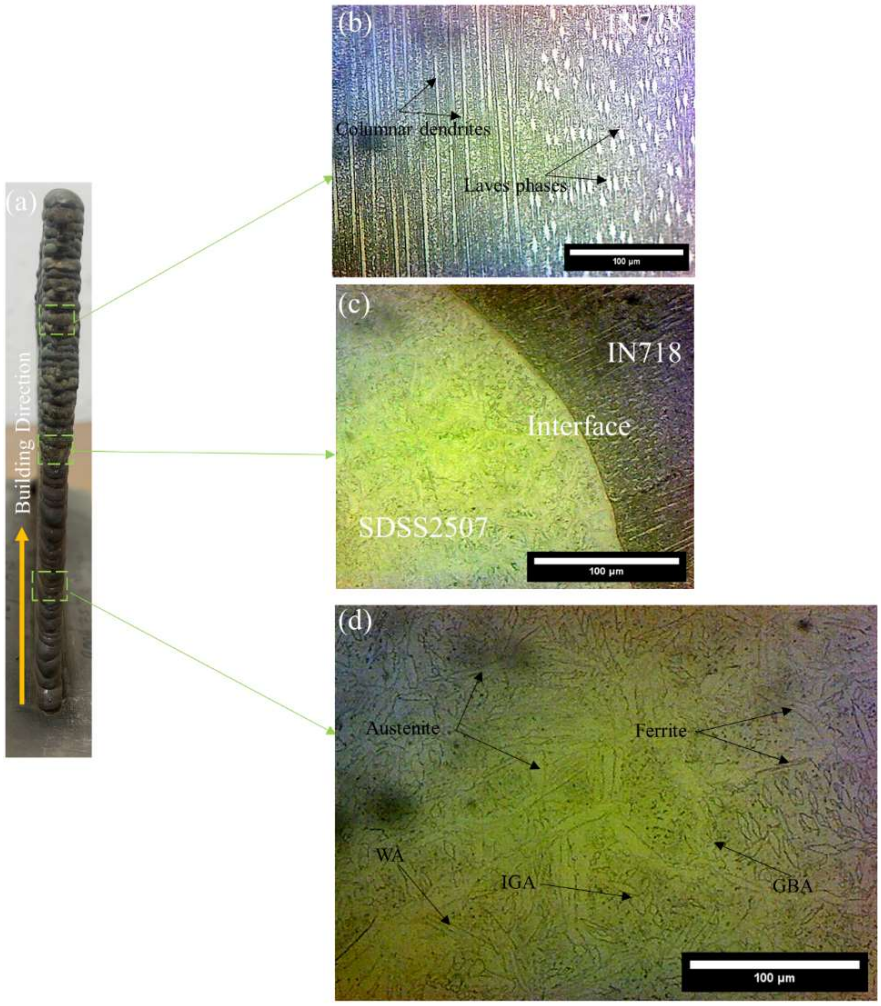

Fig. 5.2 Optical microscope image of dissimilar alloy wall (a) Macrograph (b) IN 718 region (c) Interface of SDSS2507- In718 (d) SDSS 2507 region

The micrographs show that the austenitic matrix contains delta-ferrite uniformly. Observations revealed a shift in the microstructure, progressing from cellular dendrites to fine columnar dendrites and finally to coarse columnar dendrites. The SDSS2507 consists of a ferrite matrix and different kinds of austenitic phases. The temperature gradient experienced during solidification causes grain boundary austenite (GBA) to align predominantly with the building direction. At the interface between ferrite and austenite, ferrite diffuses into the austenite. The accelerated cooling rate results in the growth of Widmanstatten austenite (WA) (Köse and Topal, 2022). Intragranular austenite (IGA) is predominantly formed near the melt pool's

boundaries. The lower layers of SDSS2507 exhibited equiaxed grains, while the dendritic structure became more prevalent as the height increased. At lower levels, heat loss is facilitated by the substrate, which promotes the formation of equiaxed structures due to constitutional supercooling. However, as the layers increase, the substrate's ability to disperse heat decreases, resulting in a reduced effective surface area for heat dissipation at the top layers. The dissimilar alloy wall achieved thermal balance as the layers increased in height and received a consistent thermal input. This resulted in uniform thickness and layer height due to heat dissipation and absorption (Sasikumar et al., 2022). Fig. 5.2(c) shows the IF region's microstructure. No solidification cracks were seen at the SDSS 2507 and IN718 layer interface due to thermal stresses from different filler wire compositions during deposition. Columnar dendrites were found in the SDSS 2507 area, while primary dendrites with small interdendritic precipitates were noticed in the IF area. The SEM image emphasizes the bonding between the two materials. The two metals are clearly separated at the interface, as shown in Fig.5.2(c). No fusion happened between the two types of microstructures, which were evenly spread on both sides of the border.

Fig. 5.3 displays the SEM of the SDSS 2507-IN718. The top, middle, and bottom parts of the wall are shown in Fig. 5.3(b), (c), and (d), correspondingly. Fig. 5.3(b) displays the presence of columnar and cellular crystals, with white bulk phases seen between the grains. Fig. 5.3(e) at high magnification clearly shows the presence of white bulk phases, known as laves phases, formed due to the segregation of Nb and Mo elements (W. Zhang et al., 2021). The two alloys form a distinct and consistent boundary in Fig. 5.3(c), similar to what is seen in Fig. 5.2(c). The microstructure of the alloys remains unchanged on either side of the border, as seen in Fig. 5.3(f). Austenite and the Laves phase were located above the boundary, while austenite and ferrite were below the barrier, as depicted in Fig. 5.3(g). The boundary exhibited no defects, such as pores, contaminants, or cracks. In Fig. 5.3(f), the highlighted portion shows the

elemental scan area for the elements composition analysis of the IF. The Nb, Mo, Mn, C, Al, and Si elements were significantly segregated, while the Ni, Cr, and Fe elements were uniformly distributed, as shown in elements mapping. Fig. 5.3(d) shows the presence of both austenite and ferrite in the lower section of the dissimilar alloy SDSS 2507-IN 718 wall. Fig. 5.3(d) shows a microstructure with a different shape than Fig. 5.3(g). The lower layer rapidly cooled down because it was in direct touch with the room-temperature substrate, allowing for most of the heat transmission. The lowest layers cool quickly, exhibiting dendritic, feathery, parallel Widmanstatten and increasing grain boundary austenite concentration, as shown in Fig. 5.3(d). Fig. 5.3(g) shows columnar equiaxed grains and coarse Widmanstatten austenite, with larger austenite resulting from insufficient heat dissipation. The dissimilar structure's central layers were far from the substrate. Middle layers' heat can only reach lower layers at high temperatures and in the air. The slow cooling rate of the middle layers led to prolonged times in high temperatures.

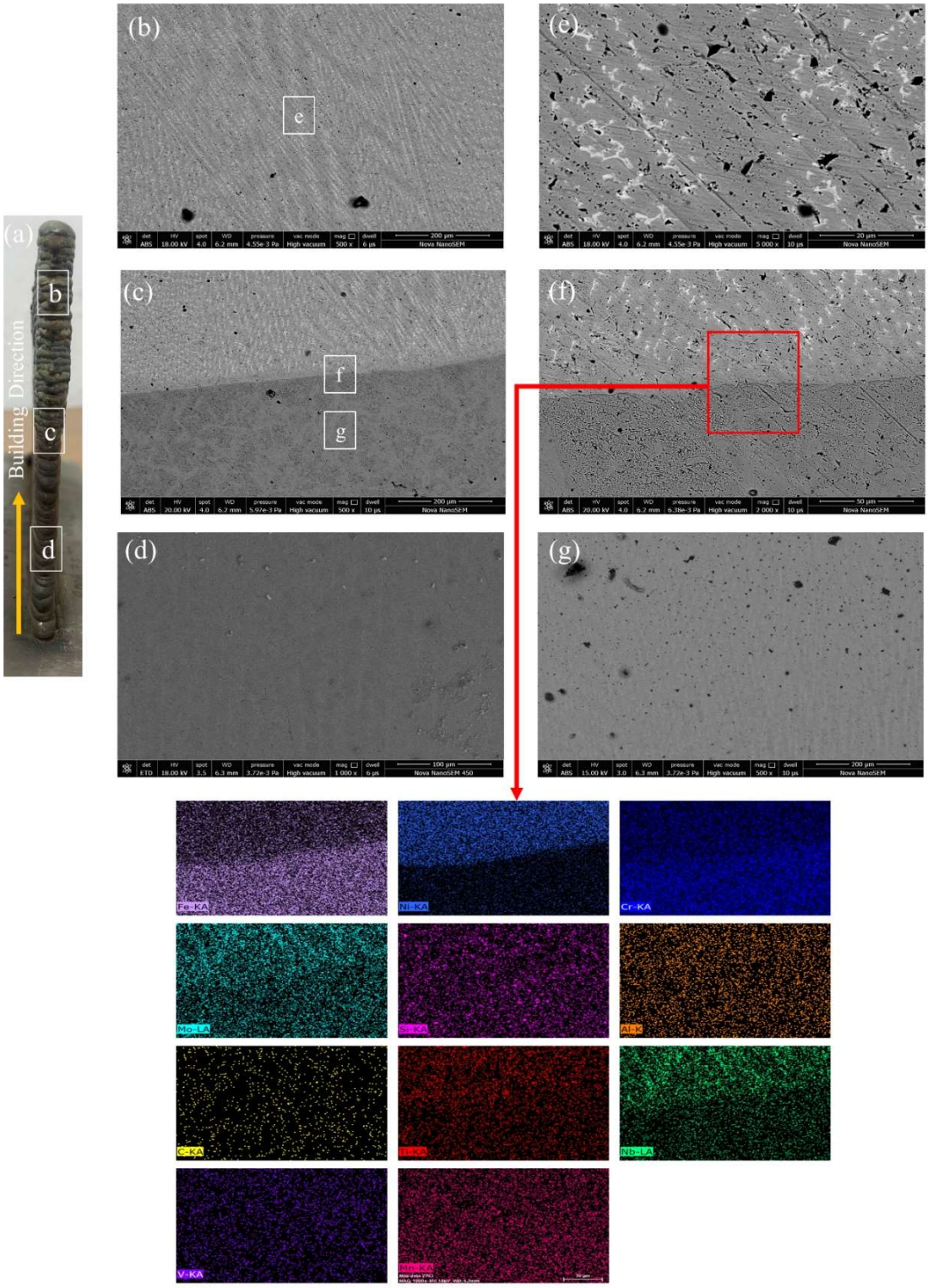

Fig. 5.3 Section morphology and SEM Micrograph of Dissimilar SDSS 2507-IN 718 (a) section morphology (b) Upper part (c) Middle part (d) Lower part (e) In 718 (f) Interface region with EDS mapping (g) SDSS 2507 microstructure close to interface zone

EDS analysis confirmed the dissolution of elements between SDSS 2507 and IN718. The EDS elemental maps reveal that Fe and Ni distribution in the IF region was predominantly high, as shown in Fig. 5.4. The results obtained are indeed valid and serve to confirm the presence of the main elements in IN718 and SDSS 2507, which are Ni and Fe, respectively. At scan area 2, the SEM picture clearly shows the boundary. Overall, there were no apparent defects in the IF, and the distribution of Cr was consistent on both sides due to the similar composition of SDSS 2507 and IN718. No signs of elemental segregation were observed in the IF from the EDS area scan.

An EDS scan was conducted in the IF region to analyze the elemental composition of the materials, as shown in Fig. 5.3. In the IF area, a scan was performed at a 200 μm distance. The major elements, including Fe, Ni, Cr, Mo, and Nb, were recorded and can be seen in Fig. 5.3(f) EDS mapping. Fig. 5.4 demonstrates significant variations in the Fe and Ni levels at the IF, which can be attributed to the varying composition ratios of Ni and Fe in the SDSS 2507 and IN718 layers. The varied amounts of Mn in the two filler wires caused an apparent change in the Mn concentration at the transition zone.

The slight fluctuation in the Cr content is confirmed to be due to the diluting of the IN718 layer over the SDSS 2507. At the IF, the IN718 filler wire is used to generate a molten pool on top of the SDSS 2507 layer that was previously deposited. Therefore, the confirmation of the dissolution of elements was observed throughout the IF. The EDS plot indicates that elements were mixed, and no significant changes in the amount of Cr were noticed. The presence of the laves phase was verified in the IN718 layers. The laves phase is thought to emerge when specific elements, such as Mo and Nb, segregate during non-equilibrium solidification (Haldar et al., 2024).

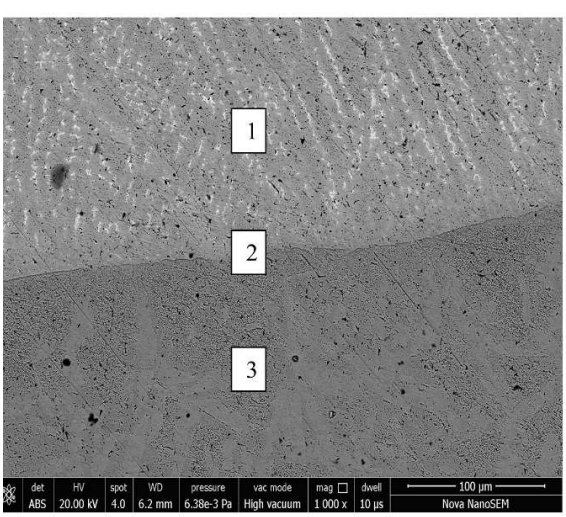

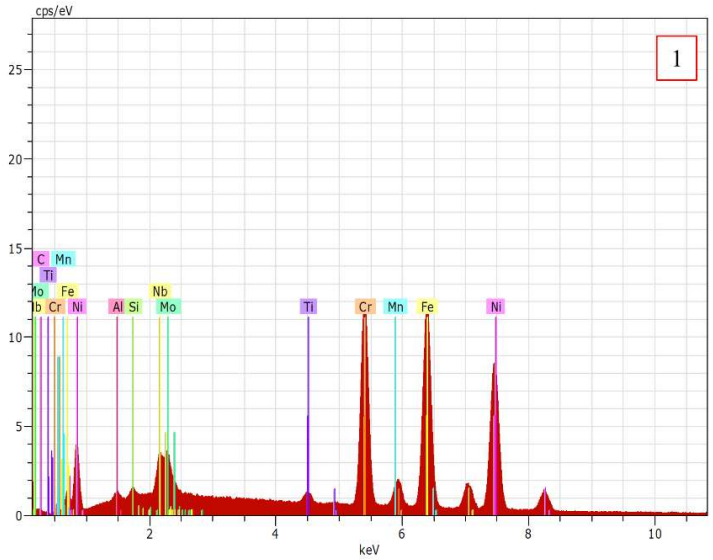

Element	Atomic %			Weight %		
Point	1	2	3	1	2	3
Ni	35.35	19.47	24.36	37.68	21.29	24.97
Cr	20.98	25.17	19.55	19.81	24.38	18.66
Fe	31.61	44.84	40.91	32.05	46.65	44.07
Mo	1.55	1.25	1.74	2.70	2.24	3.06
Mn	0.93	1.32	0.82	0.92	1.35	0.83
Nb	2.42	0.96	2.88	4.08	1.67	4.91

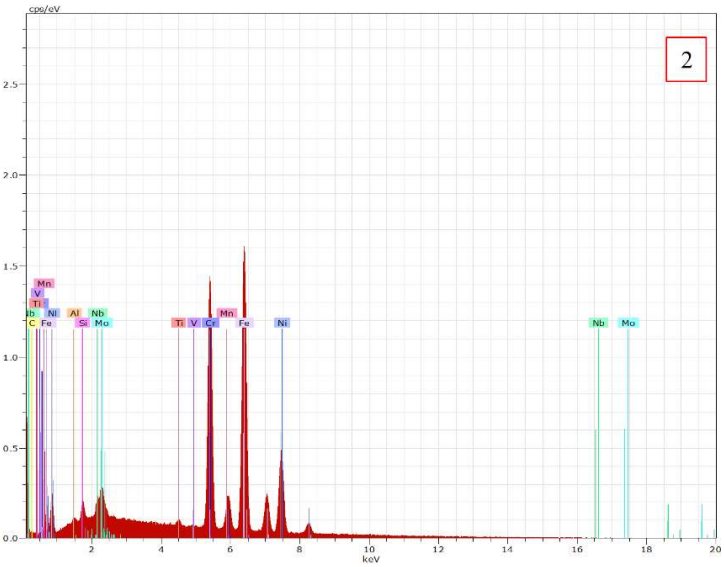

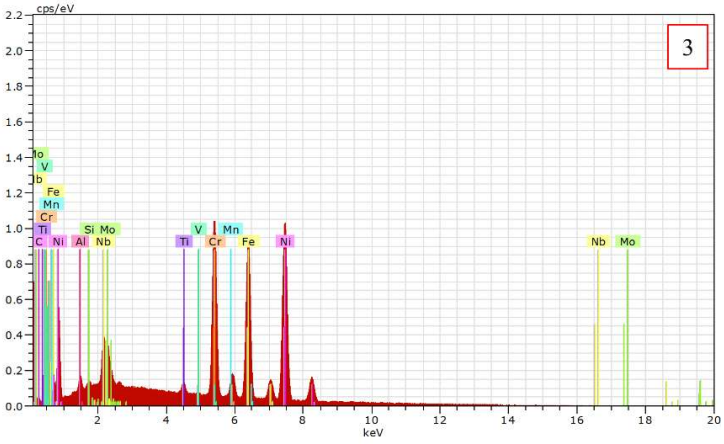

Fig. 5.4 SEM micrograph and EDS analysis at various scan areas (1) IN 718 (2) IN 718-SDSS 2507 interface (3) SDSS 2507

5.1.4 Microhardness

Microhardness measurements were conducted in three specific locations, namely SDSS 2507, IF, and IN718, along the building direction from the substrate, as shown in Fig. 5.5. In the SDSS 2507 region, the average hardness was measured at 312 ± 9 HV, while in the IN718 region, it was found to be 249 ± 5 HV. The values of hardness at the interface region range from 220 to 238 HV, indicating the dissolution of elements from SDSS 2507 to IN718. The interface's hardness value was intermediate between the two alloys' values. Microhardness changes when the indentation is placed at the interface of the deposited layers, which are linked to a finely ground microstructure with equal grain sizes. This positioning leads to higher hardness values. The microstructure evolution of the DED sample is the primary determinant of microhardness, with the temperature history of each layer influencing its microstructure evolution. The build direction shows a decreasing trend in hardness as one moves up from the substrate to the top layer. The grain structure shown in Fig. 5.2 is relatively larger due to slower cooling and higher heat accumulation towards the upper end. As a result, the microhardness decreases gradually with increasing distance from the substrate. As per the Hall-Petch strengthening effect, the presence of fine grains can lead to improved mechanical properties (Chi et al., 2023). Deposition of nickel alloy on stainless steel causes a reduction in hardness close to the contact, as also observed in earlier WAAM studies (Sasikumar et al., 2022; W. Zhang et al., 2021).

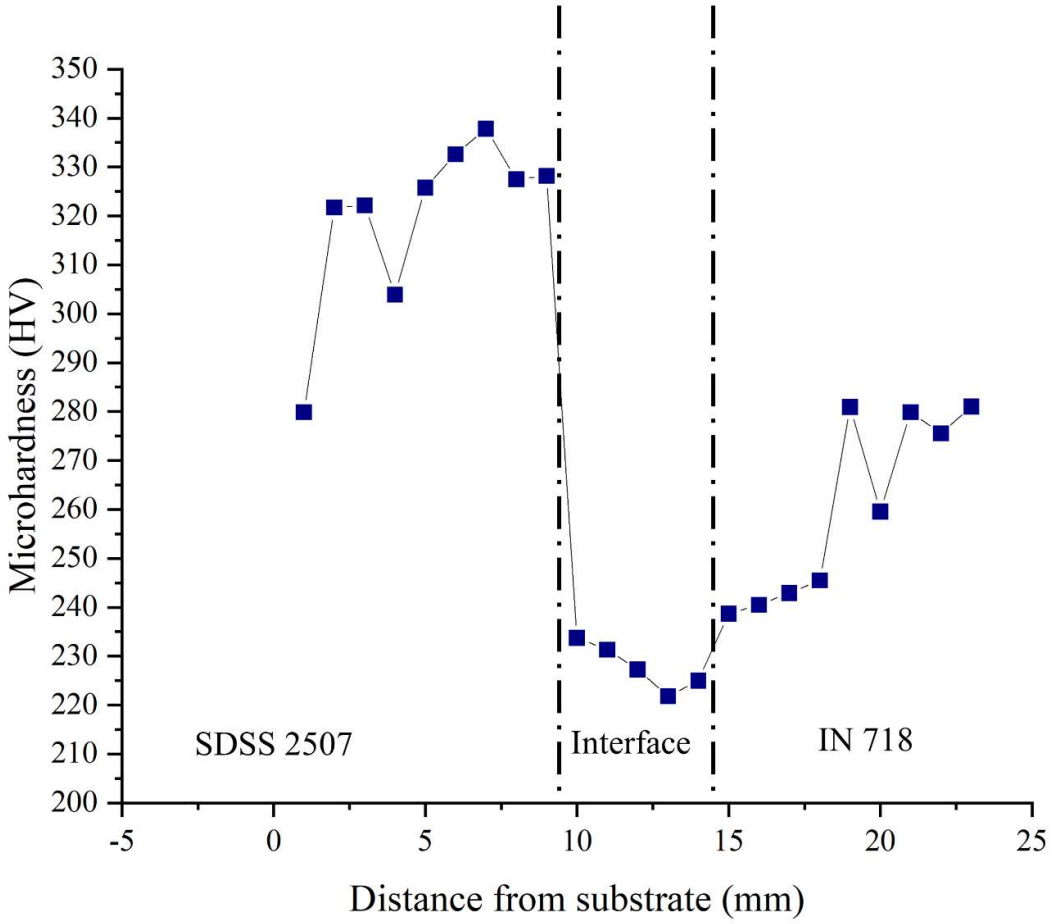

Fig. 5.5 Microhardness curve of dissimilar alloy WAAM

5.1.5 Tensile Properties

Tensile specimens made of SDSS 2507, interface, and IN 718 were subjected to tensile tests taken from various places, as shown in Fig. 3.15. Fig. 5.6 displays standard stress-strain curves and fractured specimens that demonstrate the failure of the specimen, indicating a greater strength at the vertical interface of the SDSS 2507 and 718 samples. Importantly, there is no obvious yield point indicated by the tensile curves. Two horizontal samples at SDSS 2507 and IN 718 and three vertical samples at the interface were prepared from the wall. Table 5.1 exhibits the tensile test results. The UTS of V1, V2, and V3 at the interface are 755, 745, and 718 MPa, respectively. Their yield strengths are 528, 510, and 500 MPa. In the horizontal

direction, the IN718 (H1) and SDSS 2508 (H2) have UTS values of 750 and 882 MPA, respectively, while their yield strength (YS) is measured at 501 and 725 MPa, which was also reported by other researchers (Huang et al., 2023; Kannan et al., 2021b; Sales et al., 2022). There have been no reported findings on the tensile properties of dissimilar SDSS 2507 and IN 718. The highest UTS have been discovered in H2 and V1, respectively. The mean UTS of vertical tensile specimens at the wall interface were between the horizontal SDSS 2507 and IN 718 specimens, which shows that two metal alloys bind together strongly at the interface. Generally, there is significant variance in the UTS and YS of horizontal and vertical tensile specimens. The mechanical properties appear to differ in the horizontal and vertical directions, a phenomenon called anisotropy. The non-equilibrium heat cycles throughout the WAAM process are responsible for this occurrence.

Table 5.1 Tensile testing results of as-deposited dissimilar alloy wall

Sample	Ultimate tensile strength (MPa)	Yield strength (MPa)	Elongation (%)
IN 718 Horizontal (H1)	750	501	68.32
SDSS 2507-IN718 interface Vertical (V1)	755	528	49.46
SDSS 2507-IN718 interface Vertical (V2)	745	510	48.75
SDSS 2507-IN718 interface Vertical (V3)	718	500	48.74
SDSS 2507 Horizontal (H2)	882	725	67.25

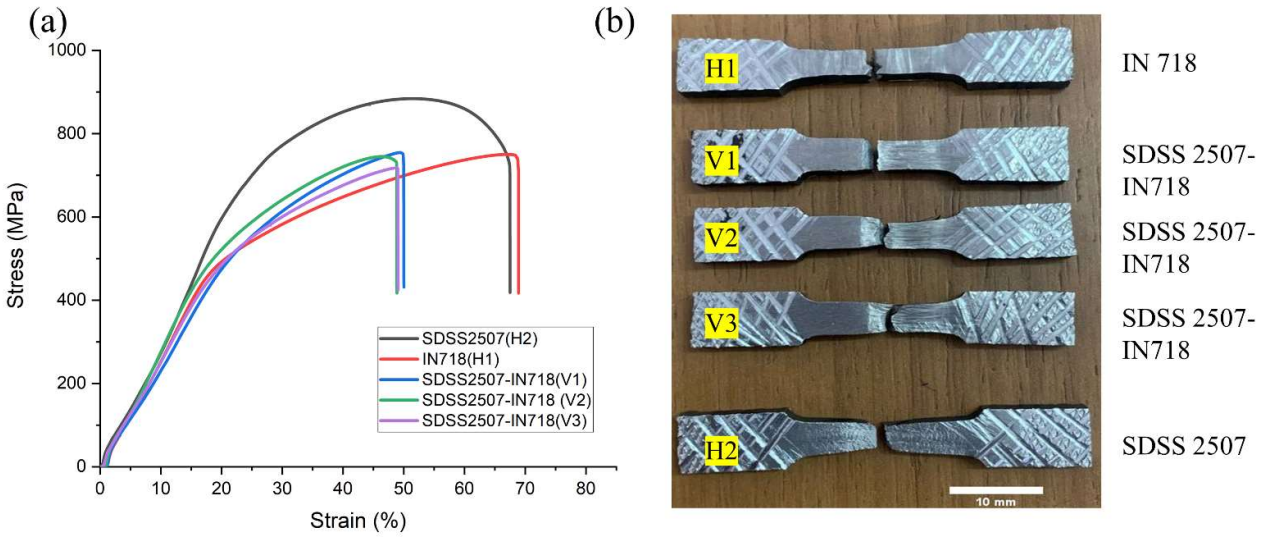

Fig. 5.6 Tensile test result for five samples (a) Stress-strain curve of the dissimilar wall (b) Fractured samples

5.1.6 Fractography of tensile specimens

Tensile specimen fractography of IN 718, Interface of SDSS 2507-IN 718, and SDSS are shown in Fig. 5.7. The general surface of the samples' fractures can be seen in Fig. 5.7 (a-c). Higher magnification shows that all specimens have dimples and microvoids, which indicates that the fracture mode is a ductile fracture. The vertical bimetallic samples experienced failure on the SDSS 2507 side, indicating a strong bond at the dissimilar interface. The appearance of large, evenly distributed equiaxed, fine dimples on the tensile failed surface indicates a ductile fracture process (Jadhav et al., 2024; Liu et al., 2024). Compared to IN718, the SEM micrographs of the interface demonstrate large-scale equiaxed dimples and cavities in a random orientation devoid of any micro-fissures. Nevertheless, there is no discernible variation in fracture morphology across the samples due to the striking similarity in fracture mode.

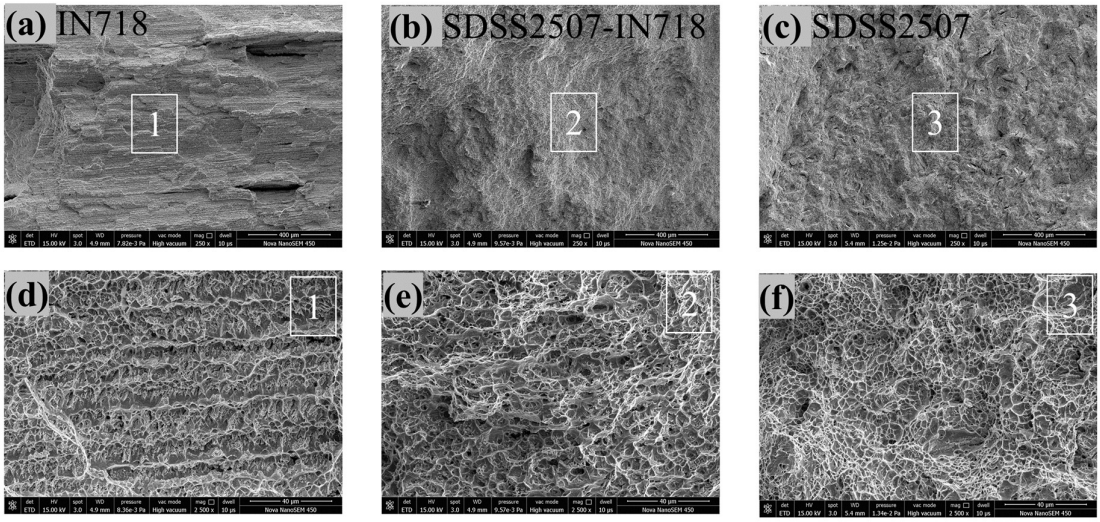

Fig. 5.7 Fracture morphology of Tensile specimens (a)IN718 (b) SDSS 2507-IN718 interface (c) SDSS 2507 (d, e, f) Magnified view of locations 1,2 and 3

5.2 Ultrasonic Vibration Assisted Microstructure and Mechanical Characterisation of Dissimilar Super Duplex Stainless Steel 2507 -Inconel 718 alloy structure

5.2.1 Introduction

Several methods, including ultrasonic vibration, electromagnetic field integration, and mechanical stirring, have been employed to reduce fabrication defects by regulating the melting and solidification behaviour of materials in thermal processes such as casting, arc welding, and cladding (Cao et al., 2008; Ezatpour et al., 2014; Kore et al., 2011; Patarić et al., 2012; Sun et al., 2009). Ultrasonic vibration is a highly regarded technique among these aiding approaches. It is favoured because it effectively transmits acoustic energy and cavitation and can remarkably control heat and mass transfer (Abramov, 1987a). Typically, when a powerful ultrasonic vibration is applied to a liquid, it produces two distinct nonlinear phenomena: acoustic streaming and acoustic cavitation (Abramov, 1987; KOMAROV et al., 2005). Ultrasonic vibration can reduce the presence of small holes, improve the quality of the grains, and break down the harmful Laves precipitated phase. This leads to enhancements in the tensile strength, modulus, microhardness, and wear resistance of the IN718 parts produced using the ultrasonic vibration-assisted (UV-A) DED method reported by Ning et al. (Ning et al., 2018). The latest study on the DED processing of Ti-6Al-4V has provided evidence for the significant impact of UV-induced grain refinement on tensile characteristics (Todaro et al., 2020). UV improved grain refining and reduced the directional growth of coarse columnar grains. Secondary phases with Mo and Nb easily precipitate in c-Ni grain boundaries. UV-CMT samples had more homogeneous secondary phase distribution due to enhanced grain boundary density by Ma et al. (Ma et al., 2021). The latest study (Jeong et al., 2024a) found that FGMs without ultrasonic treatment have columnar grains, but ultrasonic treatment refines grains into equiaxed forms, enhancing uniformity and reducing grain size. Equiaxed grains and reduced crystal size give ultrasonically treated specimens greater tensile strength and lower elongation.

Ultrasonic treatment enhances hardness from SS 308L to IN 718 by 7%-15% due to microstructural changes, solid solution strengthening, and precipitation enhancement from Ni, Mo, and Nb content.

Most studies on wire-based additive manufacturing have focused on using ultrasonic vibration-assisted GMAW, CMT, and Laser-based WAAM systems to join different alloys such as steel, aluminium, and nickel. The understanding of the effects of UV on the microstructural and mechanical properties of Dissimilar SDSS 2507 -IN 718 alloy structures fabricated by CMT WAAM is currently limited. This work successfully utilised ultrasonic assistance in the CMT-based WAAM process to fabricate walls of dissimilar SDSS 2507 and IN 718 alloys. This study examined the ultrasonic-assisted microstructure and mechanical evaluation of the interface zone and compared it with normal conditions.

5.2.2 Microstructure

The microstructural grains of the SDSS2507-IN718 interface, IN718, and SDSS2507 alloy produced by CMT WAAM without and with UV-CMT are illustrated in Fig. 5.8. From Fig. 5.8 (A0, B0, C0), it is evident that the coarse elongated grains were formed when the CMT power was used without UV. The grain size obtained under these circumstances was 6.161 μm, as depicted in Fig. 5.8(b). The locally unidirectional solidification behaviour led to the extended grain growth along the build direction. Under the influence of UV in CMT WAAM, the grains underwent a transition from columnar to equiaxed, as depicted in Fig. 5.8(A1, B1, C1). This transition resulted in a reduction in grain size to 4.5972 μm.

The grain refinement trend caused by UV can be attributed to two main mechanisms: the breaking up of dendrites due to cavitation and the increased nucleation caused by cavitation (Jeong et al., 2024b; Ruirun et al., 2017; F. Wang et al., 2016). When UV is applied to the melting materials, it can result in the rapid generation of cavitation bubbles. Once the bubbles

collapsed, the resulting shocks created intense pressure waves that propagated through the acoustic field, potentially causing the fragmentation of elongated dendrite tips. At the same time, convection carried the dendritic tips into the undercooled melt. resulting in the formation of numerous grain nuclei. The ultrasonic cavitation induced a transition from a columnar to an equiaxed form in the molten materials at the elongated dendritic boundary (Gäumann et al., 2001), resulting in a significant decrease in the size of the microstructural grains. Transitioning from columnar to equiaxed grains can offer advantages in reducing grain size. Moreover, the attainment of a consistent dispersion of grains was made easier by the standardized temperature pattern created by ultrasonic vibration in particular regions (Ning et al., 2018).

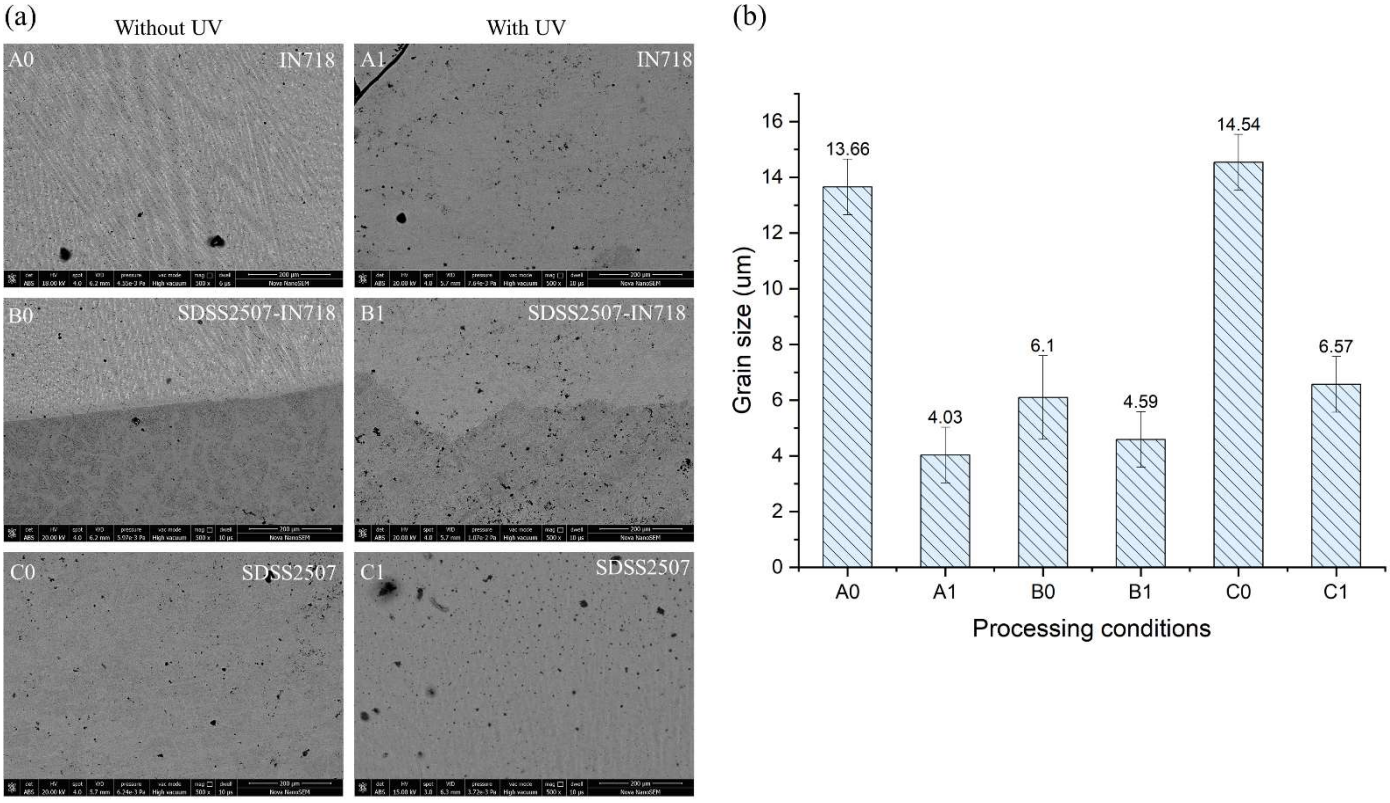

Fig. 5.8 (a) Microstructural characteristics without and with UV (b) Grain size variation under different processing conditions

5.2.3 Phase composition analysis

Fig. 5.9 displays the analysis results of the energy-dispersive X-ray spectroscope for Dissimilar SDSS2507-IN718 parts fabricated using CMT, both with and without the application of UV. It is observed that points 1 and 3 are rich in Ni, Fe, and Cr, while point 2 at the interface zone demonstrates the major variation in Ni, Cr, Fe, Nb and MO.

The white precipitated phase in IN718 point 1 was abundant in Ni, Cr, Nb, and Mo, which were the primary compositional elements of the Laves phase (Qi et al., 2009). The Laves phase was a brittle intermetallic compound abundant in Nb and had a typical composition of $(Ni, Cr, Fe)_2$ (Nb, Mo, Ti). Other investigations have also identified the Laves phase in CMT-fabricated IN718 components (Liu et al., 2013). The presence of Nb segregation in the IN718 alloy led to the development of irregularly shaped Laves phase, which was found to have a negative impact on the mechanical properties. This particular phase could potentially enhance crack propagation, resulting in a reduction in the overall strength and ductility of the IN718 alloy. SEM image shows the boundary at position 2. Due to SDSS 2507 and IN718's comparable composition, the IF had no defects, and the Cr distribution was consistent on both sides. From the EDS region scan, the IF showed no elemental segregation. The IN718 filler wire creates a molten pool on the SDSS 2507 layer at the IF. Dissolution of elements was confirmed throughout the IF. The EDS plot shows mixed components and no notable Cr changes.

According to reports, the presence of the Nb element exerts a substantial impact on the solidification sequence and the precipitation of strengthening phases in the IN718 alloy. In CMT, the solidification of IN718 starts with a primary liquid reaction, which enriches the interdendritic liquid with elements including Ti, Mo, and Nb. Eventually, the process concludes with a eutectic-type reaction (Wang et al., 2012). Because of the limited ability of larger Nb atoms to spread out, it was challenging to dissolve the Laves phase within the matrix of CMT-fabricated parts. However, using UV, the long-bar Laves phase morphology can be broken into

smaller particle shapes by delivering high-intensity shock waves. This is illustrated in the SEM images of Fig. 5.9. By introducing ultrasonic energy, the temperature of the molten pool can be raised, resulting in an increased solubility of Nb in the matrix phase. According to the results, UV helped dissolve the Laves phase partially within the matrix. The presence of a small-particle-shaped Laves phase in the matrix contributed to a uniform distribution, resulting in a homogenous phase distribution.

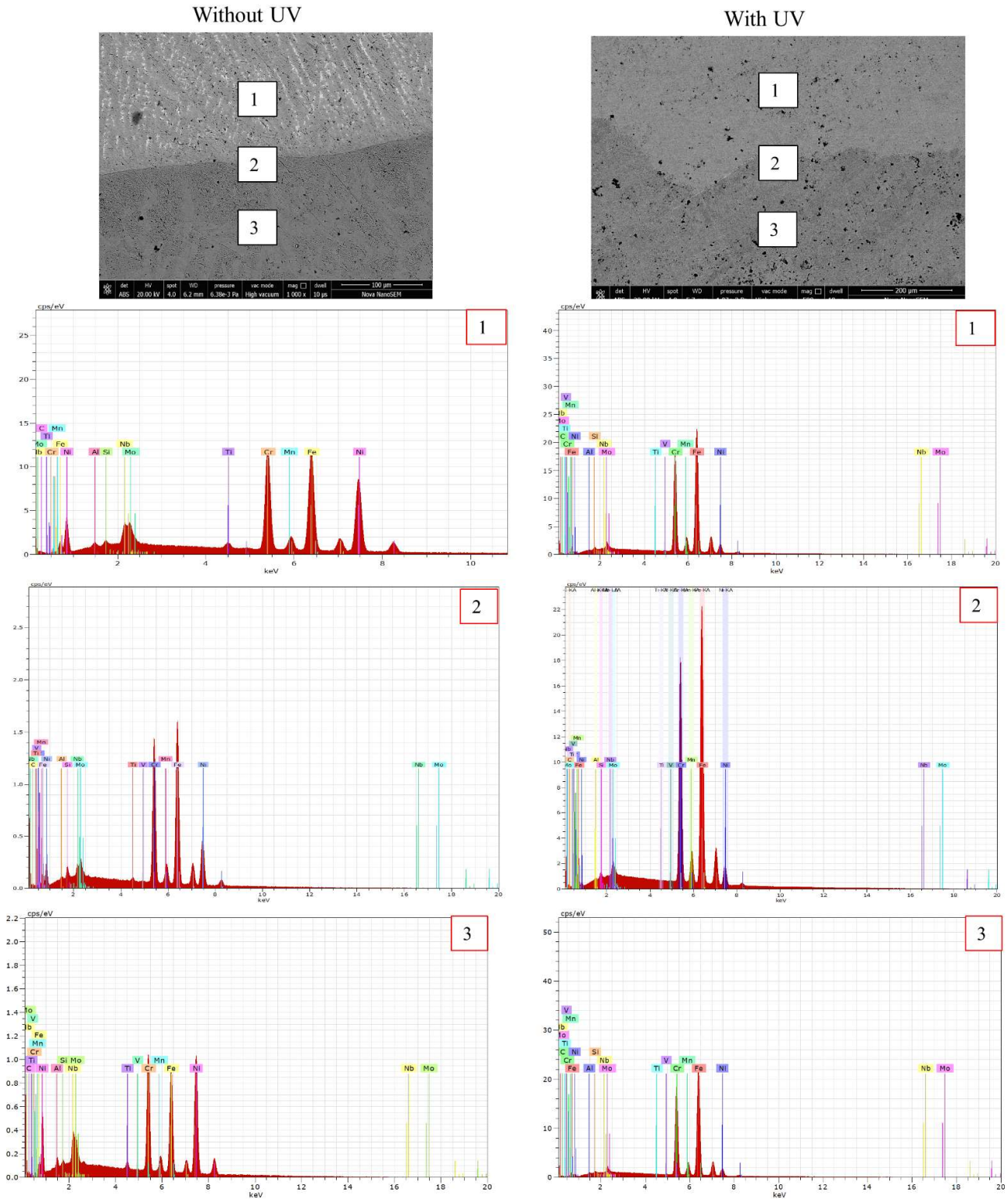

Fig. 5.9 Energy dispersive X-ray spectroscope analysis results of dissimilar SDSS2507-IN718 parts fabricated by CMT WAAM (a) Without ultrasonic vibrations (b) With ultrasonic vibrations

5.2.4 Microhardness analysis

Microhardness measurements were performed at three specific places, SDSS 2507, SDSS2507-IN 718 interface (IF), and IN718, along the building direction, as shown in Fig. 5.10 The application of UV led to a notable enhancement in microhardness, with a rise from the average value of 302 HV to 335 HV, with an 11% increment, at SDSS 2507, 233 HV to 265 HV at Interface with a 14% increment and 249 HV to 270 HV at IN 718 with a 9% increment. The findings indicate that ultrasound vibrations enhance the refinement of grain size resulting in increased microhardness. Furthermore, the hardness of the material is directly correlated with its microstructure. It is well-established that the microhardness tends to increase as the tensile strength increases. The reduction in porosity indicated earlier would be advantageous for achieving a more consistent density in the production of parts, hence increasing the quality of the parts with increased microhardness.

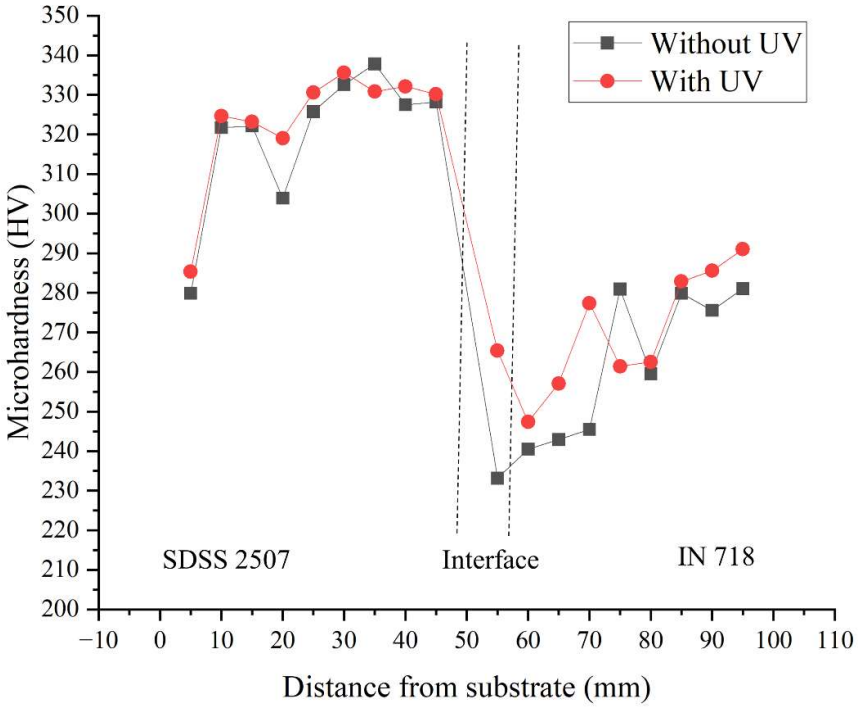

Fig. 5.10 Microhardness variation of Dissimilar SDSS 2507- IN 718 parts with or without UV

5.2.5 Tensile Properties

The stress-strain curve, UTS, yield strength, and ductility of dissimilar SDSS 2507-IN 718 components made under varying processing circumstances are shown in Fig. 5.11. The specimens' flow curves were identical with and without UV, but the results were very different. Tensile characteristics were demonstrated as a mean with one standard deviation. The addition of ultrasonic vibration in the CMT WAAM process led to a significant increase in tensile strength. However, it did not have a noticeable impact on ductility when compared to the process without ultrasonic vibration. The increase in yield strength and ultimate tensile strength can be ascribed to the reduction in grain size caused by ultrasonic vibration. Increases in yield strength and decreases in UTS are observed as grain sizes decrease in microstructure. The traditional Hall-Petch equation (Hall, 1951), states that yield strength/UTS is positively correlated with the reciprocal root of grain size, agreed with this tendency. In addition, UV reduced the presence of pores, broke down the Laves phase into smaller fragments, and promoted the even distribution of components. These factors also played a role in increasing yield strength and UTS.

To better understand how microstructure affects mechanical behaviour, specimens' tensile fracture surface morphology was examined. Fig. 5.12 displays the distinct tensile fracture surfaces of various specimens, including SDSS 2507, the interface between SDSS 2507 and IN 718, and IN 718, with or without UV. The specimens display equiaxed dimples and transgranular features in both UV and non-UV micrographs, indicating a ductile fracture mode with excellent ductility. Without UV, dimple sizes differed between locations (Fig. 5.12 a, b, c). The breakage of nearby grains caused large and deep dimples, while the fracture of a single grain caused dense and little dimples. Thus, coarse microstructure is linked to big dimples. The microstructure and grain size of the wall component were made smaller and more uniform

through the use of ultrasound. This resulted in superior mechanical properties and the presence of more evenly distributed dimples, which were smaller in size and depth (Fig. 5.12 d, e, f).

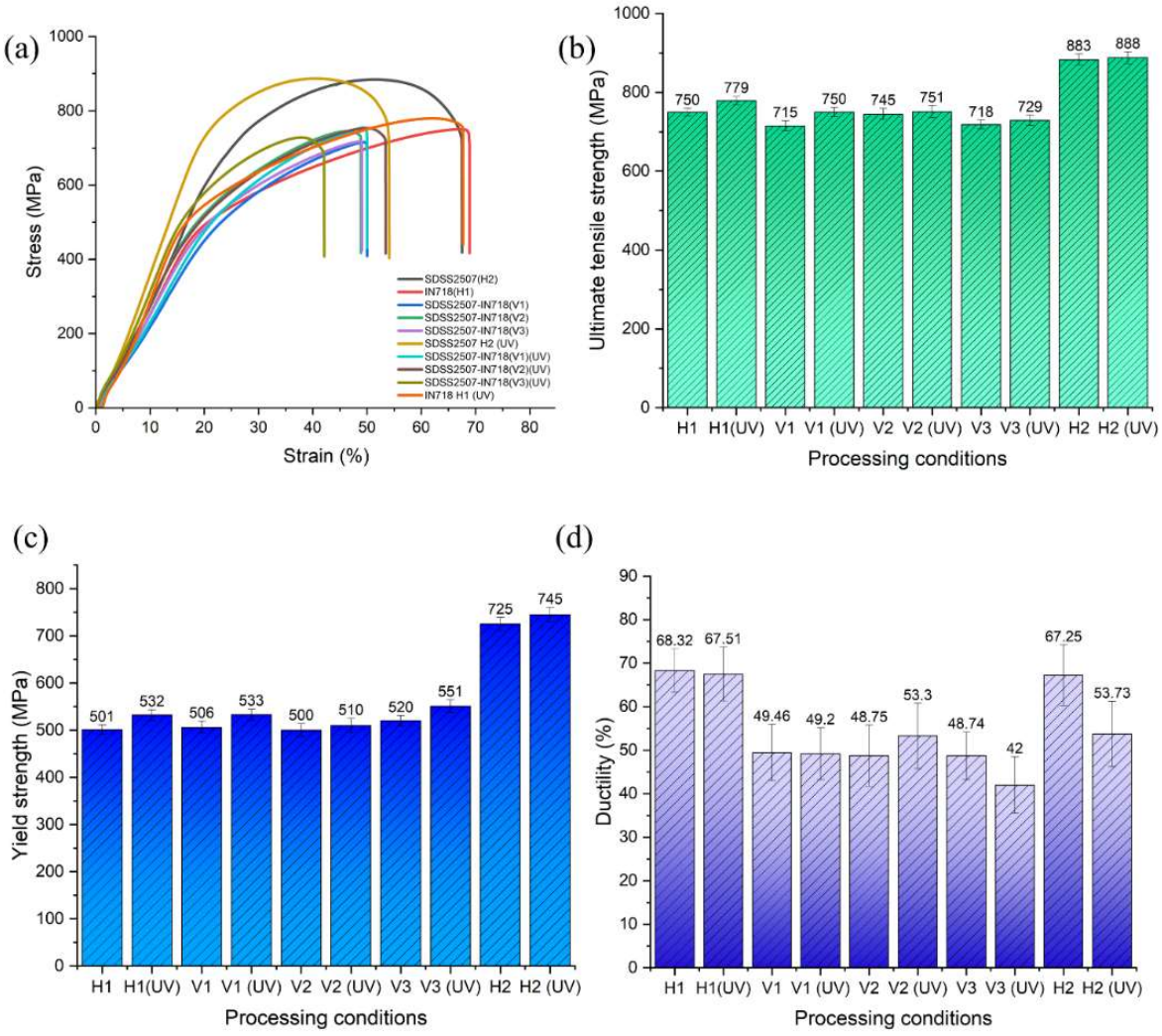

Fig. 5.11 Tensile test results of dissimilar SDSS 2507-IN 718 fabricated samples with or without UV (a) Stress- strain curve (b) UTS (c) Yield strength and (d) Ductility

As a result, the specimens experienced a notable increase in microhardness and strength when subjected to ultrasound. However, there was a slight decrease in elongation compared to specimens not treated with ultrasound. The discovery confirms the outcome that the strength of wall components experiences a notable boost while their plasticity sees a slight decline.

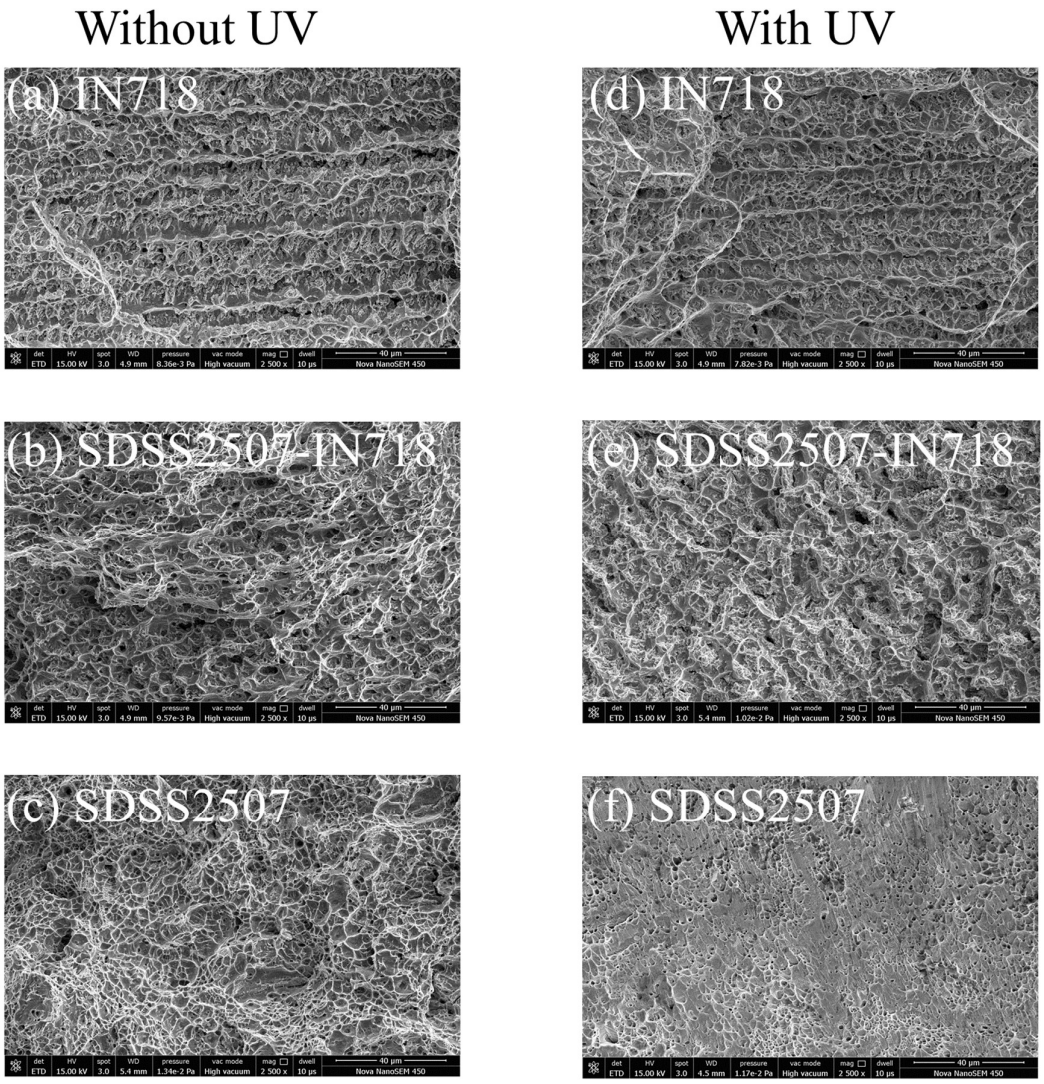

Fig. 5.12 SEM morphology of fractured surfaces (a, b, c) Without UV (d, e, f) With UV of Tensile specimens

5.3 Wear characteristics of Dissimilar SDSS 2507- IN 718 alloy WAAM wall

5.3.1 Introduction

Additive manufacturing is becoming more popular in many fields of study and industry because it can make complex parts with near-net shapes (Frazier, 2014; Herzog et al., 2016; Meena et al., 2024a). The WAAM process, which stands for wire-arc directed energy deposition, is an efficient and economical way to mass-produce almost finished components (Jeong et al., 2024c). The CMT is a highly innovative form of gas metal arc welding that significantly minimizes the heat produced while depositing metal. As a result, there is less spattering, and the arc becomes more stable. The CMT utilizes the reciprocal movements of the filler wire in the short-circuiting mode to transport materials. The CMT process is characterized by its distinct combination of wire movement and transfer mode (Cadiou et al., 2020; Rodriguez et al., 2018). The low heat in CMT WAAM proves advantageous for the deposition of dissimilar alloy additive manufacturing walls, including steel-nickel, steel-aluminium, and aluminium-nickel, which find widespread use in various industrial applications.

The wear properties of a heterogeneous functionally graded material (FGM) were examined by depositing SS316LSi and ER70S-6 utilising the twin WAAM technique by Aashish et al. (Yadav et al., 2024a). Worn surfaces indicated the presence of an adhesive wear mechanism. Results for the final deposited structure varied between SS316LSi and ER70S-6 in terms of wear rate and average coefficient of friction. The results show that when compared to SS316LSi and ER70S-6, the as-deposited FGM has superior mechanical performance and wear resistance. Yang et al.(Yang et al., 2022) investigated the tribological behaviour of Inconel 718 and tungsten carbide under lubrication. The disc material used for the ball-on-disc equipment was Inconel 718, and it exhibited a surface roughness of approximately 40 nm. On the flip side, a 10 mm tungsten carbide ball with a surface roughness of 25 nm was used as the counter body.

Experiments were carried out using input parameters of a 2 mm amplitude, a frequency of 20 Hz, and a duration of 5 minutes. The friction coefficient between Inconel 718 and tungsten carbide was significantly reduced to 0.1 through the use of sulfurized fatty acid ester as a sulphur additive. Yadav et al.(Yadav et al., 2024b) analysed the wear properties of austenitic stainless steel (ASS) produced by the wire arc direct energy deposition process. Reciprocating 10 mm diameter tungsten carbide balls were used to test ASS specimens with a stroke length of 2 mm. At 30 N, the wear rate reaches its peak, while at 20 N, the wear rate is at its lowest. Higher loads led to more pronounced plastic deformation in the wear track, resulting in an increased wear rate and coefficient of friction. In a study conducted by Brin et al.(Brin et al., 2001) wear experiments were conducted on AISI 304L to examine the structural characterization of wear debris in both water and methanol environments. Based on the wear debris observed in long-term friction experiments conducted in demineralized water or methanol, it is evident that martensite is the predominant phase.

After the literature survey, it was found that no study had been performed on the wear characteristics of dissimilar SDSS 2507-IN 718 alloys. Therefore, this study focused on the wear characteristics of SDSS 2507-IN 718 dissimilar alloy WAAM wall fabricated by the Cold Metal Transfer process. This study also covered the structure-property relationship of microstructural evolution and tribological behaviour. Fig. 5.13 shows the wear test setup and wear process.

Fig. 5.13 (a) Linear Reciprocating ball on disk wear set up (b) wear chamber with sample holder and specimen (c) ball surface contacting the disk with load (d) sliding marks on disk surface (e) Worn out samples

5.3.2 Tribological Behaviour

Fig. 5.14 demonstrates the wear rate (mm3/m) of SDSS 2507, SDSS 2507-IN 718 interface and IN 718 samples at different loads. It is evident from the findings that the wear rate exhibits a rising pattern as the load increases. The wear rate is a maximum of 55.4 × 10-3 mm3/m for IN 718 and a minimum of 2.2×10^{-3} mm^3/m for SDSS 2507. The SDSS 2507-IN 718 interface has a wear rate between the SDSS 2507 and IN 718 wear rates. Table 5.2 shows the wear properties of different samples.

Table 5.2 Wear properties of samples

Sr. No	Samples	Load (N)	Average COF	Wear rate × 10^{-3} (mm^3/m)
1	**1L (SDSS 2507)**	10	0.498	2.2
2	**2L (SDSS 2507)**	15	0.5686	2.8
3	**1M (SDSS 2507-IN718 interface)**	20	0.5899	10.8
4	**2M (SDSS 2507-IN718 interface)**	25	0.7466	15
5	**1U IN 718**	30	0.5556	49.3
6	**2U IN 718**	35	0.5727	55.4

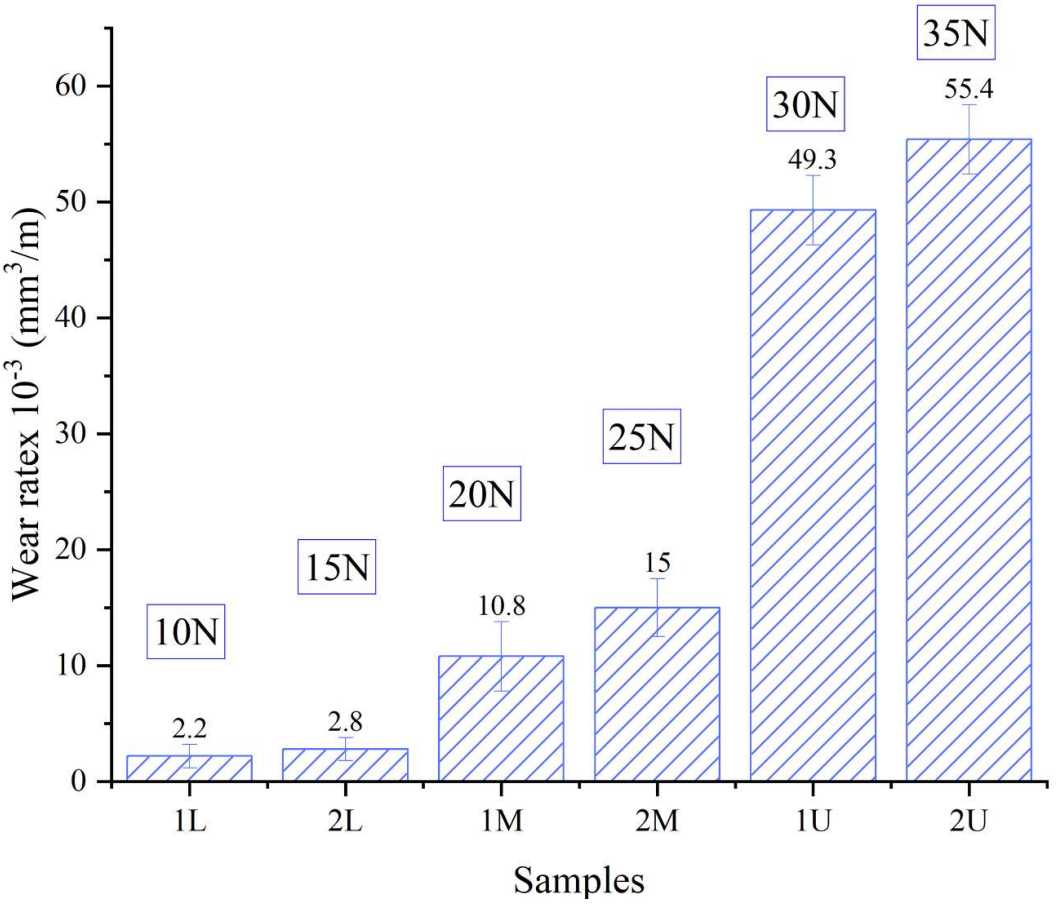

Fig. 5.14 Wear rate of different specimens at different loading conditions

Fig. 5.15 (a) displays the coefficient of friction (COF) variation with time for the SDSS 2507, SDSS 2507-IN 718 interfaces, and IN 718 samples obtained from the linear dry sliding wear test performed at normal room temperature. The COF values in almost all the samples exhibit fluctuations over time, ascribed to the accumulation of wear debris within the wear track, the presence of voids, and the impact of abrasiveness (Adesina et al., 2020a). The data clearly demonstrate that the COF exhibits a consistent upward trend as the load increases. The COF ranges from 0.49 to 0.56, 0.58 to 0.74 and 0.55 to 0.57 for SDSS 2507, SDSS 2507-IN 718 interface and IN 718 at different loads, respectively. However, the COF values obtained from the test are quite similar to those published in the literature for IN 718 superalloy, with some of the reported values ranging from 0.2 to 0.4 and 0.44 to 0.622 (Parvaresh et al., 2021; Z. Xu et al., 2021). Still, no work is reported on the wear properties of SDSS 2507 and dissimilar SDSS 2507-IN 718 alloys. SDSS 2507-IN 718 have a max COF of 0.74 while SDSS 2507 have a min COF. Fig. 5.15(b) shows the average COF for different samples at different loading conditions.

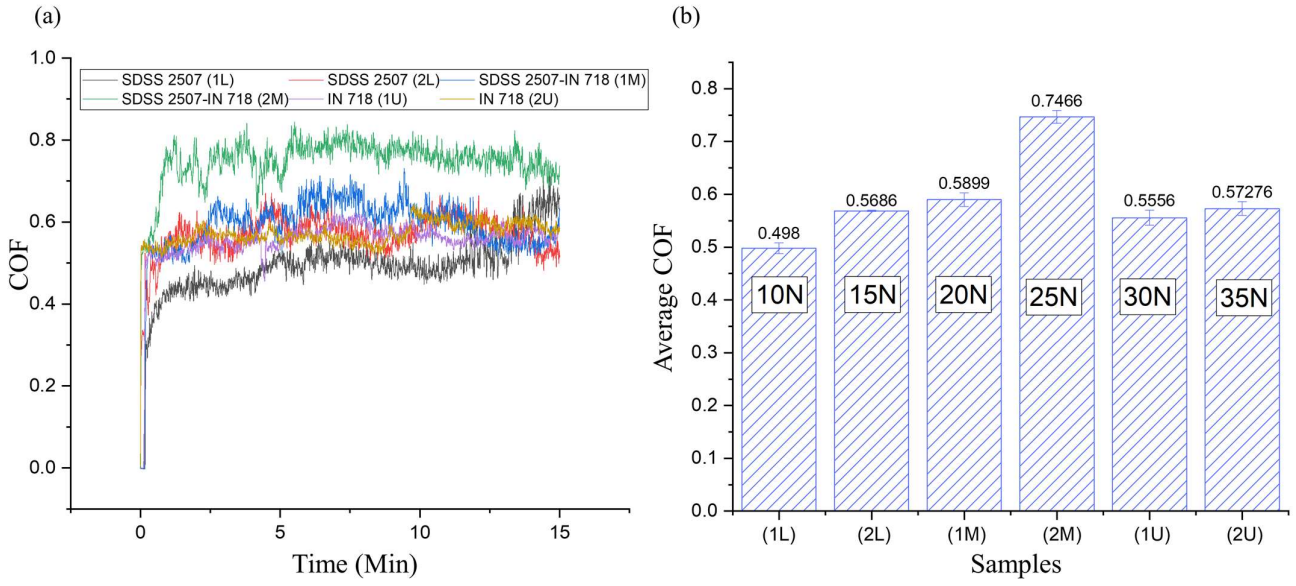

Fig. 5.15 (a) Coefficient of friction variation with time (b) Average COF of samples

5.3.3 Wear mechanism

The occurrence of sliding wear mechanisms in metals and alloys is influenced by various factors, such as the properties of the material, the shape of the contact surface, the applied force, the speed of sliding, and the distance over which sliding occurs (Straffelini et al., 2002). When two surfaces come into contact and slide against each other, they inevitably transfer both normal and tangential loads through the tiny imperfections on the material's surface. During this sliding process, the subsurface undergoes degradation or wear, with the most significant plastic strain taking place beneath the contact zone. As the strain on the material increases, it reaches a critical point where fractures occur, causing the loss of surface material. A material that is homogeneous has a strong resistance to deformation, and can withstand significant strain without breaking can exhibit excellent resistance to wear. These characteristics help to minimize plastic deformation and extend the lifespan before reaching the critical strain threshold that leads to fracture. SDSS 2507, SDSS 2507-IN718, and IN 718 are materials with varying grain morphologies that repeat along the building direction, depending on the number of layers used. Plastic deformation plays a larger role in wear when the material has lower wear resistance compared to a homogeneous material. The primary cause of wear is adhesion, which occurs when two surfaces come into contact. Even if the surfaces are not very rough, there will always be small irregularities where the contact pressure is high, leading to adhesion. The movement between the two surfaces causes significant plastic deformation and breakage of these deformed connections, resulting in the development of rigid wear particles as a result of the presence of intermetallic compounds. The SEM images (Fig. 5.16) reveal the presence of longitudinal wear scars or grooves, commonly referred to as abrasive scars, in the reciprocating direction. In addition, the images also indicate the presence of wear debris, which serves as evidence of an abrasive wear mechanism (Shang et al., 2021). Abrasive wear can occur through

two different mechanisms. The first mechanism is called two-body abrasive wear, where a harder object rubs against a softer surface, causing abrasion. The second mechanism is three-body abrasive wear (Adesina et al., 2019; Tombakti et al., 2023). The three-body abrasive wear process occurs when wear debris, which has undergone significant plastic deformation and has been trapped between the mating surfaces, abrades the relatively softer material. This debris is work-hardened and acts as an abrasive agent (Adesina et al., 2020; Fillot et al., 2007). Fig. 5.16 illustrates the prevalence of plasticity-driven wear in the ductile material under for the SDSS 2507-IN 718 interface and IN 718. Archard stated that a material's hardness has an inverse relationship with its wear volume (Wang et al., 2013). It is abundantly evident that low hardness causes IN 718 more plastic deformation at high heat input specimen (upper zone of wall); conversely, low heat input causes less plastic deformation in SDSS 2507 due to greater hardness value.

In addition, the worn surfaces had a smooth texture. The worn surfaces exhibit characteristics that suggest the occurrence of adhesive and abrasive wear mechanism under severe loads. Fig. 5.16 depicts the physical appearance of wear scars and particles on worn-out surfaces under intense loading conditions. The surfaces exhibited an appearance of metal and had seen substantial plastic deformation. FESEM investigations of worn surfaces show that the wear tracks consist of grooving, delamination, delamination cracks, ploughing grooves, parallel grooves, and particle adherence. The longitudinal scares or groves, wear debris shown indicates abrasive wear and plastic deformation, adhesive particles demonstrate adhesive wear. For all samples, there was no observation of a substantial portion of material being removed from the wear track, which suggests a significant occurrence of the adhesive wear mechanism. Therefor dissimilar SDSS-IN 718 wall depicts both adhesion and abrasion wear mechanism. Fig. 5.16 (c, f) presents the EDS analysis, which illustrates the elemental composition at several locations within the wear track of SDSS 2507-IN 718 and IN 718. Given that the counter-face silicon

carbide ball also contains silicon (Si) and carbon (C), it is likely that this debris originates from the sliding surfaces.

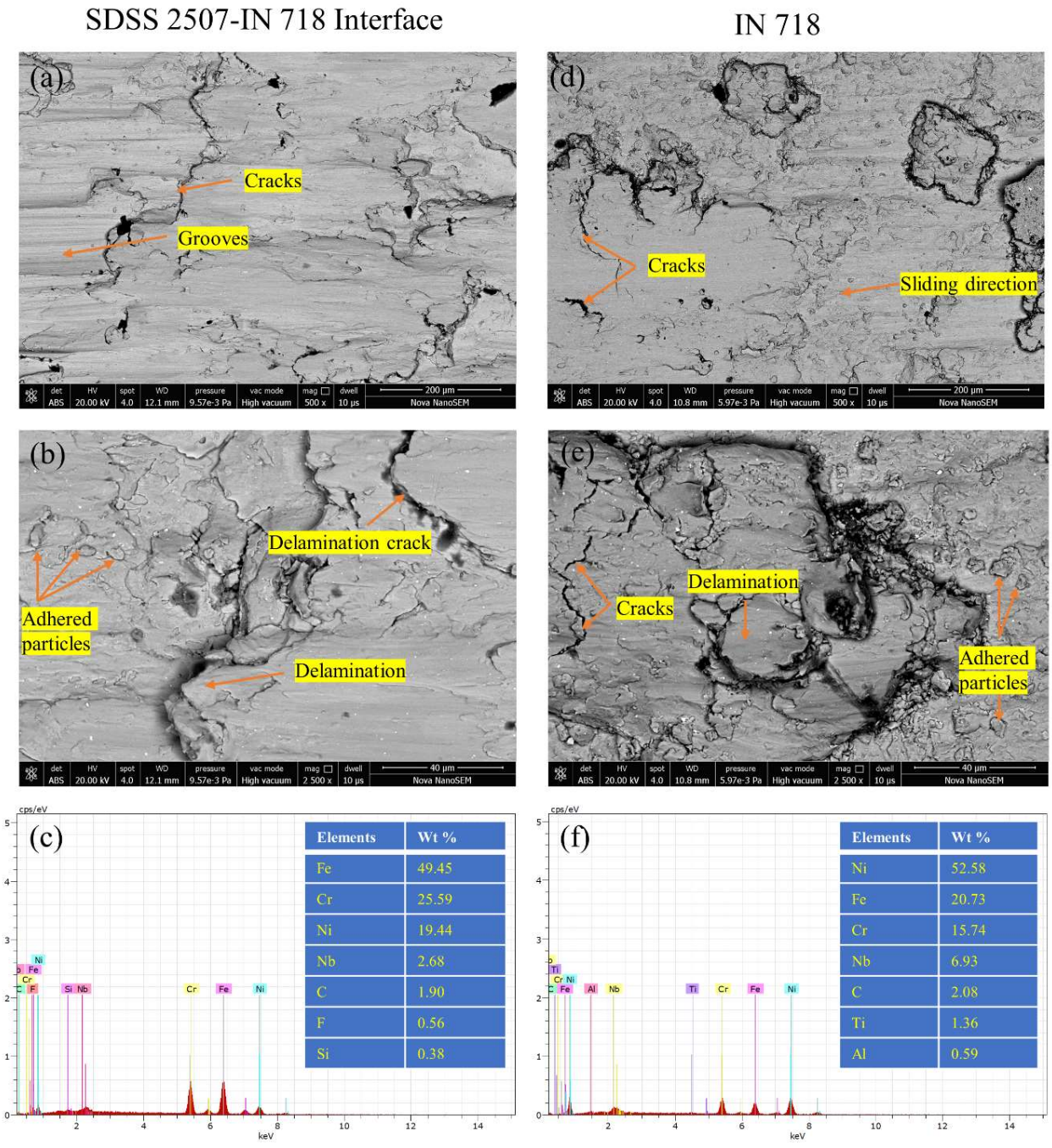

Fig. 5.16 FESEM image and EDS analysis of worn-out surface of specimens (Left column SDSS 2507-IN 718 interface, Right column IN 718)

Nevertheless, the substantial quantities of Ni, Fe, Cr, and Nb found in the debris, which closely match the composition of the SDSS 2507 and IN 718 alloy, suggest that the majority of the wear debris comes from the SDSS 2507 and IN 718 alloy. In addition, it is important to note that there is no presence of oxygen in the EDS result. It appears that there is no additional wear caused by surface oxidation or tribochemical reaction during the reciprocating tribological test.

5.4 Summary

This study delves into the microstructure and mechanical properties of a dissimilar alloy wall composed of SDSS 2507 and IN718 using CMT -WAAM. The text emphasizes the difficulties associated with combining different types of metals, specifically the issue of brittle intermetallic compounds (IMCs) forming. It also highlights the benefits of using WAAM to create strong connections between various alloys effectively. The microstructural analysis uncovered notable characteristics in SDSS 2507 and IN718, showcasing a strong bond at the interface and an absence of solidification cracks. The presence of phases such as aluminium-silicon, iron-nickel, and chromium-nickel, as well as IMCs, was confirmed through X-ray diffraction (XRD). The strong bonding and elemental distribution across the interface were confirmed using SEM and EDS. The hardness across the wall was found to vary, with a gradual decrease from the substrate upwards, as observed through microhardness testing. The tensile testing results revealed that the interface specimens exhibited robust mechanical properties. The fractography analysis of the tensile specimens showed a ductile fracture mode, where failure was observed on the SDSS 2507 side. This observation suggests a robust bond at the interface.

This study investigated the effects of UV on the microstructure and mechanical properties of dissimilar SDSS 2507-IN718 alloy structures created using CMT-WAAM. Notably, improvements were observed in the microstructure by incorporating UV into the fabrication process. The grains underwent a transformation from coarse columnar to finer equiaxed forms,

resulting in a reduction in grain size from 6.161 μm to 4.5972 μm. UV exposure also enhanced the dissolution and redistribution of the brittle Laves phase, resulting in a more uniform microstructure. The microstructural improvements resulted in significant microhardness and tensile strength enhancements, with only minimal impact on ductility.

This study explores the tribological behaviour of dissimilar alloy weldments created through CMT-based WAAM. The experiments showcased the successful creation of a 60-layer dissimilar alloy block without any cracks, achieved through alternating current. Tests using a ball-on-disc reciprocating tribometer revealed that the load directly impacted the coefficient of friction (COF) and wear rate, causing them to increase. SDSS 2507 displayed the lowest wear rate and COF, while Inconel 718 had the highest values. The SDSS 2507-IN 718 interface demonstrated behaviour that fell in between. Based on the findings, it was determined that the wear mechanism involved abrasion and significant plastic deformation in Inconel 718. This is attributed to its lower hardness. Consequently, it can be inferred that dissimilar SDSS-IN 718 walls undergo both adhesive and abrasive wear mechanisms.

CHAPTER 6

CONCLUSIONS AND SCOPE FOR FUTURE WORK

6.1 Conclusions

This chapter presents the primary findings that are drawn from the results and discussions on the CMT technique WAAM for the fabrication of WAAM samples.

6.1.1 Optimization of process parameters of CMT WAAM for fabrication of SDSS 2507 wall

- The size and shape of individual weld beads mainly affect the CMT process parameters, namely welding current, welding speed, and gas flow rate. The current and gas flow rate significantly impact weld bead width and height, while current and welding speed significantly affect dilution.
- The optimal setting of the input parameters for welding bead geometry is welding current (I) = 190.46 A, welding speed (S) = 8.6 mm/s, and gas flow rate (G) = 15 l/min. By utilizing these parameters, it becomes possible to fabricate smooth and uniform single-weld beads consistently with the desired weld bead geometry.
- The microstructure of the WAAM sample consists of austenite and ferrite phases. Widmanstädter austenite, intragranular austenite, and grain boundary austenite types of austenite found in the WAAM samples.
- The lower region of the deposited wall has the highest average microhardness, 332 ± 2.67 HV0.5. In contrast, the intermediate and upper regions have lower hardness values, 303 ± 2.36 and 289 ± 5.20, respectively, due to the variations attributed to temperature-induced distinctions in microstructural characteristics.

6.1.2 Optimization of process parameters of CMT WAAM for fabrication of IN 718 wall

- By utilizing RSM, the input processing parameters for CMT WAAM were optimized to I=210 A, S=7 mm/s, and G=25 l/min.
- The CMT WAAM Inconel 718 walls were constructed without substantial defects, resulting in solid bonding between layers.
- The typical microstructure of CMT WAAM Inconel 718 walls includes three phases: columnar, equiaxed, and fine dendrites. Columnar granules due to numerous heat cycles from consecutive depositions, the lower layer has larger grains than the top layer. The top part transitions from extended dendrites to fine dendrites since the last layer cooled faster due to an air environment around the sample and no remelting.

6.1.3 Dissimilar SDSS 2507-IN 718 Alloy CMT WAAM

- The CMT-WAAM technique can effectively manufacture dissimilar alloy SDSS 2507 and IN718 WAAM walls without any support structure. The microstructure was determined to be free of any microstructural defects, such as cracks.
- Microstructure reveals non-equilibrium microstructures in the deposited layers and epitaxial grain growth along the build direction. Due to thermal cycles and cooling rates, fine cellular grain structure shifts to a coarser structure with layer thickness.
- A SEM micrograph of SDSS 2507 reveals austenite and ferrite in the lower region, and IN718 shows columnar and cellular crystals with white bulk phases called laves phases, which develop when Nb and Mo elements segregate.
- The deposited samples exhibited isotropic mechanical characteristics. The SDSS 2507 region has an average hardness of 312 ± 9 HV, while the IN718 region had 249 ± 5 HV.

The interface area has 220–238 HV hardness, indicating SDSS 2507–IN718 element dissolution.

- The presence of numerous, uniformly distributed equiaxed, small depressions on the surface that failed under tension indicates a ductile fracture mechanism.

6.1.4 Ultrasonic Assisted Dissimilar SDSS 2507-IN 718 Alloy CMT WAAM

- The ultrasonic vibration assisted CMT WAAM used to produce of dissimilar SDSS 2507-IN 718 alloys WAAM samples.
- The microstructure investigation revealed that deposited welds consisted of dendrites and columnar grains. Utilizing ultrasonic vibration resulted in beneficial outcomes such as reducing the size of grains and inhibiting the preferential growth of large columnar grains.
- The Laves phase, which had a higher Ni concentration in the matrix phase, dissolved more easily with ultrasonic vibration. By employing ultrasonic vibration, the Laves phase morphology, which was characterized by a long bar shape, was uniformly fractured into small sphere-shaped particles. The fundamental reason for this was the extremely high pressure in the acoustic field that was created by ultrasonic vibration.
- The yield strength, UTS, and microhardness of different SDSS 2507-IN 718 components made with UV-CMT WAAM were significantly enhanced as a result of reduced porosity, refined grains, Laves phase fragmentation.

6.1.5 Wear Characterization of Dissimilar SDSS 2507-IN 718 Alloy CMT WAAM

- The CMT-WAAM method fabricated SDSS 2507 and IN718 WAAM walls without support.

- The maximum wear rate for IN 718 is 55.4 × 10-3 mm^3 /m, while the minimum wear rate for SDSS 2507 is 2.2 × 10-3 mm3/m. The wear rate of the SDSS 2507-IN 718 interfaces falls between the wear rates of SDSS 2507 and IN 718.
- Wear tracks consisting of grooving, delamination, delamination fractures, ploughing grooves, parallel grooves, and particle adherence demonstrate both adhesive and abrasive wear mechanisms, according to FESEM measurements of worn surfaces.

6.2 Scope for Future Work

- The setup can be optimized to enhance various process parameters, such as using different types of filler wire, adjusting the contact tip to workpiece distance (CTWD), and utilizing various shielding gases. Additionally, advancements like laser wire arc additive manufacturing can be explored to achieve superior mechanical properties.
- Simulation can be performed to validate experimental results, and thermal stress analysis, Distortion analysis, Microstructural analysis, and phase analysis can be performed through Simulation.
- The Cold Metal Transfer-based WAAM process can be optimised using the latest optimisation techniques, such as the Dragonfly Algorithm and Fish Swarm Optimization Algorithm (FSOA), for accuracy and precision.
- Robotic Cold Metal Transfer (CMT) technology can be utilized to carry out metal additive manufacturing with high precision and accuracy.
- High entropy alloy, Functionally Graded Material metal and Dissimilar alloy WAAM-like Steel-Aluminium, Steel -Titanium and Nickel-Titanium, Magnesium-Aluminium can be used to manufacture WAAM products and to perform their characterisation for more specific applications in industry.

REFERENCES

1) A Hosseini V, Högström M, Hurtig K, Valiente Bermejo MA, Stridh L-E, Karlsson L. Wire-arc additive manufacturing of a duplex stainless steel: thermal cycle analysis and microstructure characterization. Welding in the World 2019;63:975–87. https://doi.org/10.1007/s40194-019-00735-y.
2) Abe T, Sasahara H. Dissimilar metal deposition with a stainless steel and nickel-based alloy using wire and arc-based additive manufacturing. Precis Eng 2016a;45:387–95. https://doi.org/10.1016/J.PRECISIONENG.2016.03.016.
3) Abramov O V. Action of high intensity ultrasound on solidifying metal. Ultrasonics 1987;25:73–82. https://doi.org/10.1016/0041-624X(87)90063-1.
4) Adesina AY, Iqbal Z, Al-Badour FA, Gasem ZM. Mechanical and tribological characterization of AlCrN coated spark plasma sintered W–25%Re–Hfc composite material for FSW tool application. Journal of Materials Research and Technology 2019;8:436–46. https://doi.org/10.1016/J.JMRT.2018.04.004.
5) Adesina AY, Zainelabdeen IH, Dalhat MA, Mohammed AS, Sorour AA, Al-Badou FA. Influence of micronized waste tire rubber on the mechanical and tribological properties of epoxy composite coatings. Tribol Int 2020;146:106244. https://doi.org/10.1016/J.TRIBOINT.2020.106244.
6) Agrawal BP, Chauhan AK, Kumar R, Anant R, Kumar S. GTA pulsed current welding of thin sheets of SS304 producing superior quality of joint at high welding speed. Journal of the Brazilian Society of Mechanical Sciences and Engineering 2017;39:4667–75. https://doi.org/10.1007/s40430-017-0813-x.
7) Ali Y, Henckell P, Hildebrand J, Reimann J, Bergmann JP, Barnikol-Oettler S. Wire arc additive manufacturing of hot work tool steel with CMT process. J Mater Process Technol 2019a;269:109–16. https://doi.org/10.1016/J.JMATPROTEC.2019.01.034.
8) Artaza T, Suárez A, Veiga F, Braceras I, Tabernero I, Larrañaga O, et al. Wire arc additive manufacturing Ti6Al4V aeronautical parts using plasma arc welding: Analysis of heat-treatment processes in different atmospheres. Journal of Materials Research and Technology 2020;9:15454–66. https://doi.org/10.1016/J.JMRT.2020.11.012.
9) Ayan Y, Kahraman N. Fabrication and characterization of functionally graded material (FGM) structure containing two dissimilar steels (ER70S-6 and 308LSi) by wire arc additive manufacturing (WAAM). Mater Today Commun 2022;33:104457. https://doi.org/10.1016/J.MTCOMM.2022.104457.

10) Bai J, Ding HL, Gu JL, Wang XS, Qiu H. Porosity evolution in additively manufactured aluminium alloy during high temperature exposure. IOP Conf Ser Mater Sci Eng 2017;167:012045. https://doi.org/10.1088/1757-899X/167/1/012045.
11) Balasubramanian M, Choudary MV, Nagaraja A, Sai KOC. Cold metal transfer process – A review. Mater Today Proc 2020;33:543–9. https://doi.org/10.1016/J.MATPR.2020.05.225.
12) Barath Kumar MD, Manikandan M. Assessment of Process, Parameters, Residual Stress Mitigation, Post Treatments and Finite Element Analysis Simulations of Wire Arc Additive Manufacturing Technique. Metals and Materials International 2022;28:54–111. https://doi.org/10.1007/s12540-021-01015-5.
13) Baufeld B. Mechanical Properties of INCONEL 718 Parts Manufactured by Shaped Metal Deposition (SMD). J Mater Eng Perform 2012;21:1416–21. https://doi.org/10.1007/s11665-011-0009-y.
14) Baufeld B, Brandl E, Van Der Biest O. Wire based additive layer manufacturing: Comparison of microstructure and mechanical properties of Ti–6Al–4V components fabricated by laser-beam deposition and shaped metal deposition. J Mater Process Technol 2011;211:1146–58. https://doi.org/10.1016/J.JMATPROTEC.2011.01.018.
15) Bhuvanesh Kumar M, Sathiya P, Senthil SM. A critical review of wire arc additive manufacturing of nickel-based alloys: principles, process parameters, microstructure, mechanical properties, heat treatment effects, and defects. Journal of the Brazilian Society of Mechanical Sciences and Engineering 2023;45:164. https://doi.org/10.1007/s40430-023-04077-1.
16) Bi J, Shen J, Hu S, Zhen Y, Yin F, Bu X. Microstructure and mechanical properties of AZ91 Mg alloy fabricated by cold metal transfer additive manufacturing. Mater Lett 2020a;276:128185. https://doi.org/10.1016/J.MATLET.2020.128185.
17) Bless SJ. Drop transfer in short-circuit welding. J Phys D Appl Phys 1974;7:306. https://doi.org/10.1088/0022-3727/7/4/306.
18) Brice C, Shenoy R, Kral M, Buchannan K. Precipitation behavior of aluminum alloy 2139 fabricated using additive manufacturing. Materials Science and Engineering: A 2015;648:9–14. https://doi.org/10.1016/J.MSEA.2015.08.088.
19) Brin C, Rivière J-P, Eymery J-P, Villain J-P. Structural Characterization of Wear Debris Produced During Fric□on Between Two Austenitc Stainless Steel Antagonists. Tribol Lett 2001;11:127–32. https://doi.org/10.1023/A:1016612718139.

20) Butola R, Dev Pandey K, Murtaza Q, Walia RS, Tyagi M, Srinivas K, et al. Experimental analysis and optimization of process parameters using response surface methodology of surface nanocomposites fabricated by friction stir processing. Proceedings of the Institution of Mechanical Engineers, Part N: Journal of Nanomaterials, Nanoengineering and Nanosystems 2023:239779142311514. https://doi.org/10.1177/23977914231151485.
21) Cadiou S, Courtois M, Carin M, Berckmans W, Le masson P. 3D heat transfer, fluid flow and electromagnetic model for cold metal transfer wire arc additive manufacturing (Cmt-Waam). Addit Manuf 2020;36:101541. https://doi.org/10.1016/J.ADDMA.2020.101541.
22) Campatelli G, Campanella D, Barcellona A, Fratini L, Grossi N, Ingarao G. Microstructural, mechanical and energy demand characterization of alternative WAAM techniques for Al-alloy parts production. CIRP J Manuf Sci Technol 2020a;31:492–9. https://doi.org/10.1016/J.CIRPJ.2020.08.001.
23) Cao G, Konishi H, Li X. Mechanical Properties and Microstructure of Mg/SiC Nanocomposites Fabricated by Ultrasonic Cavitation Based Nanomanufacturing. J Manuf Sci Eng 2008;130. https://doi.org/10.1115/1.2823086.
24) Cao Q, Qi B, Zeng C, Zhang R, He B, Qi Z, et al. Achieving equiaxed microstructure and isotropic mechanical properties of additively manufactured AZ31 magnesium alloy via ultrasonic frequency pulsed arc. J Alloys Compd 2022;909:164742. https://doi.org/10.1016/J.JALLCOM.2022.164742.
25) Cao R, Feng Z, Lin Q, Chen JH. Study on cold metal transfer welding–brazing of titanium to copper. Materials & Design (1980-2015) 2014;56:165–73. https://doi.org/10.1016/J.MATDES.2013.10.044.
26) Cao R, Wen BF, Chen JH, Wang PC. Cold Metal Transfer joining of magnesium AZ31B-to-aluminum A6061-T6. Materials Science and Engineering: A 2013;560:256–66. https://doi.org/10.1016/J.MSEA.2012.09.065.
27) Carroll BE, Palmer TA, Beese AM. Anisotropic tensile behavior of Ti–6Al–4V components fabricated with directed energy deposition additive manufacturing. Acta Mater 2015;87:309–20. https://doi.org/10.1016/J.ACTAMAT.2014.12.054.
28) Caruso S, Umbrello D. Numerical and experimental validation of gas metal arc welding on AISI 441 ferritic stainless steel through mechanical and microstructural analysis. The International Journal of Advanced Manufacturing Technology 2022;120:7433–44. https://doi.org/10.1007/s00170-022-09208-x.

29) Cary HB. Modern Welding Technology 5/e. Industrial Robot: An International Journal 2004;31:376–376. https://doi.org/10.1108/ir.2004.31.4.376.3.
30) Chakkravarthy V, Jerome S. Printability of multiwalled SS 316L by wire arc additive manufacturing route with tunable texture. Mater Lett 2020;260:126981. https://doi.org/10.1016/J.MATLET.2019.126981.
31) Chandra M, Rajak S, K.E.K V. Deep learning-based framework for the observation of real-time melt pool and detection of anomaly in wire-arc additive manufacturing. Materials and Manufacturing Processes 2024;39:761–77. https://doi.org/10.1080/10426914.2023.2254386.
32) Chang T, Fang X, Liu G, Zhang H, Huang K. Wire and arc additive manufacturing of dissimilar 2319 and 5B06 aluminum alloys. J Mater Sci Technol 2022;124:65–75. https://doi.org/10.1016/J.JMST.2022.02.024.
33) Chen J, Wei H, Zhang X, Peng Y, Kong J, Wang K. Flow behavior and microstructure evolution during dynamic deformation of 316 L stainless steel fabricated by wire and arc additive manufacturing. Mater Des 2021;198:109325. https://doi.org/10.1016/J.MATDES.2020.109325.
34) Chen X, Han J, Wang J, Cai Y, Zhang G, Lu L, et al. A functionally graded material from TC4 to 316L stainless steel fabricated by double-wire + arc additive manufacturing. Mater Lett 2021;300:130141. https://doi.org/10.1016/J.MATLET.2021.130141.
35) Chi Y, Pan S, Liese M, Liu J, Murali N, Soemardy E, et al. Wire-Arc Directed Energy Deposition of Aluminum Alloy 7075 With Dispersed Nanoparticles. J Manuf Sci Eng 2023;145. https://doi.org/10.1115/1.4056257.
36) Choudhury SS, Marya SK, Amirthalingam M. Improving arc stability during wire arc additive manufacturing of thin-walled titanium components. J Manuf Process 2021;66:53–69. https://doi.org/10.1016/J.JMAPRO.2021.03.033.
37) Colegrove PA, Donoghue J, Martina F, Gu J, Prangnell P, Hönnige J. Application of bulk deformation methods for microstructural and material property improvement and residual stress and distortion control in additively manufactured components. Scr Mater 2017;135:111–8. https://doi.org/10.1016/J.SCRIPTAMAT.2016.10.031.
38) Cong B, Ding J, Williams S. Effect of arc mode in cold metal transfer process on porosity of additively manufactured Al-6.3%Cu alloy. The International Journal of Advanced Manufacturing Technology 2015;76:1593–606. https://doi.org/10.1007/s00170-014-6346-x.

39) Cornacchia G, Cecchel S, Panvini A. A comparative study of mechanical properties of metal inert gas (MIG)-cold metal transfer (CMT) and fiber laser-MIG hybrid welds for 6005A T6 extruded sheet. The International Journal of Advanced Manufacturing Technology 2018;94:2017–30. https://doi.org/10.1007/s00170-017-0914-9.

40) Corradi DR, Bracarense AQ, Wu B, Cuiuri D, Pan Z, Li H. Effect of Magnetic Arc Oscillation on the geometry of single-pass multi-layer walls and the process stability in wire and arc additive manufacturing. J Mater Process Technol 2020;283:116723. https://doi.org/10.1016/J.JMATPROTEC.2020.116723.

41) Costello SCA, Cunningham CR, Xu F, Shokrani A, Dhokia V, Newman ST. The state-of-the-art of wire arc directed energy deposition (WA-DED) as an additive manufacturing process for large metallic component manufacture. Int J Comput Integr Manuf 2023a;36:469–510. https://doi.org/10.1080/0951192X.2022.2162597.

42) Cunningham CR, Flynn JM, Shokrani A, Dhokia V, Newman ST. Invited review article: Strategies and processes for high quality wire arc additive manufacturing. Addit Manuf 2018a;22:672–86. https://doi.org/10.1016/J.ADDMA.2018.06.020.

43) Davis T. The effect of process parameters on laser-deposited TI-6A1-4V. University of Louisville, 2004. https://doi.org/10.18297/etd/319.

44) Deng D, Murakawa H. Numerical simulation of temperature field and residual stress in multi-pass welds in stainless steel pipe and comparison with experimental measurements. Comput Mater Sci 2006;37:269–77. https://doi.org/10.1016/J.COMMATSCI.2005.07.007.

45) Derekar KS. A review of wire arc additive manufacturing and advances in wire arc additive manufacturing of aluminium. Materials Science and Technology 2018;34:895–916. https://doi.org/10.1080/02670836.2018.1455012.

46) Dhinakaran V, Ajith J, Fathima Yasin Fahmidha A, Jagadeesha T, Sathish T, Stalin B. Wire Arc Additive Manufacturing (WAAM) process of nickel based superalloys – A review. Mater Today Proc 2020;21:920–5. https://doi.org/10.1016/J.MATPR.2019.08.159.

47) Dilberoglu UM, Gharehpapagh B, Yaman U, Dolen M. The Role of Additive Manufacturing in the Era of Industry 4.0. Procedia Manuf 2017;11:545–54. https://doi.org/10.1016/J.PROMFG.2017.07.148.

48) Ding D, Pan Z, Cuiuri D, Li H. Wire-feed additive manufacturing of metal components: technologies, developments and future interests. The International Journal of Advanced

Manufacturing Technology 2015a;81:465–81. https://doi.org/10.1007/s00170-015-7077-3.

49) Ding D, Wu B, Pan Z, Qiu Z, Li H. Wire arc additive manufacturing of Ti6AL4V using active interpass cooling. Materials and Manufacturing Processes 2020;35:845–51. https://doi.org/10.1080/10426914.2020.1732414.

50) Ding J, Colegrove P, Mehnen J, Ganguly S, Almeida PMS, Wang F, et al. Thermo-mechanical analysis of Wire and Arc Additive Layer Manufacturing process on large multi-layer parts. Comput Mater Sci 2011;50:3315–22. https://doi.org/10.1016/J.COMMATSCI.2011.06.023.

51) Dinovitzer M, Chen X, Laliberte J, Huang X, Frei H. Effect of wire and arc additive manufacturing (WAAM) process parameters on bead geometry and microstructure. Addit Manuf 2019;26:138–46. https://doi.org/10.1016/J.ADDMA.2018.12.013.

52) Dong M, Zhao Y, Li Q, Fei Y, Zhao T, Wang F, et al. Microstructure Evolution and Mechanical Property Anisotropy of Wire and Arc-Additive-Manufactured Wall Structure Using ER2319 Welding Wires. J Mater Eng Perform 2021;30:258–68. https://doi.org/10.1007/s11665-020-05336-1.

53) Ermakova A, Mehmanparast A, Ganguly S, Razavi N, Berto F. Investigation of mechanical and fracture properties of wire and arc additively manufactured low carbon steel components. Theoretical and Applied Fracture Mechanics 2020;109:102685. https://doi.org/10.1016/J.TAFMEC.2020.102685.

54) Ezatpour HR, Sajjadi SA, Sabzevar MH, Huang Y. Investigation of microstructure and mechanical properties of Al6061-nanocomposite fabricated by stir casting. Mater Des 2014;55:921–8. https://doi.org/10.1016/J.MATDES.2013.10.060.

55) Fang XY, Li HQ, Wang M, Li C, Guo YB. Characterization of texture and grain boundary character distributions of selective laser melted Inconel 625 alloy. Mater Charact 2018;143:182–90. https://doi.org/10.1016/J.MATCHAR.2018.02.008.

56) Farabi E, Klein T, Schnall M, Primig S. Effects of high deposition rate during cold metal transfer additive manufacturing on microstructure and properties of Ti-6Al-4V. Addit Manuf 2023a;71:103592. https://doi.org/10.1016/J.ADDMA.2023.103592.

57) Feng J, Zhang H, He P. The CMT short-circuiting metal transfer process and its use in thin aluminium sheets welding. Mater Des 2009;30:1850–2. https://doi.org/10.1016/J.MATDES.2008.07.015.

58) Fillot N, Iordanoff I, Berthier Y. Wear modeling and the third body concept. Wear 2007;262:949–57. https://doi.org/10.1016/J.WEAR.2006.10.011.

59) Frazier WE. Metal Additive Manufacturing: A Review. J Mater Eng Perform 2014;23:1917–28. https://doi.org/10.1007/s11665-014-0958-z.
60) Froes FH, Whittaker M. Titanium and Its Alloys. Encyclopedia of Materials: Metals and Alloys 2022:287–93. https://doi.org/10.1016/B978-0-12-819726-4.00066-1.
61) Fuse K, Badheka V, Oza AD, Prakash C, Buddhi D, Dixit S, et al. Microstructure and Mechanical Properties Analysis of Al/Cu Dissimilar Alloys Joining by Using Conventional and Bobbin Tool Friction Stir Welding. Materials 2022;15:5159. https://doi.org/10.3390/ma15155159.
62) Ganesh P, Kaul R, Paul CP, Tiwari P, Rai SK, Prasad RC, et al. Fatigue and fracture toughness characteristics of laser rapid manufactured Inconel 625 structures. Materials Science and Engineering: A 2010;527:7490–7. https://doi.org/10.1016/J.MSEA.2010.08.034.
63) Gao C, Chen Xiao, Su C, Chen Xizhang. Location dependence of microstructure and mechanical properties on wire arc additively manufactured nuclear grade steel. Vacuum 2019a;168:108818. https://doi.org/10.1016/J.VACUUM.2019.108818.
64) Gäumann M, Bezençon C, Canalis P, Kurz W. Single-crystal laser deposition of superalloys: processing–microstructure maps. Acta Mater 2001;49:1051–62. https://doi.org/10.1016/S1359-6454(00)00367-0.
65) Gazella MR, Polanka MD, Kemnitz RA, Eckley CC, Sexton BM, Sebastian JR, et al. High Temperature Oxidation of Additively and Traditionally Manufactured Inconel 718. J Eng Mater Technol 2024;146. https://doi.org/10.1115/1.4064180.
66) Ghaffari M, Vahedi Nemani A, Nasiri A. Microstructure and mechanical behavior of PH 13–8Mo martensitic stainless steel fabricated by wire arc additive manufacturing. Addit Manuf 2022;49:102374. https://doi.org/10.1016/J.ADDMA.2021.102374.
67) Girinath B, Shanmugam NS, Sathiyanarayanan C. Studies on influence of torch orientation on microstructure, mechanical properties and formability of AA5052 CMT welded blanks. Archives of Civil and Mechanical Engineering 2020;20:15. https://doi.org/10.1007/s43452-020-00021-5.
68) Gokhale NP, Kala P. Thermal analysis of TIG-WAAM based metal deposition process using finite element method. Mater Today Proc 2021;44:453–9. https://doi.org/10.1016/J.MATPR.2020.09.756.
69) Gu J, Ding J, Williams SW, Gu H, Ma P, Zhai Y. The effect of inter-layer cold working and post-deposition heat treatment on porosity in additively manufactured aluminum

alloys. J Mater Process Technol 2016;230:26–34. https://doi.org/10.1016/J.JMATPROTEC.2015.11.006.

70) Gu J, Wang X, Bai J, Ding J, Williams S, Zhai Y, et al. Deformation microstructures and strengthening mechanisms for the wire+arc additively manufactured Al-Mg4.5Mn alloy with inter-layer rolling. Materials Science and Engineering: A 2018;712:292–301. https://doi.org/10.1016/J.MSEA.2017.11.113.

71) Gullipalli C, Thawari N, Burad P, Gupta TVK. Residual stresses and distortions in additive manufactured Inconel 718. Materials and Manufacturing Processes 2023;38:1549–60. https://doi.org/10.1080/10426914.2023.2165663.

72) Guo N, Leu MC. Additive manufacturing: technology, applications and research needs. Frontiers of Mechanical Engineering 2013;8:215–43. https://doi.org/10.1007/s11465-013-0248-8.

73) Haldar N, Anand S, Datta S, Das A. On Fabrication of Inconel 718 Slab by Wire Arc Additive Manufacturing: Study of Built Microstructure and Mechanical Properties. Arab J Sci Eng 2024;49:2045–63. https://doi.org/10.1007/s13369-023-08095-y.

74) Hall EO. The Deformation and Ageing of Mild Steel: III Discussion of Results. Proceedings of the Physical Society Section B 1951;64:747–53. https://doi.org/10.1088/0370-1301/64/9/303.

75) Hamrani A, Bouarab FZ, Agarwal A, Ju K, Akbarzadeh H. Advancements and applications of multiple wire processes in additive manufacturing: a comprehensive systematic review. Virtual Phys Prototyp 2023;18. https://doi.org/10.1080/17452759.2023.2273303.

76) Haribaskar R, Kumar TS, Tamiloli N. Surface Integrity of additively manufactured Inconel-718 by peening approaches. Materials and Manufacturing Processes 2023;38:1009–19. https://doi.org/10.1080/10426914.2022.2146716.

77) Herzog D, Seyda V, Wycisk E, Emmelmann C. Additive manufacturing of metals. Acta Mater 2016;117:371–92. https://doi.org/10.1016/J.ACTAMAT.2016.07.019.

78) Hu Y, Ao N, Wu S, Yu Y, Zhang H, Qian W, et al. Influence of in situ micro-rolling on the improved strength and ductility of hybrid additively manufactured metals. Eng Fract Mech 2021;253:107868. https://doi.org/10.1016/J.ENGFRACMECH.2021.107868.

79) Hu Z, Hua L, Ni M, Ji F, Qin X. Microstructure and mechanical properties of directed energy deposition-arc/wire bimetallic hierarchical structures of hot-working tool steel and martensitic stainless steel. Addit Manuf 2023;67:103495. https://doi.org/10.1016/J.ADDMA.2023.103495.

80) Huan PC, Wang XN, Zhang QY, Di HS, Chen XM, Chen Y, et al. Study on droplet transition behavior, bead geometric characteristics and formability of wire + arc additively manufactured Inconel 718 alloy by using CMT MIX+ Synchropulse process. Journal of Materials Research and Technology 2022;17:1831–41. https://doi.org/10.1016/J.JMRT.2022.01.153.

81) Huang J, Liu G, Yu X, Wu H, Huang Y, Yu S, et al. Microstructure regulation of titanium alloy functionally gradient materials fabricated by alternating current assisted wire arc additive manufacturing. Mater Des 2022;218:110731. https://doi.org/10.1016/J.MATDES.2022.110731.

82) Huang X, Kwok CT, Niu B, Luo J, Zou X, Cao Y, et al. Anisotropic behavior of super duplex stainless steel fabricated by wire arc additive manufacturing. Journal of Materials Research and Technology 2023;27:1651–64. https://doi.org/10.1016/J.JMRT.2023.10.005.

83) Jadhav S, Jeong GH, Bajestani MS, Islam S, Lee H-J, Cho YT, et al. Investigation of surface roughness, microstructure, and mechanical properties of overhead structures fabricated by wire + arc additive manufacturing. The International Journal of Advanced Manufacturing Technology 2024;131:5001–21. https://doi.org/10.1007/s00170-024-13330-3.

84) James WS, Ganguly S, Pardal G. High temperature performance of wire-arc additive manufactured Inconel 718. Sci Rep 2023;13:4541. https://doi.org/10.1038/s41598-023-29026-9.

85) Jeong TW, Cho YT, Lee CM, Kim DH. Effects of ultrasonic treatment on mechanical properties and microstructure of stainless steel 308L and Inconel 718 functionally graded materials fabricated via double-wire arc additive manufacturing. Materials Science and Engineering: A 2024a;896:146298. https://doi.org/10.1016/J.MSEA.2024.146298.

86) Ji F, Qin X, Hu Z, Xiong X, Ni M, Wu M. Influence of ultrasonic vibration on molten pool behavior and deposition layer forming morphology for wire and arc additive manufacturing. International Communications in Heat and Mass Transfer 2022;130:105789. https://doi.org/10.1016/J.ICHEATMASSTRANSFER.2021.105789.

87) Jin W, Zhang C, Jin S, Tian Y, Wellmann D, Liu W. Wire Arc Additive Manufacturing of Stainless Steels: A Review. Applied Sciences 2020;10:1563. https://doi.org/10.3390/app10051563.

88) Jindal S, Chhibber R, Mehta NP. Effect of welding parameters on bead profile, microhardness and H_2 content in submerged arc welding of high-strength low-alloy steel.

Proc Inst Mech Eng B J Eng Manuf 2014a;228:82–94. https://doi.org/10.1177/0954405413495846.

89) Jurić I, Garašić I, Bušić M, Kožuh Z. Influence of Shielding Gas Composition on Structure and Mechanical Properties of Wire and Arc Additive Manufactured Inconel 625. JOM 2019;71:703–8. https://doi.org/10.1007/s11837-018-3151-2.

90) KA G, MJ J. Residual Stress and Distortion in Gas Metal Arc-Based Additive Manufacturing. SSRN Electronic Journal 2022. https://doi.org/10.2139/ssrn.4294602.

91) Kannan AR, Kumar SM, Pramod R, Shanmugam NS, Vishnukumar M, Channabasavanna SG. Microstructure and corrosion resistance of Ni-Cu alloy fabricated through wire arc additive manufacturing. Mater Lett 2022a;308:131262. https://doi.org/10.1016/J.MATLET.2021.131262.

92) Kannan AR, Shanmugam NS, Ramkumar KD, Rajkumar V. Studies on Super Duplex Stainless Steel Manufactured by Wire Arc Additive Manufacturing. Transactions of the Indian Institute of Metals 2021a;74:1673–81. https://doi.org/10.1007/s12666-021-02257-y.

93) Kannan RA, Shanmugam NS, Naveenkumar S. Effect of Arc Length Correction on Weld Bead Geometry and Mechanical Properties of AISI 316L Weldments by Cold Metal Transfer (CMT) Process. Mater Today Proc 2019;18:3916–21. https://doi.org/10.1016/J.MATPR.2019.07.331.

94) Kannan T, Yoganandh J. Effect of process parameters on clad bead geometry and its shape relationships of stainless steel claddings deposited by GMAW. The International Journal of Advanced Manufacturing Technology 2010;47:1083–95. https://doi.org/10.1007/s00170-009-2226-1.

95) Kattimani MA, Venkatesh PR, Masum H, Math MM, Bahadurdesai VN, Mustafkhadri S, et al. Design and numerical analysis of tensile deformation and fracture properties of induction hardened inconel 718 superalloy for gas turbine applications. International Journal on Interactive Design and Manufacturing (IJIDeM) 2023. https://doi.org/10.1007/s12008-023-01452-z.

96) Klein T, Arnoldt A, Lahnsteiner R, Schnall M. Microstructure and mechanical properties of a structurally refined Al–Mg–Si alloy for wire-arc additive manufacturing. Materials Science and Engineering: A 2022;830:142318. https://doi.org/10.1016/J.MSEA.2021.142318.

97) Klein T, Birgmann A, Schnall M. *In situ* alloying of aluminium-based alloys by (multi-)wire-arc additive manufacturing. MATEC Web of Conferences 2020;326:01003. https://doi.org/10.1051/matecconf/202032601003.

98) Koli Y, Yuvaraj N, Aravindan S, Vipin. Multi-response Mathematical Modeling for Prediction of Weld Bead Geometry of AA6061-T6 Using Response Surface Methodology. Transactions of the Indian Institute of Metals 2020;73:645–66. https://doi.org/10.1007/s12666-020-01883-2.

99) Koli Y, Yuvaraj N, Sivanandam A, Vipin. Control of humping phenomenon and analyzing mechanical properties of Al–Si wire-arc additive manufacturing fabricated samples using cold metal transfer process. Proc Inst Mech Eng C J Mech Eng Sci 2022;236:984–96. https://doi.org/10.1177/0954406221998402.

100) KOMAROV S V., KUWABARA M, ABRAMOV O V. High Power Ultrasonics in Pyrometallurgy: Current Status and Recent Development. ISIJ International 2005;45:1765–82. https://doi.org/10.2355/isijinternational.45.1765.

101) Koppu AK, Lautre NK, Motwani A, Puri Y. Mechanical and Microstructure Investigation of TiC-inoculated SS316LSi Thin Wall Deposited by CMT-WAAM. Transactions of the Indian Institute of Metals 2023;76:2307–14. https://doi.org/10.1007/s12666-023-02943-z.

102) Kore SD, Date PP, Kulkarni S V., Kumar S, Rani D, Kulkarni MR, et al. Application of electromagnetic impact technique for welding copper-to-stainless steel sheets. The International Journal of Advanced Manufacturing Technology 2011;54:949–55. https://doi.org/10.1007/s00170-010-2981-z.

103) Köse C, Topal C. Texture, microstructure and mechanical properties of laser beam welded AISI 2507 super duplex stainless steel. Mater Chem Phys 2022;289:126490. https://doi.org/10.1016/J.MATCHEMPHYS.2022.126490.

104) Kozamernik N, Bračun D, Klobčar D. WAAM system with interpass temperature control and forced cooling for near-net-shape printing of small metal components. The International Journal of Advanced Manufacturing Technology 2020;110:1955–68. https://doi.org/10.1007/s00170-020-05958-8.

105) Kumar M, Vaishya RO, Oza AD, Suri NM. Experimental Investigation of Wire-Electrochemical Discharge Machining (WECDM) Performance Characteristics for Quartz Material. Silicon 2020;12:2211–20. https://doi.org/10.1007/s12633-019-00309-z.

106) Kumar N, Bhavsar H, Mahesh PVS, Srivastava AK, Bora BJ, Saxena A, et al. Wire Arc Additive Manufacturing – A revolutionary method in additive manufacturing. Mater

Chem Phys 2022;285:126144. https://doi.org/10.1016/J.MATCHEMPHYS.2022.126144.

107) Kumar P, Maji K. Experimental investigations and parametric effects on depositions of super duplex stainless steel in wire arc additive manufacturing. Proceedings of the Institution of Mechanical Engineers, Part E: Journal of Process Mechanical Engineering 2023a:095440892311582. https://doi.org/10.1177/09544089231158253.

108) Kumar RR, Singh A, Kumar Amit, Ansu A kumar, Kumar Anup, Kumar S, et al. Enhancement of friction stir welding characteristics of alloy AA6061 by design of experiment methodology. International Journal on Interactive Design and Manufacturing (IJIDeM) 2023;17:2659–71. https://doi.org/10.1007/s12008-022-01106-6.

109) Langelandsvik G, Akselsen OM, Furu T, Roven HJ. Review of Aluminum Alloy Development for Wire Arc Additive Manufacturing. Materials 2021;14:5370. https://doi.org/10.3390/ma14185370.

110) Le VT, Doan QT, Mai DS, Bui MC, Tran HS, Van Tran X, et al. Prediction and optimization of processing parameters in wire and arc-based additively manufacturing of 316L stainless steel. Journal of the Brazilian Society of Mechanical Sciences and Engineering 2022a;44:394. https://doi.org/10.1007/s40430-022-03698-2.

111) Le VT, Mai DS, Paris H. Influences of the compressed dry air-based active cooling on external and internal qualities of wire-arc additive manufactured thin-walled SS308L components. J Manuf Process 2021;62:18–27. https://doi.org/10.1016/J.JMAPRO.2020.11.046.

112) Leif. Welding Duplex Stainless Steels — A Review Of Current Recommendations. Welding in the World 2012;56:65–76. https://doi.org/10.1007/BF03321351.

113) Lervåg M, Sørensen C, Robertstad A, Brønstad BM, Nyhus B, Eriksson M, et al. Additive Manufacturing with Superduplex Stainless Steel Wire by CMT Process. Metals (Basel) 2020;10:272. https://doi.org/10.3390/met10020272.

114) Li S, Ning J, Zhang GF, Zhang LJ, Wu J, Zhang LX. Microstructural and mechanical properties of wire-arc additively manufactured Al–Zn–Mg aluminum alloy: The comparison of as-deposited and heat-treated samples. Vacuum 2021;184:109860. https://doi.org/10.1016/J.VACUUM.2020.109860.

115) Li Y, Huang X, Horváth I, Zhang G. GMAW-based additive manufacturing of inclined multi-layer multi-bead parts with flat-position deposition. J Mater Process Technol 2018;262:359–71. https://doi.org/10.1016/J.JMATPROTEC.2018.07.010.

116) Li Y, Su C, Zhu J. Comprehensive review of wire arc additive manufacturing: Hardware system, physical process, monitoring, property characterization, application and future prospects. Results in Engineering 2022;13:100330. https://doi.org/10.1016/J.RINENG.2021.100330.

117) Liang Y, Hu S, Shen J, Zhang H, Wang P. Geometrical and microstructural characteristics of the TIG-CMT hybrid welding in 6061 aluminum alloy cladding. J Mater Process Technol 2017;239:18–30. https://doi.org/10.1016/J.JMATPROTEC.2016.08.005.

118) Lin J, Ma N, Lei Y, Murakawa H. Shear strength of CMT brazed lap joints between aluminum and zinc-coated steel. J Mater Process Technol 2013;213:1303–10. https://doi.org/10.1016/J.JMATPROTEC.2013.02.011.

119) Little RL. Welding and welding technology . 1973.

120) Liu F, Lin X, Leng H, Cao J, Liu Q, Huang C, et al. Microstructural changes in a laser solid forming Inconel 718 superalloy thin wall in the deposition direction. Opt Laser Technol 2013;45:330–5. https://doi.org/10.1016/J.OPTLASTEC.2012.06.028.

121) Liu J, Miao Y, Wang Z, Zhao Y, Wu Y, Li C. Improved strength in nickel-aluminum bronze/steel bimetallic component fabricated using arcing-wire arc additive manufacturing with alternating deposition strategy. J Manuf Process 2024;111:89–103. https://doi.org/10.1016/J.JMAPRO.2024.01.027.

122) Lorenzin G, Rutili G. The innovative use of low heat input in welding: experiences on ‘cladding’ and brazing using the CMT processPaper presented at the 4th National Welding Day, Workshop: “Brazing”, Genoa, 25–26 October 2007. Welding International 2009;23:622–32. https://doi.org/10.1080/09507110802543252.

123) Lu T, Liu C, Li Z, Wu Q, Wang J, Xu T, et al. Hot-wire arc additive manufacturing Ti–6.5Al–2Zr–1Mo–1V titanium alloy: Pore characterization, microstructural evolution, and mechanical properties. J Alloys Compd 2020;817:153334. https://doi.org/10.1016/J.JALLCOM.2019.153334.

124) Ma Q, Chen H, Ren N, Zhang Y, Hu L, Meng W, et al. Effects of Ultrasonic Vibration on Microstructure, Mechanical Properties, and Fracture Mode of Inconel 625 Parts Fabricated by Cold Metal Transfer Arc Additive Manufacturing. J Mater Eng Perform 2021;30:6808–20. https://doi.org/10.1007/s11665-021-06023-5.

125) Madhuri N, Jayakumar V, Sathishkumar M. Recent developments and challenges accompanying with wire arc additive manufacturing of Mg alloys: A review. Mater Today Proc 2021;46:8573–7. https://doi.org/10.1016/J.MATPR.2021.03.548.

126) Manjhi SK, Sekar P, Bontha S, Balan ASS. Effect of CMT-WAAM Process Parameters on Bead Geometry, Microstructure and Mechanical Properties of AZ31 Mg Alloy. J Mater Eng Perform 2023. https://doi.org/10.1007/s11665-023-08498-w.

127) Meena RP, N Y, Vipin. A review on wire arc additive manufacturing based on cold metal transfer. Materials and Manufacturing Processes 2024a;39:1315–41. https://doi.org/10.1080/10426914.2024.2323441.

128) Meena RP, Yuvaraj N, Vipin. Optimization of process parameters of cold metal transfer welding-based wire arc additive manufacturing of super Duplex stainless steel using response surface methodology. Proceedings of the Institution of Mechanical Engineers, Part E: Journal of Process Mechanical Engineering 2024b. https://doi.org/10.1177/09544089241230878.

129) Meena RP, Yuvaraj N, Vipin V. Investigations and Optimization of Cold Metal Transfer-based WAAM Process Parameters for Fabrication of Inconel 718 Samples using Response Surface Methodology. Arab J Sci Eng 2024c. https://doi.org/10.1007/s13369-024-08947-1.

130) Meng Y, Li J, Zhang S, Gao M, Gong M, Chen H. Wire arc additive manufacturing of Ni-Al intermetallic compounds through synchronous wire-powder feeding. J Alloys Compd 2023;943:169152. https://doi.org/10.1016/J.JALLCOM.2023.169152.

131) Mezrag B, Deschaux-Beaume F, Benachour M. Control of mass and heat transfer for steel/aluminium joining using Cold Metal Transfer process. Science and Technology of Welding and Joining 2015;20:189–98. https://doi.org/10.1179/1362171814Y.0000000271.

132) Montgomery DC. Design and analysis of experiments. John wiley & sons; 2017. n.d.

133) Motwani A, Kumar A, Puri Y, Lautre NK. Mechanical characteristics and microstructural investigation of CMT deposited bimetallic SS316LSi-IN625 thin wall for WAAM. Welding in the World 2023a;67:967–80. https://doi.org/10.1007/s40194-022-01403-4.

134) Mughal MP, Fawad H, Mufti R. Finite element prediction of thermal stresses and deformations in layered manufacturing of metallic parts. Acta Mech 2006;183:61–79. https://doi.org/10.1007/s00707-006-0329-4.

135) Mukherjee T. Recent progress in process, structure, properties, and performance in additive manufacturing. Science and Technology of Welding and Joining 2023;28:941–5. https://doi.org/10.1080/13621718.2023.2253588.

136) Mukherjee T, Zhang W, DebRoy T. An improved prediction of residual stresses and distortion in additive manufacturing. Comput Mater Sci 2017;126:360–72. https://doi.org/10.1016/J.COMMATSCI.2016.10.003.

137) Nagasai BP, Malarvizhi S, Balasubramanian V. Effect of welding processes on mechanical and metallurgical characteristics of carbon steel cylindrical components made by wire arc additive manufacturing (WAAM) technique. CIRP J Manuf Sci Technol 2022;36:100–16. https://doi.org/10.1016/J.CIRPJ.2021.11.005.

138) Nagesh DS, Datta GL. Prediction of weld bead geometry and penetration in shielded metal-arc welding using artificial neural networks. J Mater Process Technol 2002;123:303–12. https://doi.org/10.1016/S0924-0136(02)00101-2.

139) Ng CH, Bermingham MJ, Kent D, Dargusch MS. High stability and high strength β-titanium alloys for additive manufacturing. Materials Science and Engineering: A 2021;816:141326. https://doi.org/10.1016/J.MSEA.2021.141326.

140) Nikam PP, Arun D, Ramkumar KD, Sivashanmugam N. Microstructure characterization and tensile properties of CMT-based wire plus arc additive manufactured ER2594. Mater Charact 2020;169:110671. https://doi.org/10.1016/J.MATCHAR.2020.110671.

141) Ning F, Hu Y, Liu Z, Wang X, Li Y, Cong W. Ultrasonic Vibration-Assisted Laser Engineered Net Shaping of Inconel 718 Parts: Microstructural and Mechanical Characterization. J Manuf Sci Eng 2018;140. https://doi.org/10.1115/1.4039441.

142) Niu H, Jiang HC, Zhao MJ, Rong LJ. Effect of interlayer addition on microstructure and mechanical properties of NiTi/stainless steel joint by electron beam welding. J Mater Sci Technol 2021;61:16–24. https://doi.org/10.1016/J.JMST.2020.05.043.

143) Al Noman A, Kumar BK, Dickens T. Field assisted additive manufacturing for polymers and metals: materials and methods. Virtual Phys Prototyp 2023;18. https://doi.org/10.1080/17452759.2023.2256707.

144) Oliveira JP, Crispim B, Zeng Z, Omori T, Braz Fernandes FM, Miranda RM. Microstructure and mechanical properties of gas tungsten arc welded Cu-Al-Mn shape memory alloy rods. J Mater Process Technol 2019;271:93–100. https://doi.org/10.1016/J.JMATPROTEC.2019.03.020.

145) Osintsev KA, Konovalov S V., Gromov VE, Ivanov YF, Panchenko IA. Microstructure and mechanical properties of non-equiatomic Co25.4Cr15Fe37.9Mn3.5Ni16.8Si1.4 high-entropy alloy produced by wire-arc additive manufacturing. Mater Lett 2022;312:131675. https://doi.org/10.1016/J.MATLET.2022.131675.

146) Oza AD, Kumar A, Badheka V. Improving quartz micro-machining performance by magnetohydrodynamic and zinc-coated assisted traveling wire-electrochemical discharge machining process. Mater Today Proc 2020;28:970–6. https://doi.org/10.1016/J.MATPR.2019.12.334.

147) Oza AD, Kumar A, Badheka V, Arora A. Traveling Wire Electrochemical Discharge Machining (TW-ECDM) of Quartz Using Zinc Coated Brass Wire: Investigations on Material Removal Rate and Kerf Width Characteristics. Silicon 2019;11:2873–84. https://doi.org/10.1007/s12633-019-0070-y.

148) Palani PK, Murugan N. Development of mathematical models for prediction of weld bead geometry in cladding by flux cored arc welding. The International Journal of Advanced Manufacturing Technology 2006;30:669–76. https://doi.org/10.1007/s00170-005-0101-2.

149) Palmeira Belotti L, van Dommelen JAW, Geers MGD, Goulas C, Ya W, Hoefnagels JPM. Microstructural characterisation of thick-walled wire arc additively manufactured stainless steel. J Mater Process Technol 2022a;299:117373. https://doi.org/10.1016/J.JMATPROTEC.2021.117373.

150) Panchenko O, Kurushkin D, Mushnikov I, Khismatullin A, Popovich A. A high-performance WAAM process for Al–Mg–Mn using controlled short-circuiting metal transfer at increased wire feed rate and increased travel speed. Mater Des 2020;195:109040. https://doi.org/10.1016/J.MATDES.2020.109040.

151) Patarić A, Mihailović M, Gulišija Z. Quantitative metallographic assessment of the electromagnetic casting influence on the microstructure of 7075 Al alloy. J Mater Sci 2012;47:793–6. https://doi.org/10.1007/s10853-011-5855-3.

152) Pattanayak S, Sahoo SK. Gas metal arc welding based additive manufacturing—a review. CIRP J Manuf Sci Technol 2021;33:398–442. https://doi.org/10.1016/J.CIRPJ.2021.04.010.

153) Pattanayak S, Sahoo SK, Sahoo AK. Effect of electrode materials and process parameters on deposition characteristics during GMAW-AM. Materials and Manufacturing Processes 2023;38:1809–22. https://doi.org/10.1080/10426914.2023.2217895.

154) Pickin CG, Williams SW, Lunt M. Characterisation of the cold metal transfer (CMT) process and its application for low dilution cladding. J Mater Process Technol 2011;211:496–502. https://doi.org/10.1016/J.JMATPROTEC.2010.11.005.

155) Pickin CG, Young K. Evaluation of cold metal transfer (CMT) process for welding aluminium alloy. Science and Technology of Welding and Joining 2006;11:583–5. https://doi.org/10.1179/174329306X120886.

156) Piedra-Cascón W, Krishnamurthy VR, Att W, Revilla-León M. 3D printing parameters, supporting structures, slicing, and post-processing procedures of vat-polymerization additive manufacturing technologies: A narrative review. J Dent 2021;109:103630. https://doi.org/10.1016/J.JDENT.2021.103630.

157) Pollock TM, Tin S. Nickel-Based Superalloys for Advanced Turbine Engines: Chemistry, Microstructure and Properties. J Propuls Power 2006;22:361–74. https://doi.org/10.2514/1.18239.

158) Popovich VA, Borisov E V., Popovich AA, Sufiiarov VS, Masaylo D V., Alzina L. Functionally graded Inconel 718 processed by additive manufacturing: Crystallographic texture, anisotropy of microstructure and mechanical properties. Mater Des 2017;114:441–9. https://doi.org/10.1016/J.MATDES.2016.10.075.

159) Prado-Cerqueira JL, Camacho AM, Diéguez JL, Rodríguez-Prieto Á, Aragón AM, Lorenzo-Martín C, et al. Analysis of Favorable Process Conditions for the Manufacturing of Thin-Wall Pieces of Mild Steel Obtained by Wire and Arc Additive Manufacturing (WAAM). Materials 2018;11:1449. https://doi.org/10.3390/ma11081449.

160) Qi H, Azer M, Ritter A. Studies of Standard Heat Treatment Effects on Microstructure and Mechanical Properties of Laser Net Shape Manufactured INCONEL 718. Metallurgical and Materials Transactions A 2009;40:2410–22. https://doi.org/10.1007/s11661-009-9949-3.

161) Rajeev GP, Kamaraj M, Bakshi SR. Effect of correction parameters on deposition characteristics in cold metal transfer welding. Materials and Manufacturing Processes 2019;34:1205–16. https://doi.org/10.1080/10426914.2019.1628260.

162) Ramalho A, Santos TG, Bevans B, Smoqi Z, Rao P, Oliveira JP. Effect of contaminations on the acoustic emissions during wire and arc additive manufacturing of 316L stainless steel. Addit Manuf 2022;51:102585. https://doi.org/10.1016/J.ADDMA.2021.102585.

163) Rao PS, Gupta OP, Murty SSN, Rao ABK. Effect of process parameters and mathematical model for the prediction of bead geometry in pulsed GMA welding. The International Journal of Advanced Manufacturing Technology 2009;45:496–505. https://doi.org/10.1007/s00170-009-1991-1.

164) Ravi G, Murugan N, Arulmani R. Microstructure and mechanical properties of Inconel-625 slab component fabricated by wire arc additive manufacturing. Materials Science and Technology 2020;36:1785–95. https://doi.org/10.1080/02670836.2020.1836737.

165) Rodrigues TA, Bairrão N, Farias FWC, Shamsolhodaei A, Shen J, Zhou N, et al. Steel-copper functionally graded material produced by twin-wire and arc additive manufacturing (T-WAAM). Mater Des 2022a;213:110270. https://doi.org/10.1016/J.MATDES.2021.110270.

166) Rodrigues TA, Cipriano Farias FW, Zhang K, Shamsolhodaei A, Shen J, Zhou N, et al. Wire and arc additive manufacturing of 316L stainless steel/Inconel 625 functionally graded material: development and characterization. Journal of Materials Research and Technology 2022b;21:237–51. https://doi.org/10.1016/J.JMRT.2022.08.169.

167) Rodrigues TA, Duarte VR, Miranda RM, Santos TG, Oliveira JP. Ultracold-Wire and arc additive manufacturing (UC-WAAM). J Mater Process Technol 2021;296:117196. https://doi.org/10.1016/J.JMATPROTEC.2021.117196.

168) Rodrigues TA, Duarte VR, Tomás D, Avila JA, Escobar JD, Rossinyol E, et al. In-situ strengthening of a high strength low alloy steel during Wire and Arc Additive Manufacturing (WAAM). Addit Manuf 2020;34:101200. https://doi.org/10.1016/J.ADDMA.2020.101200.

169) Rodriguez N, Vázquez L, Huarte I, Arruti E, Tabernero I, Alvarez P. Wire and arc additive manufacturing: a comparison between CMT and TopTIG processes applied to stainless steel. Welding in the World 2018;62:1083–96. https://doi.org/10.1007/s40194-018-0606-6.

170) Rosli NA, Alkahari MR, bin Abdollah MF, Maidin S, Ramli FR, Herawan SG. Review on effect of heat input for wire arc additive manufacturing process. Journal of Materials Research and Technology 2021;11:2127–45. https://doi.org/10.1016/J.JMRT.2021.02.002.

171) Rubino F, Tucci F, Caruso S, Umbrello D, Carlone P. An integrated numerical approach to simulate the filler deposition and the shape distortions in gas metal arc welding. CIRP J Manuf Sci Technol 2023;45:26–34. https://doi.org/10.1016/J.CIRPJ.2023.05.010.

172) Ruirun C, Deshuang Z, Tengfei M, Hongsheng D, Yanqing S, Jingjie G, et al. Effects of ultrasonic vibration on the microstructure and mechanical properties of high alloying TiAl. Sci Rep 2017;7:41463. https://doi.org/10.1038/srep41463.

173) SAFARZADE A, SHARIFITABAR M, SHAFIEE AFARANI M. Effects of heat treatment on microstructure and mechanical properties of Inconel 625 alloy fabricated by

wire arc additive manufacturing process. Transactions of Nonferrous Metals Society of China 2020;30:3016–30. https://doi.org/10.1016/S1003-6326(20)65439-5.

174) Sales A, Kotousov A, Perilli E, Yin L. Improvement of the Fatigue Resistance of Super Duplex Stainless-Steel (SDSS) Components Fabricated by Wire Arc Additive Manufacturing (WAAM). Metals (Basel) 2022;12:1548. https://doi.org/10.3390/met12091548.

175) Sales A, Kotousov A, Yin L. Design against Fatigue of Super Duplex Stainless Steel Structures Fabricated by Wire Arc Additive Manufacturing Process. Metals (Basel) 2021;11:1965. https://doi.org/10.3390/met11121965.

176) Sames WJ, List FA, Pannala S, Dehoff RR, Babu SS. The metallurgy and processing science of metal additive manufacturing. International Materials Reviews 2016;61:315–60. https://doi.org/10.1080/09506608.2015.1116649.

177) Sarathchandra DT, Davidson MJ, Visvanathan G. Parameters effect on SS304 beads deposited by wire arc additive manufacturing. Materials and Manufacturing Processes 2020a;35:852–8. https://doi.org/10.1080/10426914.2020.1743852.

178) Sasikumar R, Kannan AR, Kumar SM, Pramod R, Kumar NP, Shanmugam NS, et al. Wire arc additive manufacturing of functionally graded material with SS 316L and IN625: Microstructural and mechanical perspectives. CIRP J Manuf Sci Technol 2022;38:230–42. https://doi.org/10.1016/J.CIRPJ.2022.05.005.

179) Schmidt P, El-Chaikh A, Christ H-J. Effect of Duplex Aging on the Initiation and Propagation of Fatigue Cracks in the Solute-rich Metastable β Titanium Alloy Ti 38-644. Metallurgical and Materials Transactions A 2011;42:2652–67. https://doi.org/10.1007/s11661-011-0662-7.

180) Selvamani ST, Yoganandan G, Bakkiyaraj M, Sivaraman V. Influence of Heat Input on Cold Metal Transfer Welded Joints. Materials and Manufacturing Processes 2022;37:1555–65. https://doi.org/10.1080/10426914.2022.2030877.

181) Selvi S, Vishvaksenan A, Rajasekar E. Cold metal transfer (CMT) technology - An overview. Defence Technology 2018a;14:28–44. https://doi.org/10.1016/J.DT.2017.08.002.

182) Shah S, Joshi A, Chauhan K, Oza A, Prakash C, Campilho RDSG, et al. Feasibility Analysis of Machining Cobalt-Chromium Alloy (Stellite-6) Using TiN Coated Binary Inserts. Materials 2022;15:7294. https://doi.org/10.3390/ma15207294.

183) Shang F, Chen S, Zhou L, Jia W, Cui T, Liang J, et al. Effect of laser energy volume density on wear resistance and corrosion resistance of 30Cr15MoY alloy steel coating

prepared by laser direct metal deposition. Surf Coat Technol 2021;421:127382. https://doi.org/10.1016/J.SURFCOAT.2021.127382.

184) Sharma S, Goyal A, Bharadwaj P, Oza AD, Pandey A. Application of metal matrix composite fabricated by reinforcement materials – A review. Mater Today Proc 2023. https://doi.org/10.1016/J.MATPR.2023.02.287.

185) Shi J, Li F, Chen S, Zhao Y, Tian H. Effect of in-process active cooling on forming quality and efficiency of tandem GMAW–based additive manufacturing. The International Journal of Advanced Manufacturing Technology 2019;101:1349–56. https://doi.org/10.1007/s00170-018-2927-4.

186) Silva L. Near-immersion active cooling for wire + arc additive manufacturing: from concept to application. Universidade Federal de Uberlândia, 2019. https://doi.org/10.14393/ufu.te.2019.2422.

187) da Silva LJ, Souza DM, de Araújo DB, Reis RP, Scotti A. Concept and validation of an active cooling technique to mitigate heat accumulation in WAAM. The International Journal of Advanced Manufacturing Technology 2020;107:2513–23. https://doi.org/10.1007/s00170-020-05201-4.

188) Singh SR, Khanna P. Wire arc additive manufacturing (WAAM): A new process to shape engineering materials. Mater Today Proc 2021;44:118–28. https://doi.org/10.1016/J.MATPR.2020.08.030.

189) Sonar T, Balasubramanian V, Malarvizhi S, Venkateswaran T, Sivakumar D. An overview on welding of Inconel 718 alloy - Effect of welding processes on microstructural evolution and mechanical properties of joints. Mater Charact 2021;174:110997. https://doi.org/10.1016/J.MATCHAR.2021.110997.

190) Soysal T, Kou S, Tat D, Pasang T. Macrosegregation in dissimilar-metal fusion welding. Acta Mater 2016;110:149–60. https://doi.org/10.1016/J.ACTAMAT.2016.03.004.

191) Sridar S, Klecka MA, Xiong W. Interfacial characteristics of P91 steel - Inconel 740H bimetallic structure fabricated using wire-arc additive manufacturing. J Mater Process Technol 2022;300:117396. https://doi.org/10.1016/J.JMATPROTEC.2021.117396.

192) Srinivasan D, Sevvel P, John Solomon I, Tanushkumaar P. A review on Cold Metal Transfer (CMT) technology of welding. Mater Today Proc 2022;64:108–15. https://doi.org/10.1016/J.MATPR.2022.04.016.

193) Srivastava M, Rathee S, Tiwari A, Dongre M. Wire arc additive manufacturing of metals: A review on processes, materials and their behaviour. Mater Chem Phys 2023a;294:126988. https://doi.org/10.1016/J.MATCHEMPHYS.2022.126988.

194) Srivastava S, Garg RK, Sharma VS, Sachdeva A. Measurement and Mitigation of Residual Stress in Wire-Arc Additive Manufacturing: A Review of Macro-Scale Continuum Modelling Approach. Archives of Computational Methods in Engineering 2021;28:3491–515. https://doi.org/10.1007/s11831-020-09511-4.

195) Straffelini G, Molinari A, Trabucco D. Sliding wear of austenitic and austenitic-ferritic stainless steels. Metallurgical and Materials Transactions A 2002;33:613–24. https://doi.org/10.1007/s11661-002-0123-4.

196) Su C, Chen X, Gao C, Wang Y. Effect of heat input on microstructure and mechanical properties of Al-Mg alloys fabricated by WAAM. Appl Surf Sci 2019a;486:431–40. https://doi.org/10.1016/J.APSUSC.2019.04.255.

197) Suárez A, Aldalur E, Veiga F, Artaza T, Tabernero I, Lamikiz A. Wire arc additive manufacturing of an aeronautic fitting with different metal alloys: From the design to the part. J Manuf Process 2021;64:188–97. https://doi.org/10.1016/J.JMAPRO.2021.01.012.

198) Sui S, Chen J, Li Z, Li H, Zhao X, Tan H. Investigation of dissolution behavior of laves phase in inconel 718 fabricated by laser directed energy deposition. Addit Manuf 2020;32:101055. https://doi.org/10.1016/J.ADDMA.2020.101055.

199) Sujan GK, Gazder AA, Awannegbe E, Li H, Pan Z, Liang D, et al. Hot Deformation Behavior and Microstructural Evolution of Wire-Arc Additively Fabricated Inconel 718 Superalloy. Metallurgical and Materials Transactions A 2023;54:226–40. https://doi.org/10.1007/s11661-022-06863-3.

200) Sun QJ, Lin SB, Yang CL, Zhao GQ. Penetration increase of AISI 304 using ultrasonic assisted tungsten inert gas welding. Science and Technology of Welding and Joining 2009;14:765–7. https://doi.org/10.1179/136217109X12505932584772.

201) Surani K, Patel S, Alrubaie AJ, Oza A, Panchal H, Kumar S, et al. Performance comparison of powder mixed EDM and traditional EDM on TZM-molybdenum super alloy using response surface methodology. International Journal on Interactive Design and Manufacturing (IJIDeM) 2023;17:2647–58. https://doi.org/10.1007/s12008-022-01088-5.

202) Suryakumar S, Karunakaran KP, Bernard A, Chandrasekhar U, Raghavender N, Sharma D. Weld bead modeling and process optimization in Hybrid Layered Manufacturing. Computer-Aided Design 2011;43:331–44. https://doi.org/10.1016/J.CAD.2011.01.006.

203) Tanrikulu AA, Farhang B, Ganesh-Ram AK, Hekmatjou H, Amerinatanzi A. Microstructure Evaluation of Magnetic Field–Assisted Dissimilar Laser Welding of NiTi to Stainless Steel. J Manuf Sci Eng 2024;146. https://doi.org/10.1115/1.4064158.

204) Tanvir ANM, Ahsan MdRU, Ji C, Hawkins W, Bates B, Kim DB. Heat treatment effects on Inconel 625 components fabricated by wire + arc additive manufacturing (WAAM)—part 1: microstructural characterization. The International Journal of Advanced Manufacturing Technology 2019;103:3785–98. https://doi.org/10.1007/s00170-019-03828-6.

205) Thomas-Seale LEJ, Kirkman-Brown JC, Attallah MM, Espino DM, Shepherd DET. The barriers to the progression of additive manufacture: Perspectives from UK industry. Int J Prod Econ 2018;198:104–18. https://doi.org/10.1016/J.IJPE.2018.02.003.

206) Tian Y, Shen J, Hu S, Wang Z, Gou J. Microstructure and mechanical properties of wire and arc additive manufactured Ti-6Al-4V and AlSi5 dissimilar alloys using cold metal transfer welding. J Manuf Process 2019;46:337–44. https://doi.org/10.1016/J.JMAPRO.2019.09.006.

207) Todaro CJ, Easton MA, Qiu D, Zhang D, Bermingham MJ, Lui EW, et al. Grain structure control during metal 3D printing by high-intensity ultrasound. Nat Commun 2020;11:142. https://doi.org/10.1038/s41467-019-13874-z.

208) Tomar B, Shiva S, Nath T. A review on wire arc additive manufacturing: Processing parameters, defects, quality improvement and recent advances. Mater Today Commun 2022;31:103739. https://doi.org/10.1016/J.MTCOMM.2022.103739.

209) Tombakti IA, Adesina AY, Alharith A, Attallah MM, AlMangour B. Effect of Laser Mode and Power on the Tribological Behavior of Additively Manufactured Inconel 718 Alloy. J Tribol 2023;145. https://doi.org/10.1115/1.4062361.

210) Tripathi U, Saini N, Mulik RS, Mahapatra MM. Effect of build direction on the microstructure evolution and their mechanical properties using GTAW based wire arc additive manufacturing. CIRP J Manuf Sci Technol 2022;37:103–9. https://doi.org/10.1016/J.CIRPJ.2022.01.010.

211) Vinoth V, Sathiyamurthy S, Natarajan U, Venkatkumar D, Prabhakaran J, Sanjeevi Prakash K. Examination of microstructure properties of AISI 316L stainless steel fabricated by wire arc additive manufacturing. Mater Today Proc 2022;66:702–6. https://doi.org/10.1016/J.MATPR.2022.04.011.

212) Vishnukumar M, Pramod R, Rajesh Kannan A. Wire arc additive manufacturing for repairing aluminium structures in marine applications. Mater Lett 2021;299:130112. https://doi.org/10.1016/J.MATLET.2021.130112.

213) Wang C, Liu TG, Zhu P, Lu YH, Shoji T. Study on microstructure and tensile properties of 316L stainless steel fabricated by CMT wire and arc additive manufacturing. Materials

Science and Engineering: A 2020;796:140006. https://doi.org/10.1016/J.MSEA.2020.140006.

214) Wang F, Eskin D, Mi J, Connolley T, Lindsay J, Mounib M. A refining mechanism of primary Al3Ti intermetallic particles by ultrasonic treatment in the liquid state. Acta Mater 2016;116:354–63. https://doi.org/10.1016/J.ACTAMAT.2016.06.056.

215) Wang F, Williams S, Rush M. Morphology investigation on direct current pulsed gas tungsten arc welded additive layer manufactured Ti6Al4V alloy. The International Journal of Advanced Manufacturing Technology 2011a;57:597–603. https://doi.org/10.1007/s00170-011-3299-1.

216) Wang J, Feng JC, Wang YX. Microstructure of Al–Mg dissimilar weld made by cold metal transfer MIG welding. Materials Science and Technology 2008;24:827–31. https://doi.org/10.1179/174328408X278411.

217) Wang J, Zhao Z, Bai P, Zhang R, Zhang Z, Wang L, et al. Microstructure and mechanical properties of AZ31 magnesium alloy prepared using wire arc additive manufacturing. J Alloys Compd 2023;939:168665. https://doi.org/10.1016/J.JALLCOM.2022.168665.

218) Wang JF, Sun QJ, Wang H, Liu JP, Feng JC. Effect of location on microstructure and mechanical properties of additive layer manufactured Inconel 625 using gas tungsten arc welding. Materials Science and Engineering: A 2016;676:395–405. https://doi.org/10.1016/J.MSEA.2016.09.015.

219) Wang K, Liu Y, Sun Z, Lin J, Lv Y, Xu B. Microstructural evolution and mechanical properties of Inconel 718 superalloy thin wall fabricated by pulsed plasma arc additive manufacturing. J Alloys Compd 2020;819:152936. https://doi.org/10.1016/J.JALLCOM.2019.152936.

220) Wang L, Xue J, Wang Q. Correlation between arc mode, microstructure, and mechanical properties during wire arc additive manufacturing of 316L stainless steel. Materials Science and Engineering: A 2019;751:183–90. https://doi.org/10.1016/J.MSEA.2019.02.078.

221) Wang L, Zhang Y, Hua X, Shen C, Li F, Huang Y, et al. Twin-wire plasma arc additive manufacturing of the Ti–45Al titanium aluminide: Processing, microstructures and mechanical properties. Intermetallics (Barking) 2021;136:107277. https://doi.org/10.1016/J.INTERMET.2021.107277.

222) Wang P, Zhang H, Zhu H, Li Q, Feng M. Wire-arc additive manufacturing of AZ31 magnesium alloy fabricated by cold metal transfer heat source: Processing,

microstructure, and mechanical behavior. J Mater Process Technol 2021a;288:116895. https://doi.org/10.1016/J.JMATPROTEC.2020.116895.

223) Wang Q, Zhang PZ, Wei DB, Chen XH, Wang RN, Wang HY, et al. Microstructure and sliding wear behavior of pure titanium surface modified by double-glow plasma surface alloying with Nb. Materials & Design (1980-2015) 2013;52:265–73. https://doi.org/10.1016/J.MATDES.2013.05.061.

224) Wang Y, Chen X, Shen Q, Su C, Zhang Y, Jayalakshmi S, et al. Effect of magnetic Field on the microstructure and mechanical properties of inconel 625 superalloy fabricated by wire arc additive manufacturing. J Manuf Process 2021a;64:10–9. https://doi.org/10.1016/J.JMAPRO.2021.01.008.

225) Wang Z, Beese AM. Effect of chemistry on martensitic phase transformation kinetics and resulting properties of additively manufactured stainless steel. Acta Mater 2017;131:410–22. https://doi.org/10.1016/J.ACTAMAT.2017.04.022.

226) Wang Z, Gao Y, Huang J, Wu C, Wang G, Liu J. Precipitation phenomena and strengthening mechanism of Al–Cu alloys deposited by in-situ rolled wire-arc additive manufacturing. Materials Science and Engineering: A 2022;855:143770. https://doi.org/10.1016/J.MSEA.2022.143770.

227) Wang Z, Guan K, Gao M, Li X, Chen X, Zeng X. The microstructure and mechanical properties of deposited-IN718 by selective laser melting. J Alloys Compd 2012;513:518–23. https://doi.org/10.1016/J.JALLCOM.2011.10.107.

228) Warsi R, Kazmi KH, Chandra M. Mechanical properties of wire and arc additive manufactured component deposited by a CNC controlled GMAW. Mater Today Proc 2022;56:2818–25. https://doi.org/10.1016/J.MATPR.2021.10.114.

229) Wei Y, Liu Fencheng, Liu Fenggang, Yu D, You Q, Huang C, et al. Effect of arc oscillation on porosity and mechanical properties of 2319 aluminum alloy fabricated by CMT-wire arc additive manufacturing. Journal of Materials Research and Technology 2023a;24:3477–90. https://doi.org/10.1016/J.JMRT.2023.03.203.

230) Williams SW, Martina F, Addison AC, Ding J, Pardal G, Colegrove P. Wire + Arc Additive Manufacturing. Materials Science and Technology 2016;32:641–7. https://doi.org/10.1179/1743284715Y.0000000073.

231) Wu B, Ding D, Pan Z, Cuiuri D, Li H, Han J, et al. Effects of heat accumulation on the arc characteristics and metal transfer behavior in Wire Arc Additive Manufacturing of Ti6Al4V. J Mater Process Technol 2017;250:304–12. https://doi.org/10.1016/J.JMATPROTEC.2017.07.037.

232) Wu B, Pan Z, Ding D, Cuiuri D, Li H. Effects of heat accumulation on microstructure and mechanical properties of Ti6Al4V alloy deposited by wire arc additive manufacturing. Addit Manuf 2018a;23:151–60. https://doi.org/10.1016/J.ADDMA.2018.08.004.

233) Wu B, Pan Z, Ding D, Cuiuri D, Li H, Xu J, et al. A review of the wire arc additive manufacturing of metals: properties, defects and quality improvement. J Manuf Process 2018b;35:127–39. https://doi.org/10.1016/J.JMAPRO.2018.08.001.

234) Wu B, Pan Z, Li S, Cuiuri D, Ding D, Li H. The anisotropic corrosion behaviour of wire arc additive manufactured Ti-6Al-4V alloy in 3.5% NaCl solution. Corros Sci 2018e;137:176–83. https://doi.org/10.1016/J.CORSCI.2018.03.047.

235) Wu W, Xu W, Xue J, Yao P. Effect of cooling and CMT mode process on additive manufacturing. Materials and Manufacturing Processes 2022a;37:1298–309. https://doi.org/10.1080/10426914.2021.2006221.

236) Wu W, Xue J, Wang L, Zhang Z, Hu Y, Dong C. Forming Process, Microstructure, and Mechanical Properties of Thin-Walled 316L Stainless Steel Using Speed-Cold-Welding Additive Manufacturing. Metals (Basel) 2019;9:109. https://doi.org/10.3390/met9010109.

237) Wu W, Xue J, Yao P. A comparative study on single- and double-arc deposition processes. Materials and Manufacturing Processes 2020;35:346–53. https://doi.org/10.1080/10426914.2020.1726947.

238) Xia C, Pan Z, Polden J, Li H, Xu Y, Chen S, et al. A review on wire arc additive manufacturing: Monitoring, control and a framework of automated system. J Manuf Syst 2020;57:31–45. https://doi.org/10.1016/J.JMSY.2020.08.008.

239) Xiong J, Liu G, Yu Y. Fabricating TiAl alloys with various compositions by twin-wire arc AM. Materials and Manufacturing Processes 2024;39:310–9. https://doi.org/10.1080/10426914.2023.2195905.

240) Xiong YB, Wen DX, Zheng ZZ, Li JJ. Effect of interlayer temperature on microstructure evolution and mechanical performance of wire arc additive manufactured 300M steel. Materials Science and Engineering: A 2022;831:142351. https://doi.org/10.1016/J.MSEA.2021.142351.

241) Xizhang Chen, Su C, Wang Y, Siddiquee AN, Sergey K, Jayalakshmi S, et al. Cold Metal Transfer (CMT) Based Wire and Arc Additive Manufacture (WAAM) System. Journal of Surface Investigation: X-Ray, Synchrotron and Neutron Techniques 2018;12:1278–84. https://doi.org/10.1134/S102745101901004X.

242) Xu F, Lv Y, Liu Y, Shu F, He P, Xu B. Microstructural Evolution and Mechanical Properties of Inconel 625 Alloy during Pulsed Plasma Arc Deposition Process. J Mater Sci Technol 2013;29:480–8. https://doi.org/10.1016/J.JMST.2013.02.010.

243) Xu M, Chen Y, Zhang T, Xie J, Wei K, Wang S, et al. Effect of post-heat treatment on microstructure and mechanical properties of nickel-based superalloy fabricated by ultrasonic-assisted wire arc additive manufacturing. Materials Science and Engineering: A 2023;863:144548. https://doi.org/10.1016/j.msea.2022.144548.

244) Xu T, Cui Y, Ma S, Wang J, Liu C. Exploring the inclined angle limit of fabricating unsupported rods structures by pulse hot-wire arc additive manufacturing. J Mater Process Technol 2021;295:117160. https://doi.org/10.1016/J.JMATPROTEC.2021.117160.

245) Xu T, Liu J, Lu T, Jing C, Wang J, Ma S, et al. Fabrication strategy and macroscopic defect control of large-size component based on double-wire arc additive manufacturing. The International Journal of Advanced Manufacturing Technology 2023a;125:2609–25. https://doi.org/10.1007/s00170-023-10882-8.

246) Xu X, Ding J, Ganguly S, Williams S. Investigation of process factors affecting mechanical properties of INCONEL 718 superalloy in wire + arc additive manufacture process. J Mater Process Technol 2019;265:201–9. https://doi.org/10.1016/J.JMATPROTEC.2018.10.023.

247) Yadav A, Srivastava M, Jain PK, Rathee S. Microstructure and tribological behaviour of dissimilar steel functional structure developed via arc-based DED process. Tribol Int 2024a;197:109782. https://doi.org/10.1016/J.TRIBOINT.2024.109782.

248) Yadav A, Srivastava M, Jain PK, Rathee S. Microstructure transformations and improving wear resistance of austenitic stainless steel additively fabricated by arc-based DED process. Defence Technology 2024b;38:194–204. https://doi.org/10.1016/J.DT.2024.02.006.

249) Yang S, Zhang J, Lian J, Lei Y. Welding of aluminum alloy to zinc coated steel by cold metal transfer. Mater Des 2013;49:602–12. https://doi.org/10.1016/J.MATDES.2013.01.045.

250) Yang X, Liu J, Wang Z, Lin X, Liu F, Huang W, et al. Microstructure and mechanical properties of wire and arc additive manufactured AZ31 magnesium alloy using cold metal transfer process. Materials Science and Engineering: A 2020a;774:138942. https://doi.org/10.1016/J.MSEA.2020.138942.

251) Yang X, Liu J, Wang Z, Lin X, Liu F, Huang W, et al. Microstructure and mechanical properties of wire and arc additive manufactured AZ31 magnesium alloy using cold metal transfer process. Materials Science and Engineering: A 2020b;774:138942. https://doi.org/10.1016/J.MSEA.2020.138942.

252) Yang Y, Luan H, Guo S, Liu F, Dai Y, Zhang C, et al. Tribological Behaviors of Inconel 718–Tungsten Carbide Friction Pair with Sulfur Additive Lubrication. Metals (Basel) 2022;12:1841. https://doi.org/10.3390/met12111841.

253) Yangfan W, Xizhang C, Chuanchu S. Microstructure and mechanical properties of Inconel 625 fabricated by wire-arc additive manufacturing. Surf Coat Technol 2019a;374:116–23. https://doi.org/10.1016/J.SURFCOAT.2019.05.079.

254) Youheng F, Guilan W, Haiou Z, Liye L. Optimization of surface appearance for wire and arc additive manufacturing of Bainite steel. The International Journal of Advanced Manufacturing Technology 2017;91:301–13. https://doi.org/10.1007/s00170-016-9621-1.

255) Yuan Q, Liu C, Wang W, Wang M. Residual stress distribution in a large specimen fabricated by wire-arc additive manufacturing. Science and Technology of Welding and Joining 2023;28:137–44. https://doi.org/10.1080/13621718.2022.2134963.

256) Zahidin MR, Yusof F, Abdul Rashid SH, Mansor S, Raja S, Jamaludin MF, et al. Research challenges, quality control and monitoring strategy for Wire Arc Additive Manufacturing. Journal of Materials Research and Technology 2023a;24:2769–94. https://doi.org/10.1016/J.JMRT.2023.03.200.

257) Zeng Z, Cong BQ, Oliveira JP, Ke WC, Schell N, Peng B, et al. Wire and arc additive manufacturing of a Ni-rich NiTi shape memory alloy: Microstructure and mechanical properties. Addit Manuf 2020;32:101051. https://doi.org/10.1016/J.ADDMA.2020.101051.

258) Zhang C, Chen F, Huang Z, Jia M, Chen G, Ye Y, et al. Additive manufacturing of functionally graded materials: A review. Materials Science and Engineering: A 2019;764:138209. https://doi.org/10.1016/J.MSEA.2019.138209.

259) Zhang HT, Feng JC, He P, Zhang BB, Chen JM, Wang L. The arc characteristics and metal transfer behaviour of cold metal transfer and its use in joining aluminium to zinc-coated steel. Materials Science and Engineering: A 2009;499:111–3. https://doi.org/10.1016/J.MSEA.2007.11.124.

260) Zhang T, Li H, Gong H, Ding J, Wu Y, Diao C, et al. Hybrid wire - arc additive manufacture and effect of rolling process on microstructure and tensile properties of

Inconel 718. J Mater Process Technol 2022a;299:117361. https://doi.org/10.1016/J.JMATPROTEC.2021.117361.

261) Zhang W, Lei Y, Meng W, Ma Q, Yin X, Guo L. Effect of Deposition Sequence on Microstructure and Properties of 316L and Inconel 625 Bimetallic Structure by Wire Arc Additive Manufacturing. J Mater Eng Perform 2021;30:8972–83. https://doi.org/10.1007/s11665-021-06137-w.

262) Zhang X, Wang K, Zhou Q, Kong J, Peng Y, Ding J, et al. Element partitioning and electron backscatter diffraction analysis from feeding wire to as-deposited microstructure of wire and arc additive manufacturing with super duplex stainless steel. Materials Science and Engineering: A 2020;773:138856. https://doi.org/10.1016/J.MSEA.2019.138856.

263) Zhang X, Zhou Q, Wang K, Peng Y, Ding J, Kong J, et al. Study on microstructure and tensile properties of high nitrogen Cr-Mn steel processed by CMT wire and arc additive manufacturing. Mater Des 2019;166:107611. https://doi.org/10.1016/J.MATDES.2019.107611.

264) Zhang Y, Cheng F, Wu S. Improvement of pitting corrosion resistance of wire arc additive manufactured duplex stainless steel through post-manufacturing heat-treatment. Mater Charact 2021a;171:110743. https://doi.org/10.1016/J.MATCHAR.2020.110743.

265) Zhang Y, Cheng F, Wu S. The microstructure and mechanical properties of duplex stainless steel components fabricated via flux-cored wire arc-additive manufacturing. J Manuf Process 2021b;69:204–14. https://doi.org/10.1016/J.JMAPRO.2021.07.045.

266) Zhang Y, Wu S, Cheng F. A duplex stainless steel (DSS) with striking tensile strength and corrosion resistance produced through wire arc-additive manufacturing (WAAM) using a newly developed flux-cored wire. Mater Lett 2022;313:131760. https://doi.org/10.1016/J.MATLET.2022.131760.

267) Zheng J, Chen S, Jiang L, Ye XX, Xu C, Li Z. Effect of carbon content on the microstructure and mechanical properties of NiCrFe-7A alloys synthesized by wire arc additive manufacturing. Materials Science and Engineering: A 2022;842:142925. https://doi.org/10.1016/J.MSEA.2022.142925.

268) Zheng Y, Yu Z, Xie J, Chen J, Yu C, Xu J, et al. A numerical model-based deposition strategy for heat input regulation during plasma arc-based additive manufacturing. Addit Manuf 2022;58:102986. https://doi.org/10.1016/J.ADDMA.2022.102986.

269) Zhong Y, Zheng Z, Li J, Wang C. Fabrication of 316L nuclear nozzles on the main pipeline with large curvature by CMT wire arc additive manufacturing and self-

developed slicing algorithm. Materials Science and Engineering: A 2021;820:141539. https://doi.org/10.1016/J.MSEA.2021.141539.

270) Zhou J, Jia C, Guo M, Chen M, Gao J, Wu C. Investigation of the WAAM processes features based on an indirect arc between two non-consumable electrodes. Vacuum 2021;183:109851. https://doi.org/10.1016/J.VACUUM.2020.109851.

271) Zhou S, Xie H, Ni J, Yang G, Qin L, Guo X. Metal transfer behavior during CMT-based Wire Arc Additive Manufacturing of Ti-6Al-4V alloy. J Manuf Process 2022;82:159–73. https://doi.org/10.1016/J.JMAPRO.2022.07.063.

272) Zhou W, Shen C, Hua X, Zhang Y, Wang L, Xin J, et al. Twin-wire directed energy deposition-arc of Ti–48Al–2Cr–2Nb alloy: Feasibility, microstructure, and tensile property investigation. Materials Science and Engineering: A 2022;850:143566. https://doi.org/10.1016/J.MSEA.2022.143566.

273) Zhou Y, Lin X, Kang N, Huang W, Wang J, Wang Z. Influence of travel speed on microstructure and mechanical properties of wire + arc additively manufactured 2219 aluminum alloy. J Mater Sci Technol 2020;37:143–53. https://doi.org/10.1016/J.JMST.2019.06.016.

274) Zhou Y, Lin X, Kang N, Huang W, Wang Z. Mechanical properties and precipitation behavior of the heat-treated wire + arc additively manufactured 2219 aluminum alloy. Mater Charact 2021;171:110735. https://doi.org/10.1016/J.MATCHAR.2020.110735.

275) Zhu M, He F, Yuan YF, Yin SM, Guo SY, Pan J. Effect of Aging Time on the Microstructure and Corrosion Behavior of 2507 Super Duplex Stainless Steel in Simulated Marine Environment. J Mater Eng Perform 2021;30:5652–66. https://doi.org/10.1007/s11665-021-05812-2.

LIST OF PUBLICATIONS

List of papers published in SCI/SCIE journals

1. **Meena, R. P.,** N, Y., & Vipin. A review on wire arc additive manufacturing based on cold metal transfer. ***Materials and Manufacturing Processes*****, Taylor & Francis** *39*(10), (2024) 1315–1341. https://doi.org/10.1080/10426914.2024.2323441 **(Impact Factor-4.8)**
2. **Meena, R.P.,** Yuvaraj, N. & Vipin, V. Investigations and Optimization of Cold Metal Transfer-based WAAM Process Parameters for Fabrication of Inconel 718 Samples using Response Surface Methodology. ***Arabian Journal for Science and Engineering*** **(2024) Springer.** https://doi.org/10.1007/s13369-024-08947-1 **(Impact Factor-2.6)**
3. **Meena RP,** Yuvaraj N, Vipin. Optimization of process parameters of cold metal transfer welding-based wire arc additive manufacturing of super Duplex stainless steel using response surface methodology. Proceedings of the Institution of Mechanical Engineers, **Part E: Journal of Process Mechanical Engineering.** 2024;0(0). https://doi.org/10.1177/09544089241230878 **(Impact Factor-2.3)**
4. **Meena, R.P.,** Yuvaraj, N., Vipin. Experimental investigation of process parameters of cold metal transfer welding-based wire arc additive manufacturing of aluminum 4047 alloy using response surface methodology. **Welding in the world (2024) Springer. DOI :** 10.1007/s40194-024-01817-2 **(Impact Factor-2.4)**

List of papers communicated in SCI/SCIE journals

1. **Meena, R.P.,** Yuvaraj, N. & Vipin. Microstructure and Mechanical Characterisation of Dissimilar Super Duplex Stainless Steel 2507 -Inconel 718 alloy structure built by Cold

Metal Transfer-based Wire Arc Directed Energy Deposition (Communicated to **Journal of Material Engineering and Performance -Springer). (Impact Factor-6.1) Under review**

2. **Meena, R.P.,** Yuvaraj, N. & Vipin. Ultrasonic Vibration Assisted Cold Metal Transfer Direct Energy Deposition of Dissimilar SDSS 2507-IN 718 Alloy parts: Microstructural and Mechanical Characterization (Communicated to **Journal of Engineering Materials and Technology-ASME). Revision Submitted**
3. **Meena, R.P.,** Yuvaraj, N. & Vipin. Wear characteristics of Dissimilar SDSS 2507- IN 718 parts fabricated by Cold Metal Transfer based Wire Arc Additive Manufacturing (Communicated to **Journal of Tribology- ASME**). **Revision submitted**

List of papers published in International Conferences

1. **Meena, R.P.,** Yuvaraj, N. & Vipin. Parameter Optimization of Cold Metal Transfer Process Using Response Surface Methodology for Fabrication of Super Duplex Stainless Steel 2507.
2. **Meena, R.P.,** Yuvaraj, N. & Vipin. Recent Developments in Wire Arc Additive Manufacturing for Sustainable Development.

CURRICULUM VITAE

Mr Rajendra Prasad Meena holds a Bachelor's degree (BTech) in Mechanical Engineering from Maulana Azad National Institute of Technology, Bhopal, India, and a Master's degree (MTech) in (Production) Mechanical Engineering from Malviya National Institute of Technology, Jaipur, India. His primary research interests encompass Wire Arc Additive Manufacturing (WAAM), high-strength alloys, dissimilar alloys, Cold Metal Transfer Welding (CMT), gas metal arc welding (GMAW), tribological characteristics, and optimization techniques. He has published four SCI/SCIE-indexed papers and two international conference papers. He is currently an Assistant Professor in the Mechanical Engineering Department at the University School of Automation and Robotics, East Campus, Guru Gobind Singh Indraprastha University, Dwarka, Delhi, India.